



**HAL**  
open science

# Adaptive full-field multi-fidelity surrogate based optimization dedicated to turbomachinery design

Hanane Khatouri

► **To cite this version:**

Hanane Khatouri. Adaptive full-field multi-fidelity surrogate based optimization dedicated to turbomachinery design. Mechanics [physics.med-ph]. Université de Technologie de Compiègne, 2021. English. NNT : 2021COMP2640 . tel-03632955

**HAL Id: tel-03632955**

**<https://theses.hal.science/tel-03632955v1>**

Submitted on 6 Apr 2022

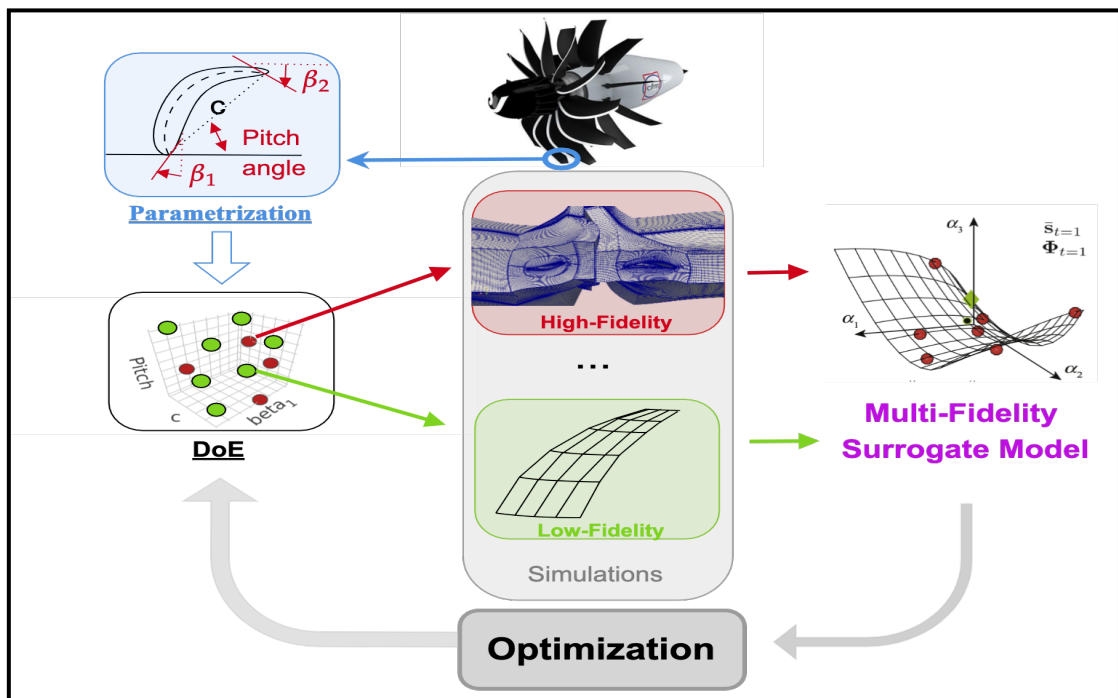
**HAL** is a multi-disciplinary open access archive for the deposit and dissemination of scientific research documents, whether they are published or not. The documents may come from teaching and research institutions in France or abroad, or from public or private research centers.

L'archive ouverte pluridisciplinaire **HAL**, est destinée au dépôt et à la diffusion de documents scientifiques de niveau recherche, publiés ou non, émanant des établissements d'enseignement et de recherche français ou étrangers, des laboratoires publics ou privés.

Par Hanane KHATOURI

*Adaptive full-field multi-fidelity surrogate based optimization dedicated to turbomachinery design*

Thèse présentée  
pour l'obtention du grade  
de Docteur de l'UTC



Soutenue le 6 décembre 2021

**Spécialité** : Mécanique Numérique : Unité de recherche en Mécanique - Laboratoire Roberval (FRE UTC - CNRS 2012)

D2640

THÈSE

**Adaptive Full-field Multi-Fidelity  
Surrogate Based Optimization  
Dedicated to Turbomachinery Design**

présentée par

**Hanane Khatouri**

En vue de l'obtention du grade de

**Docteur  
en Mécanique Numérique**

de l'Université de Technologie de Compiègne

Soutenue le 6 Décembre 2021



## PRÉSENTATION DU JURY

CETTE THÈSE A ÉTÉ ÉVALUÉE PAR UN JURY COMPOSÉ DE :

M. Tariq Benamara, directeur de thèse,  
ingénieur de recherche, CENAERO, Gosselies, Belgique

M. Pierre-Alain Boucard, examinateur,  
professeur des universités ENS Paris-Saclay, laboratoire de mécanique et technologie, Gif-sur-  
Yvette

Mme Delphine Brancherie, examinatrice,  
professeur des universités université de technologie de Compiègne, laboratoire Roberval

M. Piotr Breitkopf, directeur de thèse,  
ingénieur de recherche université de technologie de Compiègne, laboratoire Roberval

M. Pierre Duysinx, rapporteur,  
professeur, université de Liège, LTAS, Belgique

M. Abderrahmane Habbal, rapporteur,  
maître de conférences université de Nice, laboratoire J.A Dieudonné, Sophia-Antipolis

Invités :

M. Jean Demange, ingénieur de recherche, Safran Aircraft Engine, Moissy-Cramayel

Mme Caroline Sainvitu, ingénieure de recherche, CENAERO, Gosselies, Belgique

# Remerciements

Même si, en apparence, le processus d'une thèse de doctorat peut sembler solitaire, il s'agit fondamentalement d'un travail d'équipe autour d'un unique projet. Je tiens à rendre hommage et à exprimer ma profonde gratitude à tous ceux qui, de près ou de loin, ont contribué à sa réalisation et à son aboutissement.

Je remercie tout particulièrement Pr. Piotr Breitkopf et Dr. Tariq Benamara d'avoir co-dirigés cette thèse. Tout au long de ce travail, ils ont su m'apporter un soutien constant, disponibilité et écoute. Leurs connaissances, leurs critiques, et leurs conseils constructifs m'ont permis de mener à bien ce travail. Je voudrais tout d'abord remercier mon directeur de thèse, Pr. Piotr Breitkopf, pour sa compréhension, sa disponibilité permanente et pour les nombreux encouragements ainsi que ses brillantes intuitions. En plus de son appui scientifique, il a toujours été là pour me soutenir et me guider dans les moments de doute. Je remercie Dr. Tariq Benamara pour ses précieux conseils dans ma recherche bibliographique jusqu'à la mise en pratique des différentes pistes de la thèse. Je tiens tout particulièrement à le remercier pour avoir toujours su me proposer des issues là où j'avais du mal à en voir, d'avoir pris de son temps pour aller jusqu'au bout pour m'aider à avancer plus vite dans le travail d'implémentation de la méthodologie de thèse.

J'adresse tous mes remerciements au Pr. Pierre Duysinx et à Pr. Abderrahmane Habbal de l'honneur qu'ils m'ont fait en acceptant d'être rapporteurs de cette thèse. Je remercie Pr. Pierre-Alain Boucard et Pr. Delphine Brancherie qui ont bien voulu être examinateurs. J'exprime ma gratitude au Pr. Pierre-Alain Boucard d'avoir accepté de présider ce jury de thèse. Mes remerciements vont à l'ensemble de mon jury de thèse ainsi que les invités Dr. Caroline Saintvitu et Dr. Jean Demange pour leur contribution à la richesse de l'échange scientifique durant la soutenance de thèse. Leurs remarques m'ont permis d'envisager mon travail sous un autre angle. Un grand merci est consacré à Dr. Ludovic Cauvin d'avoir été le spectateur malgré les conditions actuelles.

Un grand merci aussi à tous les membres de l'équipe Minamo qui étaient présents tout au long de ma thèse. Je remercie tout d'abord Caroline Saintvitu d'avoir toujours suivi avec intérêt l'avancement de ma thèse à travers des réunions d'équipe. Je tiens aussi à remercier Anthony Hendrickx pour son aide notamment en code à mes débuts à Cenaero et son sens de l'humour. Je remercie Benoit Dompierre pour sa solution de covoiturage qui a facilité mes déplacements et rendu possible ma venue à Cenaero dès le premier jour de mon contrat. Je remercie également Kevin Mailleux du support informatique pour sa réactivité quant à la réparation des nombreux problèmes de réseaux, d'oubli de mots de passe et de bugs sur les nouveaux laptops. Je remercie également Ingrid Lepot qui a été à l'origine de l'initiation de la thèse précédente, sans qui cette thèse n'aurait pas vu le jour. Je tiens également à avoir une pensée sympathique pour toutes

les personnes qui savent si bien rendre agréable le cadre de travail et plus particulièrement à Hector Hernandez, Camilla Vieira, Karol Cascavita, Charlotte Marguerite, Margaux Boxho, Gede Parwatha, Ash Mahajan, Michaël Leborgne, . . . Il me sera très difficile de remercier tout le monde car c'est grâce à l'aide de nombreuses personnes que j'ai pu mener cette thèse dans de bonnes conditions.

Les financements accordés par l'Association Nationale Recherche Technologie et le groupe Safran m'ont permis de réaliser cette thèse. Je tiens ainsi à remercier mes encadrants industriels de Safran Aircraft Engines, tout d'abord Virgile Marguin, qui m'a accueilli dans les locaux de Safran, et qui a su m'initier au quotidien d'un ingénieur méthode lors de mes passages sur site. Je remercie Paul Féliot d'avoir repris l'encadrement, et de m'avoir conseillé sur les pistes méthodologiques à suivre, et d'avoir pris le temps de corriger avec précision mon premier article avant sa soumission. Enfin, je remercie Jean Demange d'avoir pu m'aider très rapidement, malgré sa toute récente embauche, de manière assez complète sur tous les aspects de la thèse tant pour la rédaction scientifique, que pour ses connaissances en aérodynamique et turbomachines, son aide a été précieuse. Je le remercie pour sa disponibilité, pour avoir mis en place des réunions hebdomadaires qui m'ont permis de garder un contact permanent avec Safran malgré la distance. C'est grâce à lui que j'ai pu concilier avec plaisir recherche théorique et recherche appliquée au cours de cette thèse. Je tiens à remercier l'ensemble du pôle optimisation qui m'a accueillie, Pierre-Antoine Bernard, Samuel Caillaud, Maxime Vergez, Josselyn Touzeau, Marie Guerder, Sebastien Petit, . . . ainsi que tous les ingénieurs du département méthodes et outils de conception de Safran qui m'ont aidé, répondu à mes questions mais aussi accompagné lors des pauses déjeuner et café.

Je tiens également à remercier Anthony Binder de la société Safran Aircraft Engines, qui a su donner de son temps pour me fournir le cas d'étude aérodynamique et pour ses explications et réponses à mes questions. Il m'est impossible d'oublier Chloé Dumont, ingénieure de recherche à Cenaero pour son aide précieuse pour l'initiation et l'élaboration du cas d'étude. Elle a toujours fait tout son possible pour m'aider. Je remercie également Gabriele Grasso, qui a su prendre le relais de Chloé, pour son importante contribution dans la mise en place de la chaîne de calcul qui a rendu possible son utilisation dans le cadre de ma thèse.

Je remercie toutes les personnes avec qui j'ai partagé mes études et notamment ces années de thèse. Je termine par une profonde pensée à mes parents, ma famille et mes amis pour leur soutien sans faille durant ces trois ans.

# Abstract

In the design optimization of complex systems, the surrogate model approach based on progressively enriched designs of experiments avoids the efficiency problems encountered when integrating simulation codes into optimization loops. However, efficient a priori sampling of the design space quickly becomes costly when using High-Fidelity (HF) simulators, especially in high-dimension settings. On the other hand, in aeronautical design, several simulation tools are frequently available for the same system, usually with a degree of accuracy inversely proportional to the simulation cost. The concept of Multi-Fidelity (MF) proposes to merge different levels of fidelity within a single model with a controlled variance. Based on recent reduced-order modeling techniques, an alternative approach pursues the goal of simulation budget control by replacing expensive models with their approximate full-field equivalents, providing additional insight into scalar surrogates constructed directly from the physical quantities of interest. The two approaches, MF and Reduced-Order Model (ROM), may be combined, allowing additional flexibility in choosing the degree of fidelity required in different areas of the design space.

Reduced basis and MF surrogate-based optimization raise predictability issues when relying on offline sampling, resulting in costly optimization procedures. To address this problem, offline-online strategies, also known as adaptive strategies, are employed to tune the metamodel as the optimization search progresses. The enrichment criterion uses a merit function to predict both the accuracy improvement and the optimization goal. The next point to be evaluated is selected to maximize this criterion iteratively until a suitable stopping condition is reached. The objective is to select the most relevant points in order to reduce the number of calls to the solvers, which would answer a given design problem. Adaptive selection has the advantage of making better use of the available information in a time-efficient way.

This thesis introduces and validates optimization techniques assisted by MF substitution models based on Non-Intrusive reduced basis models. A benchmark case is introduced to test the full-field MF optimization methodologies on an example with characteristics representative of turbomachinery problems. The predictability of the proposed MF Non-Intrusive Reduced-Basis (MFNIRB) surrogate models is compared to classical surrogate models of the literature on analytical and industrial applications.

# Résumé

Dans l'optimisation de la conception de systèmes complexes, l'approche des modèles de substitution basée sur des plans d'expériences progressivement enrichis permet d'éviter les problèmes d'efficacité rencontrés lors de l'intégration de codes de simulation dans les boucles d'optimisation. Cependant, un échantillonnage a priori efficace de l'espace de conception devient rapidement coûteux lors de l'utilisation de simulateurs Haute-Fidélité (HF), en particulier en haute dimension. D'autre part, dans la conception aéronautique, plusieurs outils de simulation sont fréquemment disponibles pour le même problème, généralement avec un degré de précision inversement proportionnel au coût du processeur. Le concept de Multi-Fidélité (MF) propose de fusionner différents niveaux de fidélité au sein d'un modèle unique avec une variance contrôlée. Basée sur les récentes techniques de modélisation d'ordre réduit, une autre approche poursuit l'objectif de contrôle du budget de simulation en remplaçant les modèles coûteux par leurs modèles réduits en champ complet, fournissant une vision supplémentaire des substituts scalaires construits directement à partir des quantités d'intérêt. Les deux approches, MF et modèles réduits, peuvent être combinées, ce qui permet une flexibilité supplémentaire dans le choix du degré de fidélité requis dans différentes zones de l'espace de conception.

L'optimisation assistée par métamodèles et les modèles MF basés sur la réduction de modèle posent des problèmes de prévisibilité lorsque les substituts reposent sur un échantillonnage hors-ligne, impliquant des procédures d'optimisation coûteuses. Pour résoudre ce problème, des stratégies hors-ligne / en ligne, également appelées stratégies adaptatives, sont utilisées pour ajuster le métamodèle au fur et à mesure de la progression de la recherche d'optimisation. Le critère d'enrichissement utilise une fonction de mérite pour prévoir à la fois l'amélioration de la précision et la résolution du problème d'optimisation. Le point suivant à évaluer est sélectionné pour maximiser ce critère de manière itérative jusqu'à ce qu'une condition d'arrêt appropriée soit atteinte. L'objectif est de sélectionner les points les plus pertinents afin de réduire le nombre d'appels aux solveurs, qui répondraient à un problème de conception donné. La sélection adaptative présente l'avantage de mieux utiliser les informations disponibles de manière efficace en termes de temps.

Cette thèse introduit et valide des techniques d'optimisation assistées par des approximations MF à base réduite non intrusive (MFNIRB). Un cas de référence est introduit pour tester les méthodologies d'optimisation MF sur un exemple aux caractéristiques représentatives des problèmes de turbomachines. La convergence des modèles de substitution MFNIRB proposés est comparée à celle des modèles de substitution classiques de la littérature sur des applications analytiques et industrielles.

# Contents

<b>1</b>	<b>Introduction</b>	<b>1</b>
1.1	Context . . . . .	1
1.2	Design optimization . . . . .	2
1.2.1	Overview on Design optimization . . . . .	3
1.2.2	The multi-fidelity aerodynamic physical modelization . . . . .	4
1.2.3	Algorithms to solve design optimization problems . . . . .	5
1.3	Motivation of the thesis . . . . .	7
1.4	Contributions of the thesis . . . . .	8
1.5	Thesis outline . . . . .	9
<b>2</b>	<b>Litterature review</b>	<b>11</b>
2.1	Introduction . . . . .	11
2.2	Surrogate-based optimization . . . . .	13
2.2.1	Surrogate modeling . . . . .	14
2.2.2	Off-line design of Experiment . . . . .	15
2.2.3	Adaptive sampling . . . . .	15
2.3	Multi-Fidelity management . . . . .	17
2.3.1	Correlation analysis . . . . .	17
2.3.2	Data fusion . . . . .	18
2.4	Surrogate modeling for full-field computations . . . . .	24
2.4.1	Reduced-Order Modeling . . . . .	24
2.4.2	Adaptive Reduced-Order Models . . . . .	26
2.5	Multi-fidelity reduced-order methods . . . . .	28
2.5.1	Multi-fidelity vectorial modeling . . . . .	28
2.6	Conclusion . . . . .	31
<b>3</b>	<b>Multi-Fidelity Reduced-Basis Bayesian optimization</b>	<b>32</b>
3.1	Introduction . . . . .	32
3.2	Method . . . . .	33
3.2.1	Multi-fidelity model . . . . .	33
3.2.2	Improvement-based infill criteria . . . . .	35
3.3	Numerical results . . . . .	36
3.3.1	Problem definition . . . . .	36
3.3.2	Convergence of the multi-fidelity model . . . . .	37
3.3.3	Multi-fidelity convergence for variable Low- to High- fidelity distance . . . . .	39
3.3.4	Comparison of infill criteria . . . . .	39
3.3.5	Comparison of multi-fidelity and ordinary kriging enriched surrogate models . . . . .	41

3.4	Conclusions . . . . .	41
<b>4</b>	<b>Methodology improvements for complex expensive models</b>	<b>52</b>
4.1	Introduction . . . . .	52
4.2	Methodology adopted for multi-fidelity model validation . . . . .	53
4.2.1	Construction of reduced-order model of the low-fidelity solution field . . . . .	54
4.2.2	Construction of the Multi-Fidelity Reduced-Order Model . . . . .	57
4.2.3	Infill criterion used for the enrichment strategy during the multi-fidelity optimization procedure . . . . .	60
4.2.4	Implementation of the Multi-Fidelity Reduced-Order model in optimization context . . . . .	64
4.3	Numerical experiments . . . . .	66
4.3.1	Problem definition . . . . .	67
4.3.2	Experimental setup . . . . .	68
4.3.3	Results . . . . .	69
4.4	Recommendations . . . . .	80
4.5	Conclusion . . . . .	82
<b>5</b>	<b>Industrial application</b>	<b>91</b>
5.1	Introduction . . . . .	91
5.2	Design optimization problem . . . . .	92
5.2.1	Physical quantities to optimize . . . . .	92
5.2.2	The optimization design definition of Open-Fan propeller . . . . .	94
5.2.3	Problem formulation . . . . .	95
5.2.4	Low-Fidelity model implementation . . . . .	97
5.2.5	High-Fidelity model implementation . . . . .	99
5.3	Methodology . . . . .	100
5.3.1	Multi-fidelity surrogate-based optimization implementation . . . . .	101
5.3.2	High-Fidelity adaptation to Low-Fidelity full-field outputs . . . . .	102
5.3.3	Condensation : from full-field simulations to quantities of interest . . . . .	102
5.4	Conclusion . . . . .	104
<b>6</b>	<b>Conclusion</b>	<b>105</b>
6.1	Outcomes . . . . .	105
6.2	Perspectives . . . . .	106

# List of Figures

1.1	The innovations planned within the framework of the Aeronautics Research in Europe (ACARE) roadmap for the period 2000-2050 . . . . .	2
1.2	Examples of Airfoil section parameters . . . . .	3
1.3	Propeller geometry representing the different airfoils . . . . .	3
1.4	Hierarchy of Models for Industrial Applications . . . . .	5
2.1	The offline Surrogate Based-Optimization (SBO) strategy . . . . .	13
2.2	The adaptive SBO strategy . . . . .	16
2.3	Illustration of Multi-Fidelity scaling (or corrective) approaches . . . . .	19
2.4	Baseline of an efficient supersonic air vehicle (ESAV) model [Lickenbrock et al., 2020]. . . . .	20
2.5	The full-field SBO strategy . . . . .	24
3.1	Values of the objective function and of the constraints functions of High-Fidelity (HF) and Low-Fidelity (LF) . . . . .	43
3.2	Snapshots obtained for the 4 points Design of Experiment (DoE) . . . . .	44
3.3	The convergence of the MF trend, MF and Ordinary Kriging (OK) models of the $c_1$ . . . . .	45
3.4	The convergence of the Multi-Fidelity (MF) trend, MF and OK models of $c_2$ . . . . .	46
3.5	Evolution of the relative error for a sample experiment . . . . .	47
3.6	Evolution of the relative error at the theoretical optimal point for multiple runs. . . . .	48
3.7	Optimization results obtained using the $EI_c$ criterion. . . . .	49
3.8	Optimization results obtained using the $EI_c$ and $PI_c$ . . . . .	50
3.9	Evolution of the relative error for enriched and random DoE for multiple runs . . . . .	51
4.1	Comparison between different $EI$ based enrichment results of MFNIRB assisted optimization beginning from DoE of the size $M = 4$ . . . . .	70
4.2	Comparison between $PI_c$ , $EI_{c,w}$ and $variance_c$ infill based optimization. . . . .	71
4.3	Comparison between $EI_{c,w}$ and $variance_c$ error evolution with infill . . . . .	72
4.4	Comparison between single and multi-fidelity enrichment for repeated experiments . . . . .	73
4.5	Comparison between enrichment of different initial DoE sizes . . . . .	74
4.6	Comparison between error evolutions with enrichment of the different constraints knowledge cases. . . . .	83
4.7	MFNIRB optimization using $EI_{c,w}$ infill criterion considering $\tilde{c}_1 = c_1^{HF}$ and $\tilde{c}_2 = c_2^{HF}$ . . . . .	84
4.8	MFNIRB optimization using $EI_{c,w}$ infill criterion considering $\tilde{c}_1 = c_1^{HF}$ . . . . .	85
4.9	MFNIRB optimization using $EI_{c,w}$ infill criterion considering $\tilde{c}_2 = c_2^{HF}$ . . . . .	86

4.10	Case $M_h = 4$ . Comparison between different MFNIRB cases with and without LFPOD. Evolution of $\tilde{e}_{rr}^{(iteration)}$ and its variance for multiple runs at each infill iteration. . . . .	87
4.11	Comparison between different MFNIRB cases with and without LFPOD, case $M_h = 10$ . . . . .	87
4.12	MF $\tilde{f}_{MF}$ prediction, versus LF and HF snapshots. Case where Ratio = 1 $M_h = 100$ . . . . .	88
4.13	MF $\tilde{f}_{MF}$ prediction, versus LF and HF snapshots. Case where Ratio = 1 $M_h = 5$ . . . . .	88
4.14	MF $\tilde{f}_{MF}$ prediction with HF basis truncation, versus LF and HF snapshots. Case where Ratio = 1 $M_h = 100$ . . . . .	88
4.15	MF $\tilde{f}_{MF}$ prediction with HF basis truncation, versus LF and HF snapshots. Case where Ratio = 20 $M_h = 5$ . . . . .	89
4.16	Comparison between the obtained $\tilde{J}_{MF}(\boldsymbol{\chi})$ map with its constrained $\tilde{c}_{1MF}(\boldsymbol{\chi})$ and $\tilde{c}_{2MF}(\boldsymbol{\chi})$ areas preliminary optimization. . . . .	89
4.17	Comparison between the ratio 1 and 2 based maps of $\tilde{J}_{MF}(\boldsymbol{\chi})$ with constrained $\tilde{c}_{1MF}(\boldsymbol{\chi})$ and $\tilde{c}_{2MF}(\boldsymbol{\chi})$ areas in the beginning of preliminary optimization. . . . .	90
4.18	Comparison between the obtained $\tilde{J}_{MF}(\boldsymbol{\chi})$ map with its constrained $\tilde{c}_{1MF}(\boldsymbol{\chi})$ and $\tilde{c}_{2MF}(\boldsymbol{\chi})$ areas preliminary optimization. . . . .	90
5.1	The Open-Fan Engine [Guy Norris, 2021, source : <a href="http://www.aviationweek.com">www.aviationweek.com</a> ] . . . . .	92
5.2	Forces applied on the aircraft [Gallard, 2014]. . . . .	93
5.3	Aerodynamic forces applied on a blade at its center of pressure and elementary forces at the section A-A (adapted from [Marinius, 2011]). . . . .	93
5.4	Airfoil shape parameters. . . . .	95
5.5	Typical civil transport aircraft mission profile [Gallard, 2014]. . . . .	96
5.6	LF simulation . . . . .	98
5.7	Open-Fan sytem components . . . . .	98
5.8	LF simulation discretization [Leborgne et al., 2015] . . . . .	99
5.9	HF simulation . . . . .	99
5.10	Definition of the Open-Fan aerodynamic mesh. . . . .	100
5.11	Main steps of the multi-fidelity implementation from the model construction to infill . . . . .	101
5.12	Illustration of the blade sections reconstruction from $n_r$ sections ( $n_r = 5$ in this example) . . . . .	103
5.13	The condensation step : from input $\mathbf{f}(\mathbf{r}, \boldsymbol{\chi})$ to the scalars quantities of interest $\eta_p(\boldsymbol{\chi})$ and $c_T(\boldsymbol{\chi})$ . . . . .	103

# List of Tables

3.1	Mean over the design variables $\vartheta$ of the "High-Fidelity (HF)-to-Multi-Fidelity (MF)" models relative error for the objective and constraints when the number of available HF simulations successively equals to 4, 40 and 400 points. . . . .	38
4.1	Numerical experiments performed in the present chapter. . . . .	69
4.2	$PI_c$ , $EI_{c,w}$ and $variance_c$ cases results . . . . .	72
4.3	$EI_{c,w}$ and $variance_c$ based optimization comparison results. . . . .	73
4.4	Results of MFNIRB model based on and without Low-Fidelity (LF) Non-Intrusive Proper Orthogonal Decomposition (NIPOD). . . . .	78
5.1	Open-fan blade geometry parameters . . . . .	95
5.2	Open-Fan physical conditions . . . . .	96

# List of Algorithms

1	Design of Experiment (DoE) enrichment . . . . .	36
2	Low-Fidelity (LF) Non-Intrusive Proper Orthogonal Decomposition (NIPOD) offline phase . . . . .	57
3	LF NIPOD online phase . . . . .	57
4	MFNIRB offline phase . . . . .	60
5	MFNIRB online phase . . . . .	60
6	MFNIRB assisted with single-fidelity DoE enrichment . . . . .	65
7	MFNIRB assisted with multi-fidelity DoE enrichment . . . . .	67

# Chapter 1

## Introduction

The research presented in this thesis, was carried out in the context of the growing interest of the industry for automated optimization techniques. In that regards, the present work is partially funded by the engine manufacturer Safran Aircraft Engines. This introduction is intended to provide the context, the motivations of this work, as well as an overview of the thesis content.

### 1.1 Context : the need for innovation in jet engine design

Aeronautics Research in Europe (ACARE) defined guidelines for European research from 2002 to 2008, and with the International Civil Aviation Organization (ICAO), regulations for medium-term aircraft performance to be achieved by 2020. In 2002, the targets for 2020 are a reduction of 50 % in carbon dioxide emissions, 80 % cut in nitrous oxides emissions, and 50 % of effective perceived noise from their 2000 levels. These are completed by a more ambitious plan by International Coalition for Sustainable Aviation (ICSA) governments and the aviation industry to reinforce the action with aspirations of achieving “zero climate impact” by 2050 [ICSA, 2019].

The reduction of pollutant emissions requires a consequent increase in engine efficiency. This can be achieved by combining new, lighter and stronger materials, such as composites, more efficient fuels, and a highly optimized aerodynamic design of the aircraft. This also involves innovation in engine architecture, which can significantly reduce the amount of fuel and thus pollutants released. Figure 1.1 shows the main innovations undertaken by Safran to achieve these goals between 2000 and 2050 through an improvement in fuel consumption from 20% in 2000 to 60% in 2040. The Sustainable And Green Engines (SAGE) 2 consortium was initiated by Safran as part of the European Clean Sky project [Brouckaert, 2015, source: [cleansky.eu](http://cleansky.eu)] to produce an innovative non-inducted aircraft engine architecture. In this context, the Open-Rotor project was launched in 2008 as part of the Clean Sky initiative, led by Safran. Higher propulsive efficiencies are achieved for turbofans by increasing the Bypass Ratio (BPR) through increasing the diameter of the fan, but the efficiency of this improvement decreases as the nacelle diameter, and thus weight and drag, increases. This engine architecture has the potential to deliver further improvements in specific fuel consumption compared with engines such as the LEAP family entered service in 2017, and with advanced turbofans, such as Ultra-High Bypass Ratio (UHBR) engines.

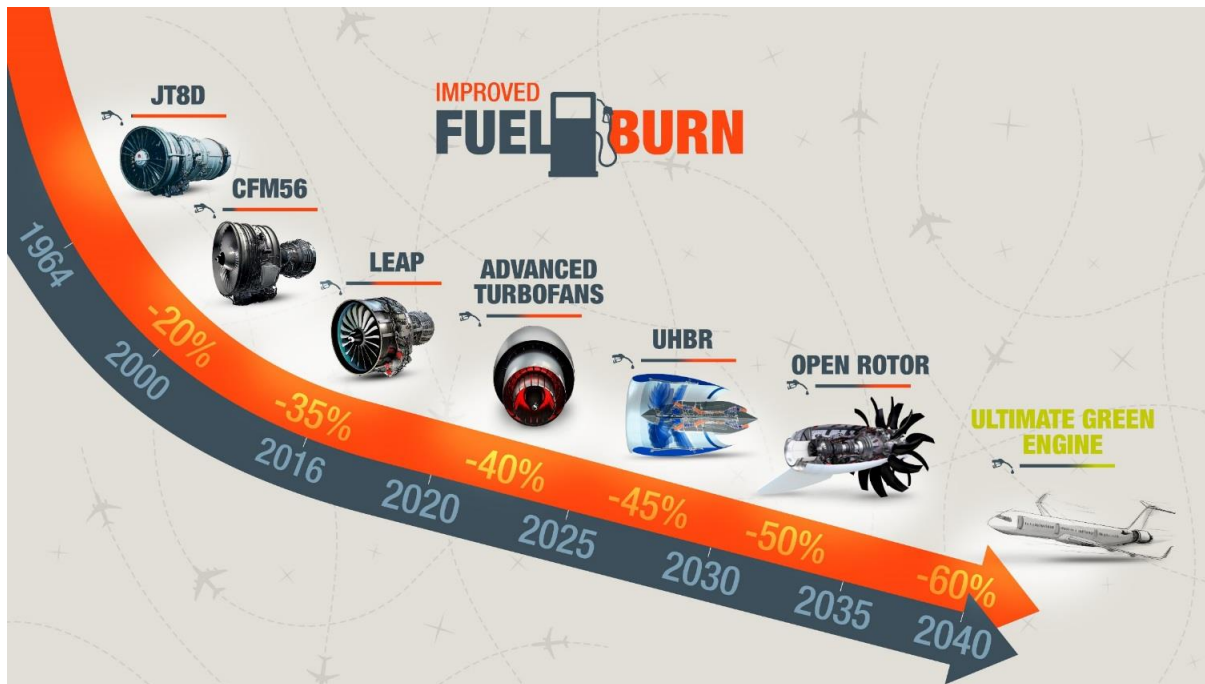


Figure 1.1: The innovations planned within the framework of the ACARE roadmap for the period 2000-2050 (source : [Safran, 2017]).

Open-rotor engines remove this limitation by operating the propeller blades without a surrounding nacelle, allowing ultra-high BPRs to be achieved. The new Contra-Rotating Open-Rotor (CROR) engine demonstrated the highest BPR, therefore fuel economy and emissions [LAAME-CROW, 2016].

However, there is still room to improve the economic viability of the CROR engine compared to the traditional turbofan. To reduce complexity, a single-rotor architecture has been investigated by General Electrics (GE) Aviation and Safran Aircraft Engines, and is so far one of the most promising answers to these environmental requirements. The main challenges are the validation of the improved acoustic performance and the promise of economic viability (but also the Safety of flights and passengers in case of loss of the engine blade or the adaptation of the ground infrastructure). Indeed, the removal of a rotor is associated with less noise, i. e. less interaction in the flows between the two rotors, mainly responsible for the noise increase [Leborgne et al., 2015], less complex maintenance, but also a considerable gain in weight, hence in overall costs and a better efficiency. The achievement of these objectives is subject to a multidisciplinary optimization, from the dynamic strength of the materials to the optimization of the noise reduction induced by this new architecture. Hence, the methodology proposed in this thesis is demonstrated on such next generation configuration.

## 1.2 Design optimization to tackle the need for engine performances improvement

Evolving the geometry can improve quantities of physical interest (such as efficiency, etc.). Several geometries are tested using simulations, which allow to evaluate the physical quantities to be improved (e.g. maximizing the efficiency, or minimizing the mass, etc.). The performances or the quantities of interest are obtained by performing aerodynamic simulations of

flows along the wing surface, in order to estimate these physical quantities. In general, the geometries are modified in a way to maximize lift and minimize drag, leading to a better use of the thrust supplied by the jet engine. Engine thrust is also improved by optimizing the control of the flow to reduce the aerodynamic losses.

### 1.2.1 Overview on Design optimization

In aerodynamic optimization, a design is parametrized, in general, using certain geometric parameters that control the shape of a blade, such as thickness, chord (represented Figure 1.2) and angles of attack  $\alpha$  (represented Figure 1.3).

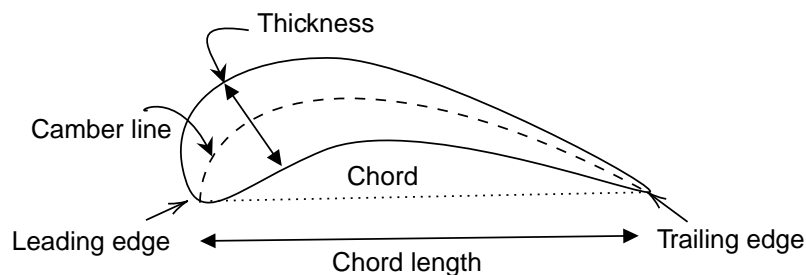


Figure 1.2: Examples of Airfoil section parameters

Some of these parameters may be chosen as design variables. These design variables are varying within a fixed range to form the design space and may be limited by constraints. The blade design is based on section profiles to be studied with parameters whose value varies for each blade section height.

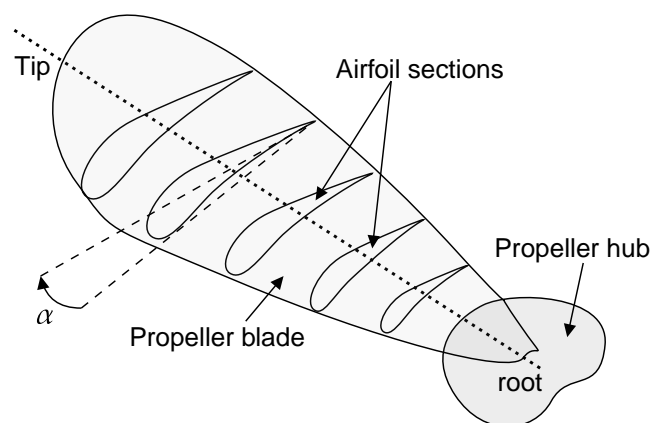


Figure 1.3: Propeller geometry representing the different airfoil sections (Adapted from : [Chopade et al., 2021])

In the context of shape optimization, the aerodynamic sections are approximated by continuous functions in order to allow their modification throughout this procedure. Several approaches have been used, in particular polynomial interpolation which is a relatively simple method to implement. However, it has limitations in terms of robustness, where a local modification can very quickly lead to large global modifications of the geometry. This is where the

Bezier curves [Farin, 2002] are useful, wherein the defined points are points orienting the curve, and not an interpolation. As a result, the changes in the control points have less impact, as interpolation is no longer a constraint. This method also has its limitations, this time due to the large number of control points needed to approximate the profile. This limitation appears more for complex shapes. For these cases, alternative to Bezier curves may be a Bspline [De Boor, 1978, Piegl, 1991]. This approach consists in assembling large portions of low order polynomial curves to represent complex geometries. Such approach is faster, however, as it is only composed of polynomials, the Bspline remains limited for the representation of certain shapes. An extension of this approach, the Non Uniform Rational Basis Spline (NURBS), has been proposed with the substitution of the polynomial model by rational fractions of polynomials.

Blades are designed using few key sections at various height of the blade. While a lot of physical quantities can be derived from 2D profiles, if a global representation of the behavior along the blade is required, some information can only be obtained from a 3D representation. Usually, the various 2D sections studied at different heights are piled up (Figure 1.3) and linked by continuous laws, corresponding to the evolution of parameters as one moves away from the axis of rotation. The piling direction may be defined by a straight line perpendicular to the axis of rotation, by a curve defined by the shape surrounding the blade, or by a curve with parameters in space.

## 1.2.2 The multi-fidelity aerodynamic physical modelization

Once aircraft engine blades or wings profiles are defined, the geometry must be tested in a virtual model intended to reproduce the engine's physical behavior as accurately as possible. There are several ways to simulate physical systems with different degrees of accuracy. Aerodynamic experiments, in particular, are very expensive and time-consuming procedures, but accurate enough for certification.

To numerically reproduce the physical conditions of expensive experiments such as the wind tunnel, assumptions about the physics are needed to provide models with different design fidelities. The Euler equations neglect shear stresses, heat conduction terms and flows assumed to be inviscid [Hirsch, 2007]. The viscosity and turbulence terms are not covered by the Euler equations, which is the case of the Navier-Stokes equations. The approaches using these assumptions are characterized by different complex models of turbulence. Other methods provide a significantly more accurate description of the physical phenomena, but are also highly expensive, like the Large Eddy Simulation (LES), which solves turbulence while modeling the small scales, and the Direct Numerical Simulation (DNS), which solves all the scales of turbulence. For transonic conditions, this method remains unaffordable even for high-performance systems [Pope, 2000, Deck et al., 2014]. Due to its low computational cost compared to the accuracy and costs of LES and DNS models, Reynolds-Averaged Navier-Stokes (RANS) simulations are now widely used in academia and industry. Figure 1.4 illustrates these models, from the most simplified to the most accurate, along with the different assumptions that allow simplifying the physical fidelity.

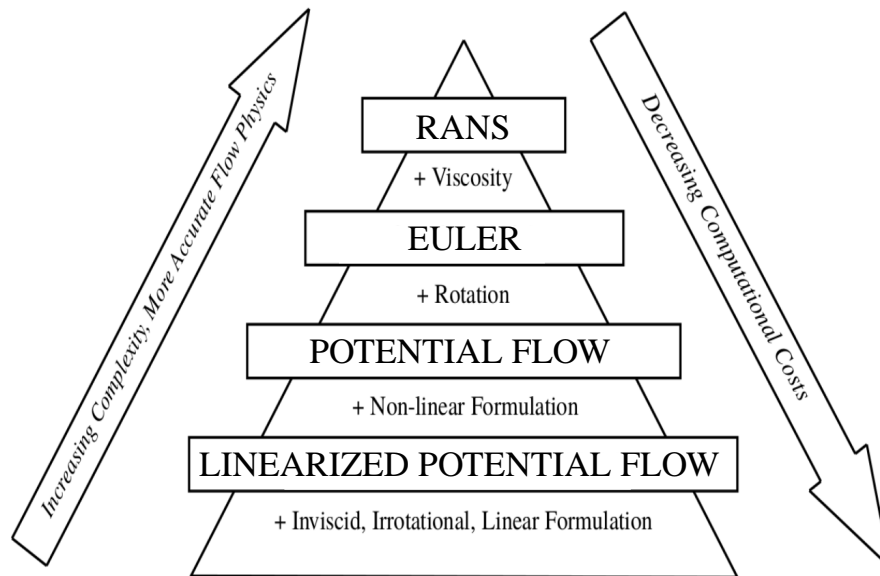


Figure 1.4: Hierarchy of Models for Industrial Applications [Jameson & Fatica, 2003]

As presented in the previous section, the full 3D geometric rendering takes into account all the sections and approaches the whole with an interpolation model. The final modeling is more realistic but involves considering not only one group of variables defining the shape of a single section, but several, and thus multiplying the data processing and physical simulation time. In such cases, other approximations and assumptions can also be useful to speed up the design and pre-design phases, namely the mesh size or the use of lowering the convergence requirements of the solver to leverage partially converged models as a first design trend. Throughout the design process, these models are essential for industrial design. Budgetary constraints direct future challenges towards a higher fidelity for lower cost, this is the main driver of the multi-fidelity modeling strategy. This approach consists in using several levels of solver costs, ranging from potential methods to Euler and RANS, to build a model with different levels of fidelity. The main interest of this strategy is to use a less accurate model when the required accuracy is sufficient and to correct with more limited accurate data, when it is not possible to have this information with the low fidelity model. This concept has begun to gain a foothold in research, industry and academia, and its efficiency has been demonstrated mainly in the Computational Fluid Dynamic (CFD) field. It is also promising in researching an optimal where the use of the solver is repetitive and sometimes only requires a trend or direction of search.

### 1.2.3 Algorithms to solve design optimization problems

In shape optimization, a first step is to define the geometry to be optimized and to use it in an optimization loop that links these parameters to a physical model, allowing to evaluate the physical quantities to be optimized (such as energy efficiency, weight, etc.). The optimization problem can then be defined mathematically and solved in the optimization loop. There are direct and inverse optimization solution methods [Li & Zheng, 2017a]. Inverse methods involve identifying the shape of the profile from the distribution of a quantity of interest such as the pressure coefficient, by iteratively changing the geometry. There are various optimization

methods that use derivatives, called adjoint methods, only in the underlying situation where the solver provides this information. The second category is direct methods, designed to maximize or minimize quantities of interest while respecting one or more constraints. The codes generate directly these quantities according to the geometry parameters to evaluate the flow solution. These values must meet the desired constraints and flow conditions, otherwise, the initial airfoil geometry is modified. This process is repeated until the conditions are met. The entire process is expensive, as it requires repeated calls to the solver until convergence is achieved. Direct solution optimization often uses both gradient and stochastic methods. Gradient methods use information about the derivative of the objective and constraint functions to identify the search direction of the optimization. The search is based on a first point where the local gradient is evaluated for a change in the design variables. The search direction can be obtained by the steepest descent method, the conjugate gradient method, quasi-Newton techniques, or adjoint formulations. The optimum is local, there is no guarantee that it is also global, and can be obtained if the functions are differentiable and locally convex.

Information about the gradient is not always available. To remedy this, more global meta-heuristics [Sahab et al., 2013] such as the optimization methods Surrogate Based-Optimization (SBO) (which will be detailed in the next section). These are most often stochastic methods and are more likely to identify the global optimum. This is the case for example with evolutionary algorithms where the starting points of the optimization are a set of candidates that will undergo transformations such as mutation and recombining in the genetic algorithm, allowing to rank the individuals to select the best candidate for the optimization problem. These transformations allow exploring the function in a more global way by avoiding that the function depends on the starting point and remains stuck at a local optimum.

These approaches, also known as gradient-free or zero-order methods, require the evaluation of the objective function, while gradient-based approaches additionally require the gradients of the objective function with respect to all design variables. The gradients can be computed by repeated evaluation of the function in a finite difference scheme [Martins et al., 2003] or by the adjoint, method [Jameson, 2000, Duta et al., 2007]. Many zero-order optimization methods are inspired by nature and are based on meta-heuristics. Some of them exploit the design space by a local search, like Tabu search [Glover, 1989] and simulated annealing [Kirkpatrick et al., 1983]. Others reproduce population evolutions inspired by nature, such as particle swarm optimization [Kennedy & Eberhart, 1995] and evolutionary algorithms [Galvan et al., 2003]. They have been successfully applied to many turbomachinery applications, including multi-objective and multidisciplinary optimization problems [Pierret, 2005, Leborgne et al., 2015, Li & Zheng, 2017b]. One of the most notable limitations of gradient-free algorithms is the high amount of function evaluation required to incrementally reach the optimum, typically for certain aerodynamic problems that can reach hundreds of design parameters.

In the context of gradient-free optimization where the search for the optimum requires many evaluations, simulations must be accelerated to maintain viable execution times. Considering the state of the art, the convergence of gradient-free optimization methods are accelerated either by reducing the complexity of the objective function evaluation by replacing it with a simpler model within SBO (a so-called meta-model or surrogate model) that generates a faster but less accurate evaluation of the design. In the same spirit, reduced-order methodologies propose to directly replace the partial differential equation (PDE) by an approximate model, these approaches require access to the solver and are called intrusive. The non-intrusive ap-

proaches [Coelho et al., 2008, Coelho et al., 2010a] are able to approximate the full-field outputs and have demonstrated a better accuracy compared to the previous approach based on an approximation of the objective function. Finally, a other way is to exploit the advances in computer science by using high performance computing (HPC) to accelerate the execution of numerical simulations [Arabnia, 2012] . The former methods accelerate the convergence of the optimization to improved designs for a given computational budget, while the latter adapt the optimization to higher computational power. In this thesis, work on HPC is out of scope, and our interest is to improve the budget of the optimization loop by accelerating convergence through the non-intrusive Multi-Fidelity (MF) SBO framework.

### 1.3 Motivation of the thesis

The focus of this thesis is to improve the computational cost by reducing the errors as much as possible through multi-fidelity. The combination of High-Fidelity (HF) and Low-Fidelity (LF) has the potential to improve the data of LF solvers while keeping a reasonable resolution time. On the other hand, the knowledge of the physical model is extended by taking into account more information, brought by the Reduced-Order Model (ROM) approaches, thus increasing the representativeness and the physical accuracy.

- **Multi-fidelity Aerodynamic modeling** : An improved benefit from low-cost information for more efficiency

HF simulation models such as 3D-RANS and LES have reached a level of maturity that allows them to be sufficiently predictive to be used in aeronautical design optimization loops. However, they imply an intensive use of computing resources ranging from a few hours to entire days of computation on supercomputer architectures and the generation of several gigabytes of data. To tackle this issues, we propose to take advantage of several levels of fidelity. LF models such as simplified physics can be used to compute approximations of fluid flow using limited resources. This is the so-called MF approach, which combines the respective cost and accuracy advantages of LF and HF in a common framework. The use of multiple fidelities has been introduced to temper the cost of high-dimensional multi-disciplinary design breaking the "curse of dimensionality" [Taylor & Einbeck, 2013, Shan & Wang, 2010]. This concept allows to predict improved design location by taking into account a large amount of LF cheap data and few expensive HF available data and have proven their efficiency in many applications in aerodynamic optimization.

- **Full-field surrogate model** : Better benefit from the available information

While surrogate modeling techniques mine embedded quantities, reduced order model captures spatial information in a model approximation by expressing the solution as a linear combination of a limited number of modes. Thereby, assuming that few independent modes govern the system dynamics, a significant reduction in the computational cost of the solution can be achieved [Coelho et al., 2008]. This approach takes into account the full field outputs of the quantities of interest. It consists in building a reduced order model of the solver and expressing, the objective function and the constraints in terms of approximate field. In addition to saving time, this approach has the potential to better understand the detailed characteristics of the flow at each optimization iteration.

- **Adaptive surrogate based optimization** : Off-line/on-line learning for a more efficient optimization

ROM-based SBO and MFM raise predictability issues when ROM-based surrogates rely on offline sampling, resulting in costly optimization procedures. To address this problem, offline-online strategies, also known as adaptive strategies, are employed to tune the metamodel as the optimization search progresses. The enrichment criterion uses a merit function to predict both the accuracy improvement and the optimization goal. The next point to be evaluated is selected to maximize this criterion iteratively until a suitable stopping condition is reached. The objective is to select the most relevant points in order to reduce the number of calls to the solvers, which would answer a given design problem. Adaptive selection has the advantage of making better use of the available information in a time-efficient way.

## 1.4 Contributions of the thesis

The present research focuses on the development of efficient adaptive non-intrusive multi-fidelity substitution models that provide a comprehensive approximation of complex turbo-machinery simulations. In this PhD thesis, three main original contributions may be identified:

- **Developpement of a stochastic Multi-fidelity modelization that take into account the full-field simulation outputs:** The proposed method is a metamodel that approaches the quantities of interest from different levels of cost and accuracy of solver. It takes the so-called multi-fidelity corrective approach from the literature with the difference that the correction is not applied to the low-fidelity but rather to the multi-fidelity directly. The multi-fidelity representation comes from a method used in the literature in the framework of reduced models. It consists in an orthogonal projection of the low-fidelity snapshots on the reduced basis built from the high-fidelity data. It is constructed from the full field data relying on a Reduced Basis method from the literature. Thereby, the physical information is better taken into account in order to improve the physical representativeness.
- **Adaptation of intermediate approximation level under expensive low-fidelity optimization** : Each MFNIRB prediction involves a call to the LF solver. The problem is that an SBO procedure requires several evaluations, like the GA which needs a high number of evaluations quickly becoming intractable for complex optimization problems. Therefore, a reduced order model for the LF function itself was introduced, thus introducing an additional level of fidelity in the MFNIRB scheme. The idea of the proposed approach is to learn the Non-Intrusive Proper Orthogonal Decomposition (NIPOD) basis in offline phase, and use it to predict the LF vectors online.
- **Enrichment criteria adapted to the proposed method** : The additive corrections are modeled by a stochastic metamodel based on the Gaussian process. The proposed idea is to use this framework to enrich the multi-fidelity metamodel online. The method improves the surrogate model by using statistical filling criteria adapted to account for the violation of constraints such as the probability of improvement and the expected improvement criteria from the literature.

- **Integration in Minamo :** The multi-fidelity methodology has been coupled to the Global Optimization commercial software Minamo used on complex multi-modal optimization at Safran Aircraft Engines.

## 1.5 Thesis outline

The thesis is divided into five chapters. The work is organized in terms of an introduction to the objectives of the thesis, followed by a literature review, the concept development, and finally, the proposed approaches are implemented and applied to analytical and industrial test cases.

Chapter 1 introduces the industrial context, the main motivations, and contributions of this thesis in optimization of aeronautical design. First, the need for innovation in aircraft engine design is presented and advances the need to optimize existing prototypes, particularly of the currently studied innovative Open-Fan engine. Then, the components of the optimization loop dedicated to the design are presented. On the one hand, the definition of the geometries by adapted parametrization methods, then simulations at different cost levels, motivate the search for multi-fidelity approaches to improve the physical representation progressively. On the other hand, solving the optimization problem requires mathematical programming methods. Integrating both aspects within a surrogate-based framework guides the research work presented in the present work.

Chapter 2 reviews the principal axes of the solutions for Central Processing Unit (CPU)-intensive optimization problems proposed in the literature. On the one hand, scalar and full-field optimization in the context of single-fidelity and multi-fidelity are presented. On the other hand, full-field SBO methods relying on the Reduced-Order Models are detailed. For each approach, the corresponding adaptive sampling strategies are presented. The purpose is to review methods integrating costly simulations within adaptive surrogate-based optimization. Adaptive methods reduce the cost by taking into account the information acquired progressively during the optimization iterations. In this spirit, the multi-fidelity concept exploits the range of available solvers, even of variable accuracy, to merge data from multiple fidelity levels. Finally, model reduction methods can also achieve cost reduction, offering better insight into detailed solution features brought by full-field consideration.

Chapter 3 details the adaptive Multi-Fidelity Non-Intrusive Reduced-order Based method, involving two-fidelity levels of full-field simulation responses and a corresponding enrichment strategy. Contrary to standard non-intrusive Proper Orthogonal Decomposition (POD) relying on the regression of POD coefficients, the proposed contribution relies on the multi-fidelity trend obtained by the projection of low-fidelity vector fields on the reduced basis obtained from a limited number of high-fidelity runs. Then, the interpolation of quantities of interest is enforced by Gaussian Process regression (kriging). The scheme is tested on an analytical two-level fidelity case derived from quantities inspired by aerodynamic vector outputs. A comparative study is performed between constrained single- and bi-fidelity optimization using a surrogate-based optimization loop. The multi-fidelity fusion appears to exhibit the potential for low-fidelity to capture features requiring otherwise expensive high-fidelity data. Thus, improving low-fidelity requires a reduced cost compared to high-fidelity only.

Chapter 4 introduces an additional, intermediate level of low-fidelity non-intrusive POD

vector approximation for the cases when even the low-fidelity requires non-negligible computational effort. The reduced multi-fidelity method is detailed and adapted to both the single and multi-fidelity enrichment procedure, exploiting the statistical information given by the mean and variance of the Gaussian Process Regression. The method requiring to call the low-fidelity solver at each evaluation within the SBO, the approach is further improved by the additional NIPOD level. Experiments are conducted to test the introduced enrichment criteria and meta-modeling approaches on constrained single-objective optimization. In addition, tests are conducted to improve the handling of multi-fidelity data, suggesting further work on the multi-level fidelity enrichment strategy.

Chapter 5 deploys the multi-fidelity framework on an industrial case and investigates how the abstract concepts presented in the previous chapters may be implemented within the simulation-based design process. The choice of the industrial application case is the Open-Fan engine, currently of interest to Safran Aircraft Engines designers. The LF consists of a Lifting Surface model and the HF RANS aerodynamic model of the Open-Fan propellers. The two fidelity levels of simulations allow stating the efficiency maximization problem constrained by mechanical resistance constraint. The corresponding MFNIRB model is illustrated within the optimization software Minamo edited by Cenaero.

Chapter 6 terminates the thesis with general Conclusions and perspectives on future research.

Chapter 3 is derived from a peer-reviewed research paper in *Advanced Modeling and Simulation in Engineering Sciences* titled "Constrained multi-fidelity surrogate framework using Bayesian optimization with non-intrusive reduced-order basis". The bibliography research proposed in Chapter 2 is issued from the paper, currently under review by *Advanced Modeling and Simulation in Engineering Sciences* journal, titled "Metamodeling techniques for CPU-intensive simulation-based design optimization - a survey".

# Chapter 2

## Literature review

### 2.1 Introduction

Several computation methods with varying fidelity<sup>1</sup> have been developed over the past decades to simulate fluid dynamics [Jameson et al., 2002]. High-Fidelity (HF) simulation models such as 3D-Reynolds-Averaged Navier-Stokes (RANS), and Large Eddy Simulation (LES) have reached a maturity level that allows them to be predictive enough to be used within aeronautical parts design optimization loops [Pinto et al., 2017]. However, these imply extensive computer resource utilization ranging from hours to full days of computation on supercomputer architectures and the generation of several gigabytes of data. On the other hand, Low-Fidelity (LF) models such as simplified physics, categorization [Fernández-Godino et al., 2016, Peherstorfer et al., 2018], mesh coarsening [Benamara, 2017, Le Gratiot, 2013] or relaxed convergence criteria [Courrier et al., 2016], can be used to compute fluid flow approximations using limited resources. The Multi-Fidelity (MF) optimization approach combines the LF's and HF's respective advantages regarding cost and precision within a common framework. The first category of Multi-Fidelity Model (MFM) consists of exploring the LF values to determine the most interesting zones in the design space (for example the region of interest for an optimization problem) to reduce the calls to the expensive HF solver. This type of methods is not properly referred to as MFMs, since the HF and LF levels are not merged into a single model. The MF combination techniques use most of the time a surrogate model to integrate multiple fidelity levels.

Surrogate modeling consists in building a regression model from a set of available samples obtained from a Design of Experiment (DoE) allowing to predict the values of the function at interesting points. It avoids repeated calls to the simulation software in the design loops. Applications are uncertainty analysis, statistical inference (data-driven) [Wang et al., 2019, Cozad et al., 2015] or multi-disciplinary [Sobieszczanski-Sobieski & Haftka, 1996, Coelho et al., 2010b, Martins & Lambe, 2013, Colomer et al., 2021], shape [Xiao et al., 2010, Skinner & Zare-Behtash, 2017, Han et al., 2020] or topology optimization [Mukherjee et al., 2021]. Reviews on Surrogate Based-Optimization (SBO) are provided by [Simpson et al., 2001, Queipo et al., 2005, Forrester & Keane, 2009, Shan & Wang, 2010] where references on DoE techniques, surrogate modeling, and SBO applications are detailed. Later, SBO techniques applied to the aerodynamic field were reviewed by [Yondo et al., 2018], and a more general review was published by [Ye & Pan, 2019] on surrogates, DoE, and adaptive strategies in engineering

---

<sup>1</sup>The term fidelity refers here to both the time of a calculation and its accuracy [Fernández-Godino et al., 2016].

applications. In the present review, we focus on the construction of surrogate models when multiple levels of fidelity are available, in the SBO context.

Alternatively to the SBO frameworks, the evaluation costs may be also reduced by two families of Reduced-Order Model (ROM)s: the intrusive projection-based models [Amsallem et al., 2012, Ștefănescu et al., 2015, Baur et al., 2011] and Non-Intrusive ROMs [Xiao, 2016, Dupuis et al., 2018]. These methods have provided important cutoffs in the computational cost of Computational Fluid Dynamic (CFD) models, but also in Numerical Structural Mechanics (CSM) especially in optimization [Xiao et al., 2017], Uncertainty Quantification (UQ) [Chocat et al., 2015, Lataniotis et al., 2018] or inverse resolution [Du et al., 2019]. Other approaches combine the MFM and ROM within a surrogate to solve costly optimization [De Lozzo, 2013, Benamara, 2017, Kast et al., 2019]. The use of multiple fidelities has been introduced to temper the cost of high-dimensional multi-disciplinary design breaking the "curse of dimensionality" [Taylor & Einbeck, 2013, Shan & Wang, 2010]. This concept allows to predict improved design location by taking into account a large amount of LF cheap data and few expensive HF available data.

However, both ROM and MFM based SBO raise predictability issues when ROM-based surrogates rely on offline sampling, leading to costly optimization procedures [Guénot et al., 2013, Choi et al., 2020, Song et al., 2018]. To address this issue, offline-online strategies, also called adaptive strategies, are employed to adapt the ROM as the optimization search progresses. These approaches have recently been highlighted by [Ye & Pan, 2019] in its state-of-the-art paper on SBOs as one of the current solutions to the challenges of large-scale modeling. The enrichment criterion uses a merit function to predict both the improvement in accuracy and the optimization objective. The next point to be evaluated is selected to maximize this criterion iteratively until an adequate stopping condition is reached. The goal is to choose the most relevant points in order to reduce the number of calls to solvers, that would answer a given design problem. The strategies for selecting sampling points can be classified as infill sampling [Sóbester et al., 2005, Guénot et al., 2013] adaptive [Guénot et al., 2013, Liu et al., 2018, Wackers et al., 2020], response-based [Boopathy & Rumpfkeil, 2013], a posteriori, sequential and online approaches. Contrary to the domain-based and space-filling approaches where the training database is selected according to its point-to-point distance distribution, the adaptive selection is based on the surrogate model's information.

The solutions to the Central Processing Unit (CPU) challenge of repetitive costly simulations reviewed in this Chapter aim at reducing the training and evaluation costs of metamodels. On the one hand, the MFMs combine variable simulation costs and, on the other hand, the ROMs allow to handle high-dimensional outputs while taking into account the vector representation of the simulation data (typically the discretized solutions of fluid state variables in CFD). Compared to scalar approximation models of Quantities of Interest (QoI), they are supposed to provide better insight into the physical model [Coelho et al., 2008]. Also, sampling methods can be used to minimize the number of calls to expensive solvers while maintaining sufficient representativeness of the simulated physical model.

This Chapter reviews scalar and full-field SBO single- and MF frameworks. Section 2.2 presents the SBO methods. Scalar MFMs are presented in Section 2.3, ROMs in Section 2.4, and finally, vectorial MFMs based on ROMs in Section 2.5. For each surrogate, the corresponding adaptive sampling strategies are overviewed.

## 2.2 Surrogate-based optimization

This section presents SBO. The surrogate models are presented on Section 2.2.1, Section 2.2.2 introduces general and non-adaptive sampling methods and Section 2.2.3 the adaptive sampling approaches.

In the context of industrial design, the QoI are used to determine whether the chosen technological solution meets the functional requirements. A performance criterion generally referred to as an objective function  $\mathcal{J}(\boldsymbol{\chi})$  can be evaluated at the design point  $\boldsymbol{\chi}^T = (\chi_1 \dots \chi_d)$ , where  $d$  is the design space dimension. This function is minimized under one or more constraints to meet the design specification. The scalar QoIs (lift, drag, ...) are post-processed from the simulator output  $f(\boldsymbol{\chi})$  (velocity, pressure field, ...). The classical optimization problem is defined in a design space  $\mathcal{D}$  by the objective  $\mathcal{J}$ , equality and inequality constraints  $h$  and  $g$  respectively

$$\begin{aligned} \boldsymbol{\chi}^* = \arg \min_{\boldsymbol{\chi} \in \mathcal{D}} \quad & \mathcal{J}(f(\boldsymbol{\chi})) \\ \text{s.t.} \quad & g_i(f(\boldsymbol{\chi})) \leq 0, \quad i = 1, \dots, p \\ & h_j(f(\boldsymbol{\chi})) = 0, \quad j = 1, \dots, q \end{aligned} \quad (2.1)$$

where  $\boldsymbol{\chi}$  is the design variable,  $\mathcal{D} \subset \mathbb{R}^d$ ,  $\boldsymbol{\chi}^*$  is the optimum of the objective function  $\mathcal{J} \in \mathbb{R}$  subjected to the constraints  $g, h$ .

In simulation-based optimizations, the QoI are evaluated by post-processing simulation results, requiring repetitive calls to time-consuming software within the optimization loops. Therefore, the SBO consists in solving the approximate problem defined by the approximate quantities noted as  $\tilde{\mathcal{J}}, \tilde{g}$ , and  $\tilde{h}$ , respectively

$$\begin{aligned} \tilde{\boldsymbol{\chi}}^* = \arg \min_{\boldsymbol{\chi} \in \mathcal{D}} \quad & \tilde{\mathcal{J}}(\boldsymbol{\chi}) \\ \text{s.t.} \quad & \tilde{g}_i(\boldsymbol{\chi}) \leq 0, \quad i = 1, \dots, p \\ & \tilde{h}_j(\boldsymbol{\chi}) = 0, \quad j = 1, \dots, q \end{aligned} \quad (2.2)$$

The SBO steps are illustrated in Figure 2.1. First, is the off-line phase, samples are evaluated  $\mathbf{X} = \{\boldsymbol{\chi}^{(0)}, \dots, \boldsymbol{\chi}^{(M)}\}$  using DoE methods as reviewed by [Giunta et al., 2003, Simpson et al., 2001] or, in the specific field of aerodynamic applications, by [Yondo et al., 2018]. Once the simulation has evaluated the samples  $f(\boldsymbol{\chi}^{(i)})$  with  $i = \{1, \dots, M\}$ , the surrogate model is built for the QoI  $\mathcal{Q} = \{\tilde{\mathcal{J}}, \tilde{g}, \tilde{h}\}$  and the optimization is performed in the online phase.

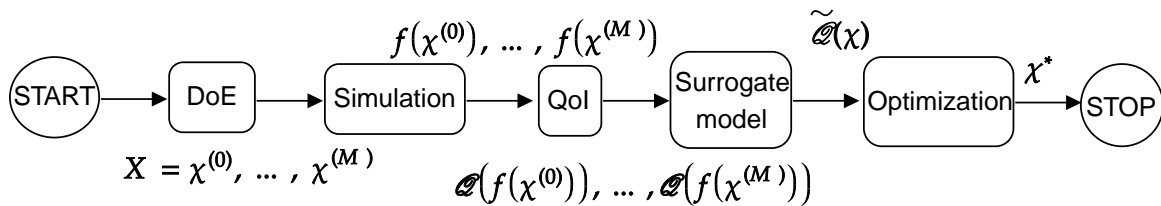


Figure 2.1: The offline SBO strategy

### 2.2.1 Surrogate modeling

Common metamodels include

- polynomial regression [Shoosmith et al., 1987, Simpson et al., 1998],
- Gaussian Process Regression (GPR) including Kriging [Cressie, 1990, Matheron, 1963, Kleijnen, 2009], developed in the geostatistical domain by [Kriging, 1951],
- Radial Basis Function (RBF) [Dyn et al., 1986, Powell, 2001, Gutmann, 2001],
- Moving Least Squares (MLS) [Lancaster & Salkauskas, 1981, Coelho et al., 2010b],
- Support Vector Regression (SVR) [Smola & Schölkopf, 2004],
- Artificial Neural Networks (ANN) [Cheng & Titterton, 1994].

Although polynomials are extensively cited in the literature, their use is mainly limited to low-dimensional, linear or quadratic cases [Shan & Wang, 2010]. RBF and Kriging metamodels can handle non-linear engineering approaches. While RBF imply isotropic kernels, Kriging models are based on the optimization of anisotropic ones requiring more hyper-parameters to tune and becoming untractable for high-dimensionality [Regis & Shoemaker, 2013].

Excellent reviews are available for response surface modeling, however, the validation of response surfaces is necessary. In simulation based applications, the number of data is generally insufficient to create distinct training validation sets. Specific approaches to model validation have therefore been proposed, some of them being independent of the surrogate method at hand. In the learning phase, an error estimator is needed to optimize the hyper-parameters of the approximate model. Gaussian-processes are commonly tuned by the likelihood maximization, employing evolutionary or gradient-based algorithms [Rasmussen & Williams, 2006, Toal et al., 2008]. Methods estimating the predictor error without generating an additional set of observations, include CV [Currin et al., 1991] and the bootstrap [Efron, 1979]. [Kohavi, 2001] compares bootstrap to CV and concludes to better performance for ten-fold CV, on the specific case considered. The overall surrogate error is usually validated by Cross-Validation (CV) or sensitivity estimation [Forrester & Keane, 2009]. K-fold-CV consists in removing  $k$  samples from the training set and estimating the model accuracy on these experiments. Setting  $k=1$  yields the Leave-One-Out (LOO) procedure. Such methods build the validation test where error metrics can be evaluated to quantify the overall error typically with the Mean Square Error (MSE), the Root MSE (RMSE) and the Integrated MSE (IMSE) [Le Gratiet, 2013]. A more local approach provides a partition of the design space using the Variable Error Value with Sampling Points (VESP) [Chowdhury et al., 2013] assigned to different partitioned regions. Thereafter, surrogate models are built iteratively using different subsets of samples and tested on the remaining points. Local accuracy can also be quantified by the Maximum Absolute Error (MAE). The correlation between two function responses can be measured by the coefficient  $R$  [Goel et al., 2007] when the relationship between the predicted response and the actual response is linear, one can also find  $r$ , the Pearson correlation coefficient [Song et al., 2019b] or its alternatives for non-linear models [Smarandache, 2008].

### 2.2.2 Off-line design of Experiment

Sampling techniques for numerical experiments can be grouped into two main categories, namely Classical DoE and Modern DoE or Design and Analysis of Computer Experiments (DACE) [Simpson et al., 2008, Manlig & Koblasa, 2014]. [Giunta et al., 2003] presents general summaries of Classical DoE and Modern DoE methods used in aeronautics.

To obtain a good quality approximation on the whole domain, the points must be distributed as evenly as possible in space. Classical DoE methods for physical (in vitro / in vivo) experiments tend to allocate the sample points in the way to minimize the effect of the random error term. They include the full factorial and the fractional factorial design [Mason et al., 2003], taking samples from regularly spaced sites. Its main limitation is that the total number of design points increases exponentially with the problem dimension [Ben Salem, 2018]. The central composite [Myers et al., 1989] and the Behnken Box design [Box & Behnken, 1960] follow a similar principle but replicate samples are taken making these methods less interesting for computer (in silico) experiments considered as deterministic.

A widely used, albeit costly, random sampling methods are defined as the Monte Carlo and the Markov Chain Monte Carlo (MCMC) algorithms [March & Willcox, 2012b], however the number of simulations involved becomes rapidly prohibitive. Quasi-random methods generate well-distributed sets of points with a controlled size. Various criteria are used to fill the DoE, such as Minimax and Maximin models, Kullback-Leibler, Audze-Eglais and Maximum Entropy Sampling (MES) [Shewry & Wynn, 1987]. Another approach maximizes Euclidean distance between all points in the DoE [Morris & Mitchell, 1995]. Among the modern DoE methods, [Giunta et al., 2003], one of the most commonly used is the Latin Hypercube Sampling (LHS) [McKay et al., 1979], distributing a fixed number of samples independently of the DoE dimensions. The Voronoi Latinized Centroid Tessellation is an extended version of the LHS technique [Saka et al., 2007], improving its coverage. Sampling can also be constructed using Analysis Of VAriance (ANOVA), Sobol [Sobol, 1967] and Halton [Halton, 1960] sensitivity analysis, often used to identify the parameters that most influence the output values.

Above space-filling techniques attempt to distribute the sampling points evenly in the design space. However, there is no general definition of an a priori number of samples in aerodynamic problems resulting in the desired precision [Yondo et al., 2018], as QoI are often non-linear or discontinuous. Therefore, adaptive sampling approaches are developed to progressively improve the quality of the surrogates.

### 2.2.3 Adaptive sampling

[Sacks et al., 1989] introduced sequential sampling using the model information to improve the sampling's quality with posterior data. In the literature, a sequential strategy is said to be adaptive if it improves the DoE without considering the experiment outputs. Sample location has been found to have a significant impact on the estimated error [Cai et al., 2017, Guo et al., 2021] and is improved when adaptive sampling methods are used to select new samples in areas of the design space where the error estimate is higher. [Liu et al., 2018] present a comprehensive review of global surrogate sampling, classifying the methods into one-shot, sequential, sequential adaptive, and multiple sampling categories. Another review presents methods tackling high-dimensional black-box problems by [Shan & Wang, 2010]. This section presents

some of the existing enrichment criteria applied to the SBO framework.

The objective of adaptive procedures is to find a sufficiently representative model allowing for an efficient convergence of the optimization problem. They are generally based on an infill criterion (Figure 2.2), selecting new sample  $\chi$  to be added to the current training set  $\mathbf{X} \subset \mathcal{D}$ .

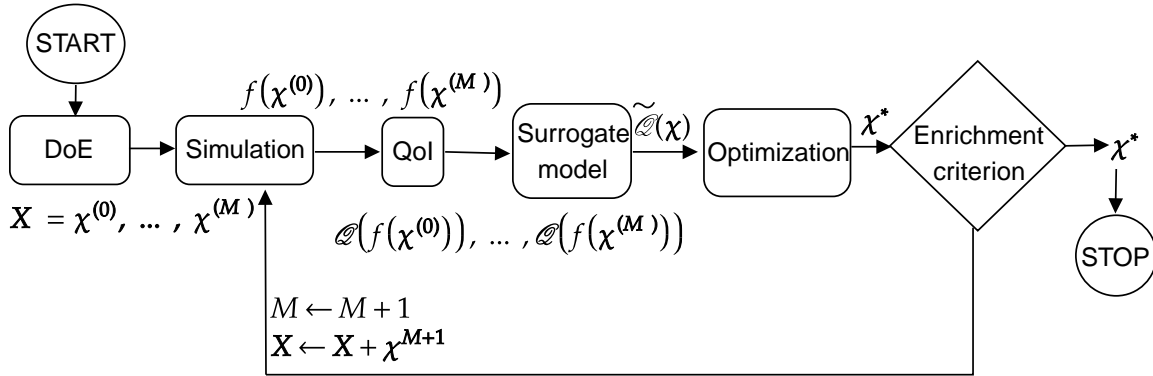


Figure 2.2: The adaptive SBO strategy

The most common infill sampling criteria are built from stochastic metamodels in a Bayesian scheme. [Žilinskas, 1992, Brochu et al., 2010] select the evaluation points sequentially taking into account a compromise between exploration of high uncertainty areas and intensification to improve over the current best observation. Regarding single-objective bound-constrained optimization, the Expected Improvement (EI) was popularised by [Jones & Schonlau, 1998] in the Efficient Global Optimization (EGO) framework. Later, the EI criterion has been extended to handle constraints [Parr et al., 2010, Parr et al., 2012] and to address multi-objective problems<sup>2</sup>. In the general EGO framework, [Picheny et al., 2013] compared EI, Augmented EI [Huang et al., 2006b] and the Weighted MSE Criterion for a noisy optimization benchmark. The weighted EI extension is proposed by [Sóbester et al., 2005] in order to control the balance between exploitation and exploration in a constrained optimization framework. [Scott et al., 2011] generalized the EGO for multidimensional variables in the noisy Gaussian process and gradient-knowledge framework. These strategies are also categorized by the survey [Liu et al., 2018] as variance-based adaptive sampling approaches including :

- Minimization and maximization of the predicted variance or Mean Square Error [Liu, 2012],
- Lower Confidence Bounds (LCB) [Brochu et al., 2010],
- Upper Confidence Bounds (UCB) [Auer, 2002]
- Gaussian Process-UCB [Srinivas et al., 2010],
- EI [Jones & Schonlau, 1998],
- Probability of Improvement (PI) [Brochu et al., 2010],
- Entropy search [Villemonteix, 2009, Hennig & Schuler, 2011].

<sup>2</sup>See, e.g., Section 2 of [Feliot et al., 2017].

[Currin et al., 1988] applied a two-stage optimal design based on the maximum entropy criterion to gain insight into a circuit-simulator example. [Sacks et al., 1989] used two-stages optimal design based on Integrated Mean Squared Error (IMSE) criterion for the same example. [Mackman & Allen, 2010] compared sequential sampling methods for the generation of surrogate aerodynamic models. [Regis, 2015] coupled the Trust Region method (TR) to the EGO and compared to the standard EI and an adaptive criterion based on the RBF [Regis & Shoemaker, 2013] on several test problems including the groundwater application based on a 36-dimensional simulation concluding that the proposed strategy is most efficient in the high-dimensional configuration. [Li et al., 2010] developed an adaptive DoE method based on accumulative error inspired by the greedy algorithm's principles [Veroy et al., 2003, Nguyen et al., 2010], and favoring regions of space where the outputs are non-linear. CAMM (Continuous And Multi-Modal) regions of the design space corresponding to multi-modal, noisy responses with a tendency to abrupt variation are identified and sampled until all suspected CAMMs are explored. This method was compared to the maximum entropy design and the maximum distance metric. It was concluded that it outperforms the other methods in terms of RMSE in the majority of the engineering examples presented.

## 2.3 Multi-Fidelity management

The MF approach consists in merging LF with HF data to produce surrogate models at affordable costs. A study of MF methods has been published by [Peherstorfer et al., 2018] in the context of uncertainty propagation, inference, and optimization. It was followed by an overview [Giselle Fernández-Godino et al., 2019], which questions the added value of MF approaches and how they can be used most effectively. MFM have been grouped by [Fernández-Godino et al., 2016] into three categories, the first where only HF quantities are estimated by a surrogate model, secondly, approaches where both levels are combined within the same metamodel, and finally, the category in which LF is only an enabler of HF modeling. This last category is related to the filtering approaches as it consists in interrogating LF to decide when to use HF models. A more general review is completed by [Yondo et al., 2018] on design space sampling, model selection, ROM, and assisted surrogate models in aeronautics. MF is presented as one of the recent solutions to improve simulation efficiency. This section gives an overview of the main MF approximation methods in order to determine each method's applicability according to our knowledge of the problem at hand.

### 2.3.1 Correlation analysis

The efficiency of MFMs is conditioned by the correlation between levels of fidelity and their evaluation cost. This section presents the MFM surrogates and introduces examples of quality metrics to improve their efficiency.

A comparison of surrogate quality criteria [Hu et al., 2018] concludes MSE to be the most efficient in the MFM framework, followed by LOO and Predictive Estimation of Model Fidelity (PEMF) error. a MFM metamodel quality metric involving PEMF proposed by [Mehmani et al., 2015] chooses between multiple fidelity levels. [Song et al., 2019b] compared the commonly used  $R^2$  metric (or performance criterion) to the Pearson Correlation Coefficient (PCC) in a context of multiple levels of fidelity in order to introduce the correlation impact on MFMs. The PCC measure between two random variables describing the correlation between HF and LF functions is defined by [Toal, 2015] for MFMs :

$$r^2 = \left( \frac{\sum_{i=1}^M (\mathcal{Q}_{HF}(\mathbf{x}^{(i)}) - \bar{\mathcal{Q}}_{HF}(\mathbf{x}^{(i)}))(\mathcal{Q}_{LF}(\mathbf{x}^{(i)}) - \bar{\mathcal{Q}}_{LF}(\mathbf{x}^{(i)}))}{\sqrt{\sum_{i=1}^M (\mathcal{Q}_{HF}(\mathbf{x}^{(i)}) - \bar{\mathcal{Q}}_{HF}(\mathbf{x}^{(i)}))^2} \sqrt{\sum_{i=1}^M (\mathcal{Q}_{LF}(\mathbf{x}^{(i)}) - \bar{\mathcal{Q}}_{LF}(\mathbf{x}^{(i)}))^2}} \right)^2 \quad (2.3)$$

where  $M$  is the number of observations of the LF and HF solvers  $\mathcal{Q}_{LF}$  and  $\mathcal{Q}_{HF}$ , respectively and  $\bar{\mathcal{Q}}_{LF}$  and  $\bar{\mathcal{Q}}_{HF}$  the corresponding means. [Toal, 2015] compares the impact of RMSE and the correlation metrics of the LF and HF functions. It has been observed that the  $r^2$  metric is better suited than RMSE to identify the LF-HF correlation. Using the correlation measures, it was shown that the amount of LF data must be greater than that of HF and the LF simulation budget must be no greater than 80% of the total simulation budget but at least higher than 10% to be worthwhile to use a MF representation. Thus, merging existing LF data with expensive HF data is not always cheaper than a single-fidelity method [Giselle Fernández-Godino et al., 2019]. Correlation, cost ratio and other error metrics are crucial to measure the benefit of MF models, which depends on the context (optimization, UQ, etc.). Many data fusion methods are detailed in the next section, but also dedicated criteria to maximize the benefit of these methods in the context of optimization.

## 2.3.2 Data fusion

### 2.3.2.1 Corrective approaches

The concept of MF was originally introduced in linear additive [Knill et al., 1999] and multiplicative [Haftka, 1991, Chang et al., 1993] approaches used in gradient-based optimization and was applied to a high speed civil transport aircraft wing. [Hutchison et al., 1994] applied a polynomial correction term on aerodynamic drag approximation. The main idea is to consider the LF model as a general trend to exploit by adding approximation of the difference (or ratio) between the LF and HF quantities. The corrective methods rely on the supposition of a relationship between different levels of fidelity, allowing to better approximate a fine HF model with its associated coarse LF using additive [Tang et al., 2005, Robinson et al., 2006, Choi et al., 2009a], multiplicative [Balabanov et al., 1998, Alexandrov et al., 2001] or hybrid (also called comprehensive) corrections [Zheng et al., 2013, Zhou et al., 2017].

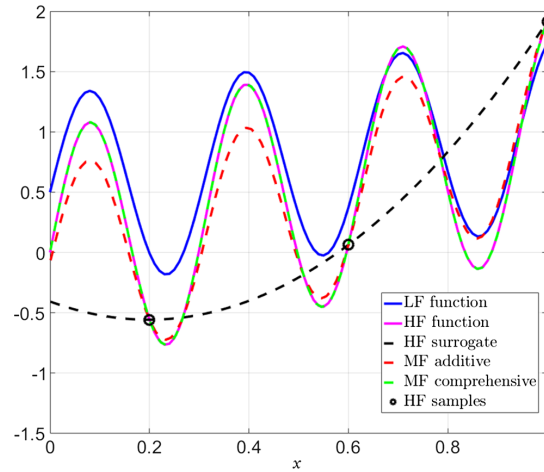


Figure 2.3: Illustration of Multi-Fidelity scaling (or corrective) approaches by [Giselle Fernández-Godino et al., 2019]

Figure 2.3 illustrates a non-linear function form in the review of MFMs methods [Giselle Fernández-Godino et al., 2019]. The comprehensive approximation is closer to the HF targeted function and appears to be the most accurate.

### 2.3.2.2 Space-Mapping

(SM) methods, developed by Bandler et al. in 1994 in cartography reviewed by [Bandler et al., 2004] and applied to the microwave circuit design make corrections at the input of a model, rather than at its output. They are based on the assumption that the set of entry points of a HF model is a geometric transformation of the HF models [Bakr et al., 2000, Leifsson & Koziel, 2015]. The main idea is to optimize the link or mapping between the spatial parameters LF and the HF model's spatial parameters to meet optimization specifications. The parameters are obtained by minimizing the difference between the available HF values and those of the metamodel. HF points generally update this approximation. This method was coupled with the Trust Region Model Management (TRMM) by [Robinson et al., 2008]. The parameters, defined on different design spaces, are linked by a corrected SM. It is used with a TRM of sequential-quadratic programming for two design optimization problems related to aerospace. These approaches allow different input dimensions [March & Willcox, 2012a] in the LF and HF models.

### 2.3.2.3 MF Kriging

are known as co-Kriging [Myers, 1984, Kennedy, 2000, Forrester et al., 2007, Perdikaris et al., 2015, Kontogiannis et al., 2020, Ruan et al., 2020] and Hierarchical Kriging (HK) [Han & Zhang, 2012, Zhang et al., 2018, He et al., 2021]. The HK model developed by [Han & Görtz, 2012] redefines co-Kriging considering the LF function's Kriging as the trend of the Kriging model for the expensive HF function avoiding the difficulty associated with building cross-covariance.

### 2.3.2.4 MF RBF

As noticed in the single-fidelity context (section 2.2), the RBF approximation is more suitable for high dimensional problems. Therefore, this motivated the adaptation of RBF to MF by [Reisenthel et al., 2006] for experimental and computational integrated data for a missile configuration, and was later applied by [Rendall & Allen, 2007] for the surface pressure of aircraft wings. [Durantin et al., 2017] developed a co-RBF extension yielding an accuracy of the same order as that of co-Kriging, while reducing its training cost, especially in high dimension.

### 2.3.2.5 MF polynomial chaos

[Ng & Eldred, 2012] originally proposed the MF Polynomial Chaos Expansion (PCE) in the UQ field using an additive correction between fidelity levels. An improvement of the HK has been proposed by [Palar & Shimoyama, 2017] through the use of PCE and Kriging as a HF surrogate model, then extended by additional polynomial terms to improve the accuracy within an inviscid RAE 2822 CFD application. The addition of a first order polynomial to the HK model has been shown to improve predictive performance. [Lickenbrock et al., 2020, Rumpfkeil et al., 2021] proposed a MF model based on a scattered PCE in the context of a CFD case illustrated in Figure 2.4. This bi-fidelity CFD case demonstrated that the MF PCE was able to capture the lift coefficient trends.

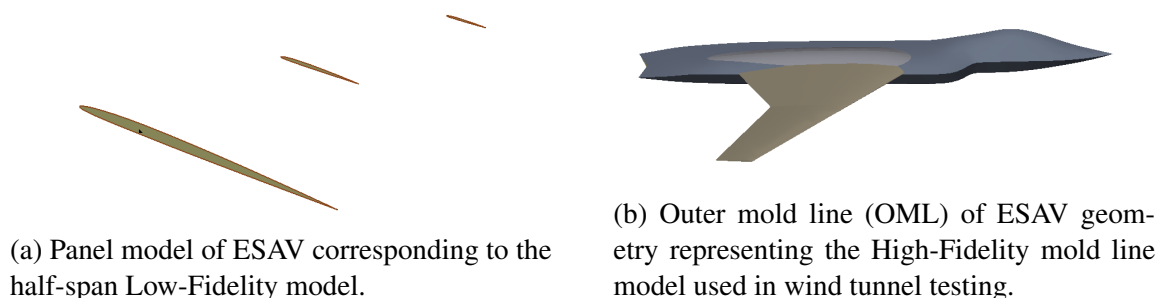


Figure 2.4: Baseline of an efficient supersonic air vehicle (ESAV) model [Lickenbrock et al., 2020].

### 2.3.2.6 Filtering approaches

:

To manage MF models in the optimization context, hierarchical methods use the LF model to filter out unpromising points before evaluating the remaining points with the HF model [Choi et al., 2009a, Dalle & Fidkowski, 2014]. This group of methods that may be considered as filtering techniques [Peherstorfer et al., 2018] consisting in using the LF to explore the design space may also be coupled to the trust-region framework [Conn et al., 2009]. [Alexandrov et al., 2001] has associated a tuned LF with a numerical optimizer subject to a confidence region constraint, where the LF model is tuned using the HF model and applied to a wing design optimization problem. [Giunta et al., 2007] applied the MFM technique to the multidisciplinary design of high-speed civil transport where the LF is used to define a sub-region of the most likely optimal location. The HF is then applied to improve the fidelity level.

### 2.3.2.7 Dedicated infill

The efficiency of MFMs depends on the trade-off between cost and accuracy [Giselle Fernández-Godino et al., 2019]. One concept of MF infill strategies is to establish a criteria for the LF models enrichment to predict the most promising locations for new HF samples. Other criterion use multiple fidelity levels to estimate the most promising fidelity level and location within the design space. Some of these methods take into account the HF/LF cost ratio to control the overall budget. In the following paragraphs, we provide an overview of the main adaptive approaches in these two categories.

### 2.3.2.8 Trust-Region MF management

Trust-Region Methods (TRMs) have been used to locate promising points in the MFM framework [Alexandrov et al., 2000], with derivative-based infill criteria [Alexandrov & Lewis, 2001] and extended to be used without gradients by [March & Willcox, 2012b, March & Willcox, 2012a] and in a multi-objective framework [Demange et al., 2016, Kontogiannis et al., 2020]. [Rodriguez et al., 2000] coupled a corrected LF model with a TR constrained numerical optimizer. They proposed a MF optimization framework based on a TR algorithm, the gradient of the objective function computed using the LF model allows the solution to converge to the HF model's optimum. The TR MFM uses a ratio between LF and HF, indicating the region of confidence [Peherstorfer et al., 2018]. The MFMs used by [Peherstorfer et al., 2018] are inspired by the approximation model management for the optimization in [Alexandrov et al., 1998] which considers the approximation model as a level of fidelity in its own right. Corrective methods are used to evaluate the sub-models within the confidence interval at each iteration  $k$  and to improve LF QoIs

$$\mathcal{Q}_{MF}(\boldsymbol{\chi}) = \mathcal{Q}_{LF}(\boldsymbol{\chi}) + e(\boldsymbol{\chi}_k) + \nabla e(\boldsymbol{\chi}_k)^T(\boldsymbol{\chi} - \boldsymbol{\chi}_k) \quad (2.4)$$

where  $e(\boldsymbol{\chi}_k)$  is the MFM correction model at iteration  $k$ ,  $\mathcal{Q}_{LF}$  and  $\mathcal{Q}_{MF}$ , respectively the LF and MFM QoI.

### 2.3.2.9 MF data fusion infill

**2.3.2.9.1 Kriging based methods** The other way to efficiently manage the optimization in a MFM framework is the EGO (see Section 2.2.3). The MF co-Kriging provides the variance that can be directly exploited to enrich the model. [Le Gratiet, 2013, Le Gratiet & Garnier, 2014] proposed a sequential version of recursive co-Kriging that uses IMSE and takes into account both the computational cost ratios between code fidelity levels and their respective contributions to the total variance. This method is used to predict a turbulence model of a particular gas composition where different refinements mesh define two levels of fidelity. The strategy, called sequential Kriging is used in an optimization framework to select new points of interest. It has been extended to parallel computing and adapted to the vectorial MF optimization application of a reservoir by [Thenon, 2017] (see Section 2.4.2).

In the same framework, [Lam et al., 2015] present a two-step space-filling strategy considering the information gain in the variance and the cost of each level of output fidelity. This strategy was tested with analytical MF extension of the 2D Rosenbrock function, a constrained optimization problem, and an aerodynamic optimization test case. The MFM was demonstrated

more efficient than the single-fidelity EGO. The approach adopted is the merging of  $L$  fidelity levels for which the level  $l_{n+1}$  of the next simulation at design point  $\boldsymbol{\chi}_{n+1}$

$$l_{n+1} = \underset{l \in \{1, \dots, L\}}{\operatorname{argmin}} \frac{C_l(\boldsymbol{\chi}_{n+1})}{\bar{\sigma}_l^2(\boldsymbol{\chi}_{n+1}) - \tilde{\sigma}_l^2(\boldsymbol{\chi}_{n+1})}, \quad (2.5)$$

where  $C_l(\boldsymbol{\chi}_{n+1})$  is the evaluation of the  $(n+1)^{\text{th}}$  predicted point cost with the simulator of level  $l$ ,  $\bar{\sigma}_l^2(\boldsymbol{\chi}_{n+1})$  and  $\tilde{\sigma}_l$  are respectively the mean and the variance of the MF surrogate model at  $l^{\text{th}}$  fidelity level. The objective is to find the lowest output cost with the highest information gain.

An adaptation of EI to MF is applied to HK by [Zhang et al., 2018]. The HK scheme of [Han & Zhang, 2012] is used to choose the fidelity level at each iteration. The adapted  $EI$  expression includes the fidelity level  $l$

$$EI_{vf}(\boldsymbol{\chi}, l) = \begin{cases} 0 & \text{if } \sigma_l(\boldsymbol{\chi}) = 0, \\ (\mathcal{Q}_{best} - \tilde{\mathcal{Q}}(\boldsymbol{\chi}))\Phi\left(\frac{\mathcal{Q}_{best} - \tilde{\mathcal{Q}}(\boldsymbol{\chi})}{\sigma_l(\boldsymbol{\chi})}\right) + \sigma_l(\boldsymbol{\chi})\phi\left(\frac{\mathcal{Q}_{best} - \tilde{\mathcal{Q}}(\boldsymbol{\chi})}{\sigma_l(\boldsymbol{\chi})}\right) & \text{if } \sigma_l(\boldsymbol{\chi}) > 0, \end{cases} \quad (2.6)$$

where  $\phi(\cdot)$  and  $\Phi(\cdot)$  denote respectively the standard normal probability density and distribution functions,  $\tilde{\mathcal{Q}}(\boldsymbol{\chi})$  the posterior mean of  $\mathcal{Q}$  and  $\sigma_{l, l \in [1, 2]}$  is the variance of the LF and HF models respectively.

[Guo et al., 2021] applied  $EI_{vf}$  and observed that compared to a single-fidelity EI, the search for the optimum was made efficient by LF exploration, were fewer HF calls were needed to solve the optimization problem. [Hao et al., 2020] developed an extension of this  $EI_{vf}$  criterion to Gradient-Enhanced Kriging (GEK). LF sample points are first used to represent the HF function trend close to the optimal solution, then HF samples are added. It is demonstrated on analytical test functions that  $EI_{vf}$  adaptively determines both the location and the fidelity level of a new design point.

Other variance-based criteria have been adapted to the variable fidelity framework. A comparative study was carried out on the LCB [Jiang et al., 2019] criterion between single-fidelity, MF EI, and other EGO criteria [Zhang et al., 2018]. Eight numerical examples, along with one physics-based aircraft fuselage design, resulted in 25% and 45% savings thanks to the VF-LCB criterion which showed an improved exploration/exploitation trade-off. Also, the Probability of Improvement (PI) criterion has been adapted to MFMs as an extended PI

$$EPI(\boldsymbol{\chi}, l) = PI_{vf}(\boldsymbol{\chi}) \times \operatorname{Corr}(\boldsymbol{\chi}, l) \times CR(l) \times \eta(\boldsymbol{\chi}, l), \quad (2.7)$$

Where  $PI_{vf}$  is the  $PI$  built from the MFM co-Kriging of [Ruan et al., 2019],  $l = 1, \dots, L$ , is the fidelity level,  $\operatorname{Corr}(\boldsymbol{\chi}, l)$  denotes the posterior correlation coefficient between the HF and fidelity level  $l$  at input  $\boldsymbol{\chi}$ .  $CR(l)$  is the cost ratio between HF and  $l^{\text{th}}$  fidelity model,  $\eta(\boldsymbol{\chi}, l)$  is the sample density function adopted by [Liu et al., 2018] to avoid clustering of training data. This criterion was compared to the Augmented Expected Improvement (AEI) of [Huang et al., 2006b],  $EI_{vf}$  of [Zhang et al., 2018], another MF PI variant, and a standard single-fidelity PI. An application to structural design optimization of the micro-aerial vehicle fuselage and stiffened cylindrical shell was carried out and led to the conclusion that the proposed VF-PI method is most efficient when the correlation between the HF and LF models is high. In contrast, the

VF-EI method is even more efficient when the correlations remain low.

In the same group of sampling methods using GPs, the GP-UCB, also known as UCB in the Bayesian framework [Brochu et al., 2010] was adapted to MFM by [Kandasamy et al., 2016]. The MF adaptation uses the largest LF uncertainty to add the next sample. This criterion was compared to the single-fidelity GP-EI, GP-UCB criteria, and the algorithm MF Mutual Information Greedy (MF-MI-Greedy) proposed by [Sen et al., 2018] where fidelities are assumed independent. This algorithm maximizes the amount of mutual information in order to take advantage of LF. MFM is modeled using additive Gaussian processes based on shared relationships with the target HF function, and the variable costs of different fidelities are taken into account. The MF-MI-Greedy was demonstrated to effectively reduce the uncertainty.

**2.3.2.9.2 Adaptive RBF models** Another extension of the EI was proposed by [Pellegrini et al., 2018] for MF UQ and adapted to RBF surrogate modelling. The enrichment aims to minimize both the uncertainty and the objective function. Several criteria are compared, including the Maximum Uncertainty Adaptive Sampling (MUAS), evaluated from the MF metamodel and minimized, the MFEI, and Aggregate Criteria Adaptive Sampling (ACAS) consisting in minimizing the difference between the MF prediction and the associated uncertainty. Finally, Multi-Criteria Adaptive Sampling (MCAS) allows identifying new training points by minimizing the objective function constrained by a maximal prediction uncertainty. This adaptive sampling strategy was tested on a dynamic Stochastic Radial Basis Functions (SRBF) [Volpi et al., 2015]. It has been observed that MUAS and MCAS were more exploratory than MFEI and ACAS, and HF evaluations were well distributed within the design space. MFEI and ACAS concentrate HF evaluations in the optimum region. The overall results lead to the conclusion that MFEI are the most efficient adaptive sampling techniques for the proposed CFD shape optimization test case of a NACA hydrofoil.

The EGO approach adapted to RBF by [Bjorkman, 2001], allowed [Durantin et al., 2017] to obtain time savings for comparable optimization results. The same conclusion was drawn by [van Rijn et al., 2018], following the co-RBF comparison with a Random Forest co-surrogate. [Gutmann, 2001] developed an adaptive sampling method for optimization using RBF models with similar principle as the Efficient Global Optimization (EGO) [Jones & Schonlau, 1998]. Gutmann-RBF is constructed using the power function to remedy the lack of MSE in RBF construction compared to a kriging-based model. This criterion was modified by [Regis & Shoemaker, 2006] to improve its local search property. The adaptive MF Sequential Radial Basis Optimization (MFSRBO) method was developed by [Reisenthel & Allen, 2014] and tested on an aerodynamic application. The compromise criterion between fidelity levels [Kennedy, 2000] of additive MF surrogate is adapted to an RBF metamodel. This scheme uses the difference between HF and  $l$  fidelity levels. The AEI criterion proposed by [Huang et al., 2006b] for co-Kriging is adapted to the MF RBF at the  $l^{th}$  fidelity levels as

$$EI(\chi, l) = EI * \alpha_1(\chi, l) * \alpha_2(\chi, l) * \alpha_3(\chi, l), \quad (2.8)$$

with  $\alpha_1(\chi, l)$  a discontinuous function of the local prediction error,  $\alpha_2(\chi, l)$  the relative reduction in the posterior standard deviation and  $\alpha_3(\chi, l)$  is the ratio of the  $l$  fidelity to the highest HF costs  $\frac{C_l}{C_{HF}}$ .

[Cai et al., 2017] adapted the CV metric associated with the Voronoi tessellation [Xu et al., 2014] to partition the design space for RBF-based MF metamodeling. Recently, [Wackers et al., 2020] proposed a MF metamodel based on the stochastic RBF (SRBF) with a MF adaptive sampling based on CV error and the Voronoi partition, sampling both LF and HF.

## 2.4 Surrogate modeling for full-field computations

The optimization problem formulation (2.2) and consequently the surrogate approaches presented in previous sections consider QoI functionals obtained by postprocessing simulation results corresponding in aerospace applications to detailed velocity, pressure, stress, or thermal fields defined on a finite element/finite volume mesh. The full-field approach consists in building a ROM  $\tilde{f}(\mathbf{x}, \boldsymbol{\chi})$  of the solver and to express, objective function and constraints in terms of the approximate field. This approach yields a better insight into detailed characteristics of the flow at every optimization iteration. The corresponding optimization problem is stated as

$$\begin{aligned} \boldsymbol{\chi}^* = \arg \min_{\mathbf{x} \in \Omega, \boldsymbol{\chi} \in \mathcal{D}} \quad & \mathcal{J}(\tilde{f}(\mathbf{x}, \boldsymbol{\chi})) \\ \text{s.t.} \quad & g_i(\tilde{f}(\mathbf{x}, \boldsymbol{\chi})) \leq 0, \quad i = 1, \dots, p \\ & h_j(\tilde{f}(\mathbf{x}, \boldsymbol{\chi})) = 0, \quad j = 1, \dots, q \end{aligned} \quad (2.9)$$

where  $\mathbf{x}$  is the set of points defining the space discretization  $\Omega \subset \mathbb{R}^n$  with  $n$  the number of nodes,  $\boldsymbol{\chi}$  the design variable,  $\in \mathcal{D} \subset \mathbb{R}^d$ , and  $\boldsymbol{\chi}^*$  is the optimum configuration of the objective function  $\mathcal{J} \in \mathbb{R}$  respecting constraints  $g, h$ .

The different steps of the full-field SBO are illustrated in Figure 2.5. First, the DoE  $\mathbf{X} = \{\boldsymbol{\chi}^{(0)}, \dots, \boldsymbol{\chi}^{(M)}\}$  is generated in  $\mathcal{D}$  with one of the a priori sampling methods cited in Section 2.2.2. Once the fields  $f(\mathbf{x}, \boldsymbol{\chi}^{(i)})$ ,  $i = \{1, \dots, M\}$  have been computed, the ROM  $\tilde{f}(\mathbf{x}, \boldsymbol{\chi})$  is built and the optimization is performed with the functionals  $\mathcal{Q}(\tilde{f}(\mathbf{x}, \boldsymbol{\chi})) = \{\mathcal{J}(\tilde{f}(\mathbf{x}, \boldsymbol{\chi})), g(\tilde{f}(\mathbf{x}, \boldsymbol{\chi})), h(\tilde{f}(\mathbf{x}, \boldsymbol{\chi}))\}$ .

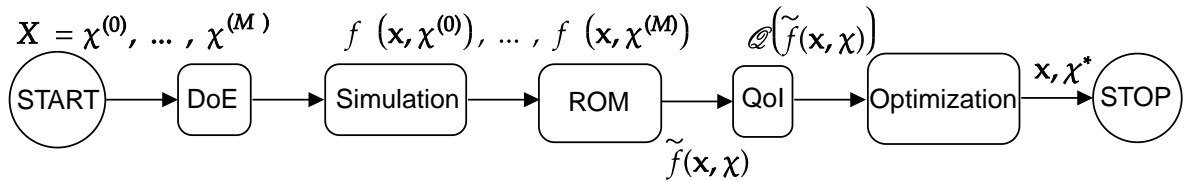


Figure 2.5: The full-field SBO strategy

Section 2.4.1 reviews the ROM techniques; associated adaptive strategies are presented in Section 2.4.2

### 2.4.1 Reduced-Order Modeling

While the surrogate modeling techniques cited in the previous Sections can exploit integrated quantities, ROM can capture spatial information in a model approximation by expressing the

solution as a linear combination of a limited number of modes. Thus assuming that few independent modes govern the system dynamics, a significant reduction in the solution's computational cost can be achieved [Coelho et al., 2008]. Applications to the description of turbulent flow have demonstrated the capture of non-linear features. [Aubry et al., 1988] constructed a 5-mode system that qualitatively reproduces the turbulent boundary layer discontinuity. This approach was extended to diverse types of flows [Rajaei et al., 1994, Gunes et al., 1997, Ukeiley et al., 2001]. The ROM can be intrusive or non-intrusive (direct or indirect) depending on whether the physical model is considered as a black box or the reduced Partial Differential Equation (PDE) is solved online.

#### 2.4.1.1 Intrusive ROMs

The intrusive ROMs require code modifications, for example, by Galerkin projection onto a subspace spanned by a set of modes [Amabili & Touzé, 2007, Amsallem et al., 2013, Xiao et al., 2020]. [Benner et al., 2015] reviewed the projection-based ROMs for dynamical systems. In a non-exhaustive way, one can also find

- Reduced-Basis Method (RBM) [Rozza et al., 2008],
- Empirical Interpolation Method (EIM) and Discrete EIM (DEIM) [Ştefănescu et al., 2015]
- Proper Generalized Decomposition (PGD) [Chinesta et al., 2011].

The modes may be obtained by Proper Orthogonal Decomposition (POD) also known as Karhunen-Loève Expansion (KLE) [Lumley et al., 1967] in the field of turbulence or Principal Component Analysis (PCA) [Jolliffe & Cadima, 2016] in machine learning applications. The Proper Orthogonal Decomposition (POD) relies on the extraction of the reduced basis by truncated Singular Value Decomposition (SVD) of the snapshots matrix. This technique produces a low rank global basis of the most impacting modes [Sirovich, 1987] and has been shown to be appropriate for coherent flow structures that can be sorted by their energy content [Berkooz et al., 2003]. Intrusive POD has been applied by [Li et al., 2018] to estimate state variables and associated variables in transonic flows in gradient-based aerodynamic shape optimization. A review of POD applications in mechanical systems is provided by [Lu et al., 2019]. Other approaches are Krylov subspace [Bai, 2002] used on turbulence, Fourier well suited for periodic signals series as in Harmonic Balance Method (HBM) [Hall et al., 2002, Yao & Jaiman, 2016], or Volterra Series [Cheng et al., 2016].

These direct approaches are closer to the simulated system behaviour being directly applied on the physical equations, but are challenging to implement, as they require source code modification.

#### 2.4.1.2 Non-Intrusive ROMs

To avoid this problem, non-intrusive approaches have been introduced, such as Non-Intrusive POD (NIPOD), also known as Galerkin-free [Shinde et al., 2019] or POD with Interpolation (PODI) [Bui-Thanh et al., 2004]. Unlike direct ROM approaches, indirect ROMs do not require calls to the differential equation solver to perform the interpolation. As in the intrusive ROM, the POD snapshot method, developed by [Sirovich, 1987], allows to empirically build the basis vectors keeping the modes whose sum of energies represents at least 90% of the total

energy, while the neglected modes represent less than 1% of the main mode's energy. This POD technique was applied by [Bui-Thanh et al., 2004] as an interpolation of known designs for inverse design purposes. [Coelho et al., 2008] successfully applied a two-step Non-Intrusive Proper Orthogonal Decomposition (NIPOD) on a 3D flexible wing shape optimization, involving weak code coupling between the solid and fluid models. On the one hand, the coupling variables were reduced by the POD, expressing the interface pressure as a linear combination of a few modes. On the other hand, the scalar coefficients obtained by the linear expansion of the POD modes were approximated by polynomial response surfaces and moving least squares surrogates.

Gappy-POD was introduced in the context of human face image reconstruction from incomplete data [Everson & Sirovich, 1995]. Such an approach has been applied by [Bui-Thanh et al., 2004], to fill in incomplete data fields from known snapshots. Gappy-POD has been used to reconstruct fields in fluid and structural applications where distributed sensors provide limited field measurements [Cohen et al., 2006].

Finally, a local POD approach, the Local Decomposition Method (LDM) was recently developed by [Dupuis et al., 2018] as an extension of the NIPOD, inspired by the mixture of experts and local reduced-order dynamic modeling. It consists in using multiple POD bases adapted to delimited regions of the design space, distinguished by the sampled snapshots features. This separation allowed to adapt the POD approximations to each physical regime, to capture local non-linearities.

### 2.4.1.3 Shape manifold for ROMs

Another approach uses the concept of shape manifold for a reduced order representation. [Meng et al., 2018] reviews the shape manifold designed for ROM representation of complex shapes encountered in mechanical problems. The general idea is to define the shape space, known as POD-morphing [Raghavan et al., 2012b], in which the structure boundary evolves. The reduced representation [Raghavan et al., 2013] is obtained by determining the intrinsic dimensionality of the problem, independent of the original design parameters, and by approximating a hyper surface, i.e., a shape manifold, connecting all the known admissible shapes using level set functions. Moreover, an optimal parameterization can be obtained for arbitrary shapes, where the parameters must be defined a posteriori. The family of manifold step algorithms for predictor-corrector optimization in a reduced shape space guarantees the admissibility of the solution without additional constraints. Applications include structural optimization [Raghavan et al., 2012a, Raghavan et al., 2012b], springback minimization in metal forming [Le Quilliec et al., 2014], microstructural design of materials [Xia et al., 2013], and inverse problems [Meng et al., 2015].

## 2.4.2 Adaptive Reduced-Order Models

The ROM models presented in the former section are often improved during the optimization process in an attempt to target the regions of interest more efficiently. In the ROM context, adaptive approaches can refer to the procedure of orthogonal basis adaptation with each new vector, adding as few samples as possible to build the whole basis. As for the scalar SBO, there are also approaches aiming at choosing samples to reduce the calls to expensive solvers. A

range of these approaches is presented in the following paragraphs.

### 2.4.2.1 Trust-Region Methods

The Sequential sampling schemes TR used on the scalar SBO (see Section 2.3.2.7) were coupled to ROM to solve constrained and unconstrained optimization [Regis & Wild, 2017]. Among intrusive ROMs, [Bergmann & Cordier, 2007] applied POD Reduced-Order Models and TR method to minimize the mean drag under rotary control of a cylinder wake in the laminar regime reducing its relative mean drag by 30% .

### 2.4.2.2 Error-based infill methods

Among error-based infill methods, a LOO (see Section 2.2) approach for POD-based models was proposed by [Braconnier et al., 2011] along with an error estimate of the POD model to select new sample locations. This strategy was compared to classical a priori uniform sampling and tested on an analytical test case and the 2D turbulent flow around a RAE2822 airfoil. It was concluded that the convergence of the LOO-CV adaptive-based procedure was faster. This infill criterion was applied to the NIPOD approach by [Guénot et al., 2013] where an improvement of the modal coefficients was obtained by taking into account each snapshot's influence to represent the full-field model. Two cases based on the RAE2822 airfoil demonstrated the error control over the whole parametric space even in the non-linear transonic region.

### 2.4.2.3 Greedy approaches

The principle of a greedy algorithm is to choose the most promising elements (or to suppress the least promising ones) iteratively to obtain the best prediction. Once the models are built in the off-line phase, the most (or least) predictive features may be selected during the online phase based on error criteria. The ROM database model's accuracy can be adjusted in the offline phase, where a local ROM database is built by a greedy procedure. The greedy algorithm is used for the selection of snapshots for the approximation of the parameterized PDE solution [Veroy et al., 2003, Nguyen et al., 2010] and in a non-intrusive framework [Dutta et al., 2021]. Such approach was applied by [Audouze et al., 2013] to time-dependent non linear problems using RBF-based Non-Intrusive ROM. This model adaptively generates snapshots based on a greedy approach to minimize the overall computational cost.

### 2.4.2.4 Adaptive Gappy POD

[Bui-Thanh et al., 2008] use an adaptive Gappy POD (GPOD) (see Section 2.4.1) for two-dimensional airfoil inverse design. This approach aims at finding the optimal sensor locations and adaptively improve the POD basis. At each iteration, the criterion used to achieve the selection is based on the Gappy POD maximum error. The complete model information is then generated by solving the system between known, and unknown data at this position, the database is enriched using the resulting snapshot, and the reduced basis is updated. These steps are then repeated, using the updated model to calculate the reduced states at each locations around the airfoil.

### 2.4.2.5 Active-learning approaches

The NIPOD was adapted to an active-learning<sup>3</sup> framework using the partitioning approach in the LDM method [Dupuis et al., 2018]. The experimental design is divided into several parts corresponding to values associated with a shock sensor allowing to identify the areas where discontinuous structures will likely appear. Once targeted, these regions are clustered and enriched using error, sensitivity, and global entropy metrics. The procedure's application reveals a capacity to better take into account the regions of high gradient and discontinuity, in the case of a shock problem in a turbulent flow around the RAE2822 wing in transonic regime.

### 2.4.2.6 PCA-based infill

Within the UQ framework, the implementation of [Hampton & Doostan, 2018] is a non-intrusive method where corrective sampling is used to improve stability and precision. PCA allows building a new basis that describes the shapes globally. The Bayesian optimization is performed in the space of reduced dimension of the active components, complemented by a random embedding in the space of the remaining components, to approach the optimization problem in reduced dimension.

## 2.5 Multi-fidelity reduced-order methods

The ROM methods of the last reviewed section outperform scalar approaches in complex non-linear optimizations. The MFM extension of these methods has been performed mainly in the CFD domain, and promising references are presented in the present section.

Section 2.5.1 reviews the MF ROM extensions; associated adaptive strategies are presented in Section 2.5.1.3 .

### 2.5.1 Multi-fidelity vectorial modeling

#### 2.5.1.1 MF extensions of the POD

**2.5.1.1.1 MF Gappy-POD** [Toal, 2014] adapted the Gappy POD (see Section 2.4.1) to a MF surrogate-based optimization. A bi-variate optimization of a NACA 0012 airfoil is performed by predicting the two-dimensional HF pressure distribution from its computed LF counterpart.

**2.5.1.1.2 MF Optimal basis POD extensions** [Mifsud et al., 2016] developed a bi-fidelity POD extension using two discretization levels of numerical experiments. It consists on building an optimal set of orthogonal basis vectors from the two fidelity snapshots subsets. The set of basis are used to construct the overall response, then predict snapshots in unknown locations. This approach is tested for flow prediction using RANS at two fidelity levels of mesh refinement. The numerical examples led to the conclusion that the efficiency depends heavily on the

---

3

Active learning consists in adding as little information as possible by selecting a group of features through unidentified observations that will be labeled by an oracle (e.g., a human annotator) [Settles, 2010].

correlation between the two fidelity levels.

Inspired by the CPOD of [Xiao et al., 2010], [Benamara et al., 2017] developed the MFNIPOD extension based on QR decomposition allowing to build a bi-fidelity orthogonal basis. Unlike the MF POD extension of [Mifsud et al., 2016], the MFNIPOD enriches the reduced space obtained from scarce HF information with LF related orthogonal modes, giving a hierarchical ROM. The method was compared to a model based on a single-fidelity RBF Neural Network (RBFNN) and co-Kriging on a constrained 2D analytical optimization and the 19-D optimization of an industrial compressor blade and its non-axisymmetric hub. The results show that MFNIPOD outperforms models based on co-Kriging and RBFNN in terms of costs and accuracy. Combining different data simulations from multiple fidelity snapshots presents difficulties because the two sets of fields lie most likely in different spaces. When fidelity levels are based on different mesh refinement, this problem may be tackled by projecting the LF outputs onto the finer HF grid [Benamara, 2017]. Problems of inconsistency were also addressed by [Perron et al., 2020] who applied a MF ROM using a common subspace, to a transonic wing problem. A reduction in computational training cost between 10% and 73% was observed compared to a single-fidelity approach of comparable accuracy.

In a different approach, the MFROM and MFNIPOD extensions inspired the development of a model based on MF PCA by [Bunnell et al., 2021]. The Shared Principal Component (SPC) MF surrogate model consists in building the POD-based model separately with the sampled HF and then LF vectors and linking them assuming that the HF variations comply with those observed on the LF functions. Consequently, LF sampled vectors are similar to the principal components of the HF samples. The separation allows having two different mesh configurations with different fidelity levels. This method allows the fusion of LF and HF samples within a common metamodel and is applied to the design of turbomachinery blades. The SPC reduced the error to about 78% with respect to single-fidelity surrogates. The Space-Mapping surrogate presented the lowest error ratio among other tested methods. SPC appeared more efficient than space mapping, co-Kriging, and MFNIPOD [Benamara et al., 2017].

**2.5.1.1.3 MF POD with interpolation** [Yondo et al., 2019] introduced MF ROM extensions based on the PODI [Bui-Thanh et al., 2004] and compared it to non-linear least squares ROM [Zimmermann & Görtz, 2010, Görtz et al., 2013] to capture non-linearities of the physical system.

### 2.5.1.2 Kriging Based MF POD

**2.5.1.2.1 MF Kriging non-intrusive POD** [Wang et al., 2020] proposed a multi-fidelity ROM for the reconstruction of a steady flow field. It performs a HF-LF corrective mapping of the bi-level ROM modal coefficients separately, and is applied to predict the flow with shock waves of a NACA0012 airfoil achieving better accuracy than the traditional Kriging ROM .

**2.5.1.2.2 Co-Kriging POD** [Poethke et al., 2019] presented a method combining MF and POD and compared it to the scalar co-Kriging and single-fidelity Kriging. Two level fidelity simulations of 2D and 3D turbine blades are tested and used in an optimization loop. The

POD-based method directly decomposes LF flow fields into main components covering a reduced solution subspace, where HF values are interpolated. Compared to a Kriging model based on design space variables, this model is smaller in size. The POD-based method showed a faster convergence than scalar and single-fidelity optimization while reaching the same profile efficiency and similar design. Using the co-Kriging MFM, [Thenon, 2017] proposed a MF extension to Principal Component Analysis (PCA), building a basis from the HF vectors and secondly projecting the LF vectors on this reduced-basis. Finally, the co-Kriging approximation is performed on the two levels coefficient projection. The method is applied to pressure maps outputs of a two-level oil tank model. It is observed that the MF vectorial metamodel is effective only if there is a minimal correlation between the fidelity levels of the simulation outputs. However, MF coKriging does not provide sufficient improvements than single fidelity Kriging for the presented cases. An alternative and more efficient approach consists in building these estimates with the dynamic outputs. [Xiao et al., 2018] proposed a co-Kriging model based on a Galerkin projection based POD in which a weight is assigned to two and three levels of MF data constructed by varying the number of basis vectors in the POD ROM. Numerical tests show better results for three-level MF Kriging than single and two-level Kriging models. Following an online POD based topological optimization, [Xiao et al., 2020] presented a MF approach to build a POD based ROM incrementally from successive variable-fidelity approximations of the global physical equations.

**2.5.1.2.3 MF Kriging and non-intrusive Polynomial Chaos Expansion (PCE)** [Cheng et al., 2019] propose a sparse non-intrusive PCE adapted to MFM. Kriging and orthogonal polynomial covariance function are used to build the full-field model and an iterative scheme detects the optimal PCE basis in each fidelity level. The Kriging POD was also adapted by [Mohammadi & Raisee, 2019] to two fidelity levels. In the same spirit as PCE-Kriging, the basis functions are evaluated from a stochastic field where it is not necessary to calculate the Kriging trend functions separately.

### 2.5.1.3 Adaptive multi-fidelity vector models

The adaptive ROMS and MFMs have been demonstrated to be a promising perspective to MFM ROM models [Benamara et al., 2017, Yondo et al., 2019]. This section explores adaptive schemes involving MFM vector models.

### 2.5.1.4 MF POD Error-based approach

An extension of the DoE Voronoi cells is performed in the framework of sequential sampling by [Thenon, 2017] selecting the points in multiple Voronoi cells associated with the highest CV errors. Then, for each level of fidelity, a point is selected iteratively from the highest to the lowest corresponding error in each cell, until the calculation's budget is reached. The fidelity level is chosen according to the IMSE weighted by the evaluation costs. In this paper, it has been observed that the two levels of fidelity should be sufficiently correlated. Besides, the LF computational cost should be limited to increase the method's efficiency. The method has been applied to a POD co-Kriging and is compared to a MF scalar approach. It was shown that the POD vectorial approach improved the prediction performance of scalar models even with a poor HF-LF correlation.

### 2.5.1.5 MF Gappy-POD infill

The corrective MF approach have been coupled to Gappy POD by [Robinson et al., 2006] allowing to reconstruct the HF discrete gappy dataset with LF data. [Benamara et al., 2016] presents a MF adaptive approach based on the Gappy POD identifying a HF subspace to be covered by the LF vectors.

### 2.5.1.6 MF adaptive Kriging

The MFNIRB proposed by [Khatouri et al., 2020] as an extension to the Non-Intrusive Reduced-Basis (NIRB) method of [Chakir & Maday, 2009] takes into account constraints and shows promising results on a 2D analytical test case [Benamara et al., 2017]. The method was compared to a scalar single-fidelity Kriging and used the constrained EI [Bagheri et al., 2017] criterion to sample iteratively the design space. However, this attempt is based on HF sampling on low-dimensional parameter space. The EI criterion was also applied by [Nachar et al., 2020] in a MF reduced-order context. The expression of the EI criterion is evaluated using the LF data variance and mean. This modified EI is used to add LF and HF data, generated from LATIN Proper Generalized Decomposition (PGD) model reduction framework [Chinesta et al., 2011], assisting a mechanical part optimization problem.

## 2.6 Conclusion

This Chapter presents a non-exhaustive review of surrogate methods that address simulation cost issues in optimizing physical systems modeled with computer codes focusing on fluid/solid mechanics in potentially multidisciplinary settings. The reviewed methods' common feature is the construction of surrogate models based on sequentially updated Design Of Experiments. The techniques reviewed include scalar, vector, and multi-fidelity surrogates, along with their associated infill strategies. Surrogate vectorial multi-fidelity models based on reduced-order approaches appear to outperform response surface approximations and control the overall simulation budget. However, the multi-fidelity approach's feasibility depends on the quality and cost of physical models available for a given application. The trade-off between cost and accuracy in the multi-fidelity model is conditioned by the correlation between LF (supposed cheap) and HF (supposed expensive) simulators and their CPU ratio. The development of dedicated infill techniques requires criteria allowing both for the site's choice and the new simulation's fidelity level under the overall simulation budget constraint.

# Chapter 3

## Constrained multi-fidelity surrogate framework using with non-intrusive reduced-order basis

### 3.1 Introduction

In the single-fidelity Surrogate Based-Optimization (SBO) framework, cheap to evaluate approximation models of the objective and constraints are used alongside an infill criterion to build a sequential Design of Experiment (DoE) optimization strategy. Multi-Fidelity (MF) approaches extend this framework by leveraging both low and high-fidelity simulators. Some approaches enhance Low-Fidelity (LF) simulations using additive [Robinson et al., 2006], multiplicative [Alexandrov et al., 2001] or hybrid [Zhou et al., 2017] corrections or space mapping [Leifsson & Koziel, 2015], learned from High-Fidelity (HF) simulations. Other approaches, such as co-kriging [Forrester et al., 2007, Le Riche et al., 2020] or co-RBF [Durantin et al., 2016], exploit the correlation between the different fidelity levels to produce a MF surrogate model. Another approach is to use hierarchical Kriging [Zhang et al., 2018] to build surrogate models recursively at each fidelity level. This Chapter addresses the problem of constrained derivative-free optimization with multiple fidelity sources.

The efficiency of MF models depends on the compromise between the cost and accuracy of the responses. The general concept of MF infill strategies consists in establishing low-cost enrichment criteria of LF models to predict new HF sample's most promising locations [Stroh, 2018, Liu et al., 2018]. Hierarchical methods identify promising points before evaluating them with the HF model [Choi et al., 2009b, Dalle & Fidkowski, 2014] within an optimization. Those methods can also be used with a Genetic Algorithm [Sefrioui et al., 2000]. Other articles proposed to use trust-region methods to manage the infill criteria, both in the gradient-based [Alexandrov & Lewis, 2001] and the derivative-free frameworks [March & Willcox, 2012b, March & Willcox, 2012a]. Albeit promising, those methods are likely to remain local. Recently, attention has been turned toward the Surrogate-Based-Optimization framework: approaches in the literature [Liu et al., 2018] are based either on the prediction error [Le Gratiot, 2013] or statistical criteria [Jones & Schonlau, 1998, Liu, 2012].

Picheny et al. [Picheny et al., 2013] compared existing infill criteria such as EI, Augmented Expected Improvement (EI) used by Huang et al. [Huang et al., 2006a], and the Weighted

Integrated Mean Square Error (Weighted IMSE) criterion for noisy optimization benchmark. The weighted EI extension is proposed by Sobester et al. [Sóbester et al., 2005] in order to control the balance between exploitation and exploration in a constrained optimization framework. In [Scott et al., 2011] the EGO was generalized for multidimensional variables in the noisy Gaussian process and gradient-knowledge framework. With similar noise assumptions, Kandasamy et al. [Kandasamy et al., 2017] used the Thompson sampling criterion to consider the variability of the evaluation time when maximizing an unknown function from noisy evaluation in a parallel computing framework. A multi-fidelity extension of the EI criterion to the sequential kriging was proposed by Huang et al. [Huang et al., 2006b, Huang et al., 2015]. This criterion allows for adding the cheapest best current LF sample. In our case, the sampling is focusing on the HF level. For the additional references, see [Song et al., 2019a], where Bayesian techniques are reviewed for applications such as constraint, single-fidelity, and multiple fidelity optimization.

Section 3.2.1 is an overview of the surrogate model used in the proposed enrichment strategy. The reduced basis methodology needed to represent the bi-level fidelity vector responses is also introduced. Then, the proposed infill strategy is detailed on Section 3.2.2. Finally, a bi-fidelity level benchmark derived from aerodynamic simulation [Benamara et al., 2017] illustrates the proposed approach Section 3.3.

## 3.2 Method

### 3.2.1 Multi-fidelity model

Given a design space  $\mathcal{D}$  of dimension  $d$  and a physical domain  $\Omega \subset \mathbb{R}^{\{2,3\}}$ , the optimization problem considered in this work is to find values  $\boldsymbol{\vartheta}^* \in \mathcal{D}$  of the design variables  $\boldsymbol{\vartheta}$  that minimize some scalar objective function  $\mathcal{J}(\mathbf{f}(\mathbf{x}, \boldsymbol{\vartheta}))$  while respecting  $n_c$  real-valued constraint functions  $(c_h)_{1 \leq h \leq n_c}$ .

$$\begin{aligned} \underset{\boldsymbol{\vartheta} \in \mathcal{D} \subset \mathbb{R}^d}{\text{minimize}} \quad & \mathcal{J}(\mathbf{f}(\mathbf{x}, \boldsymbol{\vartheta})), \\ \text{s.t.} \quad & c_h(\mathbf{f}(\mathbf{x}, \boldsymbol{\vartheta})) \leq 0, \quad h = \{1, \dots, n_c\}, \end{aligned} \quad (3.1)$$

where the objective function  $\mathcal{J}$  and the constraint functions  $(c_h)_{1 \leq h \leq n_c}$  are evaluated by running computer simulations yielding a vector  $\mathbf{f}(\mathbf{x}, \boldsymbol{\vartheta})$  of values at a fixed set  $\mathbf{x} = (x_i)_{1 \leq i \leq n}$  of  $n$  discrete positions in the physical domain  $\Omega$ .

Given a design of  $M$  experiments  $\{\boldsymbol{\vartheta}^{(1)}, \dots, \boldsymbol{\vartheta}^{(M)}\} \in \mathcal{D}^M$ , according to the Model Order Reduction paradigm [Amsallem et al., 2012, Carlberg & Farhat, 2008], a separated representation of  $\mathbf{f}(\mathbf{x}, \boldsymbol{\vartheta})$  can be formulated as

$$\mathbf{f}(\mathbf{x}, \boldsymbol{\vartheta}) \approx \sum_{k=1}^m \boldsymbol{\varphi}_k(\mathbf{x}) \alpha_k(\boldsymbol{\vartheta}), \quad \mathbf{x} \in \Omega, \boldsymbol{\vartheta} \in \mathcal{D}, \quad (3.2)$$

where the basis vectors  $\boldsymbol{\varphi}_k$  are the left singular vectors, corresponding to  $m \leq M \ll n$  non-zero singular values of the so-called snapshot matrix

$$\mathbf{S} = [\mathbf{f}(\mathbf{x}, \boldsymbol{\vartheta}^{(1)}) \dots \mathbf{f}(\mathbf{x}, \boldsymbol{\vartheta}^{(M)})]. \quad (3.3)$$

The basis vectors  $\varphi_k$  depend on the discretization of the physical domain and only the coefficients  $\alpha_k$  depend on the design variables  $\boldsymbol{\vartheta}$ . Note that since only a low number of HF snapshots is assumed available, we are skipping the usual truncation phase. However, the number  $m$  of basis vectors is not strictly equal to  $M$  due to the possible presence of null singular values.

Rather than expressing  $\alpha_k(\boldsymbol{\vartheta})$  explicitly using surrogate modeling techniques [Coelho & Pierret, 2017] or by solving a Galerkin-projected problem [Choi et al., 2020], the proposed multi-fidelity approach relies on the assumption that a LF solution  $\mathbf{f}^{LF}(\mathbf{x}, \boldsymbol{\vartheta})$  is available at a significantly lower computational effort than the HF solution  $\mathbf{f}(\mathbf{x}, \boldsymbol{\vartheta})$ . The multi-fidelity approximations  $\alpha_k^{MF}$  of the coefficients  $\alpha_k$  can then be obtained by projecting  $\mathbf{f}^{LF}(\mathbf{x}, \boldsymbol{\vartheta})$  on  $\varphi_k$  [Chakir & Maday, 2009]:

$$\alpha_k^{MF}(\boldsymbol{\vartheta}) = \varphi_k^T(\mathbf{x}) \mathbf{f}^{LF}(\mathbf{x}, \boldsymbol{\vartheta}), \quad \mathbf{x} \in \Omega. \quad (3.4)$$

A multi-fidelity approximation model  $\mathbf{f}^{MF}(\mathbf{x}, \boldsymbol{\vartheta})$  of  $\mathbf{f}(\mathbf{x}, \boldsymbol{\vartheta})$  can thus be formulated as

$$\mathbf{f}^{MF}(\mathbf{x}, \boldsymbol{\vartheta}) = \sum_{k=1}^m \varphi_k(\mathbf{x}) \alpha_k^{MF}(\boldsymbol{\vartheta}), \quad \boldsymbol{\vartheta} \in \mathcal{D}. \quad (3.5)$$

Note, that this formulation does not necessarily interpolate the data, namely

$$\mathbf{f}^{MF}(\mathbf{x}, \boldsymbol{\vartheta}^{(i)}) \neq \mathbf{f}(\mathbf{x}, \boldsymbol{\vartheta}^{(i)}), \quad 1 \leq i \leq M, \quad \mathbf{x} \in \Omega, \quad (3.6)$$

and, as a consequence, the interpolation errors,

$$\begin{cases} \Delta_{\mathcal{J}}(\boldsymbol{\vartheta}^{(i)}) &= \mathcal{J}(\mathbf{f}(\mathbf{x}, \boldsymbol{\vartheta}^{(i)})) - \mathcal{J}(\mathbf{f}^{MF}(\mathbf{x}, \boldsymbol{\vartheta}^{(i)})), \\ \Delta_{c_h}(\boldsymbol{\vartheta}^{(i)}) &= c_h(\mathbf{f}(\mathbf{x}, \boldsymbol{\vartheta}^{(i)})) - c_h(\mathbf{f}^{MF}(\mathbf{x}, \boldsymbol{\vartheta}^{(i)})), \quad 1 \leq h \leq n_c \end{cases} \quad (3.7)$$

are non-null.

The objective and constraints trends are expressed respectively by  $\mathcal{J}^{MF}(\boldsymbol{\vartheta})$  and  $c_h^{MF}(\boldsymbol{\vartheta})$  instead of  $\mathcal{J}(\mathbf{f}_{MF}(\mathbf{x}, \boldsymbol{\vartheta}))$  and  $c_h(\mathbf{f}_{MF}(\mathbf{x}, \boldsymbol{\vartheta}))$  to simplify the notations. In this work, it is assumed that the approximation  $\mathbf{f}^{MF}$  is unbiased and the correction terms  $\Delta_{\mathcal{J}}(\boldsymbol{\vartheta})$  and  $\Delta_{c_h}(\boldsymbol{\vartheta})$  are modeled using Gaussian processes with zero mean and parametrized covariance kernels  $k_{\theta}$

$$\Delta(\boldsymbol{\vartheta}) \sim \mathcal{GP}(0, k_{\theta}(\boldsymbol{\vartheta}, \boldsymbol{\vartheta})), \quad \boldsymbol{\vartheta} \in \mathcal{D}.$$

Conditional on the observations, the GP posterior distribution [Rasmussen & Williams, 2006] at a new sampling point  $\boldsymbol{\vartheta}$  is a random variable with a normal distribution characterized by its mean

$$\bar{\Delta}(\boldsymbol{\vartheta}) = \mathbf{k}_{\theta}^T(\boldsymbol{\vartheta}) \cdot \mathbf{K}_{\theta}^{-1} \cdot [\Delta(\boldsymbol{\vartheta}^{(1)}), \dots, \Delta(\boldsymbol{\vartheta}^{(M)})]^T,$$

and its variance

$$\sigma^2(\boldsymbol{\vartheta}) = k_{\theta}(\boldsymbol{\vartheta}, \boldsymbol{\vartheta}) - \mathbf{k}_{\theta}^T \cdot \mathbf{K}_{\theta}^{-1} \cdot \mathbf{k}_{\theta},$$

with  $\mathbf{K}_{\theta}$  the  $M \times M$  covariance matrix between the  $M$  sample points

$$K_{\theta,ij} = k_{\theta}(\boldsymbol{\vartheta}^{(i)}, \boldsymbol{\vartheta}^{(j)}), \quad 1 \leq i, j \leq M,$$

and  $\mathbf{k}_{\theta}$  the vector of covariates between the  $M$  sample points and  $\boldsymbol{\vartheta}$ , defined by

$$\mathbf{k}_{\theta}(\boldsymbol{\vartheta}) = [k_{\theta}(\boldsymbol{\vartheta}, \boldsymbol{\vartheta}^{(1)}), \dots, k_{\theta}(\boldsymbol{\vartheta}, \boldsymbol{\vartheta}^{(M)})]^T.$$

The approximation of the cost functional for an arbitrary parameter set  $\boldsymbol{\vartheta}$  is thus defined as

$$\tilde{\mathcal{J}}(\boldsymbol{\vartheta}) = \mathcal{J}^{MF}(\boldsymbol{\vartheta}) + \Delta_{\mathcal{J}}(\boldsymbol{\vartheta}). \quad (3.8)$$

In analogous manner, the constraint functions are modeled as :

$$\tilde{c}_h(\boldsymbol{\vartheta}) = c_h^{MF}(\boldsymbol{\vartheta}) + \Delta_{c_h}(\boldsymbol{\vartheta}), \quad h = \{1, \dots, n_c\}. \quad (3.9)$$

In the following sections, the MF model refers to the MFNIRB model (the corrected MF prediction).

### 3.2.2 Improvement-based infill criteria

Assuming that a feasible solution exists in the DoE<sup>1</sup>, the current best point can be defined as

$$\mathcal{J}_{best} = \min \{ \mathcal{J}(\mathbf{x}, \boldsymbol{\vartheta}); \boldsymbol{\vartheta} \in \mathcal{C} \}, \quad (3.10)$$

where  $\mathcal{C} = \{ \boldsymbol{\vartheta} \in \mathcal{D}; c_h(\boldsymbol{\vartheta}) \leq 0, 1 \leq h \leq n_c \}$  denotes the feasible solution set. The improvement yielded by the observation of a new point  $\boldsymbol{\vartheta}$  can then be defined as

$$I(\boldsymbol{\vartheta}) = \max(\mathcal{J}_{best} - \tilde{\mathcal{J}}(\boldsymbol{\vartheta}), 0) \cdot \mathbf{1}_{\boldsymbol{\vartheta} \in \mathcal{C}}. \quad (3.11)$$

Assuming that the constraints involved in the optimization problem are independent, the probability that a given  $\boldsymbol{\vartheta} \in \mathcal{D}$  belongs to the feasible set  $\mathcal{C}$  can be computed using the closed-form formula

$$PF(\boldsymbol{\chi}) = \prod_{h=1}^{n_c} P(\tilde{c}_h(\boldsymbol{\chi}) \leq 0) = \prod_{h=1}^{n_c} \Phi\left(\frac{-\tilde{c}_h}{\Sigma_{c_h}}\right), \quad (3.12)$$

where  $\sigma_{c_h}^2$  is the posterior variance associated to constraint  $c_h$ ,  $1 \leq h \leq n_c$ . If it is further assumed that the objective and constraints are independent, the probability of improvement can be expressed as

$$PI_c(\boldsymbol{\vartheta}) = \Phi\left(\frac{\mathcal{J}_{best} - \tilde{\mathcal{J}}(\boldsymbol{\vartheta})}{\sigma(\boldsymbol{\vartheta})}\right) \cdot PF(\boldsymbol{\vartheta}). \quad (3.13)$$

$$EI_c(\boldsymbol{\vartheta}) = EI(\boldsymbol{\vartheta}) \times PF(\boldsymbol{\vartheta}), \quad (3.14)$$

with

$$EI(\boldsymbol{\vartheta}) = \begin{cases} \max(\mathcal{J}_{best} - \tilde{\mathcal{J}}(\boldsymbol{\vartheta}), 0) & \text{if } \sigma(\boldsymbol{\vartheta}) = 0, \\ (\mathcal{J}_{best} - \tilde{\mathcal{J}}(\boldsymbol{\vartheta}))\Phi\left(\frac{\mathcal{J}_{best} - \tilde{\mathcal{J}}(\boldsymbol{\vartheta})}{\sigma(\boldsymbol{\vartheta})}\right) + \sigma(\boldsymbol{\vartheta})\phi\left(\frac{\mathcal{J}_{best} - \tilde{\mathcal{J}}(\boldsymbol{\vartheta})}{\sigma(\boldsymbol{\vartheta})}\right) & \text{if } \sigma(\boldsymbol{\vartheta}) > 0, \end{cases} \quad (3.15)$$

where  $\phi(\cdot)$  and  $\Phi(\cdot)$  denote respectively the standard normal probability density function and the normal cumulative distribution functions,  $\tilde{\mathcal{J}}(\boldsymbol{\vartheta})$  being the posterior mean of  $\mathcal{J}$ .

Either  $EI_c$  and  $PI_c$  can be used as an Infill Criterion (IC) within the optimization loop to select the most promising infill point. Whereas the PI favors the regions of likely improvement, the EI corresponds to the posterior expectation of the improvement function and hence achieves

<sup>1</sup>See, e.g., Section 2.3 of [Feliot et al., 2017] and references therein for a discussion of possible alternatives in the case where no feasible solution is known.

a natural trade-off between regions of high improvement and regions of high variance. The maximum value of IC determines the new points to be added to the training set, such as

$$\boldsymbol{\vartheta}_{new}^* = \arg \max_{\boldsymbol{\vartheta}} IC(\tilde{\mathcal{J}}(\boldsymbol{\vartheta})), \quad (3.16)$$

where  $IC$  is an infill criterion using values of the approximate cost function  $\tilde{\mathcal{J}}$ .

The algorithm 1 summarizes the proposed optimization procedure. After sampling  $M$  snapshots from the HF black-box solver, the orthogonal basis  $\Phi = (\varphi_k)_{1 \leq k \leq m}$  can be obtained with the Singular Value Decomposition (SVD). Thereby, the multi-fidelity projection coefficients (see Eq. (3.4)) are evaluated using  $\Phi$  and  $M$  snapshots sampling of the LF simulation. The multi-fidelity quantities of interest are formulated, then corrected as in equations (3.8) and (3.9) to evaluate the quantities  $\tilde{\mathcal{J}}$  and  $\tilde{c}_h$ ,  $h = \{1, \dots, n_c\}$ . The IC uses these quantities to find the next candidate. Since the IC is likely to be multi-modal, a global optimization algorithm should be used to solve the auxiliary optimization problem (3.16).

---

#### Algorithm 1 DoE enrichment

---

**Require:**  $M, \mathbf{x}, \mathbf{f}^{LF}, \mathbf{f}^{HF}, \mathcal{J}, \mathbf{c}$ ,

**Ensure:**  $\boldsymbol{\vartheta}^*$

- 1: Training DoE of  $M$  points  $\boldsymbol{\vartheta} = \{\boldsymbol{\vartheta}^{(1)}, \dots, \boldsymbol{\vartheta}^{(M)}\}$  (Latin Hypercube Sampling)
  - 2: Compute High-Fidelity snapshots  $\mathbf{S} = [\mathbf{f}^{HF}(\mathbf{x}, \boldsymbol{\vartheta}^{(1)}), \dots, \mathbf{f}^{HF}(\mathbf{x}, \boldsymbol{\vartheta}^{(M)})]$
  - 3: Compute the basis  $\Phi$  associated with  $\mathbf{S}$ ,
  - 4: Evaluate  $\mathcal{J}^{HF}(\boldsymbol{\vartheta}), \mathbf{c}^{HF}(\boldsymbol{\vartheta})$ ,
  - 5:  $i \leftarrow 0$
  - 6: **while**  $i < \text{maximum iterations}$  **do**
  - 7:   Update High-Fidelity snapshot matrix with  $\mathbf{f}^{HF}(\mathbf{x}, \boldsymbol{\vartheta})$
  - 8:   Update the basis  $\Phi$ , DoE,  $\mathcal{J}^{HF}(\boldsymbol{\vartheta}), \mathbf{c}^{HF}(\boldsymbol{\vartheta})$ ,
  - 9:   Compute LF snapshots  $\mathbf{S}^{LF} = [\mathbf{f}^{LF}(\mathbf{x}, \boldsymbol{\vartheta}^{(1)}), \dots, \mathbf{f}^{LF}(\mathbf{x}, \boldsymbol{\vartheta}^{(M)})]$
  - 10:   Evaluate Multi-Fidelity  $\mathcal{J}^{MF}(\boldsymbol{\vartheta}), \mathbf{c}^{MF}(\boldsymbol{\vartheta})$
  - 11:   Evaluate  $\tilde{\mathcal{J}}(\boldsymbol{\vartheta}), \tilde{\mathbf{c}}(\boldsymbol{\vartheta})$  using Equations (3.9) and (3.8)
  - 12:   Compute  $IC(\boldsymbol{\vartheta})$  using Equation (4.35) or (4.37)
  - 13:   Get next candidate  $\boldsymbol{\vartheta}_{new}^* = \arg \max_{\boldsymbol{\vartheta}} IC(\tilde{\mathcal{J}}(\boldsymbol{\vartheta}))$
  - 14:    $i \leftarrow i + 1$
  - 15:    $M \leftarrow M + 1$
  - 16: **end while**
- 

## 3.3 Numerical results

### 3.3.1 Problem definition

The optimization benchmark problem [Benamara et al., 2017] is used for the following numerical experiments

$$\begin{aligned} & \text{minimize} && \mathcal{J}(\boldsymbol{\vartheta}) \\ & \text{s.t.} && \boldsymbol{\vartheta} \in \mathcal{D}, c_1(\boldsymbol{\vartheta}) \leq 0, c_2(\boldsymbol{\vartheta}) \leq 0, \end{aligned} \quad (3.17)$$

where  $\mathcal{D} = [4, 6] \times [10, 14]$  is a bi-dimensional design space and the objective and constraints functions are defined by

$$\begin{cases} \mathcal{J} & : \boldsymbol{\vartheta} \in \mathcal{D} \mapsto \min_{x_i \in [0, 1]} \mathbf{f}(\mathbf{x}, \boldsymbol{\vartheta}) \\ c_1 & : \boldsymbol{\vartheta} \in \mathcal{D} \mapsto \arg \min_{x_i \in [0, 1]} \mathbf{f}(\mathbf{x}, \boldsymbol{\vartheta}) - 0.75 \\ c_2 & : \boldsymbol{\vartheta} \in \mathcal{D} \mapsto 7.5 - \max_{x_i \in [0, 1]} \mathbf{f}(\mathbf{x}, \boldsymbol{\vartheta}), \end{cases} \quad (3.18)$$

using either the HF model  $f_{HF}$  or the LF model  $f_{LF}$  defined as

$$\begin{cases} f_{HF} & : \mathbb{R}^n \times \mathcal{D} \rightarrow \mathbb{R} \\ & (x, \boldsymbol{\vartheta}) \mapsto \frac{1}{2}(6x - 2)^2 \sin(\vartheta_2 x - 4) + \sin(10 \cos(\vartheta_1 x)) \\ f_{LF} & : \mathbb{R}^n \times \mathcal{D} \rightarrow \mathbb{R} \\ & (x, \boldsymbol{\vartheta}) \mapsto \frac{1}{2}(6x - 2)^2 \sin(\vartheta_2 x - 4) + 10(x - \frac{1}{2}). \end{cases} \quad (3.19)$$

These benchmark functions feature two fidelity levels of the full-field model. It has been generalized to enable a variable Low- to High-fidelity distance

$$\mathbf{f}_{LF}(\mathbf{x}, \boldsymbol{\vartheta}, \alpha) = \alpha \mathbf{f}_{LF}(\mathbf{x}, \boldsymbol{\vartheta}) + (1 - \alpha) \mathbf{f}_{HF}(\mathbf{x}, \boldsymbol{\vartheta}), \quad (3.20)$$

by introducing the parameter  $\alpha \in [0, 1]$ . We first consider the numerical experiment with  $\alpha = 1$ , then variable values of  $\alpha$  are taken into account.

This test problem is illustrated in figure 3.1. The non-feasible regions are delimited by continuous and discontinuous lines corresponding to the  $c_1$  and  $c_2$  constraints. The red and blue lines represent the targeted HF and the LF values. As can be observed on subfigures 3.1c and 3.1d, the constraint  $c_1$  features diagonal discontinuities and a sharp cliff in the region of high  $\vartheta_2$  values (Figure 3.1c) but none of them are present in the LF model (Figure 3.1d). Similarly, the region of feasibility for the constraint  $c_2$  is poorly represented by the LF model (see subfigures 3.1e and 3.1f). Besides, it features three disconnected feasible regions which make finding the global optimum a difficult optimization problem. Considering the objective function  $\mathcal{J}$ , it can be observed on subfigures 3.1a and 3.1b that the LF model fails to represent the influence of the  $\vartheta_2$  variable, which makes it rather deceptive.

### 3.3.2 Convergence of the multi-fidelity model

In this section 3.3.2, the optimization problem (4.55) is used, with  $\alpha = 1$ , to illustrate the convergence of the MF model proposed in Section 3.2.1 towards the HF model with an increasing number of available HF simulations. The Ordinary Kriging (OK) is compared to this model to illustrate the impact and the potential benefit of the MF trend compared to a constant trend based kriging (trend of the OK). The OK model is generated using the pykriging library [Paulson & Ragkousis, 2015] adapted to each experiment in sections 3.3.2, 3.3.3 and 3.3.4.

The constraints  $c_h(\boldsymbol{\vartheta})$ ,  $\tilde{c}_h^{MF}(\boldsymbol{\vartheta})$  (see Eq. (3.9)) and  $\tilde{c}_h^{OK}(\boldsymbol{\vartheta})$  obtained for Latin Hypercube designs respectively made of 4, 40 and 400 points are illustrated in Figures 3.3 and 3.4 for  $h = 1$  and  $h = 2$  respectively, the red and black lines represent respectively the constraints limits of the HF and the approximates values (obtained with the MF and the OK models). The relative errors between the HF real values and MF models for the objective  $\mathcal{J}$  and for the constraints  $c_1$  and  $c_2$  are given in Table 3.1 and the snapshots obtained using either the MF, LF and

HF function values are represented on Figure 3.2 for the 4 points DoE. For each curve, the up and down triangles represent respectively the maximum and the minimum values of the  $f(\mathbf{x})$ . The vertical line represents the upper-bound of 0.75 on  $c_1$  and the horizontal line represents the lower-bound of 7.5 on  $c_2$  (see eq. (4.55)).

The LF snapshots minimum values illustrated in Figure 3.2 are located in the lower part of the vertical upper-bound line. The  $c_1$  constraint is confirmed to be constant as observed on Figure 3.1d and there are no non-feasible areas for this constraint (see Figure 3.1b). The LF test function is not able to capture  $c_1$  features. The multi-fidelity function values are approaching better the variation of minimum values locations (Figure 3.2). Table 3.1 compares HF to multi-fidelity and corrected multi-fidelity quantities of interest.

M	$\frac{\ \mathcal{J}-\mathcal{J}^{MF}\ }{\ \mathcal{J}\ }$	$\frac{\ c_1-c_1^{MF}\ }{\ c_1\ }$	$\frac{\ c_2-c_2^{MF}\ }{\ c_2\ }$	$\frac{\ \mathcal{J}-\tilde{\mathcal{J}}\ }{\ \mathcal{J}\ }$	$\frac{\ c_1-\tilde{c}_1\ }{\ c_1\ }$	$\frac{\ c_2-\tilde{c}_2\ }{\ c_2\ }$
4	6.97%	0.80%	8.10%	8.16%	0.83%	6.59%
40	4.77%	0.59%	7.87 %	4.10%	0.60%	2.34%
400	4.30%	0.61%	4.56 %	0.04%	0.35%	0.11%

Table 3.1: Mean over the design variables  $\vartheta$  of the "HF-to-MF" models relative error for the objective and constraints when the number of available HF simulations successively equals to 4, 40 and 400 points. The first three columns show the error between the HF model and the MF model without the additive correction. The last three columns show this error after the additive correction of MF model using Gaussian processes.

For both the objective and the constraints, the prediction errors of the MF models decrease as the size of the DoE increases. The features of the HF models are well captured, especially when the additive correction is applied (see Eq. (3.8)), with an average relative prediction error ranging from 0.04% to 0.35% which represents a reduction of 0.48% to 8.12% of the relative error (see Table 3.1 and Figures 3.3 and 3.4). The corrected model is performing better than the LF and the uncorrected multi-fidelity models. The corrected MF model errors for a training set of 400 points are lower than the uncorrected one. Moreover, the increase of the training set sizes from 40 up to 400 generates a small reduction in the MF trend model error, which seems to reach an asymptote (0.47% drop of the objective and 0.02% increase in  $c_1$ ).

In Figures 3.3 and 3.4, the MF model and the MF trend values are compared to an OK model and values of HF and LF constraints (evaluated by the functions defined by (4.56)). The OK model cannot capture discontinuities for a low-size training set (4 training points), whereas, the corrected model is better capturing the discontinuities even for scarce DoE size. The MF uncorrected model on Figures 3.3 and 3.4 converges to the LF values, whereas, as for kriging, the corrected MF is converging to the HF targeted values.

Regarding the constraint  $c_1$ , for which the LF model is unable to capture the features of the HF model, Figure 3.3 shows that the corrected MF model can capture both the high values of the constraint and the diagonal discontinuities. The LF model for constraint  $c_2$  is more informative than the one for constraint  $c_1$ . Nevertheless, it fails to represent the three disconnected basins featured by the HF model, whereas Figure 3.4 shows that these basins are recovered by the correction term using only 40 points.

### 3.3.3 Multi-fidelity convergence for variable Low- to High- fidelity distance

Section 3.3.2 illustrates the behavior of the MF model and trend in comparison to an OK model for a single run at each DoE level. As the Latin Hypercube Sampling used to generate the DoE exhibits non-deterministic behavior in successive runs, the present section is devoted to the statistical behavior over repeated runs.

This study focuses on the local results at the optimal targeted value. The criterion evaluated is defined at the theoretical optimal point  $\boldsymbol{\vartheta}^*$  by

$$\delta\mathcal{J} = \frac{\|\mathcal{J}_{HF}(\boldsymbol{\vartheta}^*) - \mathcal{J}(\boldsymbol{\vartheta}^*)\|}{\|\mathcal{J}_{HF}(\boldsymbol{\vartheta}^*)\|} \quad (3.21)$$

where  $\mathcal{J}$  can be equal to  $\tilde{\mathcal{J}}_{OK}$  or  $\tilde{\mathcal{J}}_{MF}$ .

The objective is to evaluate the capacity of MF models with different HF-LF distances (variable  $\alpha$ , see eq. (3.20)) to respond accurately to the optimization problem.

It is advised to use a size of 10 times the number of variables as the initial set of experiments [Jones & Schonlau, 1998], leading to a minimum of 20 points initial set of experiments to obtain sufficient coverage. The MF model is then evaluated with a 20 initial training set. Results obtained for two different DoEs of 20 simulations ( $M=20$ ) are presented in Figures 3.5a and 3.5b for varying  $\alpha$  values.

At the examples shown in Figure 3.5, the MF trend intersects the OK model relative error between  $\alpha = 0.2$  and  $\alpha = 0.3$ , its performances decreasing for higher  $\alpha$  values,  $\alpha \geq 0.3$  (Figure 3.5a). MF model outperforms OK model for all  $\alpha$  values in Figure 3.5b while it remains less interesting for  $\alpha \geq 0.4$  in the experiment in the Figure 3.5a. Figure 3.5 presents some variability in the MF performance, therefore, Figure 3.6 gives the mean and standard deviation for a series of 40 runs of the three models. In each run, a new LHS DoE is generated, and the results are computed for increasing values of  $\alpha$ .

The average behaviour of the MF trend outperforms the OK model up to  $\alpha \leq 0.2$ , while the average behaviour of the corrected MF model is systematically better for all values of  $\alpha$ , up to the maximum distance  $\alpha = 1$ . Given the standard deviation, Figure 3.6 shows that the MF trend is very stable, unlike the OK and MF models. Given this variability, MF seems to outperform the OK model up to  $\alpha = 0.7$ , and we can consider that the proposed MF model is more accurate up to  $\alpha \approx 0.7$ .

This study illustrates the impact of the trend on a kriging model. When the  $\alpha$  decreases, the trend error MF is reduced, and consequently, the MF model (the corrected trend MF) is improved. The proposed MF model can be an alternative to classical kriging (here OK model) when the available LF data are sufficiently close to the HF data, however, obtained at a cost comparable to the kriging model evaluation.

### 3.3.4 Comparison of infill criteria

The last sections illustrate the behavior of MF in comparison to an OK for different DoE sizes and multiple MF configurations by using the parameter  $\alpha$ . In the present section, the value of  $\alpha$

is fixed to 1, the highest HF-LF distance case, denoting the original benchmark problem [Benamara et al., 2016]. Optimization strategies using either the  $EI_c$  and  $PI_c$  infill criteria defined in Section 3.2.2 are applied on the test problem of Section 3.3.1. The convergence was tested with high DoE coverage (up to 400 points). The objective of this section is to improve the model convergence with a smaller DoE.

Starting from a Latin Hypercube design of 20 experiments (which corresponds to  $M = 10d$  as recommended by [Jones & Schonlau, 1998]), either  $EI_c$  and  $PI_c$  are performed for the OK and corrected MF models. The results obtained after 5 iterations using  $EI_c$  criterion that take into account the probability of feasibility of the constraints  $c_1$  and  $c_2$  are reported in Figure 3.7. The cartographies showing the values of each criterion in the last iteration for MF and OK models are shown in Figures 3.7e and 3.7f.

The first experiment (Figures 3.7), indicates that OK and MF optimums are in the targeted location for less than 5 infill iterations after a similar initial DoE of 20 training points. The model OK best point was obtained after only 3 iterations. The infill points are mainly covering the region of the theoretical exact best point, particularly for the model OK. The MF infill points are more distanced for iterations 1, 3, and 4 and can be considered more as an exploratory enrichment. The last maximal value of the MF  $EI_c$  is located at the theoretical optimal point. The MF model is better representing the  $c_1$  constraint at the initial iteration and remains very similar to an OK after few iterations. The global searching phase is brief and converge to the right area for this initial DoE size for both models. However, in this case, the optimal point was determined for less infill points for OK than for MF model. In this case, OK outperforms the MF model.

In the section 3.3.2, it was observed that the MF model was better representing the constraints than the OK model in a small DoE size of  $M=4$ . The DoE size for both models is then decreased to 4 points in the following experiment to test the IC capabilities of MF in comparison to OK models for a lowest evaluation costs (Figure 3.8).

In Figure 3.8, initial models are expected to be less accurate, being insufficiently explored. The objective is to test the ICs capacity to reach the optimal point or the right region of interest. In Figure 3.8c, the MF model best point was obtained after only 3 iterations in the case of  $EI_c$  infill comparing to 15 iterations for the OK model (Figure 3.8d). Concerning the  $PI_c$  infill, the best point is obtained after 20 iterations for MF model and 18 for OK model (Figures 3.8e and 3.8f). For both models, the points added are clustering in the right region of interest (close to the location of the best point). On the other hand, the  $EI_c$  criterion on Figures 3.8c and 3.8d appears more spread than  $PI_c$  on Figures 3.8f and 3.8e. The convergence of all cases is achieved after a lower number of iterations for the  $EI_c$  than  $PI_c$ . An explanation can be that the  $PI_c$  infill criterion's exploration capacity remains poor for both models. In conclusion, the  $EI_c$  overperforms the  $PI_c$  and compared to the OK model, this study shows that the enriched MF model results are better when the initial DoE remains relatively small thanks to a more efficient exploration of the design space.

### 3.3.5 Comparison of multi-fidelity and ordinary kriging enriched surrogate models

In the last section, two enrichment criteria are explored in the MF and single-fidelity (OK) frameworks. In the presented cases, the enrichment was able to find the regions of the optimal values. These observations imply that the MF can be used as a surrogate model in the constrained optimization problem to reduce its cost. The present section aims at quantifying the gain induced by the enrichment strategy. The reference solution for a random design space is compared to a sequentially enriched space. Experiments are performed for multiple runs with random LHS DoEs, for varying values of  $\alpha$  using the  $EI_c$  criterion.

Figure 3.9 describes the evolution of the local relative error (defined by (3.21)) of the objective function at the optimum location with and without the enrichment. The same LHS training sets are used for the MF and the OK model to compare both procedures. The dotted lines represent values obtained after insertion of 4 infill points to a 20 points LHS DoE.

The OK values obtained from the random and the enriched DoE have the same values, the local error is not improved by the enrichment. Even for the MF model, the enrichment does not significantly reduce the error. The gap remains very low until  $\alpha = 0.5$ , where the impact of the enrichment in the error reduction appears higher, particularly for MF distances starting from  $\alpha > 0.5$ . Moreover, the standard deviation is strongly correlated to  $\alpha$  as it tends toward 0, allowing a very low uncertainty about the MF results for small  $\alpha$ . As a result of this study, when the LF function is close enough to the HF function, the approximation's confidence is higher than for a single-fidelity surrogate model. In this boundary case, the MF is shown to be better for a well-chosen LF-HF combination.

## 3.4 Conclusions

The proposed methodology uses a multi-fidelity model approximation to accelerate the optimization process by applying additive corrections based on the Gaussian process. The method improves the surrogate model by using statistical infill criteria adapted to account for the violation of constraints such as the probability of improvement and the expected improvement criteria.

In the presented cases, the enrichment strategy allows finding the region of interest when the distance between the low- and the high-fidelity models is the highest. The optimization cost was lower for the multi-fidelity model with a small initial design of experiments than for the ordinary kriging when using the expected improvement infill criterion. This can be further improved with a lower distance between the high and the low-fidelity response values used in the optimization framework. On the other hand, it has to be observed that the model's quality is less improved than these models' capacity to solve an optimization problem. A global quality criterion would have to be considered to qualify the multi-fidelity enrichment's overall gain as a follow-up to this study.

Corrected multi-fidelity is a promising approach for capturing various delicate high-fidelity features. Based on this paper's results, the reduced-order model of full-field multi-fidelity can provide additional information on complex systems' behavior compared to usual scalar substitutes. Further work is needed to combine the infill criteria into an optimized strategy

adapted to more sophisticated feature sets required to treat real engineering optimization test cases.

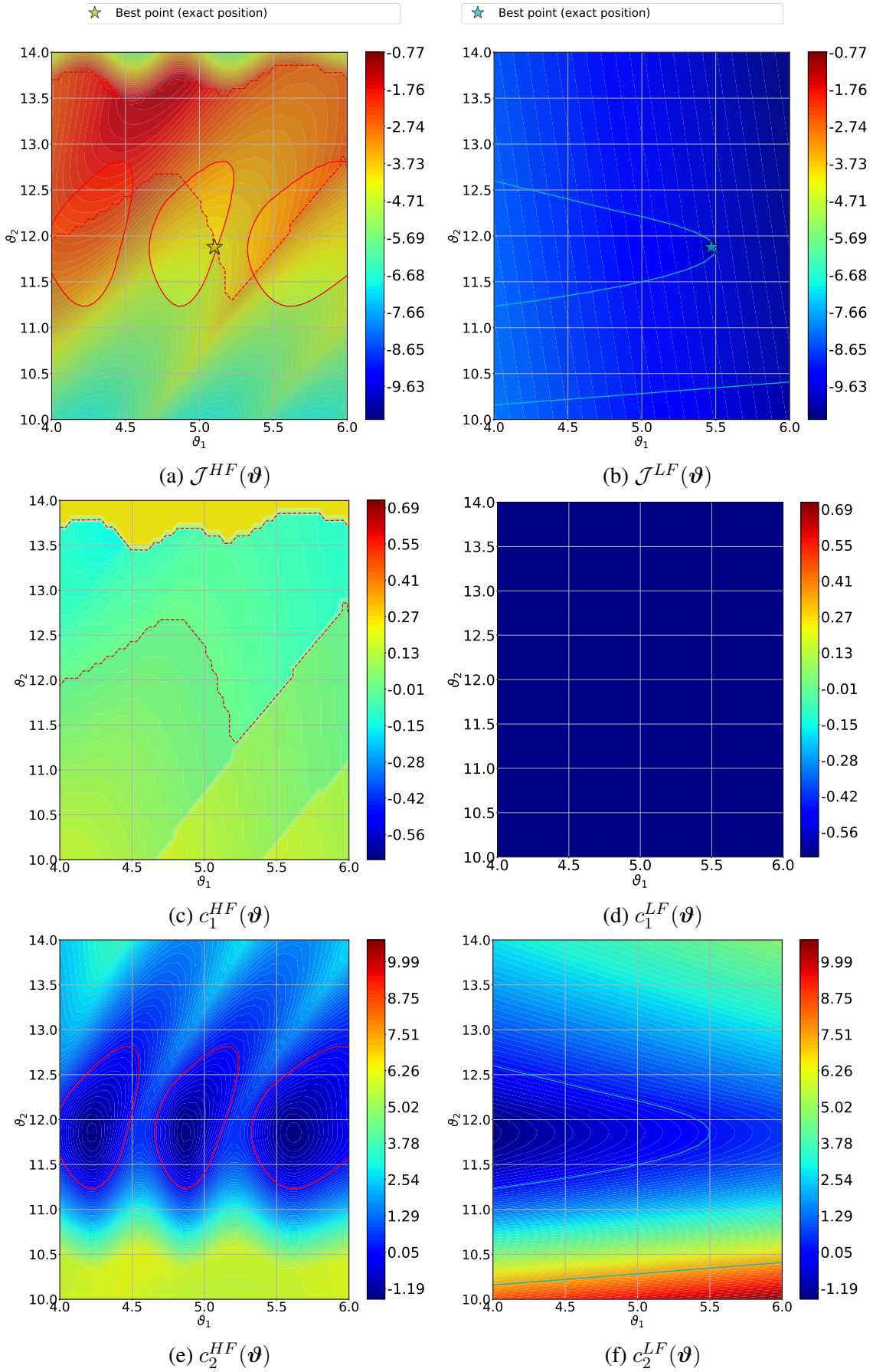


Figure 3.1: Values of the objective function (first row) and of the constraints functions  $c_1$  (second row) and  $c_2$  (third row) of HF (left column) and LF (right column).

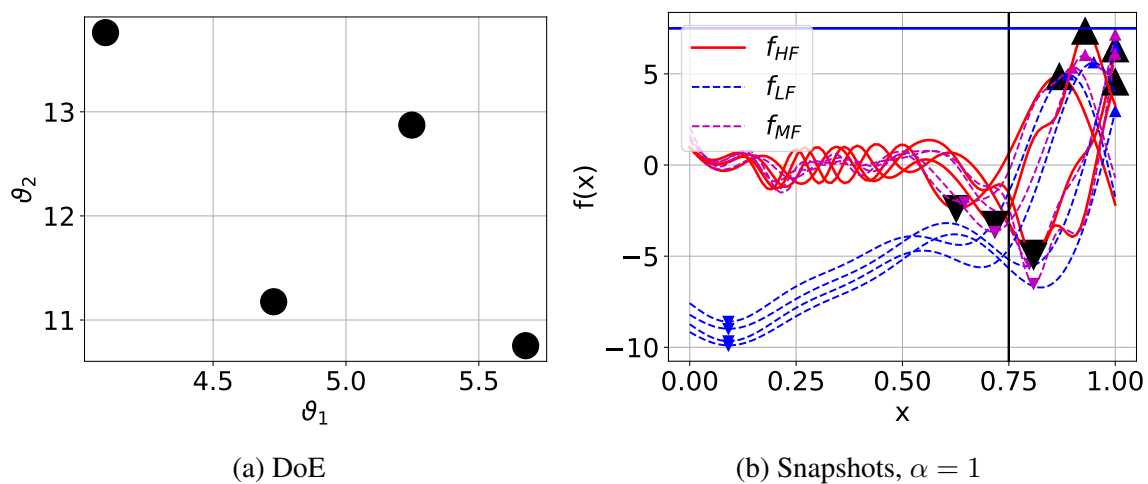


Figure 3.2: Snapshots obtained for the 4 points DoE when the HF (continuous red curves), LF (dashed blue curves), and MF (dotted purple curves) models are used with  $\alpha = 1$ .

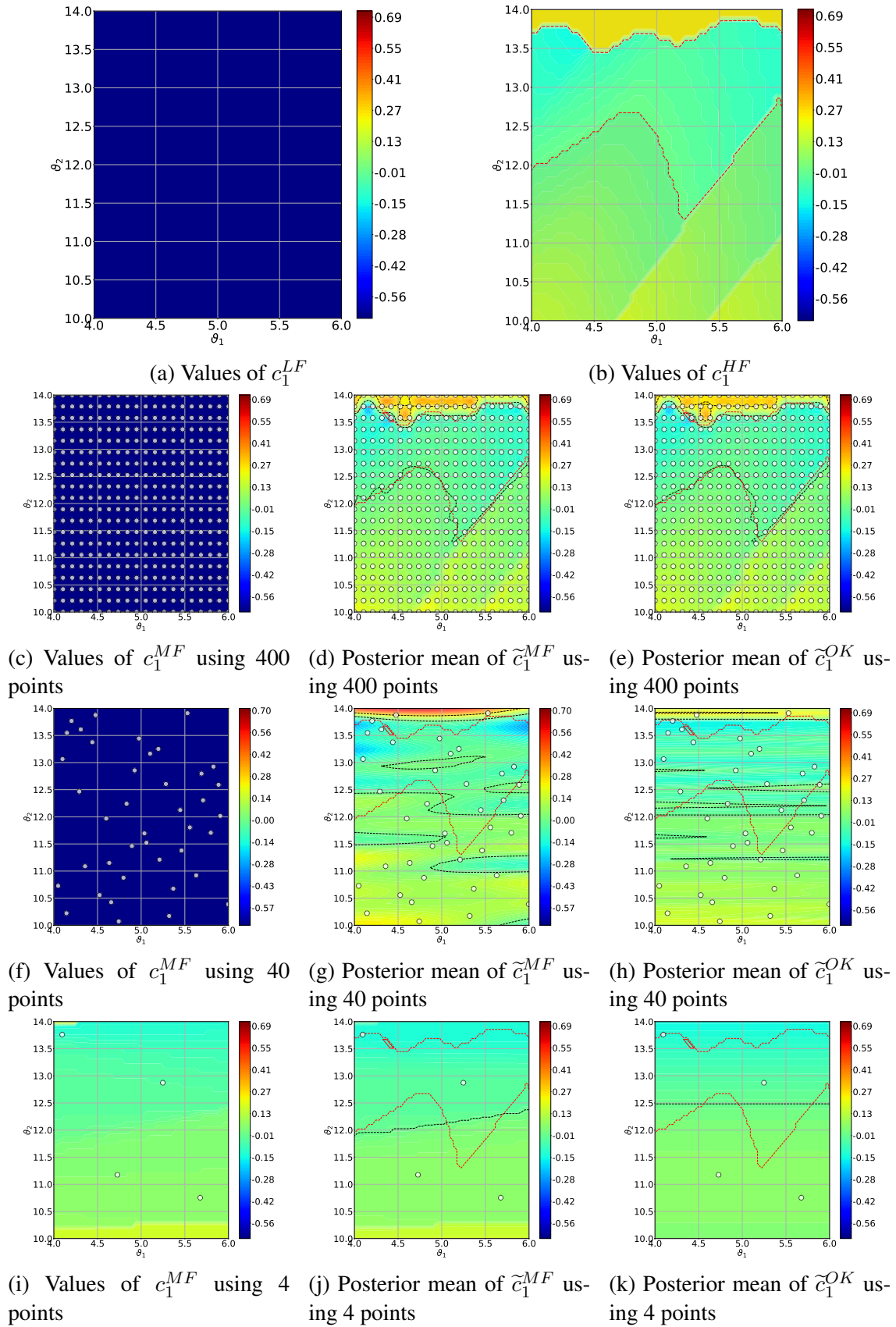


Figure 3.3: The convergence of the MF trend, MF and OK models of the  $c_1$ . In the subfigures (c) to (h), the left, the middle and the right columns show the values of  $c_1^{MF}$ ,  $\tilde{c}_1^{MF}$  (see Eq. (3.9)) and  $\tilde{c}_1^{OK}$ . The points in the DoE are represented as white dots.

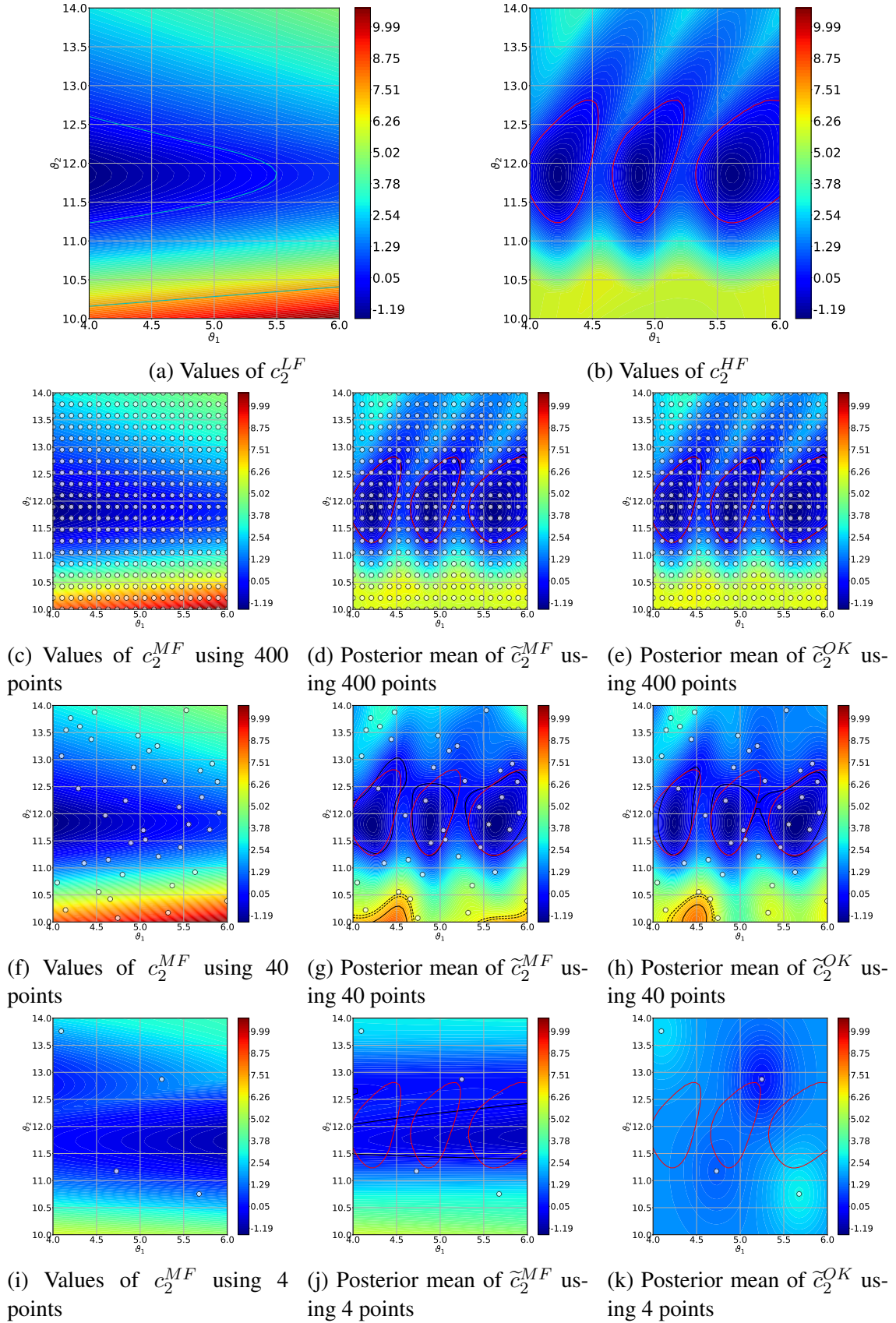


Figure 3.4: The convergence of the MF trend, MF and OK models of  $c_2$ . In the subfigures (c) to (h), the left, the middle and the right columns show the values of  $c_2^{MF}$ ,  $\tilde{c}_2^{MF}$  (see Eq. (3.9)) and  $\tilde{c}_2^{OK}$ . The points in the DoE are represented as white dots.

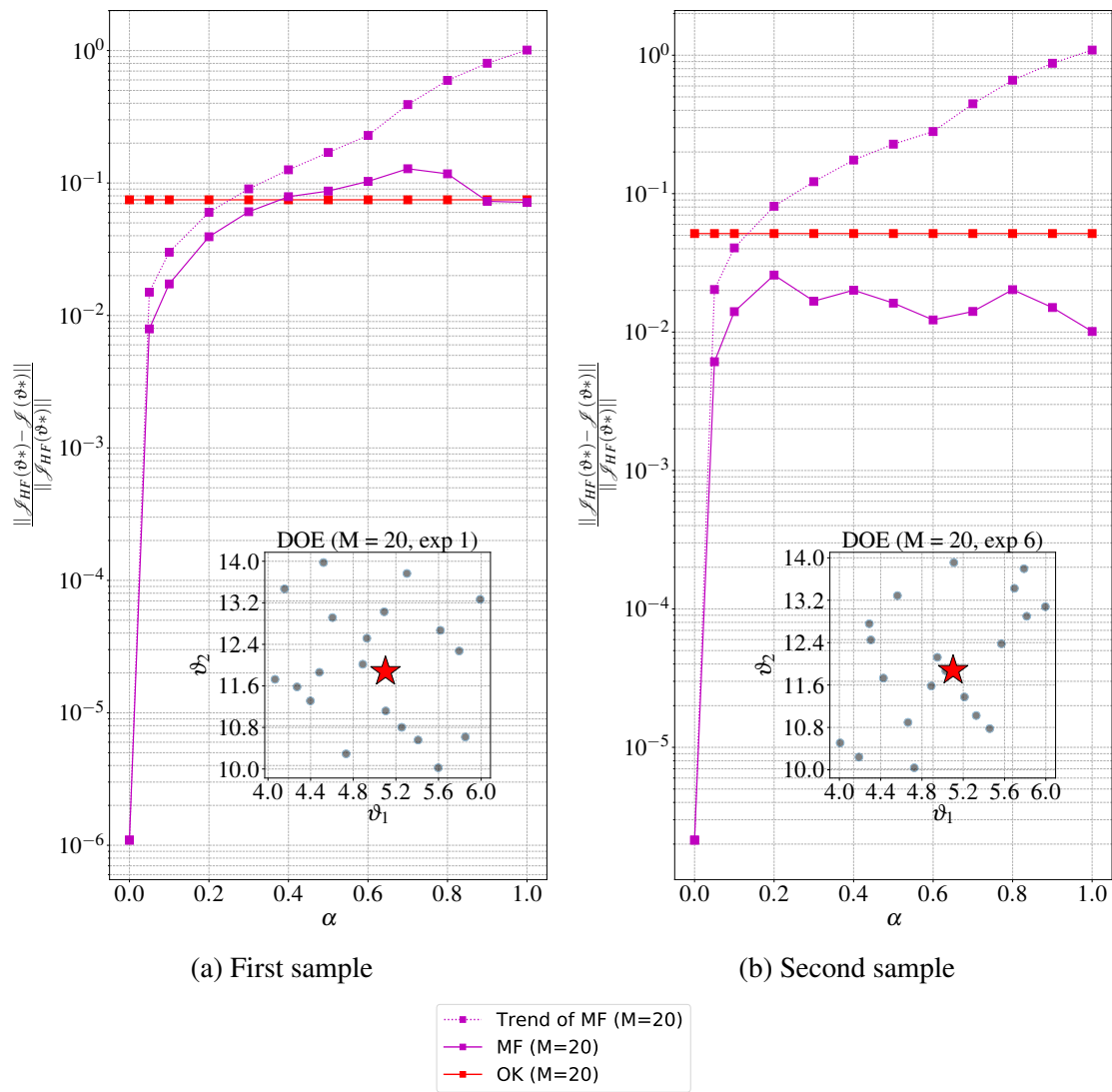


Figure 3.5: Evolution of the relative error for a sample experiment  
 The black dots are the DoE points and the red star is the location of the theoretical optimum of the HF model.

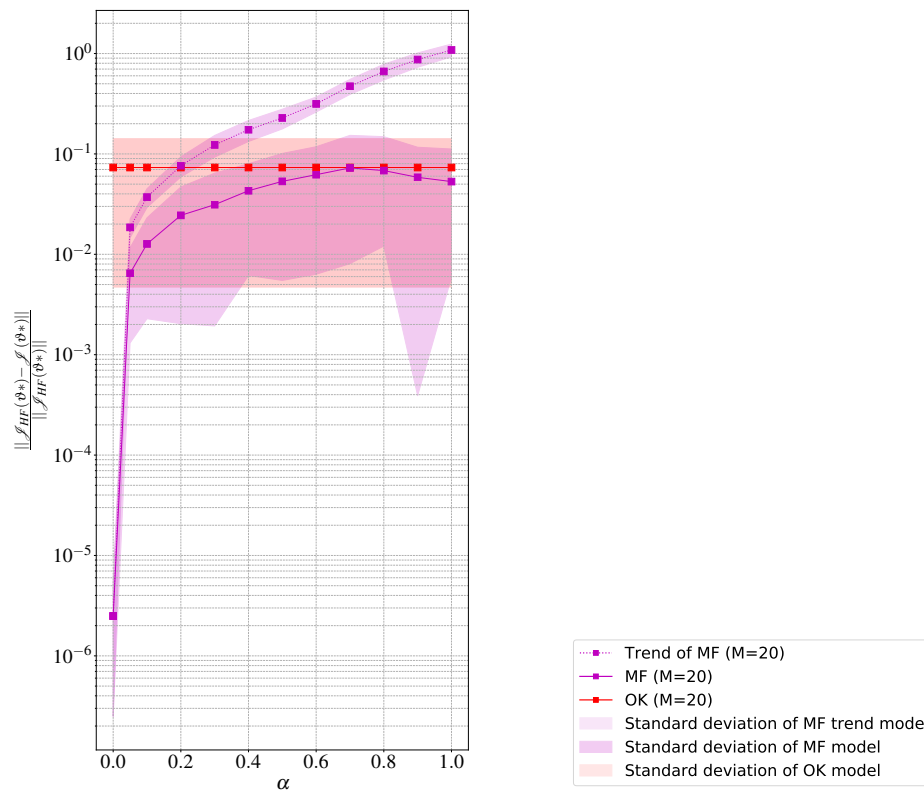


Figure 3.6: Evolution of the relative error at the theoretical optimal point for multiple runs. The mean error values are represented by purple continuous and dotted lines for the MF model and its trend, the OK by a red line, with their corresponding standard deviation (shaded areas) obtained from 40 independent LHS experiments for each  $\alpha$  value. Same LHS DoE is used for model comparison.

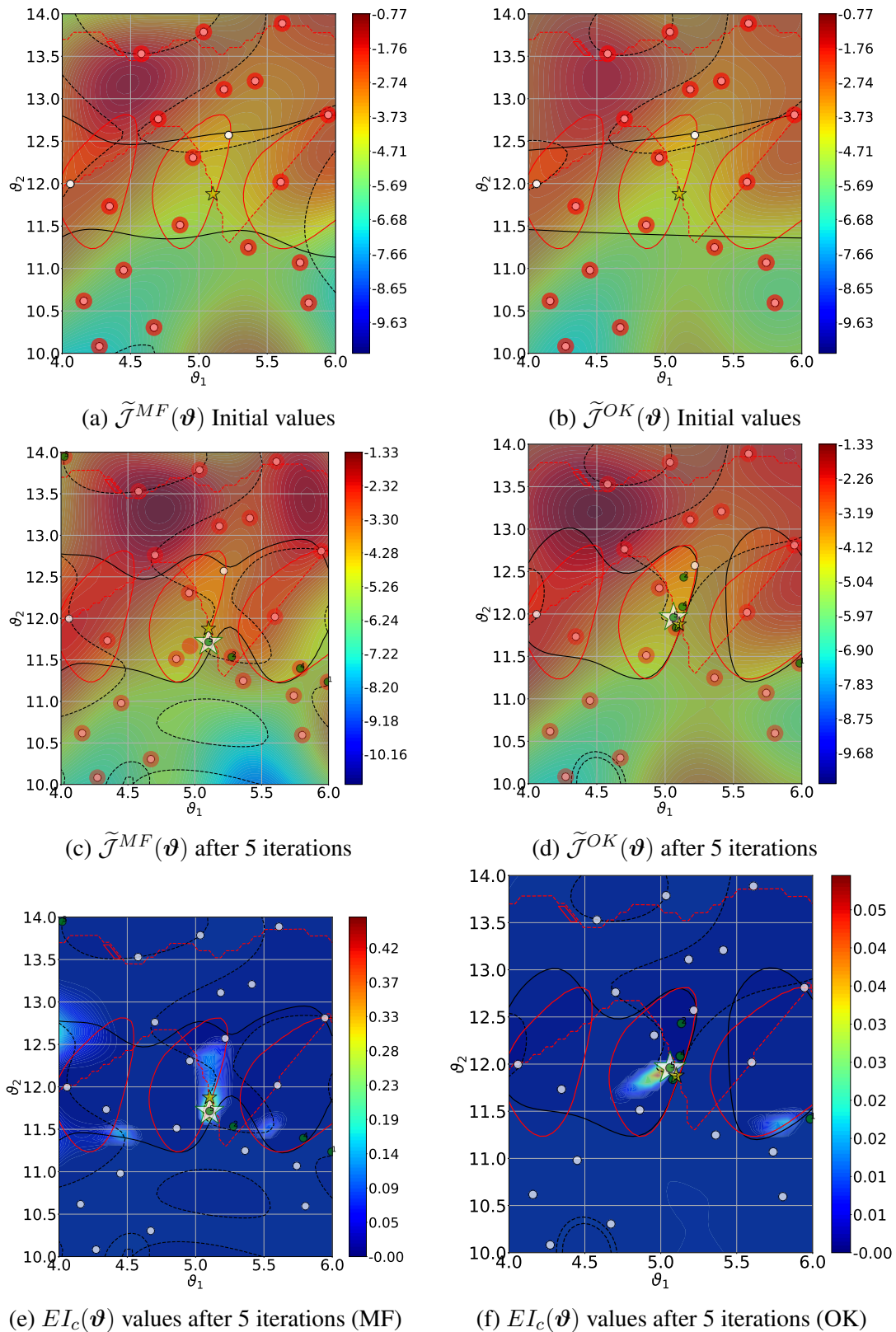


Figure 3.7: Optimization results obtained using the  $EI_c$  criterion. Starting from 20 points (first row), the algorithm is iterated for 5 iterations (the other subfigures).

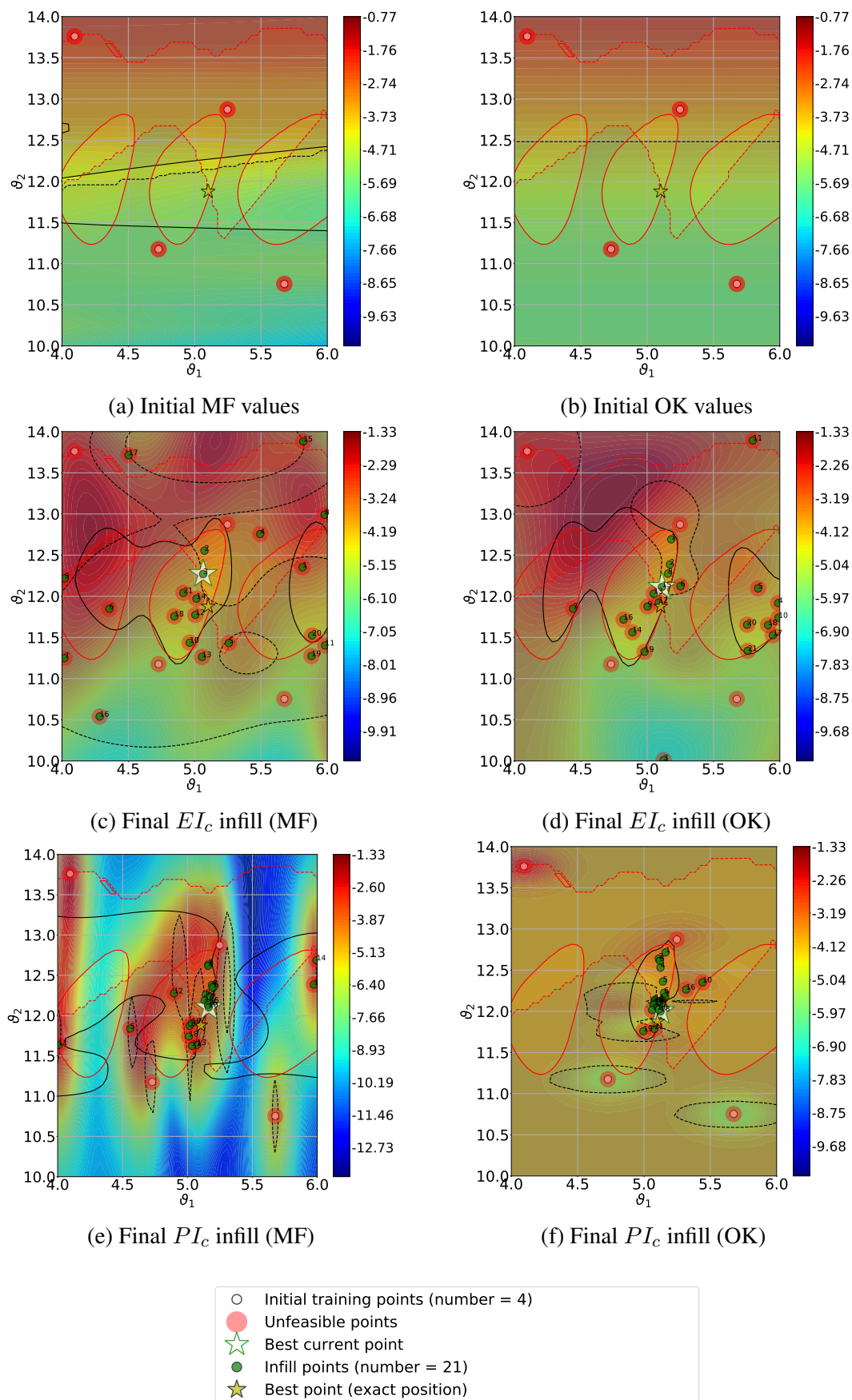


Figure 3.8: Optimization results obtained using the  $EI_c$  and  $PI_c$ . Starting from 4 points (first row), the algorithm is iterated for 21 iterations. The first column corresponds to results using the MF model, and the second column results using the OK model.

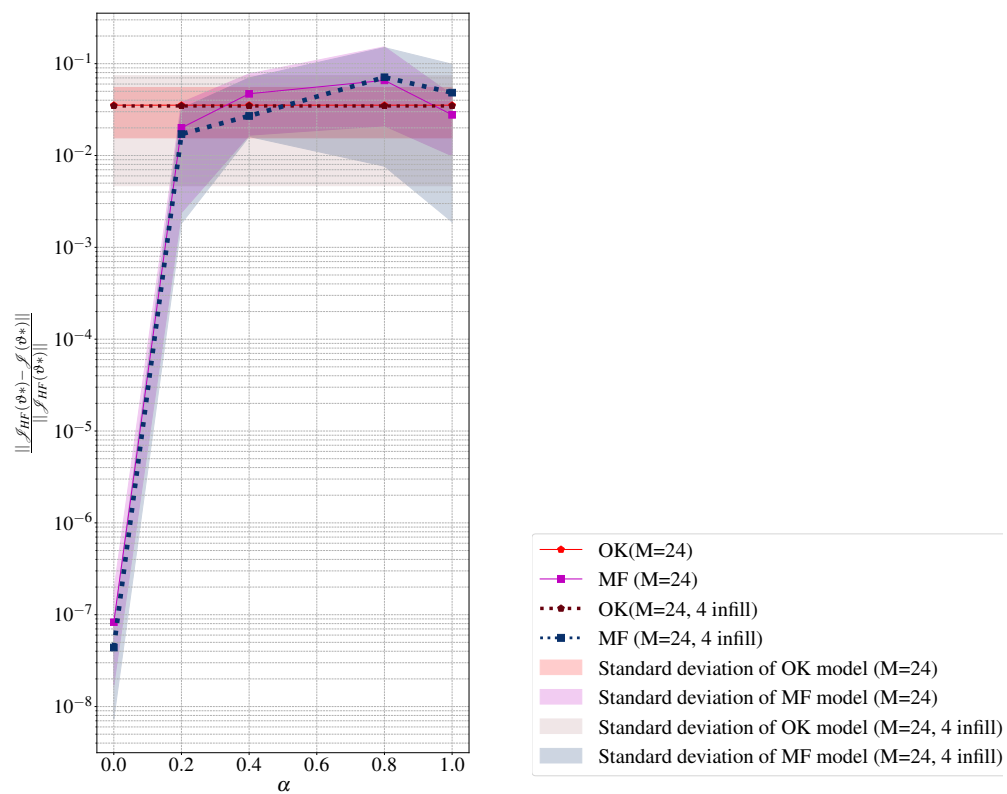


Figure 3.9: Evolution of the relative error for enriched and random DoE for multiple runs

# Chapter 4

## Methodology improvements and investigations for complex expensive models

### 4.1 Introduction

Chapter 3 introduced the MFNIRB methodology in the context of constrained optimization. It was shown that employing the Low-Fidelity (LF) information as in MFNIRB yielded better accuracies for small Design of Experiment (DoE)s when compared to the single-fidelity Ordinary Kriging (OK) model based solely on High-Fidelity (HF) data. LF was exploited to better capture features that are difficult to represent for a single-fidelity metamodels such as OK (plateau-like variations in the design space). Another advantage is the higher LF data availability compared to HF, due to the difference in cost and complexity. The limited budget does not allow intensive calls to the HF solver while LF data can be obtained at a very low cost, MFNIRB is cheaper than OK.

However, the success of the multi-fidelity approach depends on the correlation between the different model levels. Another limitation is the assumption that the LF cost is negligible. This assumption was made in Chapter 3 to allow the exploration of the MFNIRB method. However, a few seconds, minutes, or even hours may be required to obtain a single LF response. While the optimization procedure involves a genetic algorithm to maximize the enrichment criterion, it requires multiple iterations with extensive evaluations of the evolving population, and consequently might exceed the allowed budget.

Therefore, in the present chapter, we introduce an additional level of Non-Intrusive Proper Orthogonal Decomposition (NIPOD) approximation of the LF model. The experiments are conducted to compare MFNIRB to the OK Surrogate Based-Optimization (SBO) convergence (OK is the single-fidelity Kriging metamodel tested in Chapter 3) in different configurations, considering :

- **The availability of LF and HF data :** LF is less expensive (or less complex to compute), meaning that LF responses are available in a more abundant amount. LF can be called in parallel to HF, so the aim is to determine the best LF-HF ratio to support the optimization.
- **The enrichment criteria :** the purpose of enrichment is to reduce the number of evaluations needed to find the optimization solution. The multi-fidelity approach offers the

possibility to add LF values as well as HF values to the optimization. The enrichment criterion must take into account the LF-HF cost ratio in order to perform either the HF or LF evaluation when relevant and better control the overall cost.

- **The ability to represent complex constraints :** MFNIRB requires less HF training to represent complex features. Thus, the influence of MFNIRB accuracy on the efficiency of SBO needs to be explored.

Section 4.2 presents the multi-fidelity reduced-basis, enrichment and NIPOD methodologies. The section 4.3 provides the experiments conducted to test the enrichment and metamodelling approaches introduced.

## 4.2 Methodology adopted for multi-fidelity model validation

The use of  $\vartheta$  as design parameters will be replaced by  $\chi$  to distinguish the new notations of the present and following chapters.

This section defines the methodology proposed to solve efficiently a constrained single objective optimization problem defined as follows

$$\begin{aligned} \chi^* = \arg \min_{\chi} \quad & \mathcal{J}(f(x, \chi)) \\ \text{s.t.} \quad & g_i(f(x, \chi)) \leq 0, \quad i = 1, \dots, p \\ & h_j(f(x, \chi)) = 0, \quad j = 1, \dots, q \end{aligned} \quad (4.1)$$

$$\begin{aligned} x &\in \Omega \subset \mathbb{R}^{dim} \\ \chi &\in \mathcal{D} \subset \mathbb{R}^d \end{aligned}$$

where  $x$  is a point in the physical space of dimension  $dim$ ,  $\chi$  the vector of the design variables,  $\mathcal{D} \subset \mathbb{R}^d$  is the design domain of dimension  $d$  corresponding to the number of design variables which can be varied independently, and  $\chi^*$  is the optimum value of design variables minimizing the objective functional  $\mathcal{J} \in \mathbb{R}$  respecting inequality and equality constraints  $g$ , and  $h$  respectively. In the discrete  $f(x, \chi)$  is evaluated on a finite set of  $n$  points (nodes of the finite element mesh)  $\mathbf{x} \in \mathbb{R}^{dim \times n}$  yielding function snapshots  $\mathbf{f}(\mathbf{x}, \chi) \in \mathbb{R}^n$ . The functional  $\mathcal{J}$  is then obtained by operations of integration/maximization/minimization of the spatially discretized snapshot. The formulation 4.1 becomes

$$\begin{aligned} \chi^* = \arg \min_{\chi} \quad & \mathcal{J}(\mathbf{f}(\mathbf{x}, \chi)) \\ \text{s.t.} \quad & g_i(\mathbf{f}(\mathbf{x}, \chi)) \leq 0, \quad i = 1, \dots, p \\ & h_j(\mathbf{f}(\mathbf{x}, \chi)) = 0, \quad j = 1, \dots, q \end{aligned} \quad (4.2)$$

$$\begin{aligned} \mathbf{x} &\in \Omega \subset \mathbb{R}^{dim \times n} \\ \chi &\in \mathcal{D} \subset \mathbb{R}^d \end{aligned}$$

The computer simulation of  $\mathbf{f}(\mathbf{x}, \chi)$  is considered expensive, and will be approximated using MFNIRB method introduced in the previous Chapter by  $\tilde{\mathbf{f}}(\mathbf{x}, \chi)$ , yielding the following formulation of the full-field optimization problem

$$\begin{aligned}
\boldsymbol{\chi}^* = \arg \min_{\boldsymbol{\chi}} \quad & \mathcal{J}(\tilde{\boldsymbol{f}}(\mathbf{x}, \boldsymbol{\chi})) \\
\text{s.t.} \quad & g_i(\tilde{\boldsymbol{f}}(\mathbf{x}, \boldsymbol{\chi})) \leq 0, \quad i = 1, \dots, p \\
& h_j(\tilde{\boldsymbol{f}}(\mathbf{x}, \boldsymbol{\chi})) = 0, \quad j = 1, \dots, q
\end{aligned} \tag{4.3}$$

$$\begin{aligned}
\mathbf{x} &\in \Omega \subset \mathbb{R}^{\dim \times n} \\
\boldsymbol{\chi} &\in \mathcal{D} \subset \mathbb{R}^d
\end{aligned}$$

Note that the proposed approach approximates the full-field simulation output rather than the functional itself, and, in general, aiming at a better capture of detailed features of the flow when Computational Fluid Dynamic (CFD) simulations are considered

$$\tilde{\mathcal{J}}(\boldsymbol{\chi}) \neq \mathcal{J}(\tilde{\boldsymbol{f}}(\mathbf{x}, \boldsymbol{\chi})). \tag{4.4}$$

The following sections aim to explore the MFNIRB model, introduced in Chapter 3, as a substitute to the vectors  $\boldsymbol{f}(\mathbf{x}, \boldsymbol{\chi})$  used in the optimization procedure. Such model used the low-fidelity at each call during the SBO solving, considering these simulations negligible. However, in the context of optimization, its Central Processing Unit (CPU) budget becomes non-negligible when multiple calls are made through a computational chain, including meshing, solving and post-processing. The fundamental hypothesis behind the family of NIPOD methods is that the full-field model provides a better insight into a physical system behavior when compared to scalar surrogate models. LF simulations are considered cheap and valuable for designers willing to meet design budgets or get insight into design direction. Compared to the previous chapter, the NIPOD will be introduced for the call to the LF to avoid accessing the code in the online phase for the call to the LF to avoid repetitive calls to the LF code in the online phase and consequently reduce its cumulative costs.

This section presents the implementation of the suggested methodologies to solve the costly full-field SBO problems. Section 4.2.1 presents the construction of the output LF vectors. Section 4.2.2 details the structure of the MFNIRB model. Section 4.2.3 introduces the study of the proposed infill criteria. Finally, Section 4.2.4 details the different steps of the optimization conducted using MFNIRB.

### 4.2.1 Construction of reduced-order model of the low-fidelity solution field

Let us remind that MFNIRB model relies on an orthogonal projection of the LF snapshots onto the HF Proper Orthogonal Decomposition (POD) basis. Each MFNIRB prediction involves a call to the LF solver. The issue is that the SBO procedure requires multiple evaluations, as the Genetic Algorithm (GA) needs a high number of evaluations rapidly becoming intractable for complex optimization problems. If a LF evaluation requires, for example, five minutes, and the genetic algorithm is performed for 30 iterations and 300 evaluations, at each iteration, about 1 month is needed to solve the SBO problem ( $300 \times 30 \times 5 = 45000$  minutes  $\approx$  one month). It appears, therefore, interesting to rely on a reduced order model for the LF function itself, introducing *de facto* an additional level of fidelity in the MFNIRB scheme. In the online phase, the LF solution vectors are then approached with the linear combination of the LF basis vectors.

The idea of the proposed approach is to learn the NIPOD basis in the offline phase, and use it to predict the LF vectors online. Algorithms 2 and 3 describe the different steps of the offline and online phases, from the training to the evaluation of the  $\tilde{\mathbf{f}}_{LF}(\mathbf{x}, \boldsymbol{\chi})$  approximation of  $\mathbf{f}_{LF}(\mathbf{x}, \boldsymbol{\chi})$ . The first step is to store  $M_l$  sampled vectors in the snapshot matrix  $\mathbf{S}_{LF}$ . Considering the ratio of the runtime cost of High- and Low-Fidelity simulations,  $M_l \gg M_h$  is assumed,  $M_l$  and  $M_h$  respectively LF and HF sample DoE sizes. The LF DoE  $\mathcal{X}_{LF} = \{\boldsymbol{\chi}^{(1)}, \dots, \boldsymbol{\chi}^{(M_l)}\}$  is generated using an ad hoc sampling method, in the present case LHS. Other choices for initial sampling are obviously possible (LCVT, hypercube, etc.). The snapshot matrix  $\mathbf{S}_{LF}$  is constructed with the  $\mathbf{f}_{LF}$  function evaluating the DoE  $\mathcal{X}_{LF}$

$$\mathbf{S}_{LF} = [\mathbf{f}_{LF}(\mathbf{x}, \boldsymbol{\chi}^{(1)}) \dots \mathbf{f}_{LF}(\mathbf{x}, \boldsymbol{\chi}^{(M_l)})] \quad (4.5)$$

where  $\mathbf{x}$  is the discretised space vector of the size  $dim \times n$ . Without loss of generality  $n \geq M_l$  is considered in the following. The snapshots matrix is also defined as the sum of the mean  $\bar{\mathbf{s}}_{LF}$  of all the snapshots

$$\bar{\mathbf{s}}_{LF} = \frac{1}{M_l} \sum_{i=1}^{M_l} \mathbf{f}_{LF}(\mathbf{x}, \boldsymbol{\chi}^{(i)}) \quad (4.6)$$

and the matrix of fluctuations  $\mathcal{S}_{LF}$

$$\mathbf{S}_{LF} = \bar{\mathbf{s}}_{LF} \cdot \begin{pmatrix} 1 \\ \vdots \\ 1 \end{pmatrix}_{M_h \times 1}^T + \mathcal{S}_{LF}. \quad (4.7)$$

Note the difference between  $\mathbf{S}_{LF}$  and  $\mathcal{S}_{LF}$  symbols, denoting snapshot and fluctuation matrices, respectively.

To eigen decompose the covariance matrix  $\mathbf{C} = \mathbf{S}_{LF} \mathbf{S}_{LF}^T$ , the Singular Value Decomposition (SVD) of a rectangular matrix  $\mathbf{S}_{LF}$  of the size  $n \times M_l$  may be considered.

$$\mathbf{S}_{LF} = \boldsymbol{\Phi}_{LF} \boldsymbol{\Sigma}_{LF} \boldsymbol{\Psi}_{LF}^T \quad (4.8)$$

where  $\boldsymbol{\Phi}_{LF}$  and  $\boldsymbol{\Psi}_{LF}^T$  matrices are respectively composed of the left and right singular vectors, of size  $n \times M_l$  and  $M_l \times n$ ,  $\boldsymbol{\Sigma}_{LF}$  is a diagonal matrix containing the singular values of  $\mathbf{S}_{LF}$  and equivalent when squared to eigen values of the "big" ( $n \times n$ )  $\mathbf{C} = \mathbf{S}_{LF} \mathbf{S}_{LF}^T$  or "small"  $M_l \times M_l$  correlation matrix  $\mathbf{c} = \boldsymbol{\Sigma}_{LF}^T \boldsymbol{\Sigma}_{LF}$ .

Note that the decomposition may be performed by different approaches, the most common being "economical" SVD. In the offline phase, this method is used to obtain the decomposition for the initial dataset, and once in the online phase, its incremental version [Phalippou et al., 2020] uses only the newly added points instead of the overall DoE at each iteration.

Considering  $n$  the size of each snapshot vector and  $M_l$  DoE samples, the size of the snapshot matrix is  $n \times M_l$ . The left matrix  $\boldsymbol{\Phi}_{LF}$  is chosen for the NIPOD approximation. In the context of multi-fidelity, truncation is performed on the most abundant data, which are usually generated by low-fidelity simulations. This results in a truncated basis  $\boldsymbol{\Phi}_{LF, m_l}$  when  $m_l < M_l \ll n$  such that

$$\tilde{\mathbf{S}}_{m_l, LF} = \bar{\mathbf{s}}_{LF} \cdot \begin{pmatrix} 1 \\ \vdots \\ 1 \end{pmatrix}_{M_h \times 1}^T + \mathbf{\Phi}_{LF, m_l} \mathbf{\Phi}_{LF, m_l}^T \mathbf{S}_{LF} \quad (4.9)$$

The idea behind the truncation is to consider the most relevant modes only. The latter are determined by minimizing the relative Frobenius error norm of the difference between the original  $\mathbf{S}_{LF}$  and its reconstruction  $\mathbf{S}_{m_l, LF}$  with  $m_l < M_l$  basis vectors

$$\varepsilon_{LF}(m_l) = \frac{\|\mathbf{S}_{LF} - \tilde{\mathbf{S}}_{m_l, LF}\|_F}{\|\mathbf{S}_{LF}\|_F}. \quad (4.10)$$

The  $m_l$  optimal value  $m_l^*$  is evaluated from the minimization of  $\varepsilon_{LF}(m_l)$

$$m_l^* = \arg \min_{m_l \in \{1, \dots, M_l\}} \varepsilon_{LF}(m_l). \quad (4.11)$$

Once the NIPOD basis  $\mathbf{\Phi}_{LF}$  is obtained, the snapshots matrix  $\mathbf{S}_{LF}$  is projected into this basis to determine the scalar coefficients  $\alpha_{LF}(\boldsymbol{\chi}^{(i)})$  for the DoE points belonging to  $\mathcal{X}_{LF}$

$$\alpha_{LF}^i(\boldsymbol{\chi}) = \mathbf{\Phi}_{LF}(\mathbf{x})^T (f_{LF}(\mathbf{x}, \boldsymbol{\chi}_i) - \bar{\mathbf{s}}_{LF}), \quad \boldsymbol{\chi}_i \in \mathcal{X}_{LF}, \quad i = 1, \dots, M_l \quad (4.12)$$

The  $\tilde{\mathbf{f}}_{LF}(\mathbf{x}, \boldsymbol{\chi})$  can then be approximated for an arbitrary point  $\boldsymbol{\chi}$  by

$$\tilde{\mathbf{f}}_{LF}(\boldsymbol{\chi}, \mathbf{x}) = \bar{\mathbf{s}}_{LF} + \mathbf{\Phi}_{LF}(\mathbf{x}) \tilde{\alpha}_{LF}(\boldsymbol{\chi}, \boldsymbol{\theta}_{LF}), \quad \forall \boldsymbol{\chi} \in \mathcal{D} \quad (4.13)$$

with  $\tilde{\alpha}_{LF}(\boldsymbol{\chi})$  the surrogate model of the projection coefficients  $\alpha_{LF}(\boldsymbol{\chi})$  that requires model parameters (hyperparameters)  $\boldsymbol{\theta}_{LF}$ , to be identified in the offline phase.

The construction of the NIPOD approximation of the LF function is then composed of a training and an evaluation phases detailed respectively in Algorithm 2 and 3. First, a sampling of  $M_l$  points in the domain  $\mathcal{D}$  is performed, then the LF vector values are evaluated at these points and stored in the LF snapshot matrix  $\mathbf{S}_{LF}$ . This offline phase ends with the assessment of the LF NIPOD basis  $\mathbf{\Phi}_{LF}$  of the discrete LF coefficients projection  $\alpha_{LF}$ . Next, the prediction model for  $\tilde{\alpha}_{LF}(\boldsymbol{\chi})$  is trained yielding the hyperparameters  $\boldsymbol{\theta}_{LF}$ .

The LF evaluation for a new parameter  $\boldsymbol{\chi}_{new}$  is achieved in the online phase presented by the Algorithm 3, using the approximate model  $\tilde{\alpha}_{LF}(\boldsymbol{\chi})$  for the coefficients  $\alpha_{LF}(\boldsymbol{\chi})$ . That allows the prediction of new parameters values  $\boldsymbol{\chi} \in \mathcal{D}$ , not belonging to the training DoE set  $\mathcal{X}_{LF}$ . New snapshots are evaluated by  $\tilde{\mathbf{f}}_{LF}(\mathbf{x}, \boldsymbol{\chi})$  instead of the actual LF function  $\mathbf{f}_{LF}(\mathbf{x}, \boldsymbol{\chi})$  during the optimization. The choice of using the full or the approximate version depends on the CPU cost of the LF solver and on simulation software accessibility.

The online phase consists merely of evaluating the LF at a desired point  $\boldsymbol{\chi}$  using NIPOD modeling. It is considered that the offline algorithm has provided the average snapshots  $\tilde{\mathbf{S}}_{LF}$ , the LF POD basis  $\mathbf{\Phi}_{LF}$  and the discrete coefficients PODLF. The POD basis and its discrete coefficients  $\alpha_{LF}(\boldsymbol{\chi}, \boldsymbol{\theta}_{LF})$ . Thus, from the approximate LF coefficients, the new vectors may be predicted without using LF solver.

In a similar spirit, the following paragraph details the construction of the orthogonal basis HF, from the HF snapshots. This time, this step is followed by the projection of the snapshots on the latter basis. LF may be evaluated with LF or with simulation outputs. The projection gives the deterministic part of the MFNIRB.

**Algorithm 2** LF NIPOD offline phase**Require:**  $M_l$  : LF DoE size,  $\mathbf{x}$  : Discretization,  $\mathbf{f}^{LF}(\mathbf{x}, \boldsymbol{\chi})$  : LF function**Ensure:**  $\Phi_{LF}(\mathbf{x})$ ,  $\theta_{LF}$ 1: Training DoE of  $M_l$  points  $\mathcal{X}_{LF} = \{\boldsymbol{\chi}^{(1)}, \dots, \boldsymbol{\chi}^{(M_l)}\}$  (Latin Hypercube Sampling)2: Compute Low-Fidelity snapshots  $\mathcal{S}_{LF} = [\mathbf{f}^{LF}(\mathbf{x}, \boldsymbol{\chi}^{(1)}), \dots, \mathbf{f}^{LF}(\mathbf{x}, \boldsymbol{\chi}^{(M_l)})]$ 3: Compute the mean snapshot  $\bar{\mathbf{s}}_{LF}$  using Equation (4.6)

4: 
$$\mathcal{S}_{LF} = \mathcal{S}_{LF} - \bar{\mathbf{s}}_{LF} \cdot \begin{pmatrix} 1 \\ \vdots \\ 1 \end{pmatrix}^{T}_{M_h \times 1}$$

5: Compute the basis  $\Phi_{LF}$  associated with  $\mathcal{S}_{LF}$  using SVD Compute  $\mathcal{S}_{LF} = \Phi_{LF} \Sigma_{LF} \Psi_{LF}^T$  using SVD6: Find the truncation best rank  $m_l^*$  using Equation (4.11).7: Compute  $\alpha_{LF, m_l^*}$  using Equation (4.13) and the truncated orthogonal basis  $\Phi_{LF, m_l^*}$ 8:  $\Phi_{LF} \leftarrow \Phi_{LF, m_l^*}$ 9:  $\alpha_{LF} \leftarrow \alpha_{LF, m_l^*}$ 10: Train the metamodel hyperparameters  $\theta_{LF}$  for  $\tilde{\alpha}_{LF}(\boldsymbol{\chi}, \theta_{LF})$ , using metamodeling method (e.g. Polynomial, RBF, Diffuse Approximations)**Algorithm 3** LF NIPOD online phase**Require:**  $\bar{\mathbf{s}}_{LF}$  : mean of LF snapshots,  $\boldsymbol{\chi}_{new} \in \mathcal{D}$  : the input to evaluate (outside the training LF DoE),  $\Phi_{LF}(\mathbf{x})$  : LF POD basis,  $\theta_{LF}$  : hyperparameters**Ensure:**  $\tilde{\mathbf{f}}^{LF}(\mathbf{x}, \boldsymbol{\chi}_{new})$ 1: Compute  $\tilde{\alpha}_{LF}(\boldsymbol{\chi}_{new}, \theta_{LF})$ 2: Compute approximated Low-Fidelity output  $\tilde{\mathbf{f}}^{LF}(\mathbf{x}, \boldsymbol{\chi}_{new})$  using Equation 4.13.**4.2.2 Construction of the Multi-Fidelity Reduced-Order Model**

This section covers the steps of the MFNIRB metamodel construction, divided into two main phases, online and offline.

Initially and once the the LF and HF simulation outputs are available, the offline phase is performed. In the context of MFNIRB, it consists in building the HF POD basis from the HF outputs in a first step. The LF output vectors are projected onto the reduced space, built yielding HF vectors in a second step. Then, the Kriging of the difference between Multi-Fidelity (MF) and HF Quantities of Interest (QoI)s is trained. Once the Kriging interpolation is optimized yielding the multi-fidelity trend, the online phase may be performed directly to predict objective and constraints at new points outside the training DoE set. Algorithm 4 details the offline training phase that builds the NIPOD HF basis and MFNIRB Kriging interpolation. The training is performed on a limited number of samples  $M_h$  within the design space  $\mathcal{D}$ . The training is performed on a limited sample  $\mathcal{X}_{HF} = \{\boldsymbol{\chi}^{(1)}, \dots, \boldsymbol{\chi}^{(M_h)}\}$  within the design space  $\mathcal{D}$ , of size  $M_h$  using a sampling method that allows a wide coverage of  $\mathcal{D}$  such as LHS, LCVT, etc. These are evaluated by the given HF function  $\mathbf{f}^{HF}(\mathbf{x}, \boldsymbol{\chi})$ , representing the HF simulator black box. The  $M_h$  output vectors obtained from  $\mathcal{X}_{HF}$  are stored in the snapshot matrix  $\mathcal{S}_{HF}$  of size  $n \times M_h$

$$\mathcal{S}_{HF} = [\mathbf{f}^{HF}(\mathbf{x}, \boldsymbol{\chi}^{(1)}) \dots \mathbf{f}^{HF}(\mathbf{x}, \boldsymbol{\chi}^{(M_h)})] \quad (4.14)$$

where  $\mathbf{x}$  is the discretized space vector of the size  $n$ .

The snapshots matrix is also defined as the sum of the mean snapshot

$$\bar{\mathbf{s}}_{HF} = \frac{1}{M_h} \sum_{i=1}^{M_h} \mathbf{f}^{HF}(\mathbf{x}, \boldsymbol{\chi}^{(i)}) \quad (4.15)$$

and the matrix of fluctuations  $\mathcal{S}_{HF}$

$$\mathcal{S}_{HF} = \bar{\mathbf{s}}_{HF} \cdot \begin{pmatrix} 1 \\ \vdots \\ 1 \end{pmatrix}_{M_h \times 1}^T + \mathcal{S}_{HF}. \quad (4.16)$$

In a similar manner to NIPOD eigen decomposition presented Section 4.2.1, the left orthogonal basis  $\boldsymbol{\Phi}_{HF}$ <sup>1</sup> is obtained using SVD

$$\mathcal{S}_{HF} = \boldsymbol{\Phi}_{HF} \boldsymbol{\Sigma}_{HF} \boldsymbol{\Psi}_{HF}^T \quad (4.17)$$

where  $\boldsymbol{\Phi}_{HF}$  and  $\boldsymbol{\Psi}_{HF}^T$  are respectively composed of the left and right orthogonal basis of the size  $n \times M_h$  and  $M_h \times n$ ,  $\boldsymbol{\Sigma}_{HF}$  is a diagonal matrix containing the singular values of  $\mathcal{S}_{HF}^T$ .

Once  $\boldsymbol{\Phi}_{HF}$  is obtained, the LF snapshot is projected onto this basis to determine the scalar coefficients  $\alpha_{MF}(\boldsymbol{\chi})$  for the design point  $\boldsymbol{\chi}$

$$\alpha_{MF}(\boldsymbol{\chi}) = \boldsymbol{\Phi}_{HF}(\mathbf{x})^T (\mathbf{f}_{LF}(\mathbf{x}, \boldsymbol{\chi}) - \bar{\mathbf{s}}_{HF}), \boldsymbol{\chi} \in \mathcal{D} \quad (4.18)$$

The approximation of  $HF$  may then be performed

$$\tilde{\mathbf{f}}_{MF}(\boldsymbol{\chi}, \mathbf{x}) = \bar{\mathbf{s}}_{HF} + \boldsymbol{\Phi}_{HF}(\mathbf{x}) \alpha_{MF}(\boldsymbol{\chi}), \forall \boldsymbol{\chi} \in \mathcal{D} \quad (4.19)$$

Note that considering the high cost of HF and therefore a low  $M_h$ , preferably no truncation is performed on  $\boldsymbol{\Phi}_{HF}$  (except for null singular values). Also, LF may also become unaffordable when called repeatedly during the online phase, it is recommended to substitute this level by the LF NIPOD approximation as introduced in Section 4.2.1. For this reason, an additional centering of the LF training vectors using the mean snapshot  $\bar{\mathbf{s}}_{LF}$  is required, as defined in Equation (4.6) :

$$\mathbf{f}_{LF}(\mathbf{x}, \boldsymbol{\chi}) \approx \bar{\mathbf{s}}_{LF} + \boldsymbol{\Phi}_{LF} \tilde{\boldsymbol{\alpha}}_{LF} \quad (4.20)$$

therefore the multi-fidelity coefficients are

$$\alpha_{MF}(\boldsymbol{\chi}) = \boldsymbol{\Phi}_{HF}(\mathbf{x})^T ((\bar{\mathbf{s}}_{LF} + \boldsymbol{\Phi}_{LF} \tilde{\boldsymbol{\alpha}}_{LF}) - \bar{\mathbf{s}}_{HF}), \boldsymbol{\chi} \in \mathcal{X}_{LF}. \quad (4.21)$$

The idea behind the MFNIRB representation is to consider the QoIs obtained from MF approximation as the Kriging trend corrected by a stochastic model to enforce the interpolation property. As defined in Chapter 3, the models of objective  $\mathcal{J}$  and constraints  $\mathbf{c}$  are then defined

<sup>1</sup>Considering  $n$  the size of each snapshot vector and that there are  $M_h$  samples among DoE, the size of the snapshot matrix is  $n \times M_h$ , where  $n$  is considered much higher than  $M_h$ . In such case, the left matrix  $\boldsymbol{\Phi}_{HF}$  is chosen for the POD approximation.

as a Kriging representation with a MF trend added to a stochastic model of the difference  $\Delta_{\mathcal{J}}$  between MF and HF objective  $\mathcal{J}_{MF}$  and  $\mathcal{J}_{HF}$

$$\tilde{\mathcal{J}}_{MF}(\boldsymbol{\chi}) = \mathcal{J}_{MF}(\tilde{\mathbf{f}}_{MF}(\mathbf{x}, \boldsymbol{\chi})) + \tilde{\Delta}_{\mathcal{J}}(\boldsymbol{\chi}) \quad (4.22)$$

and  $\Delta_c$  between constraints  $c_{MF}$  and  $c_{HF}$

$$\tilde{c}_{MF}(\boldsymbol{\chi}) = c_{MF}(\tilde{\mathbf{f}}_{MF}(\mathbf{x}, \boldsymbol{\chi})) + \tilde{\Delta}_c(\boldsymbol{\chi}) \quad (4.23)$$

where  $\tilde{\Delta}_c(\boldsymbol{\chi}) \sim \mathcal{GP}(0, k_{\theta}(\boldsymbol{\chi}, \boldsymbol{\chi}))$  and  $\tilde{\Delta}_{\mathcal{J}_{MF}}(\boldsymbol{\chi}) \sim \mathcal{GP}(0, k_{\theta}(\boldsymbol{\chi}, \boldsymbol{\chi}))$ ,  $k_{\theta}(\boldsymbol{\chi}, \boldsymbol{\chi})$  is the QoIs Gaussian kernel and  $\sigma^2$  the variances on the difference between MF and HF

$$k_{\theta}(\boldsymbol{\chi}, \boldsymbol{\chi}') = \sigma^2 \sum_{k=1}^d \exp(-\theta_k |\chi_k - \chi'_k|^2) \quad (4.24)$$

defining the covariance matrix  $K_{\theta}$  for the  $M_h$  points of the training set  $\boldsymbol{\chi}_{HF}$  as

$$K_{\theta}(\boldsymbol{\chi}^{(i)}, \boldsymbol{\chi}^{(j)}) = \sigma^2 \sum_{k=1}^d \exp(-\theta_k |\chi_k^{(i)} - \chi_k^{(j)}|^2), \quad i, j = \{1, \dots, M_h\} \quad (4.25)$$

where  $\theta$  are  $d$  hyperparameters and  $d$  is the design space dimension.

The hyperparameters are optimized using the Maximum Likelihood Estimation (MLE) as in [Rasmussen & Williams, 2006], allowing to choose the best  $\theta$  values. The difference between HF objective and MFNIRB prediction can be then expressed by

$$\tilde{\Delta}_{\mathcal{J}}(\boldsymbol{\chi}) = k_{\theta}^T(\boldsymbol{\chi}) K_{\theta}^{-1} [\Delta_{\mathcal{J}}(\boldsymbol{\chi}^{(1)}) \cdots \Delta_{\mathcal{J}}(\boldsymbol{\chi}^{(M_h)})]^T \quad (4.26)$$

and similar for the constraints

$$\tilde{\Delta}_c(\boldsymbol{\chi}) = k_{\theta}^T(\boldsymbol{\chi}) K_{\theta}^{-1} [\Delta_c(\boldsymbol{\chi}^{(1)}) \cdots \Delta_c(\boldsymbol{\chi}^{(M_h)})]^T. \quad (4.27)$$

The online phase of MFNIRB is presented by Algorithm 5. It details the prediction of the difference between the training values MF and  $\tilde{\Delta}$  of the objective  $\mathcal{J}$  and the constraints  $\mathbf{c}$ , respectively, the predictions  $\tilde{\Delta}_{\mathcal{J}}$  and  $\tilde{\Delta}_c$  of  $\Delta_{\mathcal{J}}$  and  $\Delta_c$ . The Kriging interpolation model is defined by a multi-fidelity trend that plays the role of centering the Kriging predictions. Since HF QoI is assumed accurate and expensive compared to LF QoI, the idea of the model MFNIRB is to interpolate HF QoI in priority. As the multi-fidelity full-field approximation is defined, there is no guarantee that the HF QoI are interpolated. It consists on adding a correction, assumed to be unknown among the set of DoE LF  $\mathcal{X}_{LF}$ . Therefore, given the approximated MFNIRB, the solver LF is called at each evaluation (or NIPOD approximation), the correction model is added to the final functional values of the vector LF obtained at a new given point  $\mathcal{X}_{LF}$ .

The use of Kriging allows us therefore to interpret  $\tilde{\mathcal{J}}$  and  $\tilde{\mathbf{c}}$  as the trend and mean of the QoI along with corresponding variances that are used in the following section to construct the infill criterion for DoE enrichment.

**Algorithm 4** MFNIRB offline phase

**Require:**  $\mathcal{D}$  : Design domain ;  $M_h$ : HF initial DoE size ;  $M_l$ : LF initial DoE size, where  $M_l \gg M_h$  ;  $\mathbf{x}$ : discretization ;  $\mathbf{f}^{HF}(\mathbf{x}, \boldsymbol{\chi})$ : HF function ;  $\mathbf{f}^{LF}(\mathbf{x}, \boldsymbol{\chi})$ : LF function

**Ensure:**  $\Phi_{HF}$ ,  $\tilde{\Delta}_{\mathcal{J}}(\boldsymbol{\chi})$ ,  $\tilde{\Delta}_c(\boldsymbol{\chi})$

- 1: Create DoE points  $\mathcal{X}_{HF} = \{\boldsymbol{\chi}^{(1)}, \dots, \boldsymbol{\chi}^{(M_h)}\}$
- 2: Compute HF snapshots  $\mathbf{S}_{HF} = [\mathbf{f}^{HF}(\mathbf{x}, \boldsymbol{\chi}^{(1)}) \dots \mathbf{f}^{HF}(\mathbf{x}, \boldsymbol{\chi}^{(M_h)})]$
- 3: Compute HF mean snapshot  $\bar{\mathbf{s}}_{HF}$  using equation (4.15)
- 4: Compute  $\Phi_{HF}$  using SVD  $\mathbf{S}^{HF} - \bar{\mathbf{s}}_{HF} \cdot \begin{pmatrix} 1 \\ \vdots \\ 1 \end{pmatrix}^T_{M_h \times 1} = \Phi_{HF} \Sigma_{HF} \Psi_{HF}^T$
- 5:  $\mathbf{f}^{MF}(\mathbf{x}, \boldsymbol{\chi}^{(j)}) \leftarrow \bar{\mathbf{s}}_{HF} + \Phi_{HF} \Phi_{HF}^t (\mathbf{f}^{LF}(\mathbf{x}, \boldsymbol{\chi}^{(j)}) - \bar{\mathbf{s}}_{HF})$ ,  $j = \{1, \dots, M_h\}$
- 6: Evaluate MF trend QoIs  $\mathcal{J}^{MF}(\boldsymbol{\chi}^{(j)}) = \mathcal{J}(\mathbf{f}^{MF}(\mathbf{x}, \boldsymbol{\chi}^{(j)}))$ ,  $\mathbf{c}^{MF}(\boldsymbol{\chi}^{(j)}) = \mathbf{c}(\mathbf{f}^{MF}(\mathbf{x}, \boldsymbol{\chi}^{(j)}))$ ,  $j = \{1, \dots, M_h\}$
- 7: Compute HF QoIs  $\mathcal{J}^{HF}(\boldsymbol{\chi}^{(j)}) = \mathcal{J}(\mathbf{f}^{HF}(\mathbf{x}, \boldsymbol{\chi}^{(j)}))$ ,  $\mathbf{c}^{HF}(\boldsymbol{\chi}^{(j)}) = \mathbf{c}(\mathbf{f}^{HF}(\mathbf{x}, \boldsymbol{\chi}^{(j)}))$ ,  $j = \{1, \dots, M_h\}$
- 8: Compute  $\Delta_{\mathcal{J}}(\boldsymbol{\chi}) \leftarrow \mathcal{J}^{HF}(\boldsymbol{\chi}) - \mathcal{J}^{MF}(\boldsymbol{\chi}) \sim \mathcal{GP}(0, k_{\theta}(\boldsymbol{\chi}, \boldsymbol{\chi}))$
- 9: Compute covariance matrix  $K_{\theta}$  and covariate vector at  $\boldsymbol{\chi} \in \mathcal{X}_{HF}$ ,  $k_{\theta}(\boldsymbol{\chi})$
- 10:  $\bar{\Delta}_{\mathcal{J}}(\boldsymbol{\chi}) \leftarrow k_{\theta}^T(\boldsymbol{\chi}) K_{\theta}^{-1} [\Delta_{\mathcal{J}}(\boldsymbol{\chi}^{(1)}) \dots \Delta_{\mathcal{J}}(\boldsymbol{\chi}^{(M_h)})]^T$
- 11: Compute  $\Delta_c(\boldsymbol{\chi}) \leftarrow \mathbf{c}^{HF}(\boldsymbol{\chi}) - \mathbf{c}^{MF}(\boldsymbol{\chi}) \sim \mathcal{GP}(0, k_{\theta}(\boldsymbol{\chi}, \boldsymbol{\chi}))$
- 12: Compute covariance matrix  $K_{\theta}$  and covariate vector at  $\boldsymbol{\chi} \in \mathcal{X}_{HF}$ ,  $k_{\theta}(\boldsymbol{\chi})$
- 13:  $\bar{\Delta}_c(\boldsymbol{\chi}) \leftarrow k_{\theta}^T(\boldsymbol{\chi}) K_{\theta}^{-1} [\Delta_c(\boldsymbol{\chi}^{(1)}) \dots \Delta_c(\boldsymbol{\chi}^{(M_h)})]^T$
- 14: Establish MFNIRB models  $\tilde{\Delta}_{\mathcal{J}}(\boldsymbol{\chi})$ ,  $\tilde{\Delta}_c(\boldsymbol{\chi})$  using Equations (3.9) and (3.8) and optimize Kriging hyperparameters  $\boldsymbol{\theta} \in \mathbb{R}^2$  using MLE global optimization

**Algorithm 5** MFNIRB online phase

**Require:**  $\Phi_{HF}$ : MFNIRB orthogonal basis;  $\tilde{\Delta}_{\mathcal{J}}(\boldsymbol{\chi})$ : MFNIRB model of  $\Delta_{\mathcal{J}}(\boldsymbol{\chi})$ ;  $\tilde{\Delta}_c(\boldsymbol{\chi})$ : MFNIRB model of  $\Delta_c(\boldsymbol{\chi})$ ;  $\boldsymbol{\chi}_{new}$ : point to evaluate in the design space  $\mathcal{D}$ ;  $\mathbf{x}$ : discretization;  $\tilde{\mathbf{f}}_{LF}(\mathbf{x}, \boldsymbol{\chi})$ : exact LF or approximate NIPOD LF function;  $\mathcal{J}(\mathbf{f}(\mathbf{x}, \boldsymbol{\chi}))$ : objective functional;  $\mathbf{c}(\mathbf{f}(\mathbf{x}, \boldsymbol{\chi}))$ : constraints functional

**Ensure:**  $\tilde{\mathcal{J}}^{MF}(\boldsymbol{\chi}_{new})$ ,  $\tilde{\mathbf{c}}^{MF}(\boldsymbol{\chi}_{new})$

- 1: Compute  $\tilde{\mathbf{f}}_{LF}(\mathbf{x}, \boldsymbol{\chi})$  using exact LF function  $f_{LF}$  (or solver) or using LF NIPOD approximation Equation (4.13)
- 2:  $\mathbf{f}_{MF}(\mathbf{x}, \boldsymbol{\chi}) \leftarrow \Phi_{HF} \Phi_{HF}^t \tilde{\mathbf{f}}_{LF}(\mathbf{x}, \boldsymbol{\chi})$
- 3: Evaluate MF trend QoIs  $\mathcal{J}^{MF}(\boldsymbol{\chi}) = \mathcal{J}(\mathbf{f}_{MF}(\mathbf{x}, \boldsymbol{\chi}))$ ,  $\mathbf{c}^{MF}(\boldsymbol{\chi}) = \mathbf{c}(\mathbf{f}_{MF}(\mathbf{x}, \boldsymbol{\chi}))$
- 4:  $\tilde{\mathcal{J}}^{MF}(\boldsymbol{\chi}) \leftarrow \mathcal{J}^{MF}(\boldsymbol{\chi}) + \tilde{\Delta}_{\mathcal{J}}(\boldsymbol{\chi})$
- 5:  $\tilde{\mathbf{c}}^{MF}(\boldsymbol{\chi}) \leftarrow \mathbf{c}^{MF}(\boldsymbol{\chi}) + \tilde{\Delta}_c(\boldsymbol{\chi})$

### 4.2.3 Infill criterion used for the enrichment strategy during the multi-fidelity optimization procedure

This section defines an adapted version of the Expected Improvement and a multi-fidelity Bayesian criterion. First, we provide an overview of the criteria and their notations compared to the adapted proposed criteria. Then a MF best suitable optimization strategy is identified.

Assuming that a feasible solution exists in the DoE, and considering the design space  $\mathcal{D}$ ,

the current best point can be defined as

$$\boldsymbol{\chi}_{it}^* = \arg \min \left\{ \tilde{\mathcal{J}}(\mathbf{x}, \boldsymbol{\chi}); \boldsymbol{\chi} \in \mathcal{C} \right\}, \quad (4.28)$$

where  $\mathcal{C} = \{\boldsymbol{\chi} \in \mathcal{X}; c_h(\boldsymbol{\chi}) \leq 0, 1 \leq h \leq n_c\}$  denotes the feasible subset of the DoE solution set at iteration  $it$ . The objective functional is evaluated at  $\boldsymbol{\chi}_{it}^*$  as the current best minimized value under the  $n_c$  constraints  $\mathbf{c}$  such as

$$\tilde{\mathcal{J}}_{it}^* = \mathcal{J}(\boldsymbol{\chi}_{it}^*). \quad (4.29)$$

Note that to alleviate notations, we skip equality constraints as they may always be represented by two inequalities.

#### 4.2.3.1 Reminder of some infill criteria used in the context of single-fidelity constrained optimization

The improvement yielded by the observation of a new point  $\boldsymbol{\chi}$  can then be defined as

$$I(\boldsymbol{\chi}) = \max(\mathcal{J}_{it}^* - \tilde{\mathcal{J}}(\boldsymbol{\chi}), 0), \boldsymbol{\chi} \in \mathcal{C}. \quad (4.30)$$

with  $\tilde{\mathcal{J}}(\boldsymbol{\chi})$  defined by Equation (4.22).

Assuming that the constraints involved in the optimization problem are independent, the probability that a given  $\boldsymbol{\chi} \in \mathcal{D}$  belongs to the feasible set  $\mathcal{C}$  can be computed using the closed-form formula

$$PF(\boldsymbol{\chi}) = \prod_{h=1}^{n_c} P(\tilde{c}_h(\boldsymbol{\chi}) \leq 0) = \prod_{h=1}^{n_c} \Phi\left(\frac{-\tilde{c}_h}{\Sigma_{c_h}^2}\right), \quad (4.31)$$

where  $\Sigma_{c_h}^2$  is the posterior variance [Rasmussen & Williams, 2006] associated to constraints  $c_h$   $1 \leq h \leq n_c$ . The posterior variance is defined by

$$\Sigma_{c_h}^2 = k_{\boldsymbol{\theta}}(\boldsymbol{\chi}, \boldsymbol{\chi}) - k_{\boldsymbol{\theta}}(\boldsymbol{\chi})^T K_{\boldsymbol{\theta}}^{-1} k_{\boldsymbol{\theta}}(\boldsymbol{\chi}), \quad (4.32)$$

$\Phi(\cdot)$  is the normal cumulative distribution functions, and the covariate

$$k_{\boldsymbol{\theta}}(\boldsymbol{\chi}) = [k_{\boldsymbol{\theta}}(\boldsymbol{\chi}, \boldsymbol{\chi})^{(1)}, \dots, k_{\boldsymbol{\theta}}(\boldsymbol{\chi}, \boldsymbol{\chi}^{(M_h)})]. \quad (4.33)$$

$\sigma^2$  denotes the variance of  $\tilde{\mathcal{J}}(\boldsymbol{\chi})$  defined by

$$\sigma^2(\boldsymbol{\chi}) = \sigma^2 (1 - k_{\boldsymbol{\theta}}(\boldsymbol{\chi}))^T K_{\boldsymbol{\theta}}^{-1} k_{\boldsymbol{\theta}}(\boldsymbol{\chi}). \quad (4.34)$$

If it is further assumed that the objective and constraints are independent, the probability of improvement may be expressed as

$$PI_c(\boldsymbol{\chi}) = \Phi\left(\frac{\mathcal{J}_{it}^* - \tilde{\mathcal{J}}(\boldsymbol{\chi})}{\sigma(\boldsymbol{\chi})}\right) \cdot PF(\boldsymbol{\chi}). \quad (4.35)$$

where  $\sigma(\boldsymbol{\chi})$  is the standard deviation of  $\tilde{\mathcal{J}}(\boldsymbol{\chi})$  at an arbitrary sample  $\boldsymbol{\chi}$ . The Expected Improvement (EI) in the presence of constraints is defined as the expected value of  $I(\boldsymbol{\chi})$  conditional on the observations (see, e.g., [Bagheri et al., 2017])

$$EI_c(\boldsymbol{\chi}) = EI(\boldsymbol{\chi}) \times PF(\boldsymbol{\chi}), \quad (4.36)$$

with

$$EI(\boldsymbol{\chi}) = \begin{cases} \max\left(\mathcal{J}_{it}^* - \tilde{\mathcal{J}}(\mathbf{x}, \boldsymbol{\chi}), 0\right) & \text{if } \sigma(\boldsymbol{\chi}) = 0, \\ (\mathcal{J}_{it}^* - \tilde{\mathcal{J}}(\mathbf{x}, \boldsymbol{\chi}))\Phi\left(\frac{\mathcal{J}_{it}^* - \tilde{\mathcal{J}}(\mathbf{x}, \boldsymbol{\chi})}{\sigma(\boldsymbol{\chi})}\right) + \sigma(\boldsymbol{\chi})\phi\left(\frac{\mathcal{J}_{it}^* - \tilde{\mathcal{J}}(\mathbf{x}, \boldsymbol{\chi})}{\sigma(\boldsymbol{\chi})}\right) & \text{if } \sigma(\boldsymbol{\chi}) > 0, \end{cases} \quad (4.37)$$

where  $\phi(\cdot)$  and  $\Phi(\cdot)$  denote respectively the standard normal probability density function and the normal cumulative distribution functions,  $\tilde{\mathcal{J}}(\mathbf{x}, \boldsymbol{\chi})$  being the posterior mean of  $\mathcal{J}(\mathbf{x}, \boldsymbol{\chi})$ .

#### 4.2.3.2 Adaptive compromise between exploitation and exploration within expected Improvement criterion

A weight can be added to the infill to favor the exploration in the beginning of the optimization procedure, and to intensify the exploitation at the last iterations. The weighted expected improvement is inspired from [Cinquegrana & Iuliano, 2015]. The  $EI_{c,w}$  or  $EI_w$  are defined by the original infill criterion  $EI$  or  $EI_c$  multiplied by the weight  $w$ , giving a weighted EI,  $EI_w$  defined by

$$EI_w(\boldsymbol{\chi}, it) = (1 - w(it)) \times \underbrace{\left(\mathcal{J}_{it}^* - \tilde{\mathcal{J}}(\mathbf{x}, \boldsymbol{\chi})\right) \Phi\left(\frac{\mathcal{J}_{it}^* - \tilde{\mathcal{J}}(\mathbf{x}, \boldsymbol{\chi})}{\sigma(\boldsymbol{\chi})}\right)}_{Exploitation} + w(it) \times \underbrace{\sigma(\boldsymbol{\chi})\phi\left(\frac{\mathcal{J}_{it}^* - \tilde{\mathcal{J}}(\mathbf{x}, \boldsymbol{\chi})}{\sigma(\boldsymbol{\chi})}\right)}_{Exploration} \quad (4.38)$$

with the following strategy to update  $w(it)$

$$w(it) = \frac{1}{it + 1} \quad (4.39)$$

where  $it$  is the number of the infill iterations.

#### 4.2.3.3 Automatic selection of the fidelity level

The modeling method chosen in this thesis is based on integrating two different levels of information fidelity through the non-intrusive Reduced-Basis (RB) projection. Consider a particular case, the basis HF, an accurate, comprehensive basis containing LF basis vectors. The fundamental assumption of this method is that LF is sufficiently correlated to HF to be represented by the HF basis. Once the projection of LF onto the HF basis is performed, the resulting modal coefficients retain only the similarities between the two fidelity levels. It was shown in Chapter 3 that the correlation is increasingly important with the convergence of the optimization. Given this statement, the idea is to integrate the best correlated LF of the experimental design into the enrichment. [Toal, 2015] has previously proposed to consider correlation and demonstrates the importance of LF-HF correlation over cost on expensive numerical problem solving efficiency. Basic correlation criteria are integrated into the  $IC$  to identify the location of the most interesting LF for the multi-fidelity projection on the one hand and on the other hand to drive the fidelity level selection strategy.

In the literature, correlation coefficients are generally used to evaluate the relationship between different types of data. The Pearson coefficient is one of the usual ones, it consists in

evaluating the linear correlation between two variables. In our context, we assume that the continuous random variables are defined by

$$X_{HF}^{(i)} = \mathbf{f}_{HF}(\mathbf{x}, \boldsymbol{\chi}^{(i)}), i = \{1, \dots, n_v\} \quad (4.40)$$

for HF and

$$X_{LF}^{(i)} = \mathbf{f}_{LF}(\mathbf{x}, \boldsymbol{\chi}^{(i)}), i = \{1, \dots, n_v\} \quad (4.41)$$

for LF outputs follow a normal distribution. In the present context, these are obtained by an approximation, constructed from the available simulation outputs that are trained with a chosen approximation model (e.g. the non-intrusive POD). Such coefficient is defined by

$$r_p = \frac{Cov(X_{LF}, X_{HF})}{\sigma_{X_{LF}} \sigma_{X_{HF}}} \quad (4.42)$$

where

$$Cov(X_{LF}, X_{HF}) = \frac{1}{n_v} \sum_{i=1}^{n_v} (X_{LF}^{(i)} - \bar{X}_{LF})(X_{HF}^{(i)} - \bar{X}_{HF}), \quad (4.43)$$

$$\sigma_{X_{LF}} = \sqrt{\frac{1}{n_v} \sum_{i=1}^{n_v} (X_{LF}^{(i)} - \bar{X}_{LF})^2}, \quad (4.44)$$

and

$$\sigma_{X_{HF}} = \sqrt{\frac{1}{n_v} \sum_{i=1}^{n_v} (X_{HF}^{(i)} - \bar{X}_{HF})^2}. \quad (4.45)$$

$n_v$  is the number of validation points to predict outside the DoE,  $\bar{X}_{LF}$  and  $\bar{X}_{HF}$  are respectively the mean of  $\mathbf{f}_{LF}(\mathbf{x}, \boldsymbol{\chi}^{(j)})$  and  $\mathbf{f}_{HF}(\mathbf{x}, \boldsymbol{\chi}^{(j)})$ ,  $j = \{1, \dots, n_v\}$  for  $n_v$  validation points.

The higher the correlation between  $f_{LF}$  et  $f_{HF}$ , the closer to 1 is the Pearson coefficient  $r$ . The other coefficient of Spearman [Kokoska & Zwillinger, 1999] is defined as

$$r_s = 1 - \frac{\sum_{i=1}^{n_v} (X_{HF}^{(i)} - X_{LF}^{(i)})^2}{n_v(n_v^2 - 1)}. \quad (4.46)$$

takes into account continuous monotonic relations. This coefficient varies between -1 and +1, 0 when there is no correlation. Correlations of -1 or +1 imply an exact monotonic relationship. Positive correlations imply that when  $f_{LF}$  increases,  $f_{HF}$  also increases. Negative correlations imply that when  $f_{LF}$  increases,  $f_{HF}$  decreases. These criteria do not capture the differences in magnitude of one response compared to another. It is assumed in the multi-fidelity context that the HF and LF data are correlated.

Since the a priori relation between the two fidelity levels of the solvers is not necessarily known, two coefficients are added to take into account two possibilities of correlations, linear and nonlinear. Then, the value is higher when there are two types of correlations, and lower when there is neither linear nor nonlinear correlation. The proposed criterion is dedicated to guide the choice of the LF enrichment, as an extension of the weighted Expected Improvement  $EI_w$  (defined Section 4.2.3.1)

$$EI_{w_l}(\boldsymbol{\chi}, it) = (1 - w_l(it)) \times \underbrace{\left( \mathcal{J}_{it}^* - \tilde{\mathcal{J}}(\mathbf{f}(\mathbf{x}, \boldsymbol{\chi})) \right) \Phi \left( \frac{\mathcal{J}_{it}^* - \tilde{\mathcal{J}}(\mathbf{f}(\mathbf{x}, \boldsymbol{\chi}))}{\sigma(\boldsymbol{\chi})} \right)}_{Exploitation} + \quad (4.47)$$

$$w_l(it) \times \sigma(\boldsymbol{\chi}) \underbrace{\phi \left( \frac{\mathcal{J}_{it}^* - \tilde{\mathcal{J}}(\mathbf{f}(\mathbf{x}, \boldsymbol{\chi}))}{\sigma(\boldsymbol{\chi})} \right)}_{Exploration}, \quad (4.48)$$

where

$$w_l(it) = \frac{1 - Cost_{ratio}}{(1 + \langle r_s(\boldsymbol{\chi}) \rangle + \langle r_p(\boldsymbol{\chi}) \rangle)(1 + it)} \quad (4.49)$$

where  $\langle r_s(\boldsymbol{\chi}) \rangle$  and  $\langle r_p(\boldsymbol{\chi}) \rangle$  are respectively the non-negative part of Spearman and Pearson correlation between  $X_{LF}(\mathbf{x}, \boldsymbol{\chi})$  and  $X_{HF}(\mathbf{x}, \boldsymbol{\chi})$  equal to 0 when the correlation values are negative,  $it$  is the number of iterations,  $\phi(\cdot)$  and  $\Phi(\cdot)$  denote the standard normal probability density and the normal cumulative distribution functions, respectively, with  $\tilde{\mathcal{J}}(\mathbf{f}(\mathbf{x}, \boldsymbol{\chi}))$  being the posterior mean of  $\mathcal{J}(\mathbf{f}(\mathbf{x}, \boldsymbol{\chi}))$  and

$$Cost_{ratio} = \frac{Cost(\mathbf{f}_{LF}(\mathbf{x}, \boldsymbol{\chi}))}{Cost(\mathbf{f}_{HF}(\mathbf{x}, \boldsymbol{\chi}))} \quad (4.50)$$

is the LF-HF computational cost ratio comprises between 0 and 1.

At the first iterations,  $it \rightarrow 0$ ,  $w_l(it)$  tends to

$$w_l(it) = \frac{1 - Cost(\mathbf{f}_{LF}(\mathbf{x}, \boldsymbol{\chi}))}{1 + \langle r_s(\boldsymbol{\chi}) \rangle + \langle r_p(\boldsymbol{\chi}) \rangle} \quad (4.51)$$

For low  $it$  numbers, the criterion tends to exploitation when the cost ratio  $Cost_{ratio}$  is high ( $Cost_{ratio} \rightarrow 1$ ), so  $w_l \rightarrow 0$ . It is decreasing when the linear and/or non-linear LF-HF correlations are high, so the criterion tends to exploit. During the infill procedure, when  $it$  increases,  $w_l(it) \rightarrow 0$ , the exploitation part of the criterion is increasing with optimum enrichment at the end of the optimization. In the multi-fidelity context, the proposed criterion is dedicated to LF infill, and when the LF-HF correlation is high,  $w_l(it)$  decreases, and exploitation increases.

The proposed infill strategy relies on exploring LF DoE when the solver call is cheap, thereafter interesting in terms of time saving. It favors low over higher cost solver calls when adding low accurate data, and more exploitation when the accuracy of the outputs is better. In parallel with each iteration, HF infill is achieved as long as the maximum optimization budget is not reached.

#### 4.2.4 Implementation of the Multi-Fidelity Reduced-Order model in optimization context

While MFNIRB is a full-field method, it requires approximation techniques. In the following we choose Kriging, in order to benefit from the available statistical information to guide the SBO search toward the area of interest. Other possible choices include Radial Basis Functions, Polynomial Response Surfaces or Diffuse Approximation. Since the LF simulation is expected

to be significantly cheaper than the HF simulation, the goal is to combine a low number of HF data with a high number of LF responses. The fundamental hypothesis of the multi-fidelity approach is that despite a lower quality of information, LF is representative enough to allow the optimization progress. In this section two infill approaches are presented. The first one consists on the enrichment of only the highest fidelity level, and the second consists on considering two levels of fidelity using one infill criterion  $IC$  to add HF vector, and another  $IC_{LF}$  to add LF vector. Algorithm 6 presents the different optimization steps assisted by MFNIRB with single-fidelity DoE enrichment.

---

**Algorithm 6** MFNIRB assisted with single-fidelity DoE enrichment
 

---

**Require:**  $\mathcal{D}$  : Design domain,  $M$ : initial DoE size;  $\mathbf{x}$ : discretisation;  $\mathbf{f}^{LF}(\mathbf{x}, \boldsymbol{\chi})$ : LF function;  $\mathbf{f}^{HF}(\mathbf{x}, \boldsymbol{\chi})$ : HF function;  $\mathcal{J}(\mathbf{f}(\mathbf{x}, \boldsymbol{\chi}))$ : objective;  $\mathbf{c}(\mathbf{f}(\mathbf{x}, \boldsymbol{\chi}))$ : constraints

**Ensure:**  $\boldsymbol{\chi}^*$

- 1: Create DoE points  $\mathcal{X} = \{\boldsymbol{\chi}^{(1)}, \dots, \boldsymbol{\chi}^{(M)}\}$  (Latin Hypercube Sampling)
  - 2: Compute HF snapshots  $\mathbf{S}_{HF} = [\mathbf{f}^{HF}(\mathbf{x}, \boldsymbol{\chi}^{(1)}) \dots \mathbf{f}^{HF}(\mathbf{x}, \boldsymbol{\chi}^{(M)})]$
  - 3: Compute LF snapshots  $\mathbf{S}_{LF} = [\mathbf{f}^{LF}(\mathbf{x}, \boldsymbol{\chi}^{(1)}) \dots \mathbf{f}^{LF}(\mathbf{x}, \boldsymbol{\chi}^{(M)})]$
  - 4:  $it \leftarrow 0$
  - 5: **while** stopping condition is not met **do**
  - 6:   find  $\boldsymbol{\chi}^*$  using HF QoIs  $\mathcal{J}^{HF}(\boldsymbol{\chi})$ ,  $\mathbf{c}^{HF}(\boldsymbol{\chi})$ ,  $\boldsymbol{\chi} \in \mathcal{X}$  with Equation (4.52)
  - 7:   Compute  $S^{HF} = \Phi \Sigma \Psi^T$  using Incremental SVD
  - 8:   Compute MF projections  $\mathbf{f}^{MF}(\mathbf{x}, \boldsymbol{\chi}^{(j)}) = \Phi \Phi^t \mathbf{f}^{LF}(\mathbf{x}, \boldsymbol{\chi}^{(j)})$ ,  $j = \{1, \dots, M\}$
  - 9:   Evaluate MF trend QoIs  $\mathcal{J}^{MF}(\boldsymbol{\chi}^{(j)}) = \mathcal{J}(\mathbf{f}^{MF}(\mathbf{x}, \boldsymbol{\chi}^{(j)}))$ ,  $\mathbf{c}^{MF}(\boldsymbol{\chi}^{(j)}) = \mathbf{c}(\mathbf{f}^{MF}(\mathbf{x}, \boldsymbol{\chi}^{(j)}))$ ,  $j = \{1, \dots, M\}$
  - 10:   Establish MFNIRB QoI  $\tilde{\mathcal{J}}^{MF}(\boldsymbol{\chi})$ ,  $\tilde{\mathbf{c}}^{MF}(\boldsymbol{\chi})$  using Equations (3.9) and (3.8) and optimize Kriging hyperparameters
  - 11:   Get next candidate  $\boldsymbol{\chi}_{it}^* = \arg \max_{\boldsymbol{\chi}} IC(\boldsymbol{\chi}^*, \tilde{\mathbf{c}}^{MF}(\boldsymbol{\chi}), \Sigma_{\tilde{\mathcal{J}}^{MF}}(\boldsymbol{\chi}))$  using GA with  $IC$  input Equations (4.37) or (4.35)
  - 12:   Compute LF and HF snapshots  $\mathbf{f}_{LF}(\mathbf{x}, \boldsymbol{\chi}_{it}^*)$  and  $\mathbf{f}_{HF}(\mathbf{x}, \boldsymbol{\chi}_{it}^*)$  at  $\boldsymbol{\chi}_{it}^*$
  - 13:    $\mathbf{S}_{HF} \leftarrow [\mathbf{S}_{HF}, \mathbf{f}_{HF}(\mathbf{x}, \boldsymbol{\chi}_{it}^*)]$
  - 14:    $\mathbf{S}_{LF} \leftarrow [\mathbf{S}_{LF}, \mathbf{f}_{LF}(\mathbf{x}, \boldsymbol{\chi}_{it}^*)]$
  - 15:    $\boldsymbol{\chi}^* \leftarrow \arg \min_{\boldsymbol{\chi} \in \mathcal{X}} \mathcal{J}_{fitness}(\boldsymbol{\chi})$
  - 16:    $M \leftarrow M + 1$
  - 17:    $it \leftarrow it + 1$
  - 18: **end while**
- 

In the first step, a sampling of  $M$  Design of Experiments (DoE) points  $\mathcal{X} = \{\boldsymbol{\chi}^{(1)}, \dots, \boldsymbol{\chi}^{(M)}\}$  is performed on the design domain  $\mathcal{D}$ . The solvers of the different fidelity levels are represented by the HF level  $\mathbf{f}_{HF}$  and LF level  $\mathbf{f}_{LF}$  functions. These functions depend on the design parameters  $\boldsymbol{\chi}$  and the physical space discretization  $\mathbf{x}^2$ . The output vectors of the  $\mathbf{f}^{HF}$  and  $\mathbf{f}^{LF}$  functions of these parameter samples are evaluated to build two matrices of size  $n \times M$ . The quantities evaluated from this set of outputs are used to train the Gaussian processes meta-model, yielding the variance and the mean. On the next step, the criterion  $IC$  ( $IC = EI_c, PI_c, \sigma_c$ ) is estimated from the variance and the optimal point<sup>3</sup> at each iteration  $\boldsymbol{\chi}^*$ . This criterion is maximized by a genetic algorithm from the *inspyred* python library<sup>4</sup>. The enrichment point  $\boldsymbol{\chi}_{it}^*$

<sup>2</sup>Represents the finite element nodes among discretized space.

<sup>3</sup>The point minimizing the objective function that best satisfies the optimization constraints.

<sup>4</sup>Garrett, A. (2012). *inspyred* (Version 1.0.1) [software]. Inspired Intelligence. Retrieved from <https://github.com/aarongarrett/inspyred>

is located at the maximum of the criterion  $IC$ . Once the new point is added to the DoE, the dataset is updated and the procedure stops when a stopping condition is reached, and the best point  $\boldsymbol{\chi}^*$  determined.

At each iteration of infill, a point is added to the DoE may be an exploration point, therefore, is not necessarily at the optimal point (typically the case of the EI). Thus, at the  $it^{th}$  iteration, an optimal point  $\boldsymbol{\chi}_{it}^*$  is determined using the penalization of constraints violation [Deb, 2000]. This consists in building a merit (or fitness) function  $\mathcal{J}_{fitness}$  from the objective function values  $\mathcal{J}$  and constraints  $\boldsymbol{c}$  for each point of the training DoE

$$\mathcal{J}_{fitness}(\boldsymbol{\chi}^{(j)}) = \mathcal{J}(\boldsymbol{\chi}^{(j)}) + \sum_{h=1}^{n_c} P_h \langle c_h(\boldsymbol{\chi}^{(j)}) \rangle, j = \{1, \dots, M\} \quad (4.52)$$

Again, we drop the equality constraints as each equality constraint may be represented by two non-strict inequalities.  $M$  is the current DoE size,  $\langle \cdot \rangle$  measures the constraints violation and is defined as the absolute value when  $c_h \geq 0$ , and 0 when  $c_h$  is negative, meaning that the constraint is satisfied. In the case where the constraints are not satisfied,  $\mathcal{J}(\boldsymbol{\chi}^{(j)})$  takes its worst penalisation value  $\mathcal{J}_{max}$ , the maximum value among the current DoE, in the case of a minimization problem.  $P_h$  is a parameter defined in two steps, first scaling the constraints to be in the same order of magnitude, then multiplied by a penalty parameter  $\beta_h$  individually set for every constraint and updated according to the chosen penalty strategy (interior/exterior/interior-exterior)

$$P_h = \frac{\beta_h}{||c_h^{max} - c_h^{min}||}, \quad (4.53)$$

where  $c_h^{max}$  and  $c_h^{min}$  are respectively the maximum and the minimum value of each constraint  $c_h$  among the  $M$  values of the current DoE. These are adapted following the search window, which is panned and zoomed with the optimization advancement.

The MFNIRB model relies on two fidelity levels of training data, and the enrichment usually performed consists in adding only the most accurate data. The goal is to reduce the number of HF values by using the enrichment criteria. In the context where a LF solver is available, another method may support the optimization with less accurate but cheap data. The criterion  $EI_{w_i}$  defined in Section 4.2.3.1 may be used when the cost of LF is lower than that of HF. The different steps of the multi-level of fidelity enrichment are detailed by Algorithm 7. Similar steps to the single-fidelity MFNIRB enrichment of the Algorithm 6 are reproduced only when using  $IC$  criterion. in the case where LF and HF can be parallelized, we can add LF several times during the evaluation of HF, whose duration is longer than LF. Thus, it is the second criterion,  $IC_{LF}$ , that we propose to use to add a second vector LF.  $IC_{LF}$  requires the LF and HF snapshots to evaluate their correlation and the cost of the LF solver  $Cost(\boldsymbol{f}_{LF}(\mathbf{x}, \boldsymbol{\chi}))$ .

### 4.3 Numerical experiments

This Section presents the evaluation of the MFNIRB capabilities in the context of constrained single-objective optimization. The main concern is the value added in terms of time saving and accuracy.

**Algorithm 7** MFNIRB assisted with multi-fidelity DoE enrichment

**Require:**  $\mathcal{D}$ : Design domain,  $M$ : initial DoE size;  $\mathbf{x}$ : discretisation;  $\mathbf{f}^{LF}(\mathbf{x}, \boldsymbol{\chi})$ : LF function;  $\mathbf{f}^{HF}(\mathbf{x}, \boldsymbol{\chi})$ : HF function;  $\mathcal{J}(\mathbf{f}(\mathbf{x}, \boldsymbol{\chi}))$ : objective;  $\mathbf{c}(\mathbf{f}(\mathbf{x}, \boldsymbol{\chi}))$ : constraints

**Ensure:**  $\boldsymbol{\chi}^*$

- 1: Create DoE points  $\mathcal{X} = \{\boldsymbol{\chi}^{(1)}, \dots, \boldsymbol{\chi}^{(M)}\}$  (Latin Hypercube Sampling)
- 2: Compute HF snapshots  $\mathbf{S}_{HF} = [\mathbf{f}^{HF}(\mathbf{x}, \boldsymbol{\chi}^{(1)}) \dots \mathbf{f}^{HF}(\mathbf{x}, \boldsymbol{\chi}^{(M)})]$
- 3: Compute LF snapshots  $\mathbf{S}_{LF} = [\mathbf{f}^{LF}(\mathbf{x}, \boldsymbol{\chi}^{(1)}) \dots \mathbf{f}^{LF}(\mathbf{x}, \boldsymbol{\chi}^{(M)})]$
- 4:  $it \leftarrow 0$
- 5: **while** stopping condition is not met **do**
- 6: find  $\boldsymbol{\chi}^*$  using HF QoIs  $\mathcal{J}^{HF}(\boldsymbol{\chi})$ ,  $\mathbf{c}^{HF}(\boldsymbol{\chi})$ ,  $\boldsymbol{\chi} \in \mathcal{X}$  with Equation (4.52)
- 7: Compute  $\mathbf{S}^{HF} = \Phi \Sigma \Psi^T$  using Incremental SVD
- 8: Compute MF projections  $\mathbf{f}^{MF}(\mathbf{x}, \boldsymbol{\chi}^{(j)}) = \Phi \Phi^t \mathbf{f}^{LF}(\mathbf{x}, \boldsymbol{\chi}^{(j)})$ ,  $j = \{1, \dots, M\}$
- 9: Evaluate MF trend QoIs  $\mathcal{J}^{MF}(\boldsymbol{\chi}^{(j)}) = \mathcal{J}(\mathbf{f}^{MF}(\mathbf{x}, \boldsymbol{\chi}^{(j)}))$ ,  $\mathbf{c}^{MF}(\boldsymbol{\chi}^{(j)}) = \mathbf{c}(\mathbf{f}^{MF}(\mathbf{x}, \boldsymbol{\chi}^{(j)}))$ ,  $j = \{1, \dots, M\}$
- 10: Establish MFNIRB QoI  $\tilde{\mathcal{J}}^{MF}(\boldsymbol{\chi})$ ,  $\tilde{\mathbf{c}}^{MF}(\boldsymbol{\chi})$  using Equations (3.9) and (3.8) and optimize Kriging hyperparameters
- 11: Get next candidate  $\boldsymbol{\chi}_{it}^* = \arg \max_{\boldsymbol{\chi}} IC(\boldsymbol{\chi}^*, \tilde{\mathbf{c}}^{MF}(\boldsymbol{\chi}), \Sigma_{\tilde{\mathcal{J}}^{MF}}(\boldsymbol{\chi}))$  using GA with  $IC$  input Equations (4.37) or (4.35)
- 12: Compute HF snapshots  $\mathbf{f}_{HF}(\mathbf{x}, \boldsymbol{\chi}_{it}^*)$  at  $\boldsymbol{\chi}_{it}^*$
- 13:  $\mathbf{S}_{HF} \leftarrow [\mathbf{S}_{HF}, \mathbf{f}_{HF}(\mathbf{x}, \boldsymbol{\chi}_{it}^*)]$
- 14: Get next candidate  $\boldsymbol{\chi}_{it}^* = \arg \max_{\boldsymbol{\chi}} IC_{LF}(\boldsymbol{\chi}^*, \tilde{\mathbf{c}}^{MF}(\boldsymbol{\chi}), \Sigma_{\tilde{\mathcal{J}}^{MF}}(\boldsymbol{\chi}), Cost(\mathbf{f}_{LF}(\mathbf{x}, \boldsymbol{\chi})), \mathbf{S}_{LF}, \mathbf{S}_{HF})$  using GA with  $IC_{LF}$  input Equation (4.47) to evaluate  $EI_{w_i}$  then take into account optimization constraints using (4.37)
- 15: Compute LF snapshots  $\mathbf{f}_{LF}(\mathbf{x}, \boldsymbol{\chi}_{it}^*)$
- 16:  $\mathbf{S}_{LF} \leftarrow [\mathbf{S}_{LF}, \mathbf{f}_{LF}(\mathbf{x}, \boldsymbol{\chi}_{it}^*)]$
- 17:  $\boldsymbol{\chi}^* \leftarrow \arg \min_{\boldsymbol{\chi} \in \mathcal{X}} \mathcal{J}_{fitness}(\boldsymbol{\chi})$
- 18:  $M \leftarrow M + 1$
- 19:  $it \leftarrow it + 1$
- 20: **end while**

### 4.3.1 Problem definition

The bi-fidelity benchmark test case of [Benamara et al., 2017] demonstrates the performances through a single-objective constrained optimization problem. For the sake of independance of the chapter, we remind<sup>5</sup> the problem settings of the objective function  $\mathcal{J}$  minimization subjected to two constraints  $c_1$  and  $c_2$  within the design space  $\mathcal{D}$

$$\begin{aligned} & \text{minimize } \mathcal{J}(\boldsymbol{\chi}) \\ & \text{s.t. } \boldsymbol{\chi} \in \mathcal{D}, c_1(\boldsymbol{\chi}) \leq 0, c_2(\boldsymbol{\chi}) \leq 0, \end{aligned} \quad (4.54)$$

where  $\mathcal{D} = [4, 6] \times [10, 14]$  is a bi-dimensional design space and the objective and constraints functions are given by

$$\begin{cases} \mathcal{J} : \boldsymbol{\chi} \in \mathcal{D} \mapsto \min_{x \in [0, 1]} f(x, \boldsymbol{\chi}) \\ c_1 : \boldsymbol{\chi} \in \mathcal{D} \mapsto \arg \min_{x \in [0, 1]} f(x, \boldsymbol{\chi}) - 0.75 \\ c_2 : \boldsymbol{\chi} \in \mathcal{D} \mapsto 7.5 - \max_{x \in [0, 1]} f(x, \boldsymbol{\chi}), \end{cases} \quad (4.55)$$

<sup>5</sup>From the test case Chapter 3, Section 3.3.1.

using either the HF model  $f_{HF}$  or the LF model  $f_{LF}$  defined as

$$\left\{ \begin{array}{l} f_{HF} : \mathbb{R}^n \times \mathcal{D} \rightarrow \mathbb{R} \\ \quad (x, \boldsymbol{\chi}) \mapsto \frac{1}{2}(6x - 2)^2 \sin(\chi_2 x - 4) + \sin(10 \cos(\chi_1 x)) \\ f_{LF} : \mathbb{R}^n \times \mathcal{D} \rightarrow \mathbb{R} \\ \quad (x, \boldsymbol{\chi}) \mapsto \frac{1}{2}(6x - 2)^2 \sin(\chi_2 x - 4) + 10(x - \frac{1}{2}). \end{array} \right. \quad (4.56)$$

This benchmark involves the features encountered in optimization of aeronautical problems : minimizing/maximizing QoI, discontinuous feasible domain, functions computed from a full-field response (velocities, shockwave, pressure maps, etc.).

### 4.3.2 Experimental setup

In the previous Chapter, the MFNIRB contribution to continuous functions approximations was investigated, more particularly, the approximation performances of challenging functions such as the  $c_1$  constraint flat areas and the separate feasible areas. It has been observed that for the  $c_1$  function, the multi-fidelity presents an interest compared to the single-fidelity approximation, given that the combination of LF and HF allows capturing the plateau area. However, the MF trend would tend towards the LF function as the training size of the HF basis increases. In a first step, one will seek to identify the limitations of MF representation for well-selected points, hence using an enrichment criterion and investigate the relevance of such a metamodel in finding regions of interest. Then following the same models, multi- and single-fidelity models to investigate further and compare both MFNIRB and OK methods are being studied respectively. Experiments are performed on the bi-fidelity benchmark test case to respond to these issues.

In the first experiment, several infill criteria are studied to assess the different optimization behaviors of MFNIRB introduced in Section 4.3.3.1. A second experiment is performed using a well-chosen infill criterion to compare MFNIRB to a single-fidelity model from Section 4.3.3.2. The optimization assisted by MFNIRB and OK is compared for different DoE sizes. The objective is to determine the potential benefit, in terms of optimization performance, of each model for reducing the size of the DoE, therefore the overall cost. In the Section 4.3.3.3, the enrichment criterion is decomposed into  $EI$ , the unconstrained part, and  $PF$ , the constrained part. The objective is to test the performance of the constrained  $EI$  SBO defined by the multiplication  $PF(c_1) \times PF(c_2) \times EI$ , based on a strong assumption of independence of constraints and objective. Section 4.3.3.4 presents an adaptation of MFNIRB that increases the sizes of LF DoE  $M_l$  compared to HF  $M_h$ . The objective of the experiment is to identify the parameters that influence the convergence of this model with respect to the original MFNIRB in its Full-Order Model (FOM) version (where LF function was not approximated). Finally, MF projections are compared for different ratios  $k$  in Section 4.3.3.5, then single-fidelity infill and multi-fidelity infill based enrichment are compared for different initial DoEs. The objective is to analyse the impact of the  $k$  LF-HF ratio, MF and HF enrichment on the optimization results. Table 4.1 summarizes the experimental setup of the OK and MFNIRB metamodel-assisted enrichment, which are detailed in the following sections.

The results obtained from each experiment are compared using an error metric that measures the mean precision of the obtained optimal point for  $n_{rep}$  independent DoEs of the same size  $\mathcal{X} = \{\mathcal{X}^{(i)}, \dots, \mathcal{X}^{(n_{rep})}\}$ . Each of these DoEs gives different snapshots therefore distinct sets of modes. To validate the method it is necessary to measure the performance on a

Section	Low-fidelity model	Experiments settings
4.3.3.1	FOM	Comparison between different criteria.
4.3.3.2		Comparison with single-fidelity Ordinary Kriging.
4.3.3.3		Investigation of different exact/approximate constraints.
4.3.3.4	NIPOD	Variable sizes of LF training sets.
4.3.3.5		MF trend with variable $k$ ratios.
4.3.3.5	$M_l = kM_h$	Bi-fidelity infill with variable $k$ ratios and LF training sets sizes .

Table 4.1: Numerical experiments performed in the present chapter.

case where the exact solution is known. Assuming that a feasible solution exists in the DoE<sup>6</sup>, considering the design space  $\mathcal{D}$  the optimal value is assumed known as

$$\boldsymbol{\chi}_{it}^* = \arg \min \{ \mathcal{J}_{HF}(\mathbf{x}, \boldsymbol{\chi}); \boldsymbol{\chi} \in \mathcal{C} \}, \quad (4.57)$$

where  $\mathcal{C} = \{ \boldsymbol{\chi} \in \mathcal{X}; c_h(\boldsymbol{\chi}) \leq 0, h = \{1, 2\}, \forall \boldsymbol{\chi} \in \mathcal{D} \}$  denotes the feasible subset of the DoE solution set.

The  $i^{th}$  independent DoE  $\mathcal{X}^{(i)}$  defines the initial training set, an enrichment point is added at each iteration  $it$ , is detailed in algorithm 6. At each iteration  $it$ , the current optimum is evaluated as  $\boldsymbol{\chi}_{it}^* \in \mathcal{X}^{(i)}$ . The relative mean error is defined by

$$\bar{e}_{rr}^{(it)} = \frac{1}{n_{rep}} \sum_{i=1}^{n_{rep}} \frac{\mathcal{J}_{HF}(f_{HF}(\mathbf{x}, \boldsymbol{\chi}_{it}^*)) - \mathcal{J}_{HF}^*}{\mathcal{J}_{HF}^*}, \boldsymbol{\chi}_{it}^* \in \mathcal{X}^{(i)} \subset \mathcal{X} \quad (4.58)$$

where  $it$  is the infill iteration,  $\mathcal{J}_{HF}$  the objective function.

### 4.3.3 Results

This Section presents the results obtained from the experiments, where the benchmark case optimization problem is solved using different enrichment strategies. Repeated runs are performed to quantify the overall performance regardless of the DoE distribution. Such a study is unaffordable with a real physical simulation case, so the benchmark test case appears as an appropriate alternative to validate the proposed methodology.

#### 4.3.3.1 Comparison between different infill criteria

Comparisons between different infill criteria are performed in this part. The objective is to demonstrate the convergence of the  $EI$ -based infill procedure and to compare the role of each criterion. Multiple runs are required due to the random nature of the Latin Hypercube Sampling (LHS) sampling. This allows us to identify the criterion best suited to the constrained optimization test case. Different  $EI$  alternatives are compared:

- Expected Improvement ( $EI$ ) is a compromise between exploitation and exploration. This is the original version [Jones & Schonlau, 1998] that does not take into account constraints.

<sup>6</sup>See, e.g., Section 2.3 of [Feliot et al., 2017] and references therein for a discussion of possible alternatives in the case where no feasible solution is known.

- Constrained  $EI$  ( $EI_c$ ): This version takes into account the GP variance and mean of the Kriging approximation constraints through the Probability of Feasibility ( $PF$ ) (studied in the Chapter 3, Section 3.2.2).
- Constrained and weighted  $EI$  ( $EI_{c,w}$ ): The  $EI_c$  is improved to intensify the exploration at the beginning of the optimization procedure and the exploitation at the end, leading to a better convergence only if the exploration is sufficiently achieved.
- The weighted  $EI$  ( $EI_w$ ): The weighted  $EI$  does not take into account constraints, however, it provides a useful comparison to the  $EI$  and the  $EI_{c,w}$ , allowing to highlight the weighting part added value.

The objective is to highlight the impact of the constrained part added to the  $EI$ . Figure 4.1 illustrates the evolution of the  $\log$  relative error  $\bar{e}_{rr}$  along the infill iterations using the different  $EI$  formulations, in the case where the initial DoE size is  $M = 4$ .

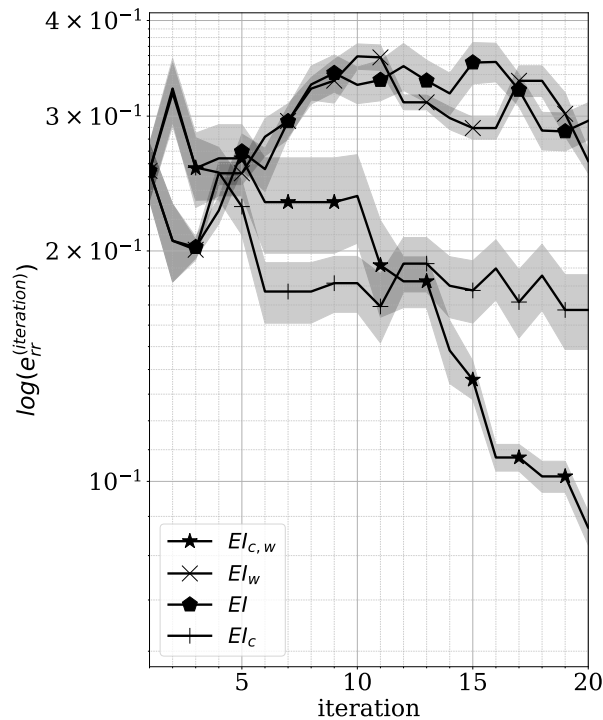


Figure 4.1: Comparison between different  $EI$  based enrichment results of MFNIRB assisted optimization beginning from DoE of the size  $M = 4$ .

The unconstrained optimization results represented by the diamond and cross markers obtained with  $EI$  and  $EI_w$  respectively, does not take into account constraints  $PF$ , show a divergence. This illustrates the impact of the  $PF$  method, presented in the former chapter. It allows to conduct the optimization toward the optimum value. On the other hand, the constrained optimization results are marked by the star and plus scatters are obtained with the  $EI_c$  and  $EI_{c,w}$  respectively. Concerning, the weighted version of  $EI_c$ , the  $EI_{c,w}$  criterion, the corresponding curve shows the highest error reduction. The  $EI_{c,w}$  presents promising results on the  $M = 4$  case,  $M$  being the initial DoE size. This criterion is then compared to other classical  $ICs$  on different  $M$  sizes.

The second experiment consists in comparing the performances of the best  $EI$  criterion identified previously to other criteria:

- The Probability of Improvement ( $PI$ ) is guided by the constrained best objective value, therefore, it directs the optimization search toward the optimal value, favoring the exploitation.
- The  $variance$  is guided by the uncertainty of the database available and does not take into account the best optimization candidate. It is a more exploratory search within the DoE.

This test aims to highlight the compromise between exploration and exploitation made by  $EI_{c,w}$  comparing to the exploitation driven criterion  $PI_c$  and exploration driven  $variance_c$ . The Figures 4.2a and 4.2a show respectively the optimization  $\bar{e}_{rr}(\mathcal{J})$  error results from  $M = 4$  and  $M = 10$  initial DoE sizes for each infill iteration.

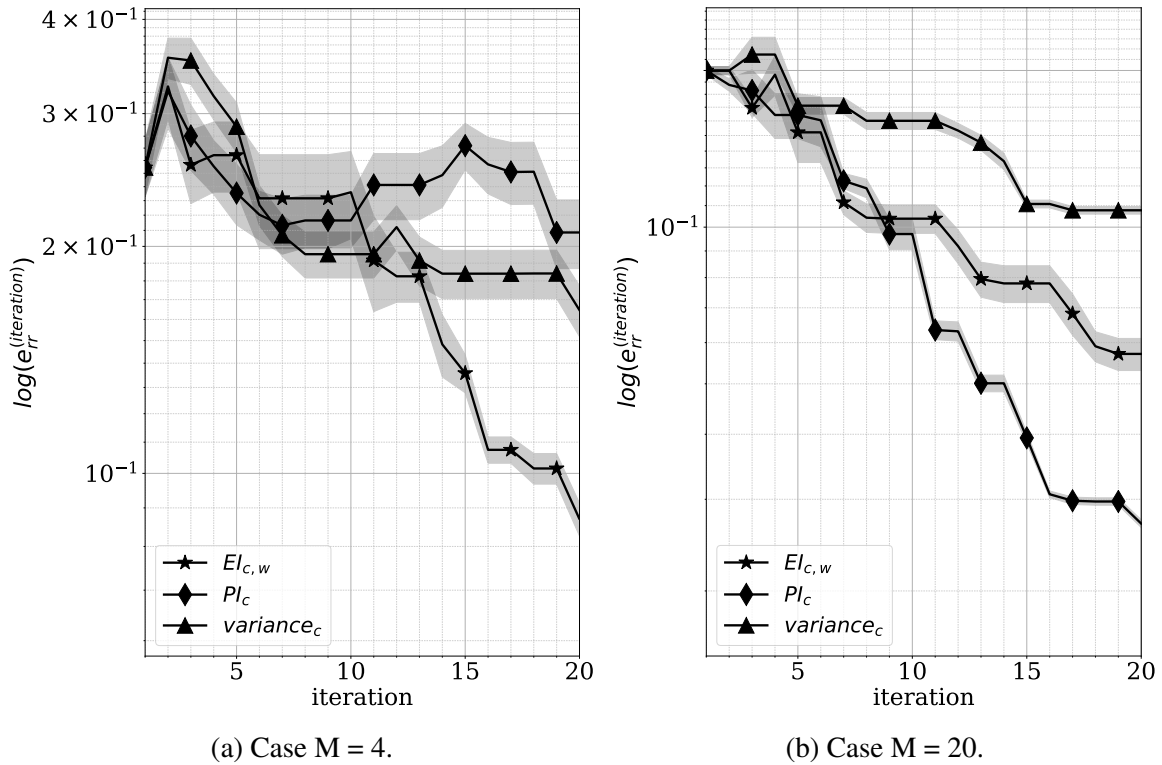


Figure 4.2: Comparison between  $PI_c$ ,  $EI_{c,w}$  and  $variance_c$  infill based optimization.

Table 4.2 details the error results, beginning from the same independent initial DoE training sets of the size of  $M = 4$  and  $M = 20$ . Multiple independent enrichment procedures are conducted. Error mean  $\bar{e}_{rr}$  and variance  $\sigma$  of errors results in each infill iteration in percentage unit % are given

$$\delta \bar{e}_{rr} = |\bar{e}_{rr} - \bar{e}_{rr}^{(it=0)}| \quad (4.59)$$

where  $\bar{e}_{rr}^{(it=0)}$  and  $\bar{e}_{rr} = \bar{e}_{rr}^{(it=20)}$  is the mean relative error at the first and the last iteration, in this case  $it = 20$ .

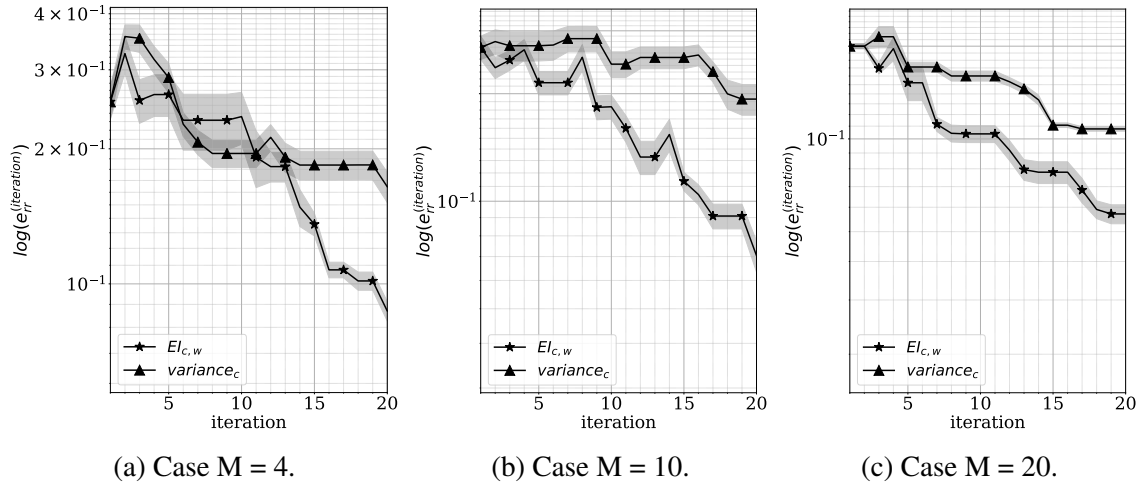
The error values on both Figures are on a close magnitude order of  $10^{-1}$ . The smallest error is obtained at the last iteration for 20, with the  $EI_{c,w}$  and with  $PI_c$  respectively in the  $M = 4$  and the  $M = 20$  DoE size cases. Thus, with  $EI_{c,w}$ , 24 HF calls were needed to reduce the mean error from 25.4% to 8.7% and with  $PI_c$  40 HF calls to reduce the error from 19.9% to

	M=4			M=20		
	$\bar{e}_{rr}[\%]$	$\sigma$	$\frac{\delta\bar{e}_{rr}}{\bar{e}_{rr}(it=0)}$	$\bar{e}_{rr}[\%]$	$\sigma$	$\frac{\delta\bar{e}_{rr}}{\bar{e}_{rr}(it=0)}$
First iteration	25.4	0.022	-	19.9	0.003	-
$PI_c$	20.8	0.022	18.1	2.6	0.0004	86.9
$EI_{c,w}$	8.7	0.004	65.8	5.7	0.004	71.3
$variance_c$	16.4	0.013	35.4	10.7	0.001	54.8

Table 4.2:  $PI_c$ ,  $EI_{c,w}$  and  $variance_c$  cases results

2.6% with the lowest results variance.

Figure 4.3 plots the relative  $\log$  error  $\bar{e}_{rr}$  at each iteration, using  $EI_{c,w}$  versus the constrained variance  $variance_c$ . Each figure 4.3a, 4.3a and 4.3a represents the enrichment procedures performed for an increasing initial size of the DoE respectively from  $M = 4$ ,  $M = 10$  to  $M = 20$ . This comparison allows us to highlight the impact of the exploration behavior on the  $variance_c$  and to compare it to that performed by  $EI_{c,w}$ . Variance will tend to explore, while  $EI_{c,w}$  explores at the beginning and then exploits at the end. This means that when the initial DoE is not explored extensively, the use of  $EI_{c,w}$  is potentially as interesting as using the variance only. However, the interest of the  $EI_{c,w}$  exploitation/Exploration compromise on the whole optimization should appear differently in each case.

Figure 4.3: Comparison between  $EI_{c,w}$  and  $variance_c$  error evolution

For both criteria, the higher initial DoE size provides better convergence, however in all DoE cases, the  $EI_{c,w}$  search outperforms the SBO  $variance_c$  search. For a low DoE size, the  $variance_c$  based SBO has a very poor reduction in the mean error, therefore we can conclude that there is no convergence in the  $M = 4$  and  $M = 10$  cases. The Table 4.3 details these results for each case obtained in the first iteration in comparison with the last iteration results.

The error variations of the case using the  $variance_c$  criterion remain low compared to the initial results of the random DoE. When the DoE is sufficiently explored, the search for the optimum ought to proceed towards the optimum and intensify the exploitation, which is underlined by the convergence of the SBO based on  $EI_{c,w}$ .

	M=4		M=10		M=20	
	$\bar{e}_{rr}$ [%]	$\sigma$	$\bar{e}_{rr}$ [%]	$\sigma$	$\bar{e}_{rr}$ [%]	$\sigma$
First iteration	25.4	0.022	26.9	0.020	19.9	0.003
$EI_{c,w}$	8.7	0.004	7.0	0.007	5.7	0.004
$variance_c$	16.4	0.013	19.3	0.019	10.7	0.001

Table 4.3:  $EI_{c,w}$  and  $variance_c$  based optimization comparison results.

### 4.3.3.2 Comparison with single-fidelity Ordinary Kriging

This section compares the multi-fidelity methodology to the single-fidelity approach in the optimization framework.

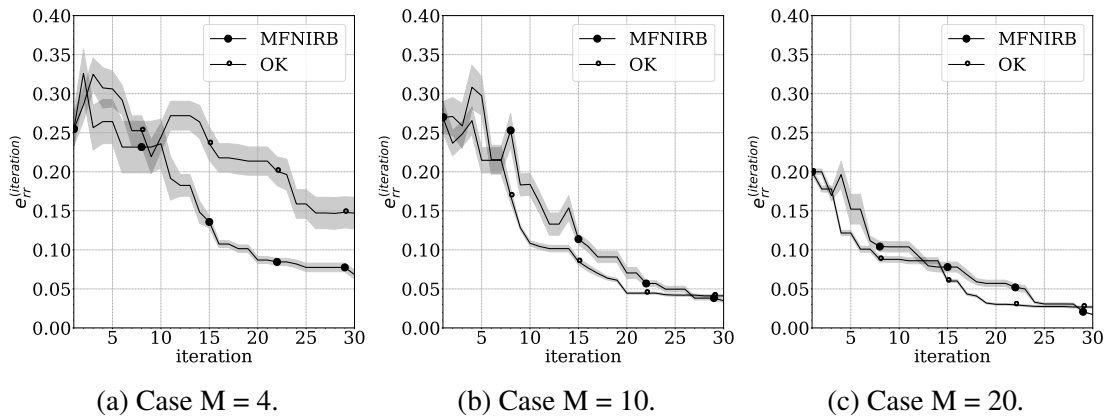


Figure 4.4: Comparison between single and multi-fidelity error resulting from enrichment, for repeated experiments.

The single-fidelity method considered is the Ordinary Kriging and the multi-fidelity method is MFNIRB. The difference between these models lies in the Kriging trend which depends on the LF evaluations projected on the HF basis while the OK trend is constant and depends only on the HF samples. The Figures 4.4 show the evolution of the  $\log$  of  $\bar{e}_{rr}$  with infill points added using the  $EI_{c,w}$  criterion. The evolution of the error is obtained from the solution of the constrained optimization benchmark problem with the use of the adaptive infill criterion  $EI_{w,c}$  presented in the Section 4.2.3.1. Three different DoE sizes are compared, namely  $M = 4, 10,$  and  $20,$  and their results are shown respectively in Figures 4.4a, 4.4b and 4.4c.

In the case of  $M = 4,$  the MFNIRB outperforms the single-fidelity model. In the first case presented in Figure 4.4a, where the initial DoE size is the lowest, the mean error  $\bar{e}_{rr}$  is reduced by 40% ( $\approx \frac{0.25-0.15}{0.25}$ ) under performing the MFNIRB error reduction of 80% ( $\approx \frac{0.25-0.05}{0.25}$ ). However, the OK performances are better when increasing the initial DoE size. For both cases  $M=10$  and  $M=20,$  the mean error evolves toward the same value at the end of the enrichment procedure iteration = 30, the error is reduced by 85% to  $4 \cdot 10^{-2}$  from its initial value  $2,7 \cdot 10^{-1}$  in the case  $M = 10$  and 92% ( $2 \cdot 10^{-2}$ ) in the case  $M = 20.$  The optimization based on the infill search shows better convergence when the initial training set is larger, especially when using the single-fidelity model.

Figure 4.5 shows the evolution of the relative mean error for the different DoE sizes  $M=4,$

$M=10$  and  $M=20$ , in logarithmic scale to illustrate more precisely the difference between each case.

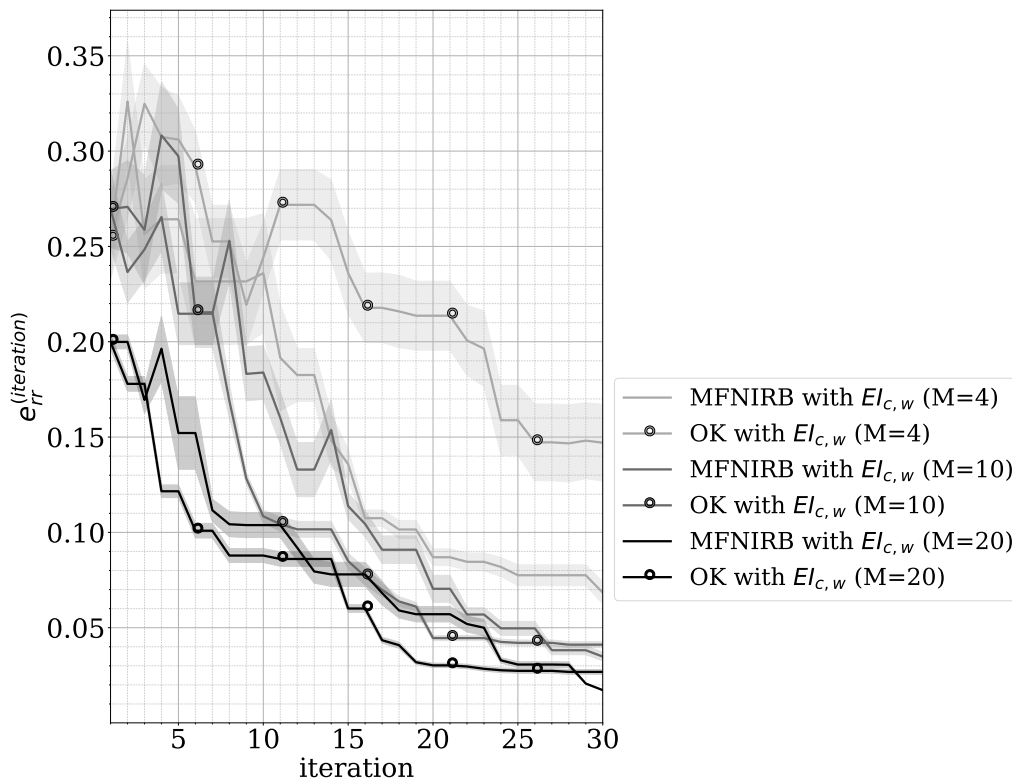


Figure 4.5:  $e_{rr}^-$  and its variance for multiple runs at each infill iteration for  $M = 4$ ,  $M = 10$  and  $M = 20$  initial DoE cases.

The errors reach a lower value when the number of initial training points is increased, as expected. Although the initial error is not much different between the  $M=4$  and  $M=10$  cases, we can see that prior knowledge of the experimental design leads to a better benefit from the enrichment criterion. Note that this criterion is the weightedEI, and thereby consists in intensifying exploitation and exploration respectively at the end and the beginning of enrichment. A better knowledge of the model at the beginning of enrichment allows for a better location of the region of interest.

The importance of the initial size  $M$  of the DoE is further displayed by the OK wherein for  $M = 4$ , one observes that the optimum is the furthest of the best point  $\chi_{it}^*$  and the curve does not converge (although the error is reduced). For a higher  $M = 10$  and  $M = 20$ , the OK performs better where the MFNIRB reaches the final error value and exceeds it. For the  $M = 10$  case and  $M = 20$  MFNIRB exceeds the OK in both cases for the last few iterations respectively beginning from iteration 27 and 29. The OK performs poorly when the DoE is not explored well enough initially, but it converges faster for a minimum amount of initial data of  $M=10$  in this case. However, the MFNIRB model has a better convergence for all DoE sizes. Its convergence is slower than OK's for  $M \geq 10$  but the error reached by the MF model is lower at the end of the procedure.

### 4.3.3.3 Investigation of analytical and approximate constraints

In the former Section, the constrained infill criterion is analysed. In the present sections, experiments are conducted to identify the limits of the constrained infill criterion. The two first experiments test each constraints approximation impact on the optimization convergence. The last experiment demonstrates the  $EI$  convergence for the objective approximation only.

#### Infill criteria performance analysis

Figure 4.6 plots the relative error values  $\bar{e}_{rr}^{(iteration)}$  corresponding to enrichment points added by the  $EI_{c,w}$  criterion in the following cases:

- both constraints  $c_1$  and  $c_2$  are analytical, only the objective function  $\mathcal{J}$  is approximated by the OK and by the MFNIRB,
- only the constraint  $c_2$  is approximated,
- only the constraint  $c_1$  is approximated.

The objective is to separate different constrained criterion components' impact on the optimization efficiency of the OK compared to the MFNIRB. Figures 4.6a, 4.6b and 4.6c present the results obtained for an initial DoE size of  $M=4,10$  and  $20$ , respectively.

Under cases of analytical  $c_1$  and  $c_2$ , the curve associated with the MF model outperforms all OK cases, and converges respectively at iteration 12 for  $M = 4$ , requiring 16 points in total to find the optimum, at iteration 7 for  $M = 10$  (17 points in total), and at the subsequent infill iteration 18 for  $M = 20$ . In all cases, the OK needs more points to converge.

When only one of the constraints is approximated, we observe that the lowest performances are obtained for approximated  $c_1$  and exact  $c_2$ . For  $M = 20$ , OK and MFNIRB are even less efficient in the exact  $c_2$  case. Hence, approximating  $c_2$  would give better results than having its exact values. The approximation quality of  $c_1$  appears to have a negative impact on all the OK cases, especially when comparing to the results obtained with the meta-model MFNIRB. As a matter of fact, the latter converges to the minimal value of  $10^{-3}$  between iteration 15 and 20, the same value as the case where all constraints are exact. In the case of initial DoEs of sizes  $M = 4$  and  $M = 10$ , thereby, the smallest ones, MFNIRB outperforms the OK for its best configuration (all constraints are exact).

The MFNIRB meta-model outperforms the OK in its ability to use the  $c_1$  constraint approximation. The  $c_1$  function features difficulties of plateaus-like variations, whereas continuous functions without sharp variations appear to be more suitable for Kriging. In the Chapter 3, the correlation between the MF trend with the HF results was illustrated for both fidelity levels. It was observed that the MF trend provides information that LF or HF had not captured within the single-fidelity configuration <sup>7</sup>. One can conclude that there is a real benefit of a MF in the representation of non-continuous functions.

#### Comparison to a prescribed trajectory

This Section presents the comparison between a "well chosen" enrichment path to the one obtained using  $EI_{c,w}$ . Such an "optimal" path is based on intuitive heuristics. In a first step,

<sup>7</sup>For the OK, a Kriging with a constant mean trend based only on HF training points.

this approach is tested on the cases where all constraints are exact. Then, the two cases where one of each constraints are given analytically or approximated, are treated to illustrate the contribution of the Probability of Feasibility (PF).

The Figures 4.7 illustrate the infill criterion  $EI_{c,w}$  evaluated on a  $50 \times 50$  grid along with corresponding  $\bar{e}_{rr}$  curves obtained for 30 infill points. Columns contain results obtained beginning from a DoE size of  $M = 4$  and  $M = 20$ . White dots represented on Figures 4.7c, and 4.7d correspond to iterations from 1 to 30, respectively on Figures 4.7a, and 4.7b red and green bold lines localise the constraints feasibility limits using respectively the HF and MFNIRB values. the yellow and red stars correspond to the best current points at each iteration and the theoretical optimal point. The feasible regions are located at three separated areas. In Figures 4.7, the red and green lines are merged together because the first case assumes the both analytical constraints, therefore MFNIRB and HF constraints limits are equal.

The convergence of the MFNIRB-assisted optimization appears better than that obtained along prescribed trajectory. In the MFNIRB case, only the objective function is used for enrichment which is therefore only done at the feasible regions. The enrichment criterion allows to place points which improve the model accuracy but also allows to move from one feasible region to another, as a result of the exploration provided by the  $EI$ . The proposed trajectory has been chosen to go towards the optimum in a linear way. The curves in the first row of the Figures converge at the very first iterations, hence faster than the trajectory. This highlights the interest of the exploration, however, the behavior is not representative for constrained problems as both  $c_1$  and  $c_2$  are analytical in this first case.

In a second experiment, only the  $c_1$  constraint is analytical and  $c_2$  is approximated. As the previous experiments, the results are illustrated on maps Figures 4.8c and 4.8d and their corresponding  $\bar{e}_{rr}(iteration)$  curves Figures 4.8a and 4.8b for similar initial DoEs.

The curves present also better convergence than the heuristic trajectory. The approximation of  $c_2$  seems to have a low impact on the convergence, there are 6 and 5 (respectively for  $M = 4$  and 20) additional iterations comparing to the experiment where  $c_2$  is exact. The three oval areas wrapped with the red and green lines corresponding to the feasible domain are accurately approached particularly in the finest initial DoE size case Figure 4.8d.

The last experiment considers approximation of  $c_1$ , therefore  $EI_{c,w}$  takes into account  $PF(\tilde{c}_1)$  and  $EI(\tilde{\mathcal{J}})$ . The Figures 4.9a, and 4.9b illustrate the error  $\bar{e}_{rr}(\mathcal{J})$  evolution along with the infill procedure and the corresponding illustration of the DoE, infill points, constraints limits and the  $EI_{c,w}(\chi)$  values.

Only the criterion  $EI_{c,w}$  only converges for the case under consideration. This allows us to conclude that the quality of the constraints approximation impacts the convergence curves. These observations confirm, as expected, the importance of adapting the criteria of the constrained probabilities according to their difficulty of representation.

#### 4.3.3.4 Variable sizes of LF training sets

This Section presents the results of the Experiment 3, which consists in a comparisons between different  $\frac{M_l}{M_h}$  ratio = {1,2,3}

Figure 4.10 presents the evolution of the relative mean and variance of the error  $\bar{e}_{rr}$  at each infill iteration, from an initial HF DoE size of  $M_h = 4$  compared to different  $M_l$  values. First, an initial set of training points is used to build the MFNIRB model. Different MFNIRB models are compared based on different assumptions of the cost of the LF model. The best configuration is the one considering the LF infinitely available  $M_l = \infty$ , the other cases use limited number of LF evaluations through LF NIPOD models with different LF-HF ratio. Figure 4.10 shows more than 60% error reduction from 20 to 25 iterations in the case of  $M_l = \infty$  and  $M_l = 3 \times M_h$  using all POD modes. The other cases are weakly convergent, therefore, in these cases a higher LF DoE size improves the optimization performances. However, there is no significant performance difference between the cases where ratios are 1, 2 and the truncated NIPOD cases.

Figure 4.11 presents the evolution of the relative mean and variance of the error  $\bar{e}_{rr}$  from an initial HF DoE size of  $M_h = 10$  with different  $M_l$  values. Table 4.4 summarizes the initial and final mean relative error and variance results illustrated Figure 4.10 and 4.11.

Figure 4.11 shows that the convergence is better with a higher HF and LF initial DoE size. The case where the ratio is 2 without POD basis truncation, outperforms the infinite LF case for all the iterations. The lowest error reductions may be observed for the cases of the lowest

	$M_h = 4$			$M_h = 10$		
	$\bar{e}_{rr}[\%]$	$\sigma$	$\frac{\delta \bar{e}_{rr}}{\bar{e}_{rr}(it=0)}$	$\bar{e}_{rr}[\%]$	$\sigma$	$\frac{\delta \bar{e}_{rr}}{\bar{e}_{rr}(it=0)}$
First iteration	25.4	0.022		26.9	0.020	
Without LF NIPOD	6.8	0.006	73.2	3.4	0.002	87.3
<i>ratio</i> = 1, all modes	18.9	0.016	25.6	6.9	0.004	74.3
<i>ratio</i> = 2, all modes	15.4	0.014	39.4	2.7	0.001	90
<i>ratio</i> = 3, all modes	9.4	0.005	63	3.2	0.001	88.1
<i>ratio</i> = 1, 1 mode	16.9	0.026	33.5	4.4	0.020	83.6
<i>ratio</i> = 2, 1 mode	14.4	0.014	43.3	2.7	0.001	90

Table 4.4: Results of MFNIRB model based on and without LF NIPOD.

$M_l$  (ratio 1). However, the gap between these error values stays low for a maximum difference of 15% of the initial value. The reduction is 74.3% for the worst and 90% for the best convergence, obtained for  $M_h = 10$  with the ratio 2 LF NIPOD cases (see Table 4.4).

This comparison allows to test the MFNIRB in presence of different types of LF approximations showing that the LF NIPOD based MFNIRB presents comparable performances with the direct LF based MFNIRB. However, the LF NIPOD needs a sufficient number of training values to converge. A criterion may identify the best LF-HF ratio needed to train the LF NIPOD to solve general SBO problems.

#### 4.3.3.5 Management of the low and high-fidelity ratio and its impact on the optimization time savings and the accuracy of the multi-fidelity model

The above experiments show that the size LF DoE can be managed independently to improve the accuracy of the multi-fidelity approximation. Increasing the number of training samples improves the prediction accuracy of the LF. We can legitimately assume that the quality of the multi-fidelity approximation will also be improved when the knowledge of LF is larger. On the other hand, it has been observed that the correlation between the vectors LF and HF improves the tendency to multi-fidelity, and consequently increases the prediction quality of the MFNIRB. In this section, a new adaptive strategy is proposed to address the following questions:

- Is there a method that provides low-fidelity snapshot in a way to find balance between a higher accuracy and a lower cost in a similar mindset as the expected improvement?
- Does the correlation provide an optimal LF-HF combination for the best SBO performance ?

First, the LF-HF ratio of 1 and above is tested and the corresponding snapshots compared. Based on these observations, further tests are performed with the optimization from a ratio of 1 to a higher initial ratio LF-HF DoE. The main objective is to analyze the potential impact of the ratio on the multi-fidelity snapshots and, consequently, on the performance in the context of the optimization.

#### Construction of the multi-fidelity vectors starting from different DoE with LF-HF ratio

The HF DoE is nested in LF DoE,  $\chi_{HF} \subset \chi_{LF}$ . DoE of 100 LF samples is considered with

two ratios,  $M_l/M_h = 1$  and  $M_l/M_h = 20$ . The Figures represent the snapshots evaluated for  $(M_l, M_h) = (100, 100)$ , Figures 4.12, then  $(M_l, M_h) = (100, 5)$ , Figures 4.13. The small red and blue dots respectively, in left figures column represent the HF and LF DoEs. The small red samples generate the HF snapshots, from which a reduced base is evaluated. The blue samples generate the snapshots which are projected onto the evaluated reduced basis, obtaining the MF snapshots. An example of the training snapshots MF, HF and LF at  $\chi_{test}$  is represented in the right figures by magenta, red and blue curves respectively. The snapshots are reconstructed by LF NIPOD defined in section 4.2.1 as  $\tilde{f}_{LF}(\chi)$ , as in this figure, or, are directly the generated snapshots if the budget allows it.

First, it can be observed that at high training point ratios for both fidelity levels, the MF approximation is close to the LF curve. Whereas when the ratio is higher, and the basis HF is constructed from far fewer vectors than the number of LF vectors, the MF approximation better follows the HF curve. However, it should be noted that the MF curves present a lot of noise. This may come from the small eigenvalues of the projection, meaning that it would be better to truncate the basis HF to the set of modes corresponding to a threshold on the singular values. This is a shortcoming, as it is the most accurate and expensive basis. In the following, we study the influence of the truncation of the HF basis.

Figures 4.14 and 4.15, present the application of the truncation of the HF basis, according to the evolution of the residual  $\varepsilon_{modes}$  as a function of different truncation levels using criterion of Equation (4.11).

The vector MF shows oscillations and no longer represents the trend of the curves as in the case where the ratio LF-HF is larger. The orthogonal basis is not optimal when  $M_h$  becomes as high as  $M_l$ . The basis seems too complex for a simple  $M_l$  representation, then less compatible with a  $M_l$  vector, reminding a phenomenon of over-fitting. Truncation for  $M_h = 100$  results in a prediction of MF closer to HF, Figure 4.14 compared to Figure 4.12 but a significant error is still present. The situation is improved by considering truncation and a higher LF-HF ratio, which gives a better approximation Figure 4.15. Quantifying the limit of the ability of the basis HF to represent the vectors LF is thereafter worthwhile to refine the MF trend of MFNIRB.

### LF-HF ratio management in the context of optimization

Tests are first performed to compare the paths of the single- and multi-fidelity enrichment, using the enrichment criterion  $EI_{c,w_l}$  to add LF samples (presented in the section 4.2.3.3). The idea is to call a solver LF in regions where it is most likely to be close to the model HF, when the LF-HF cost ratio is advantageous. The goal is to find ways to better control optimization costs in the presence of different levels of solver fidelity.

From the observation of the previous sections, it appeared that a ratio greater than 1 and automatic truncation of the HF basis is more suitable. Figures 4.18a, 4.18b, 4.16a, 4.16b, 4.17a, and 4.17b represent the objective function  $\mathcal{J}(\chi)$  on a validation grid with hatched non-feasible areas, evaluated from MFNIRB model (green lines) and from exact HF constraints (red lines). Non-feasible areas are defined by constraint values below 0.75 for  $c_1$  and higher than 7.5 for  $c_2$ .

The first test Figure 2 starts with an LF DoE twice as dense as that of HF, then 9 points

are added based only on the single-fidelity criterion  $EI_{c,w}$  (adding only HF vectors). Starting from the same DoE, 9HF vectors are added, together LF vectors, the results are shown in figure 4.16a.

On the one hand, we can observe that the LF points are added close to the locations of the HF infill points. This reflects the very limited variability of the test case LF-HF correlation across the DoE. The difference between the two levels is linear in this benchmark. As a result, the correlation has low impact on the multi-fidelity criterion  $EI_{c,w_l}$ .

The model accuracy varies with the ratio variation. This can be observed not only from the differences in the amplitude of the objective map, but also from the different distribution of infeasible areas. It is therefore possible to state that the addition of values of a second level of fidelity has an impact on the accuracy of the model. However, at this stage, it remains to be seen whether this impact is positive or not, due to the stochastic aspect of the model. From the perspective of this work, it would be interesting to see how the model has evolved since the first iteration.

Now, the optimization results are compared to the values obtained in the first iteration on Figure 4.17b and to values obtained if there are equal LF-HF training points on Figure 4.17a.

In both Figures 4.17a and 4.17b, we can observe that initially, the model MFNIRB with a higher ratio of 2, is slightly more accurate, as it allows to capture both the top and bottom parts of the  $c_2$  constraint. This can be seen at the green 7.5 limits of the model MFNIRB which are represented only by the part below the level below  $\chi_2 < 12.0$ . In the case of the  $c_1$  constraint, we can see that the limits at 0.75 of the model with a ratio of 2 are closer to the exact HF values corresponding to the limits of this constraint.

The final test compares the optimization performance. For ratio 1 and 2, Figures 4.18a and 4.18b, represent similar scenario as in the previous optimization case, but begin with a DoE of equal LF and HF training points number.

In this case, in the single-fidelity infill results shown in Figure 4.18b, the accuracy of the constraints is not improved, when comparing the red and green lines. Regarding the multi-fidelity infill (Figure 4.18a), there is a more accurate separation of the two non-feasible regions of the  $c_2$  constraints. However, the distribution of  $c_1$  limits is closer to the exact  $c_1$  red lines for the single-fidelity infill than for the multi-fidelity infill. Thus, the ratio 2 appears to give better overall accuracy for the multi-fidelity infill.

To conclude, there are no significant differences confirmed when using the multiple-fidelity or single-fidelity enrichment level, however, some improvement trends of MFNIRB were made visible by these preliminary results. Indeed, it was observed that the MF vectors construction has limitations to its evolution during the enrichment, due to the truncation of the HF basis, noted very low even for a high training size. To improve the efficiency of the optimization, the multi-fidelity infill needs to take better advantage of the contribution of HF.

## 4.4 Recommendations on multi-fidelity management toward an optimal control of cost during the optimization

The computational environment allowing to use multiple fidelity of simulations may be provided by parallel computing. LF is assumed cheaper than HF solver calls, therefore multiple LF

may be performed for only a single HF evaluation. The first parameter to consider is the DoE initial sampling. Therewith, the first step should consider the LF versus HF's cost parameter.

In a second step, there are different possible scenarios:

- Adding HF infill point and consequently equivalent LF values considering the cost LF-HF ratio (used in the initial DoE sampling :  $cost(1f_h) = kcost(f_l)$ ),
- Adding only LF infill point: in this case the LF-HF correlation may be added to infill criteria, therefore the infill is likely to be done in the areas where the LF-HF correlation is the highest.

The main condition of an accurate MFNIRB is the LF correlation to HF vectors. To represent the MFNIRB model, the HF training set needs to be similar to the LF one. Such model is build from two levels of fidelity, where the LF function can be called more often than HF. Thus, the HF DoE is embedded in the LF DoE. Thereafter, during the infill procedure the number of LF samples stays constant, whereas the HF is added at each infill iteration, allowing to search for the regions of interest. As introduced in this Section, the LF simulation is  $k$  times cheaper HF. It can then be interesting to include the LF into the enrichment procedure, during the HF assesment. This strategy depends highly on the  $k$  number, representing the relative CPU cost LF-HF ratio. Thus, the MF infill strategies steps are

1.  $k = 1$  : first LF are added on the same locations as HF.
2.  $k \geq 2$  : LF are added indepently using a multi-fidelity criterion, such as  $EI_{c,w_l}$ , and HF using a chosen single fidelity level infill criterion, only if the budget allows to call this solver.

Additionally, this strategy needs to benefit from the best LF NIPOD representation, then the choice of the NIPOD modes number is determined from the NIPOD basis energy metric (see Section 4.2.1), that may be further integrated to the infill to improve the HF basis during the optimization procedure.

## 4.5 Conclusion

In this chapter, a multi-level, multi-fidelity model has been introduced and tested for a single and multi-fidelity optimization. The model starts from the idea that different levels of fidelity of output vectors may be represented by an orthogonal basis. Previous research has led to a model based on the construction of a multi-fidelity orthogonal basis and the projection of low and high-fidelity vectors.

In the present work, a similar spirit founded the model MFNIRB. This time, the orthogonal basis is a single-fidelity one constructed from the higher-fidelity dataset, and by projecting onto this basis, a set of LF vector outputs. Different experiments were presented for a better understanding of optimization in the context of multi-fidelity. First, a comparison between the infill criteria showed in section 4.3.3.1, a different convergence according to exploration, exploitation, and a better balance between exploration and exploitation with  $EI_w$ . This criterion was chosen to conduct the experiment in section 4.3.3.2, which compares the convergence of single and multi-fidelity models, and showed better convergence potential for MFNIRB on poorly explored DoE and comparable performance for an initially sufficiently explored DoE. Finally, the chosen criterion is studied to understand the impact of its component for solving a constrained problem in such a context and studying if the approximation is a driver of an optimal infill procedure, and what are the origins for the limitations of Kriging-based optimization. These limitations can further be addressed by improving the modeling and multi-fidelity optimization. Consequently, an analysis is conducted in section 4.3.3.4 to compare different LF-HF ratios using the multi-level extension of MFNIRB that used the NIPOD approximation of the LF data. It was concluded that the ratio and the HF basis truncation might impact the optimization performances. The higher ratio is not always the one that performed the best. At least, the results between different ratios also depend on the truncation level of the HF basis. Therefore, in the next Section, the truncation is evaluated from the minimization of the residual error. It was observed that using the HF presents limitations when using it to represent LF vectors. Only, few modes are useful to the final MF vector. Thereby, improving such a basis is not always possible if the only data used are HF outputs. Future work may integrate LF to improve the orthogonal reduced-basis. Finally, analyses of the impact of the LF-HF ratio are presented, along with preliminary results of the multi-level of fidelity compared to single-fidelity enrichment.

Observations and preliminary results have shown the potential of using a multi-fidelity enrichment procedure during optimization. However, the multi-fidelity vectors improvement during the enrichment is limited to the potential of the HF basis to evolve, which is not always the case when only few modes are able to represent the LF model. These limitations are partly tackled by the stochastic correction of the MFNIRB model, which is able to evolve the correction by adding LF and/or HF infill points. Further work should be performed on the reduced HF basis to complete the missing modes of the multi-fidelity representation. That may better take advantage of the similarities between the two levels if the time savings are interesting enough.

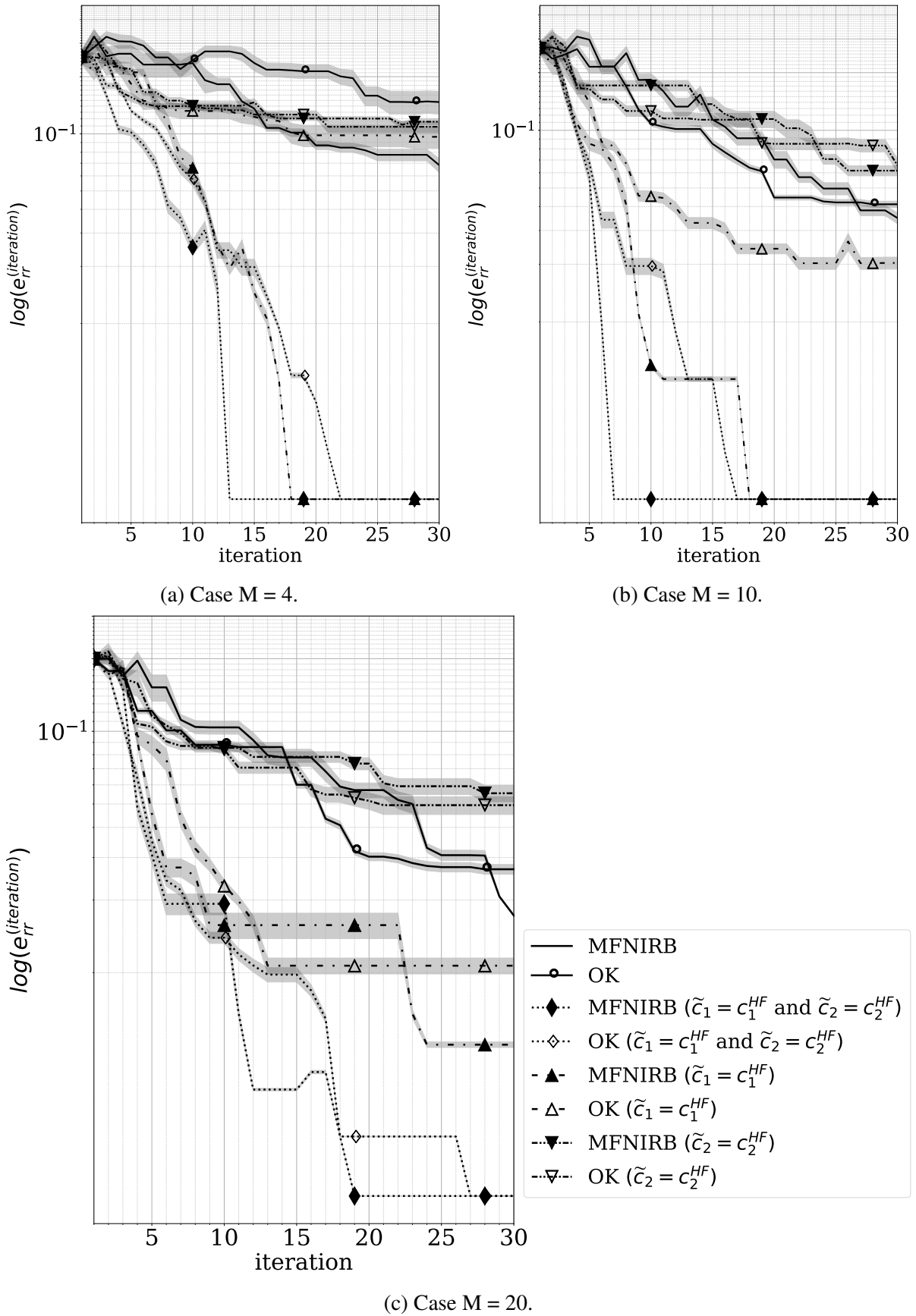


Figure 4.6: Comparison between error evolutions with enrichment of the different constraints knowledge cases.

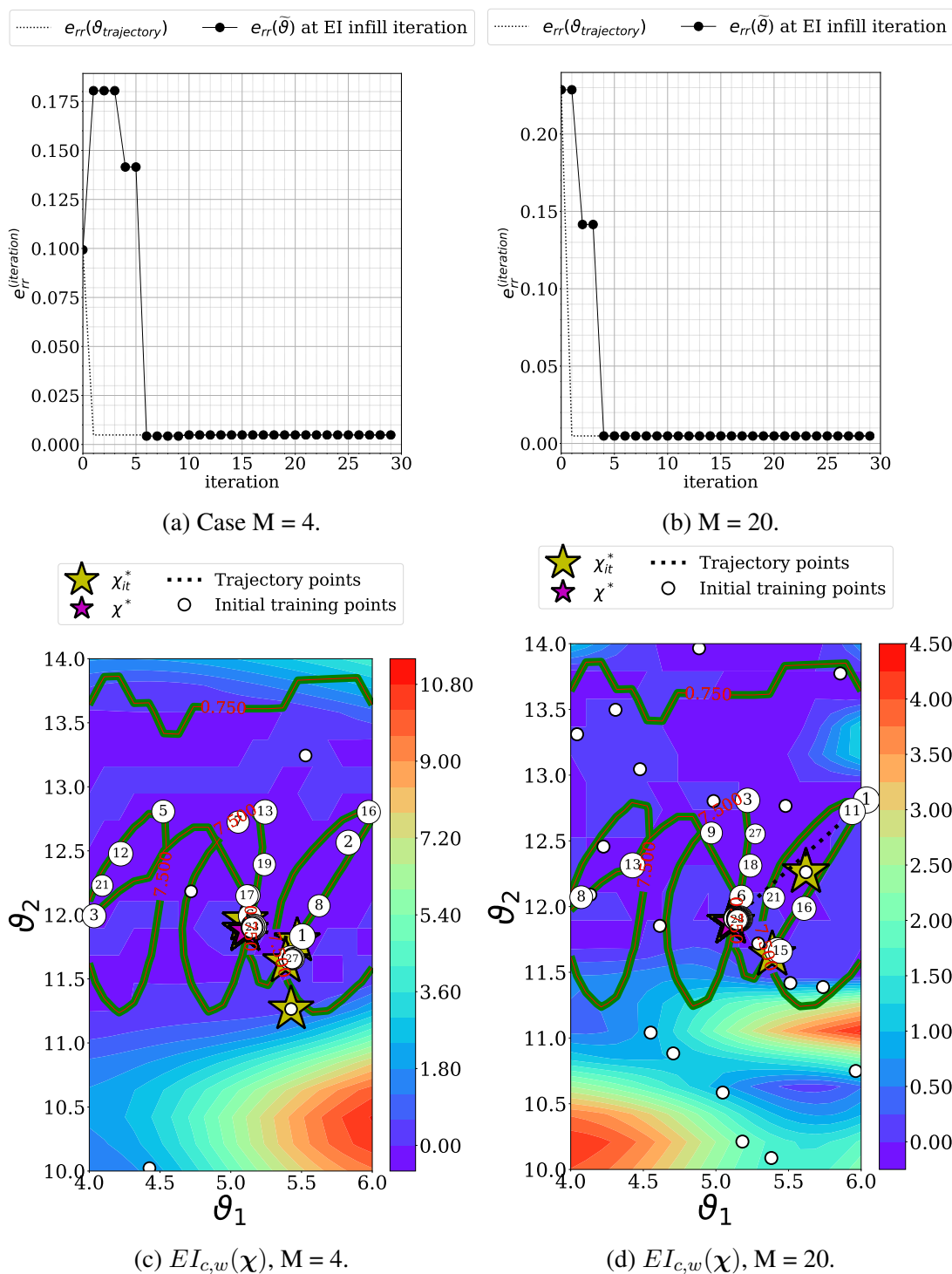


Figure 4.7: MFNIRB optimization using  $EI_{c,w}$  infill criterion considering  $\tilde{c}_1 = c_1^{HF}$  and  $\tilde{c}_2 = c_2^{HF}$ .

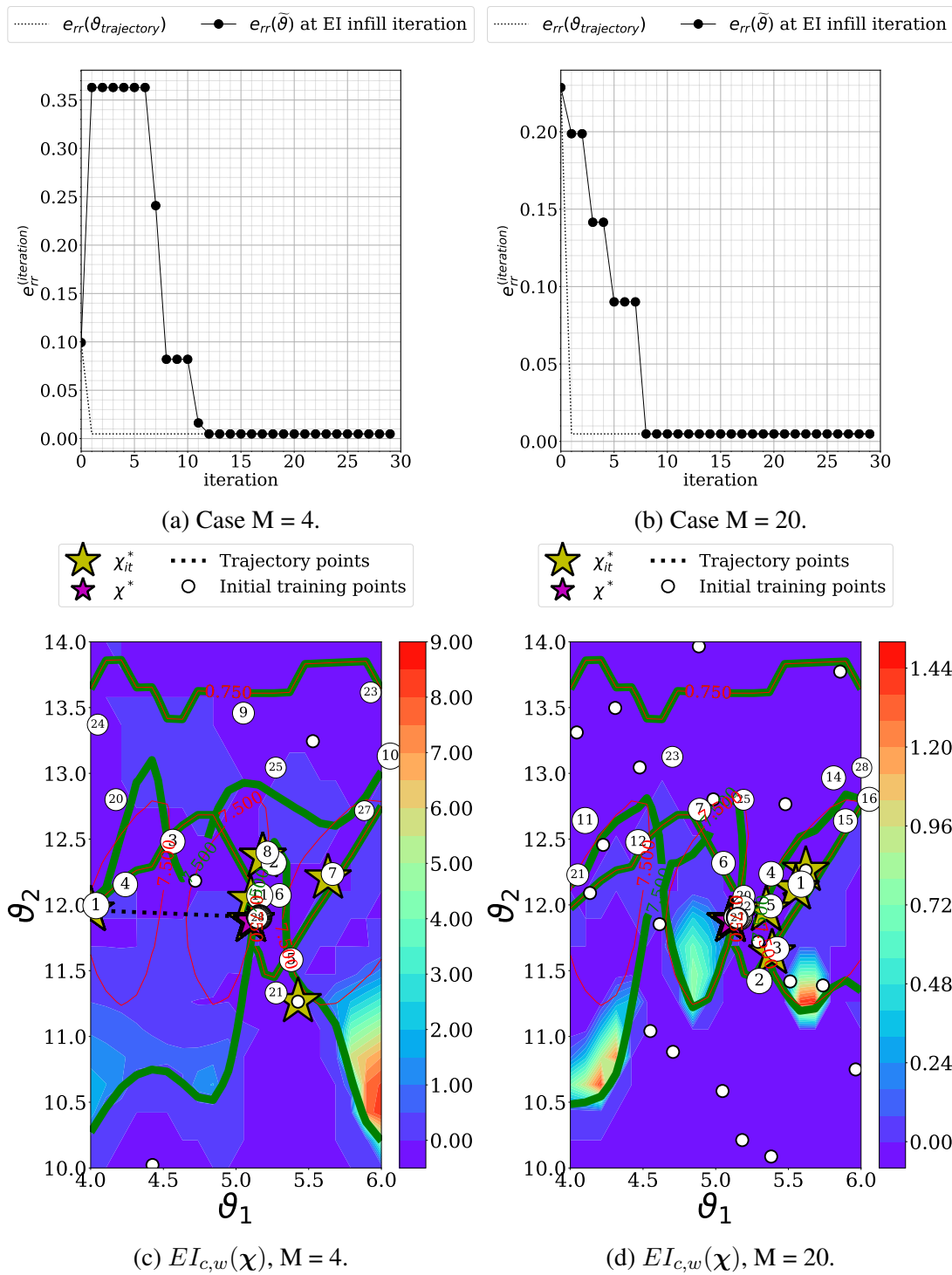


Figure 4.8: MFNIRB optimization using  $EI_{c,w}$  infill criterion considering  $\tilde{c}_1 = c_1^{HF}$ .

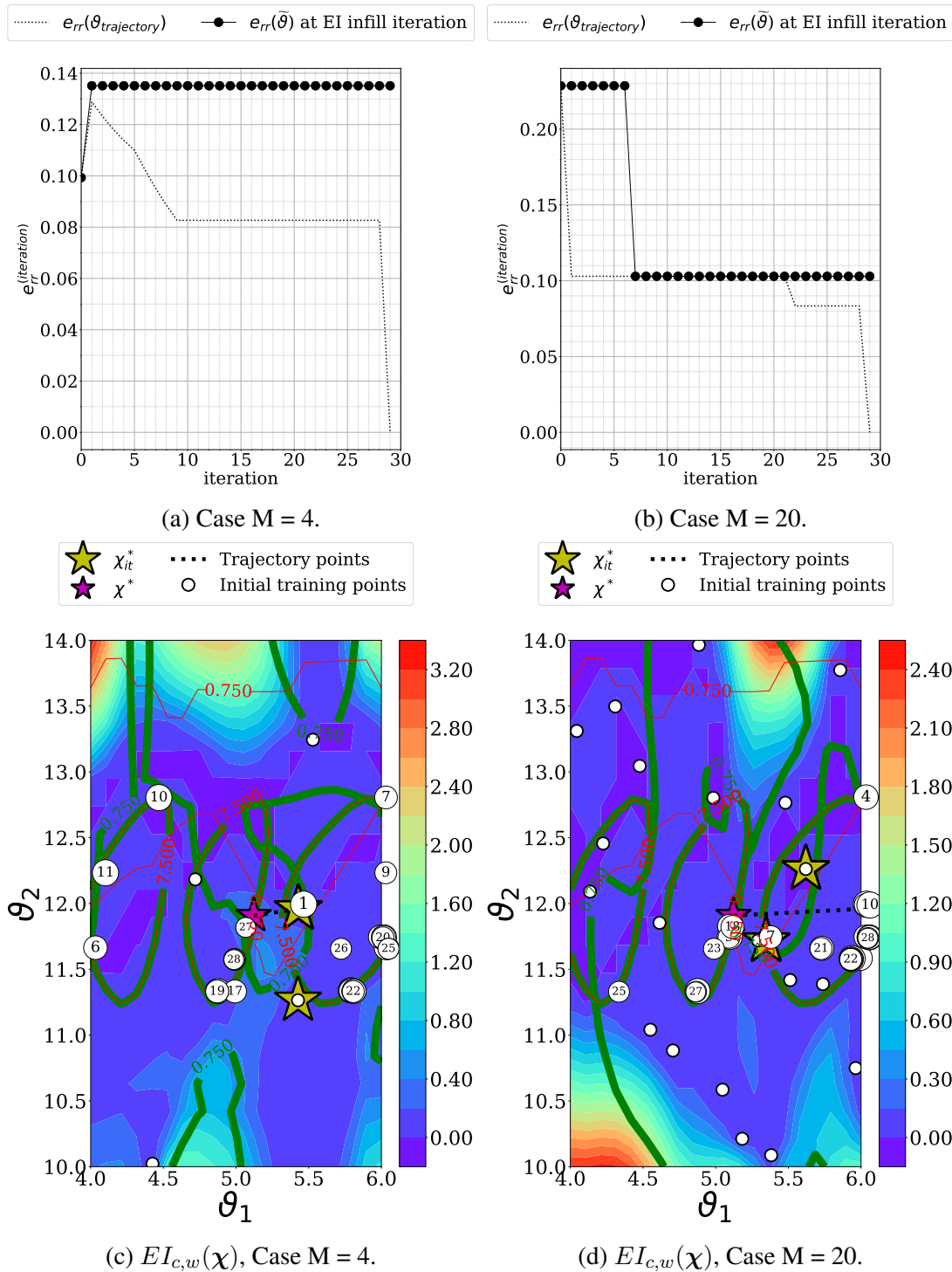


Figure 4.9: MFNIRB optimization using  $EI_{c,w}$  infill criterion considering  $\tilde{c}_2 = c_2^{HF}$

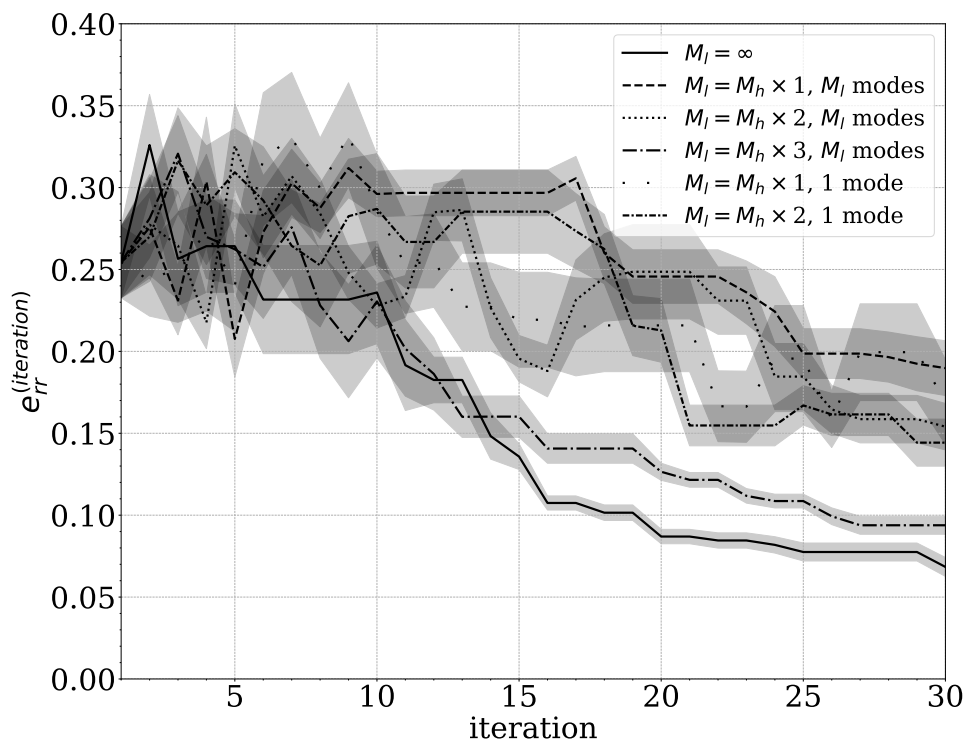


Figure 4.10: Case  $M_h = 4$ . Comparison between different MFNIRB cases with and without LFPOD. Evolution of  $\bar{e}_{rr}^{(iteration)}$  and its variance for multiple runs at each infill iteration.

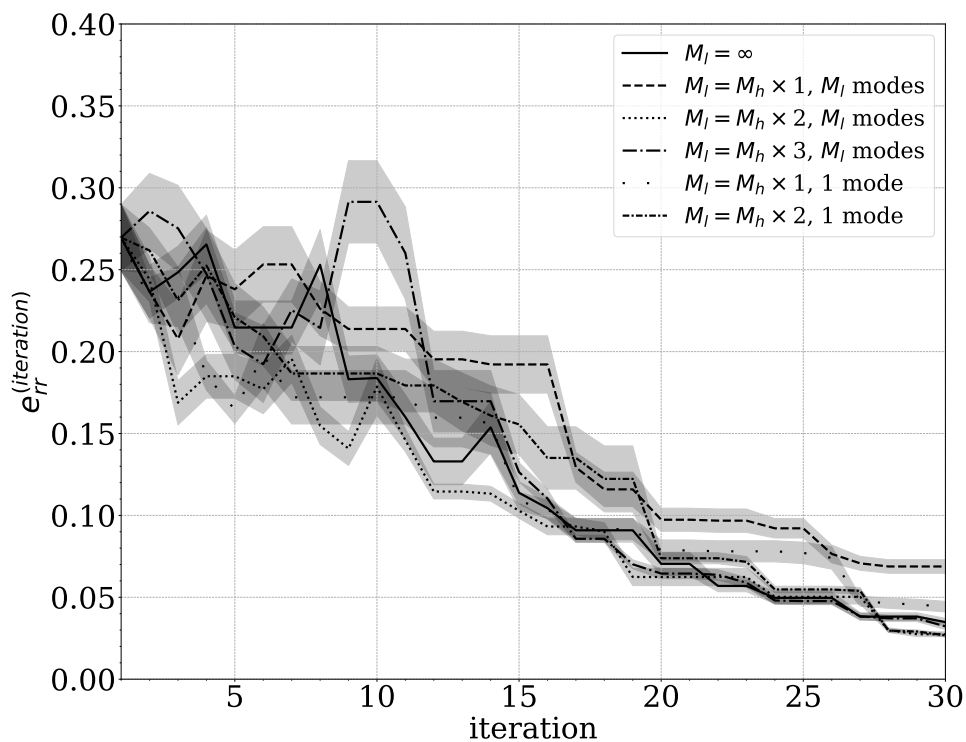


Figure 4.11: Case  $M_h = 10$ . Comparison between different MFNIRB cases with and without LF NIPOD. Evolution of  $\bar{e}_{rr}^{(iteration)}$  and its variance for multiple runs at each infill iteration.

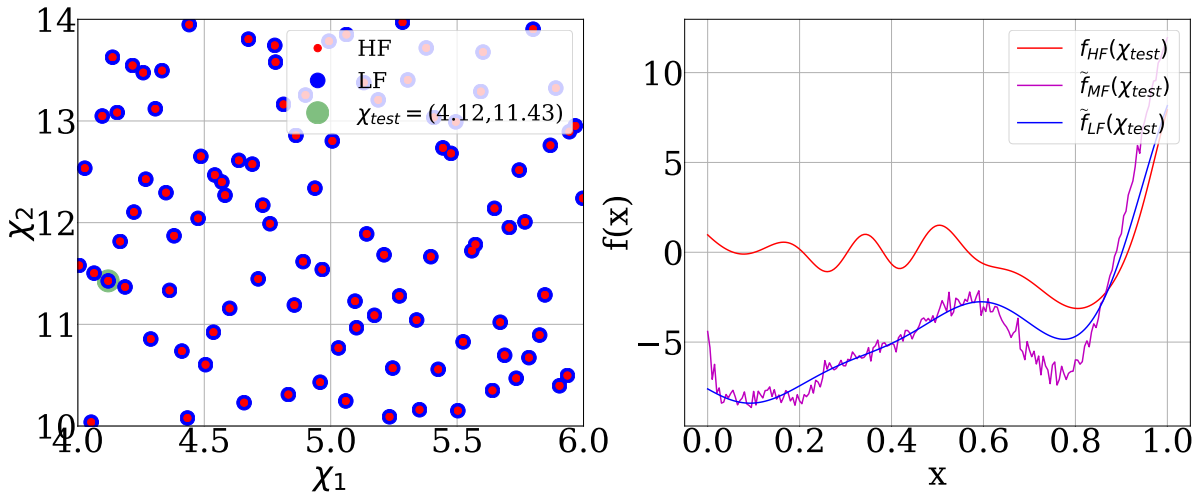


Figure 4.12: MF  $\tilde{f}_{MF}$  prediction, versus LF and HF snapshots, evaluated at  $\chi_{test} = (4.12, 11.43)$ . Case where Ratio = 1  $M_h = 100$  HF.

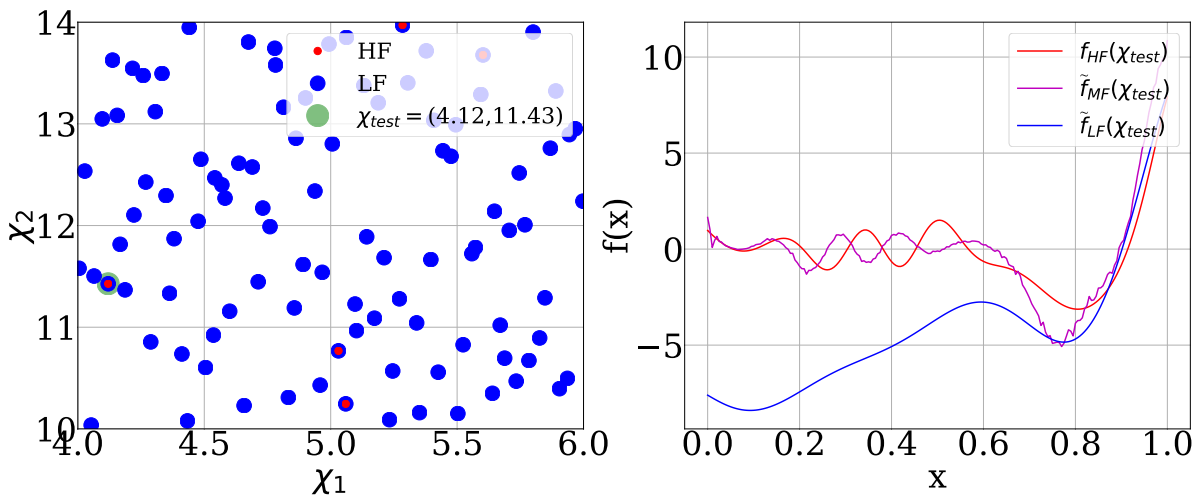


Figure 4.13: MF  $\tilde{f}_{MF}$  prediction, versus LF and HF snapshots, evaluated at  $\chi_{test} = (4.12, 11.43)$ . Case where Ratio = 20,  $M_h = 5$ .

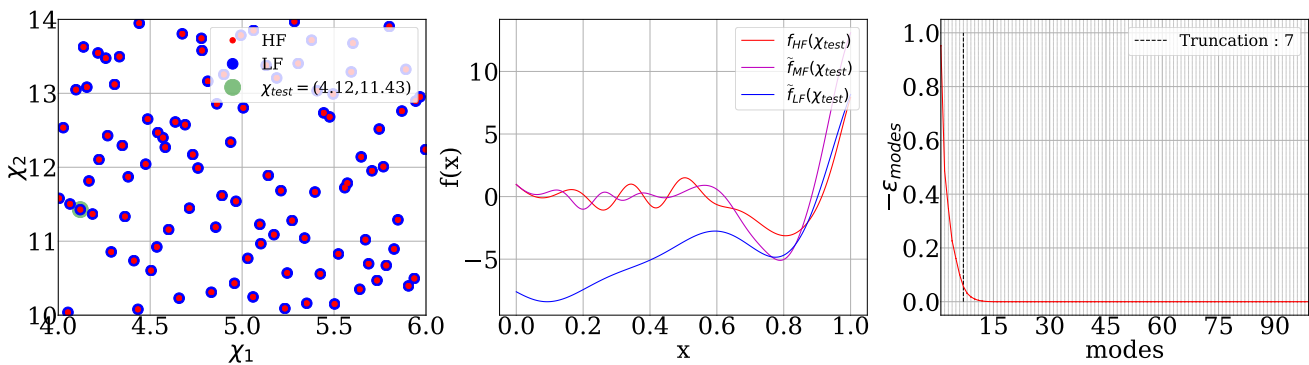


Figure 4.14: MF  $\tilde{f}_{MF}$  prediction with HF basis truncation, versus LF and HF snapshots, evaluated at  $\chi_{test} = (4.12, 11.43)$  (Ratio = 1,  $M_h = 100$ ). The truncation choice is illustrated on the right figure.

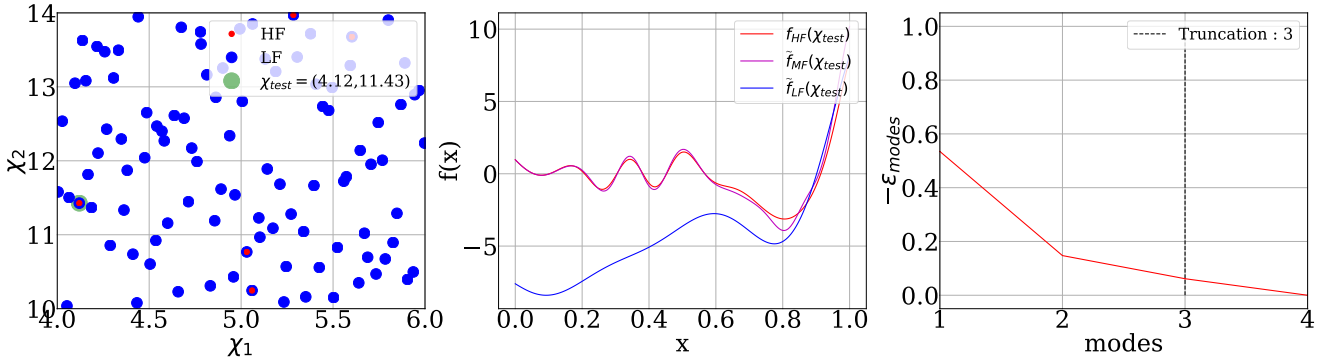


Figure 4.15: MF  $\tilde{f}_{MF}$  prediction with HF basis truncation, versus LF and HF snapshots, evaluated at  $\chi_{test} = (4.12, 11.43)$  (Ratio = 20,  $M_h = 5$  HF). The truncation choice is illustrated on the right figure.

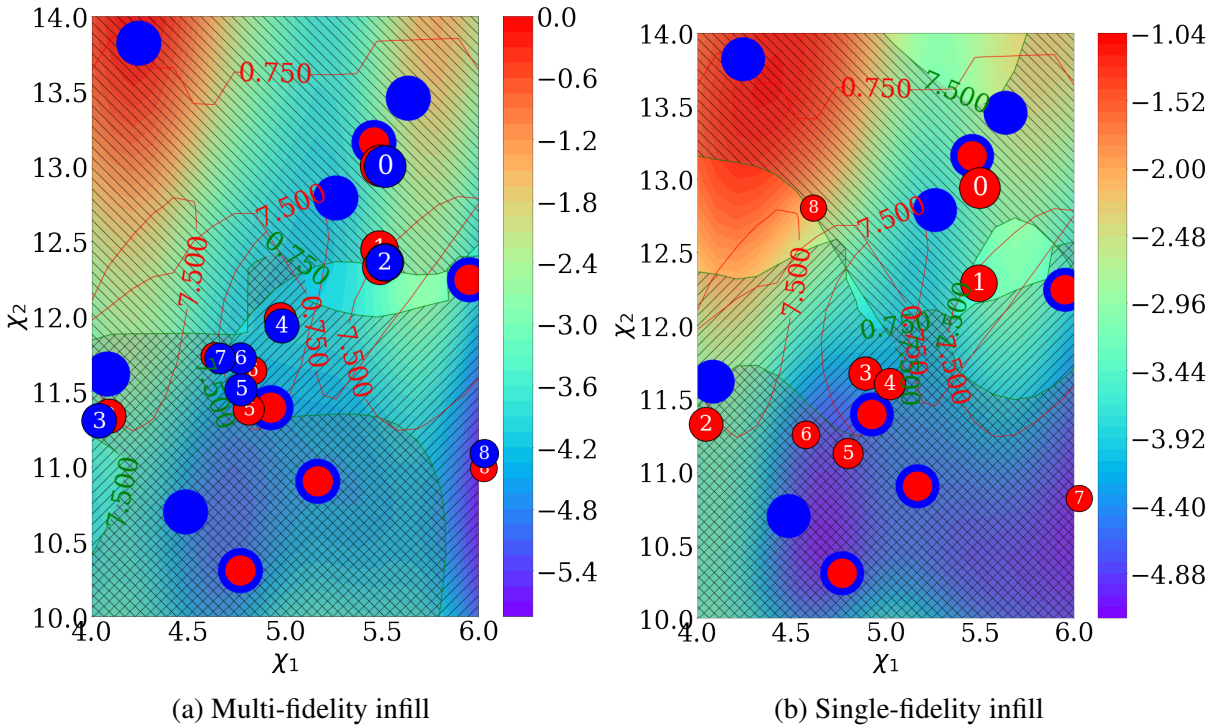


Figure 4.16: Comparison between the obtained  $\tilde{J}_{MF}(\chi)$  map with its constrained  $\tilde{c}_{1MF}(\chi)$  and  $\tilde{c}_{2MF}(\chi)$  areas (hatched) preliminary optimization. The tests are evaluated on validation grid, and conducted using single-fidelity and multi-fidelity infill beginning from the same HF (red dots) and LF (blue dots) DoE sizes of  $M_h = 5$  and  $M_l = 10$  (ratio = 2).

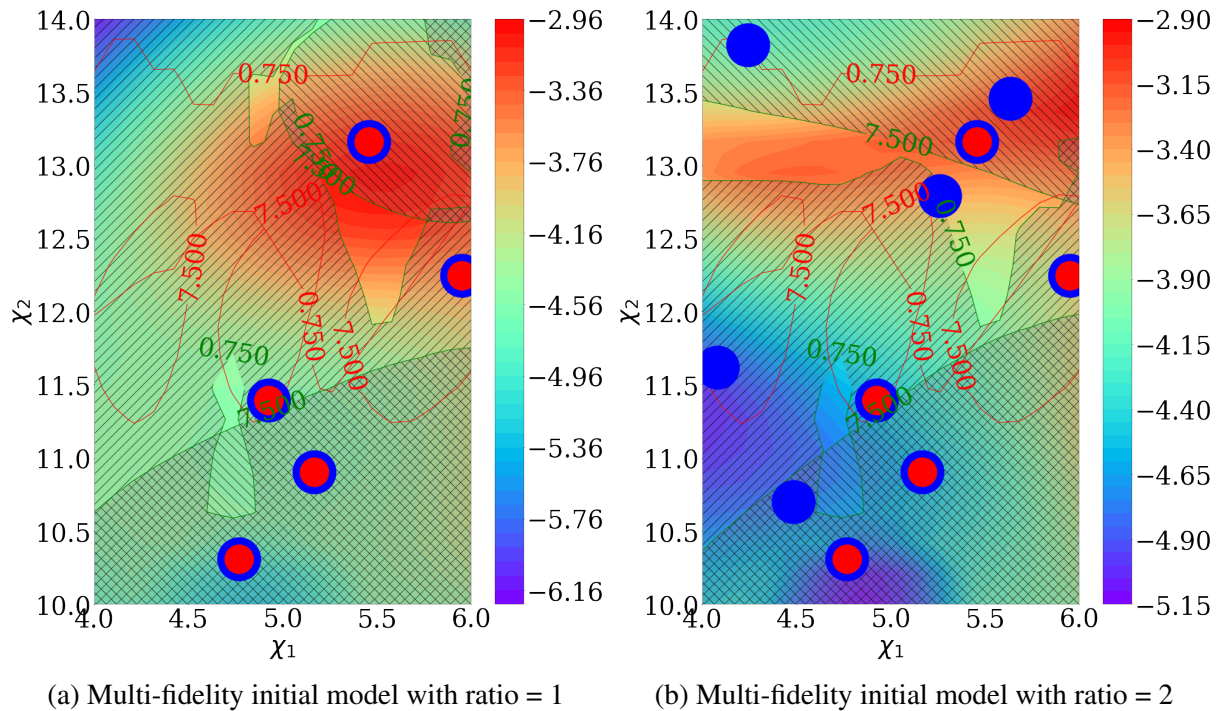


Figure 4.17: Comparison between the ratio 1 and 2 based maps of  $\tilde{\mathcal{J}}_{MF}(\boldsymbol{\chi})$  with constrained  $\tilde{c}_{1MF}(\boldsymbol{\chi})$  and  $\tilde{c}_{2MF}(\boldsymbol{\chi})$  areas (hatched) in the beginning of preliminary optimization. The tests are evaluated on validation grid, and conducted using single-fidelity and multi-fidelity infill beginning from two different ratios, resulting to HF (red dots) and LF (blue dots) DoE sizes of  $M_h = 5$  and  $M_l = 5$  (First column), then,  $M_h = 5$  and  $M_l = 10$  (second column).

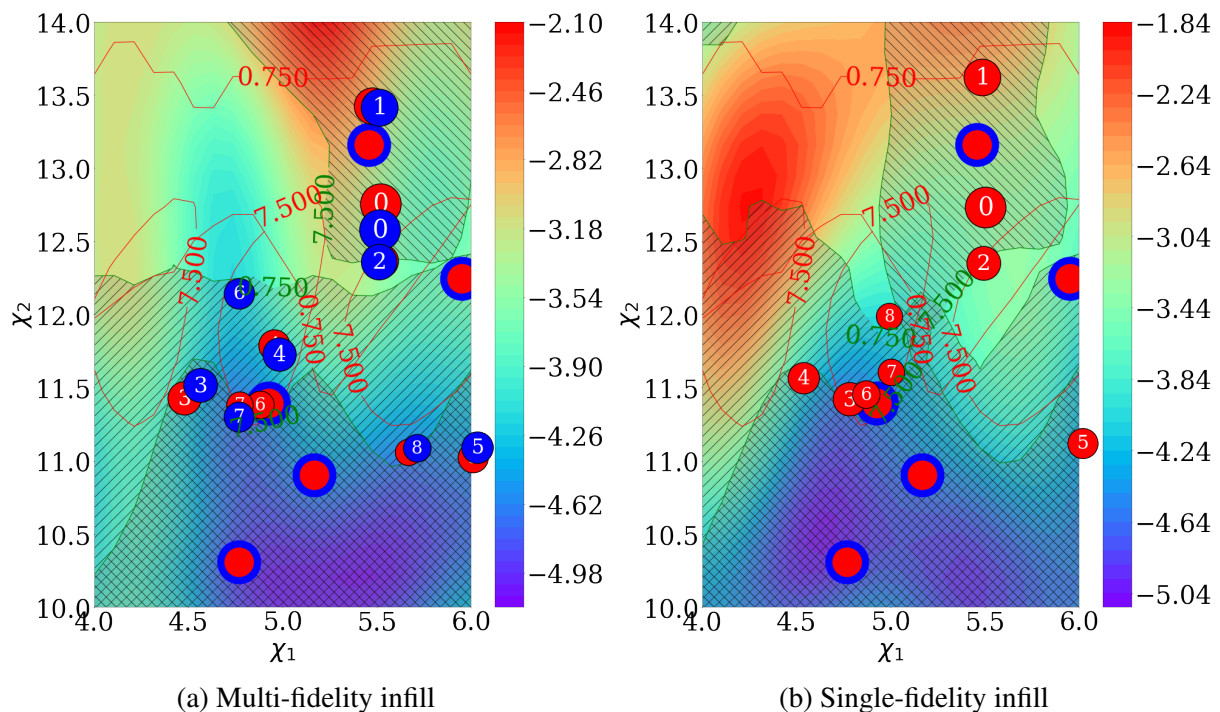


Figure 4.18: Comparison between the obtained  $\tilde{\mathcal{J}}_{MF}(\boldsymbol{\chi})$  map with its constrained  $\tilde{c}_{1MF}(\boldsymbol{\chi})$  and  $\tilde{c}_{2MF}(\boldsymbol{\chi})$  areas (hatched) preliminary optimization. The tests are evaluated on validation grid, and conducted using single-fidelity and multi-fidelity infill beginning from the same HF (red dots) and LF (blue dots) DoE sizes of  $M_h = 5$  and  $M_l = 5$  (ratio = 1).

# Chapter 5

## Industrial application : Optimization of an Open-Fan aircraft engine

### 5.1 Introduction

The proposed multi-fidelity method is designed to address optimization problems that need several calls to expensive High-Fidelity (HF) simulations. This approach is proposed together with an infill strategy to reduce the number of less relevant expensive evaluations to solve the design problem, and to use the available solvers only when relevant. Some simulations are much faster to use but generally less accurate. The idea is to take advantage of their low cost to use them extensively to reduce the need for expensive solvers. In this Chapter, the objective is to demonstrate how a multi-fidelity model is expressed from a physical point of view compared to a single-fidelity one and then evaluate the performance of the enrichment method for an industrial problem. The chosen industrial application is an Open-Fan engine and the suggested problem is a single-objective optimization of its multi-regime weighted efficiency with a constrained thrust.

The Open-Fan engine is an unducted ultra high-Bypass Ratio (BPR) fan engine composed of a turbine driving two composite propellers and a gas generator, that may be integrated in the tail of the fuselage. The Sustainable And Green Engines (SAGE) 2 project originally proven the potential of Contra-Rotating Open-Rotor (CROR) where the two propellers rotate on opposite directions. The idea is to add a second propeller that rotates in the opposite direction to increase the axial velocity of the air while also converting the first propellers tangential velocity increments into axial increases. The first propeller drives the air-inducing vortices that the second one recovers making the speed increase. The propulsive efficiency is then improved compared to a single-propeller configuration. Such prototype was not enough to achieve the industrial and economic requirement as, the complexity required to produce the counter-rotation of the two rotors make its maintenance harder and costly [Li, 2019]. In this regard, a promising single-rotor solution, the Open-Fan, is on the table to scale back operating costs. This Open-Fan motor can be seen as a puller with a fixed rear rotor, behaving like a stator. Figure 5.1 presents a picture of this new generation of unducted engine, where the first row of blades is rotating while the second is fixed.

In this chapter, bi-fidelity Computational Fluid Dynamic (CFD) modeling of the Open-Fan engine prototype is adapted to the MFNIRB framework. The objective is to illustrate the multi-fidelity along with the full-field paradigms onto physically meaningful quantities in an industrial scale (high DoE dimensions, etc.). The HF and Low-Fidelity (LF) models are respectively

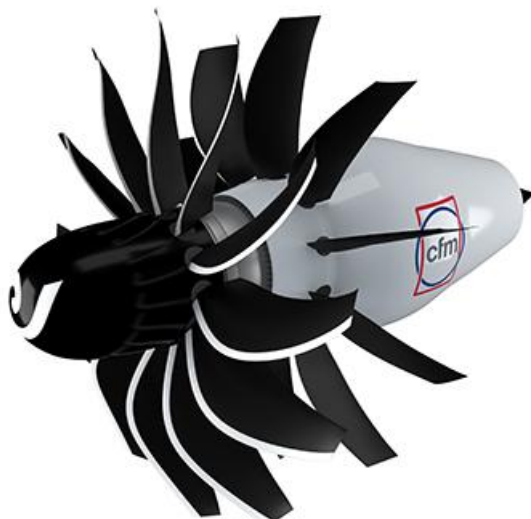


Figure 5.1: The Open-Fan Engine  
[Guy Norris, 2021, source : [www.aviationweek.com](http://www.aviationweek.com)]

a 3D and 2D representation where a Reynolds-Averaged Navier-Stokes (RANS) solver and a Lifting Surface solver are used to generate Quantities of Interest (QoIs). In order to represent a typical industrial case, several operating points are treated in the definition of the optimization problem. The optimization problem sought to maximize the efficiency subjected to a constant thrust. The optimization problem is formulated and adapted to the Multiple-Fidelity Non-Intrusive Reduced-Basis metamodels. Outputs used to train the MFNIRB are taken directly among the spatial discretization locations.

Section 5.2 presents the physical and numerical problem related to the Open-Fan design optimization. Section 5.2.1 defines the physical quantities to optimize. The main parameters that describes the propeller blade of the Open-Fan are presented in Section 5.2.2. Section 5.2.3 presents the optimization problem formulation as a physical quantity to optimize by varying these shape parameters. To solve this problem, two fidelity levels of existing solvers are introduced on Section 5.2.4 and Section 5.2.5. Section 5.3 describes the methodology used to adapt the two-fidelity levels of the simulations outputs to the MFNIRB model.

## 5.2 Design optimization problem

This section describes the various elements needed to define and solve the open fan design optimization problem. Note that the problem is to maximize the efficiency of the propulsion under thrust constraints. For this purpose, the concepts of efficiency and thrust are defined in their physical context. Then, the geometrical input parameters of the problem are described. Finally, the specificities of the two levels of simulations, which will generate the physical quantities, are presented.

### 5.2.1 Physical quantities to optimize

The Open-Fan is a prototype with a single propeller consisting of a row of rotating blades connected to the aircraft engine shaft. The purpose of a propeller is to generate thrust in the direction of flight. The ultimate goal is to allow lift and thrust to maintain the elevation and

motion of flight, thereby counterbalancing the opposing effect of its own weight and the drag produced by air flow forces on the surfaces of the jet. Figure 5.2 is a schematic representation of these forces applied to the aircraft during flight.

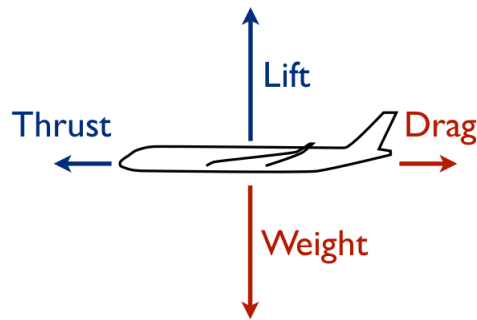
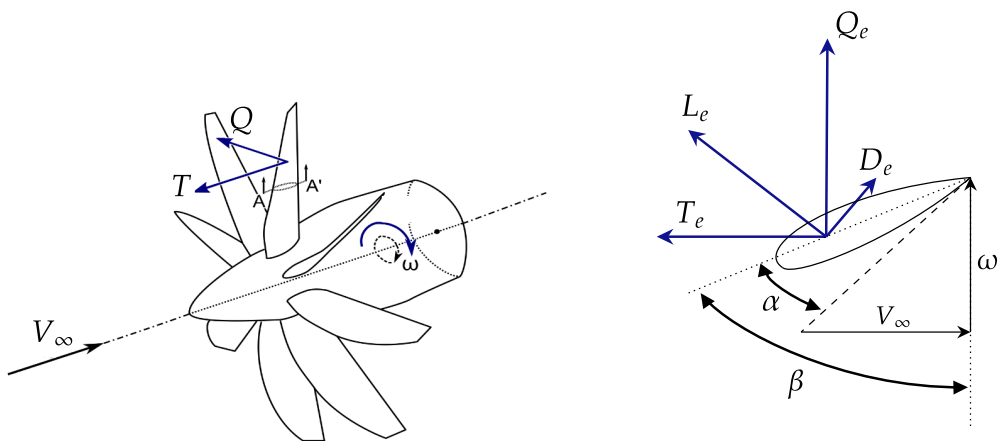


Figure 5.2: Forces applied on the aircraft [Gallard, 2014].

The overall aerodynamic force produced by a single blade of the propeller can be divided into two components: the thrust  $T$  and a propeller torque force  $Q$ . These are illustrated in Figure 5.3a.



(a) Forces applied to a typical engine blade profile. (b) Elementary forces applied on each fan section A-A

Figure 5.3: Aerodynamic forces applied on a blade at its center of pressure and elementary forces at the section A-A (adapted from [Marinius, 2011]).

The propeller blade is designed by assembling radial sections. The forces applied to the blade are decomposed into elementary forces applied to each section. The corresponding aerodynamic profile shape depends on the radial position of A - A section (illustrated Figure 5.3b). The aerodynamic force is decomposed into lift  $L_e$  and drag  $D_e$  elements or thrust  $T_e$  and  $Q_e$ . In Figure 5.3b,  $V_\infty$  is the free flow velocity,  $\omega$  the induced velocity,  $\omega_r$  the local tangential velocity resulting from the rotation. The angle  $\beta$  is the local blade angle and  $\alpha$  is the angle of attack for that particular section. In typical cases, the outer sections of the blade are mainly contributing to thrust generation. As with airfoils and wings, propeller performance may be described by non-dimensional coefficients. These are usually computed from simulation outputs at the post-processing phase. The pressure and shear force distributions around the blade are integrated to

compute the thrust  $T$  and propulsive power  $P$  required to drive the blade.

Propeller Efficiency  $\eta_p$  defines the performances of the propeller propulsion. It is expressed in Equation 5.3 as the ratio of the Power output

$P_{out}$  of the propeller [Béchet et al., 2011] over  $P$ , given  $V_\infty$ , the free stream velocity, with

$$P = TV_\infty \quad (5.1)$$

and

$$P_{out} = 2\pi\omega Q, \quad (5.2)$$

$$\eta_p = \frac{P_{out}}{P} = \frac{TV_\infty}{2\pi\omega Q}. \quad (5.3)$$

The efficiency is an essential quantity that characterizes the performance of the engine. It is part of the presented problem formulation and solving, depending on the blade geometry parameters, further described in the next section.

## 5.2.2 The optimization design definition of Open-Fan propeller

The Open-Fan is an unducted aircraft engine prototype with a single propeller consisting of a row of rotating blades connected to the engine axis. The Open-Fan blades lower section, called hub is mounted on the engine shaft through pivot connections allowing their orientation to vary. A basic propeller is defined in three dimensions [Philippe, 1999, Techniques de l'ingénieur], the x being the engine axis, the y axis is colinear with the blade span, and z defined to complete the direct system. Its geometry is defined with the following parameters :

- **Span** : radial position along the blade with respect to the axis y
- **Pitch** : is the angle between the chord and the z axis
- **Twist**: angle variation between the chords of the different profiles of the blade and the reference profile and the reference profile according to the height.

A series of sections are used to decompose the aerodynamic forces as they vary with the blade span. In the defined coordinates, an airfoil may be any section obtained by cutting the blade with a plan orthogonal to the y-axis. As illustrated on Figure 5.4, a propeller profile is defined by the following parameters

- **Chord**  $c$  : the distance between the leading edge and the trailing edge.
- **the wedge angles**  $\beta_1$  and  $\beta_2$  : angles between the tangent to the frame respectively at the leading edge and the trailing edge. These two parameters are relevant to define the camber of the profile, reflecting the work that the propellers can handle.
- **Thickness** is generally defined by the distance between the extrados and the intrados<sup>1</sup>.

Each section is generated according to the parametrization defined in Section 1.2.3. The geometry parameters above varies over a given variation interval. The parameter sets are integrated into an automated optimization that takes into account the overall blade. The optimization chain involves the geometry, mesh generation, simulation and post-processing. The objective is to generate the most suitable blade geometry according to the defined objective and constraints.

<sup>1</sup>Corresponding to upper and lower surface of the blade, respectively

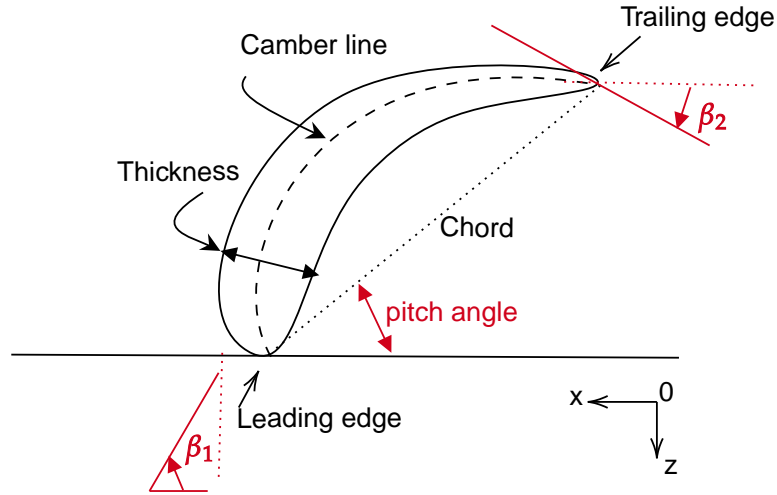


Figure 5.4: Airfoil shape parameters.

### 5.2.3 Problem formulation

The proposed optimization problem is aiming to find the four optimal parameters of  $c$ ,  $\beta_1$ ,  $\beta_2$  and  $\beta$  within four sections. Hence, a total of 16 design variables are defined with their corresponding variation range in 5.1.

Variable	Number	Variation range
Chord length $\frac{c(r)}{D}$	4	$[-20\%, 20\%]$
Wedge angles $\beta_1(r)$ $\beta_2(r)$	8	$[-5, 5]$
Rotor pitch $\beta(r)$	4	$[-10, 20]$

Table 5.1: Open-fan blade geometry parameters

Any civil flight is described by its mission profile defining the different flight conditions and engine regimes from Take-off to landing. Fans are optimised to provide the necessary traction at take-off and max-climb (where thrust must be higher) and a suitable efficiency during cruise, the longest phase. Furthermore, the mechanical constraints ensure the viability of the fan at those various conditions. Figure 5.5 illustrates these different phases that depend on the variable height levels of the aircraft from the take-off, initial Climb, Climb to Cruise, the longest phase where the level is mostly stable. The last phases are divided onto the descent and the landing.

The forces applied to the aircraft engine fluctuate with the flight regimes. It is therefore necessary to take into account the multiple flight condition specifications. The objective is then defined by the weighted efficiency of the propeller subjected to the constant thrust and defined as the maximization of the efficiency among the three chosen operating points: Cruise, Climb and Take-off (see table 5.2).

The design variables, objective and constraint are defined in  $\mathcal{D} = [-20\%, 20\%]^4 \times [-5, 5]^8 \times [-10, 20]^4 \in \mathbb{R}^{16}$ . The optimization problem is defined by

$$\begin{aligned} \boldsymbol{\chi}^* &= \arg \max_{\boldsymbol{\chi} \in \mathcal{D}} \eta_p(\boldsymbol{\chi}) \\ &\text{s.t. } C_T(\boldsymbol{\chi}) = \text{constant} \end{aligned} \quad (5.4)$$

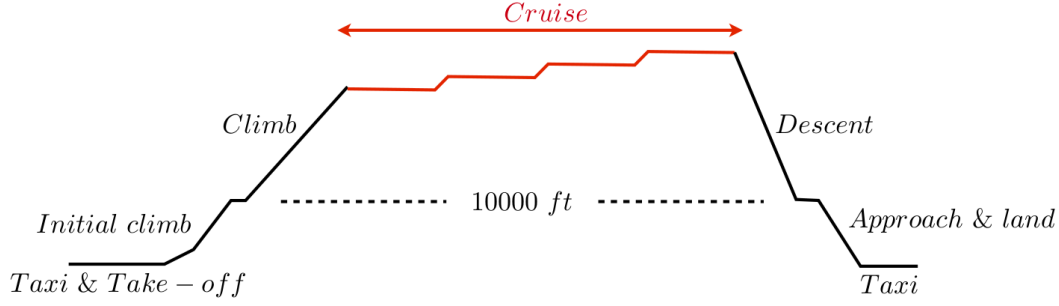


Figure 5.5: Typical civil transport aircraft mission profile [Gallard, 2014].

Flight conditions	Units	Cruise	Max climb	Take-off
Altitude	ft	37 000	33 000	0
Mach Number	-	0.75	0.74	0.25
Delta Temperature	K	0	10	15
Ambient Pressure	Pa	21 662	26 200	101325
Ambient Temperature	K	216.65	232.77	303.15
Propeller air density	kg/m <sup>3</sup>	0.35	0.39	1.16
Propeller Rotational Speed	rpm	n.c.	n.c.	n.c.
Propeller Thrust	N	n.c.	n.c.	n.c.

Table 5.2: Open-Fan physical conditions

where

$$\eta_p(\boldsymbol{\chi}) = w^{(cr)}\eta_p^{(cr)}(\boldsymbol{\chi}) + w^{(to)}\eta_p^{(to)}(\boldsymbol{\chi}) + w^{(cl)}\eta_p^{(cl)}(\boldsymbol{\chi}) \quad (5.5)$$

and constraint

$$C_T(\boldsymbol{\chi}) = w^{(cr)}C_T^{(cr)}(\boldsymbol{\chi}) + w^{(to)}C_T^{(to)}(\boldsymbol{\chi}) + w^{(cl)}C_T^{(cl)}(\boldsymbol{\chi}) \quad (5.6)$$

where  $\eta_p$  and  $C_T$  are the Open-Fan propulsion efficiency and thrust respectively,  $w^{(cr)}$ ,  $w^{(to)}$  and  $w^{(cl)}$  are fixed weight coefficients depending on the desired impact on the optimization directions given to each operating points.

Efficiency and thrust are scalar coefficients evaluated from physical simulation outputs. In this study, they refer to three different flight phases and are obtained from two fidelity levels of open-fan aerodynamic simulations. Our goal is to adapt the proposed multi-fidelity methodology MFNIRB to the solving of such Surrogate Based-Optimization (SBO). There is an additional step to be performed to adapt the different fidelities of the available simulations, and to calculate the performances to be optimized. The two following sections, therefore, give the required details on the available simulations, then the proposed implementation is presented in Section 5.3.1.

### 5.2.4 Low-Fidelity model implementation

The performance of propellers can be characterized by different physical models. Simplified models have been developed to reduce the computation cost of more demanding though more accurate models such as the RANS or Large Eddy Simulation (LES). They can be quoted in a non exhaustive way as follows

- The **element theory** [Froude, 1878, Gur & Rosen, 2008] consists in dividing the propeller blade into sections, and then studying each force acting on these sections. It requires knowledge of the characteristics of the section, such as the local lift and drag coefficients ( $C_l$  and  $C_d$ ), but does not take into account the velocity induced by the thrust production.
- The **moment theory** [Rankine, 1865, Kuik, 2018] of the combined blade elements gives the propeller performance by obtaining the blade load which includes the induced velocity.
- For a given velocity profile, a **lifting-line** approach is used to predict the blade loading. The lifting-line approach is applied for low-aspect ratio & swept wing : it is an extension of the Prandtl's lifting-line theory [Glauert, 1983] developed for slender lifting geometry (based on Guermont's theory [Guermont, 1990]). The propeller is assumed to behave like 2D airfoils connected to each others with vortex lines. The vortex lines are connected to a common wake shed sought to respect the continuity of the vortex lines (Helmholtz theorem). The airfoil behaviour is characterized by  $C_L$  and  $C_d$  coefficients as a function of angle of attack, Mach number and Reynolds number. Those coefficients are computed using a 2D RANS solver.
- The **Lifting Surface** [Gruber et al., 2015] is another simplified vortex based method, can be seen as an a lifting line approach that takes into account the 2D effects and does not need RANS solver to generate coefficient polars.

In our case, the chosen LF methodology is the lifting surface. The blade is represented by a distribution of vortices to model the thickness effect and by doublets for the camber effects, while the wake is represented by doublets. This allows to describe the flow along the profiles with respect to the refinement of the mesh, and partially remedies the limitations imposed by the lifting line. However, the drag losses of the profile are not taken into account in the calculations. The rotor blade is replaced by a surface along which the flow varies. It is subdivided into a set of elementary panels identified by helical vortices. The induced velocities produced by the set of trailing vortices at the control point of each panel are calculated by the Biot-Savart law. Then, using the Kutta-Jukowski theorem and the 2D lift and drag coefficients as a function of angle of attack, the aerodynamic forces acting on the blade are calculated. The compressibility effect is addressed by using a Prandtl-Glauert correction on the lift, and the airflow is modeled as an inviscid-incompressible flow.

This model is used in the simulation chain, that takes the optimization parameters as input and generates physical quantities for the corresponding mesh of the open-fan blade. The resulting scheme is illustrated in Figure 5.6 and corresponds to each call to the solver to evaluate the corresponding lifting surface simulation outputs  $f_{LF}(\mathbf{x}, \boldsymbol{\chi})$  for a given set of parameters  $\boldsymbol{\chi} \in \mathcal{X}_{LF}$  of the LF Design of Experiment (DoE), within the SBO loop. Each LF DoE sampling of the parameter  $\boldsymbol{\chi}$  requires the generation of a new blade geometry using in-house geometry modeler CARMA with the appropriate parametrization approach.

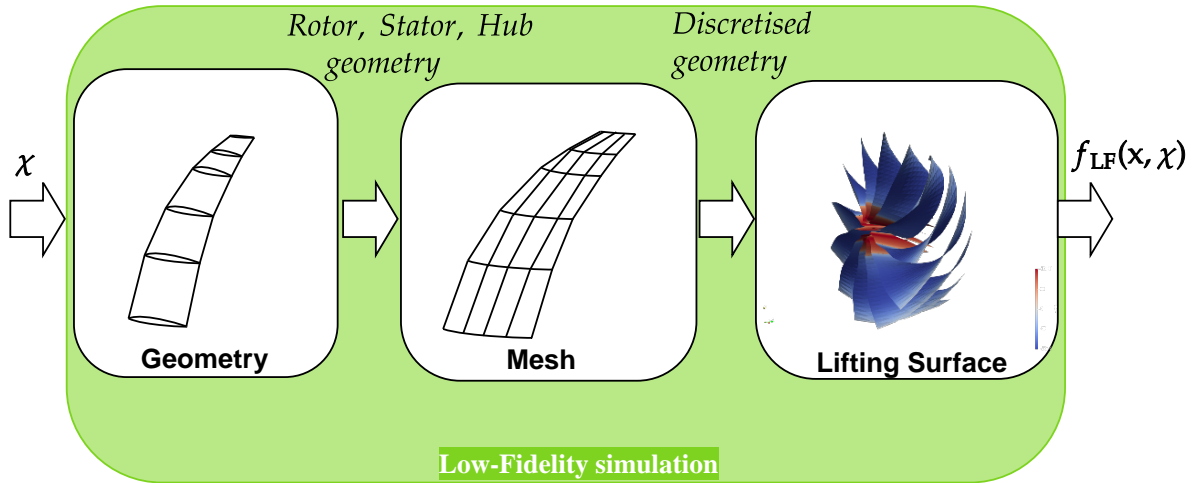


Figure 5.6: LF simulation

The Open-Fan is modeled as 12 rotor blades (Figure 5.7a) and stator (Figure 5.7b) attached to the hub (Figure 5.7c), covering the intern part of the Open-Fan engine. It is represented by a curved lower line delimiting the mesh regions. The rotor and stator blade surfaces are discretized with a structured mesh. The wake and physical quantities  $f_{LF}(\mathbf{x}, \chi)$  of each blade are computed with the in-house solver *Sandra*.

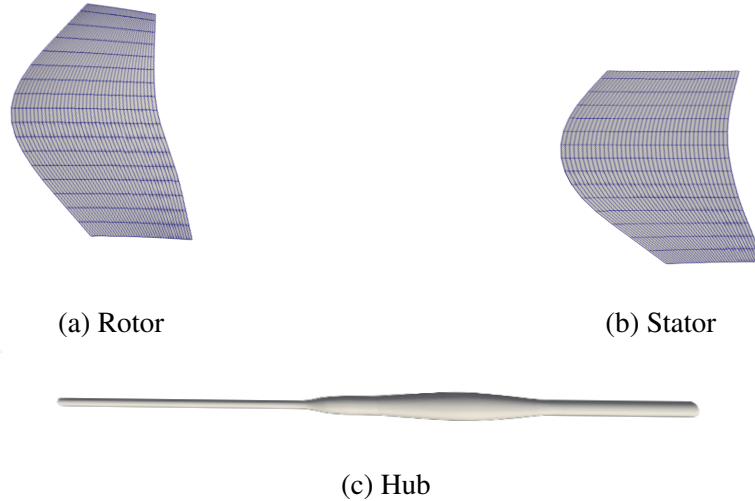


Figure 5.7: Open-Fan system components

The discretization is performed at the surface of the mean camber with quadrilateral vortices. Figure 5.8 represents the discretization of the lifting surface model. The  $j^{th}$  height of the blade corresponds to the discretizations  $x_{j,1}$  to  $x_{j,M+1}$ , in this Figure there are  $N + 1$  section heights.

Following the discretization of the lifting surface method, the output defined by  $f_{LF}(\mathbf{x}, \chi)$  is constructed from a 2D discretisation such as  $\mathbf{x}_{i,j}, \forall i \in [1, N]$  and  $j \in [1, M]$ . The  $M$  and  $N$  values are taken into account to compare the LF and HF outputs. This step is further detailed in the following sections.

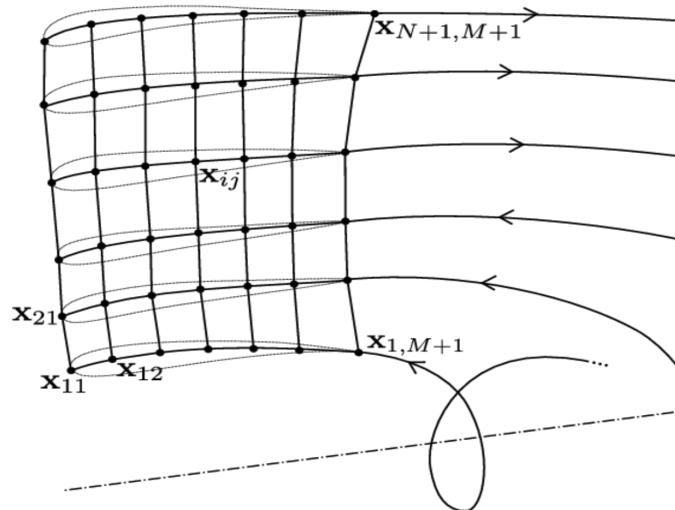


Figure 5.8: LF simulation discretization [Leborgne et al., 2015]

### 5.2.5 High-Fidelity model implementation

The available higher fidelity level of simulation is a steady state 3D RANS model applied to evaluate the open-fan aerodynamic QoIs. The so-called RANS consists in numerically solving the continuous conservation equations of the mass, momentum and energy. This approach is able to compute non-linear phenomena, such as shocks occurring in the passage of the blades, in a relatively accurate way, but conceding a significant increase in computational cost compared to the traditional methods such as the lifting surface model previously introduced. In the present study case, the 3D steady RANS system of equations is solved by the ONERA code elsA [Cambier & Gazaix, 2012]. Figure 5.9 illustrates the main steps of the solver call that evaluates the corresponding simulation outputs  $f_{HF}(\mathbf{x}, \chi)$  for the modified parameter  $\chi \in \mathcal{X}_{HF}$  of the HF DoE, within a SBO loop. The fluid areas around the rotor and stator are meshed using *Autogrid* (NUMECA). Finally, the RANS solver is called to evaluate the physical field quantities  $f_{HF}(\mathbf{x}, \chi)$ .

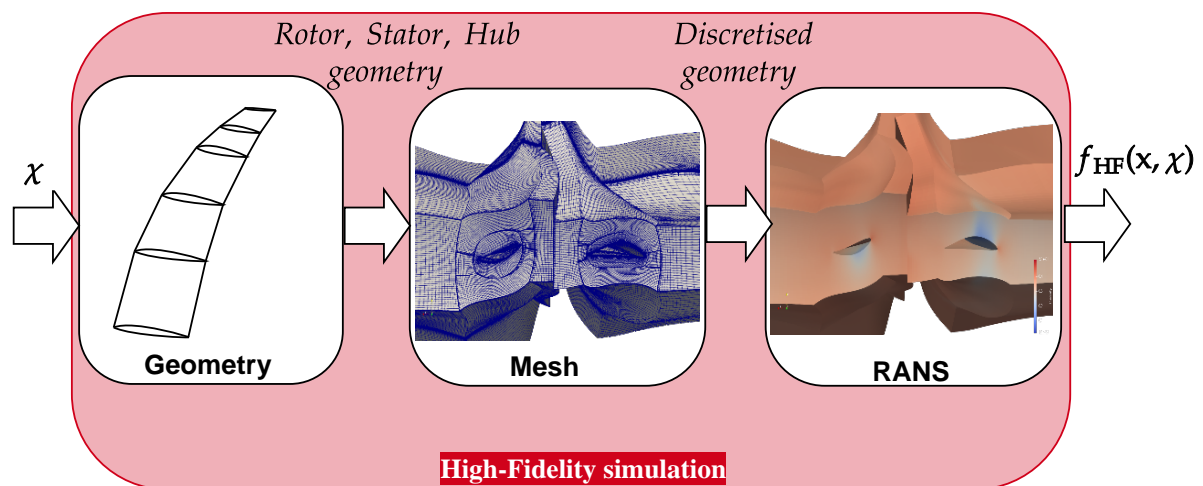


Figure 5.9: HF simulation

Figure 5.10a is a meridional view of the global mesh divided into two parts composed of

the farfield on the top region and the propeller region. Both parts are divided into Rotor and Stator corresponding regions as illustrated in Figure 5.10b. The blades are fixed to the hub, separating the flowpath from the internal part of the Open-Fan engine. The final grid contained 4.7 million points, consisting of 1.3 million for each blade region and 0.23 million for each farfield region. The modeler generates the geometry on which an adapted mesh will be applied. The mesh is of O4H topology, composed by an O-type block surrounded by 4 H-type blocks (see Figure 5.10c).

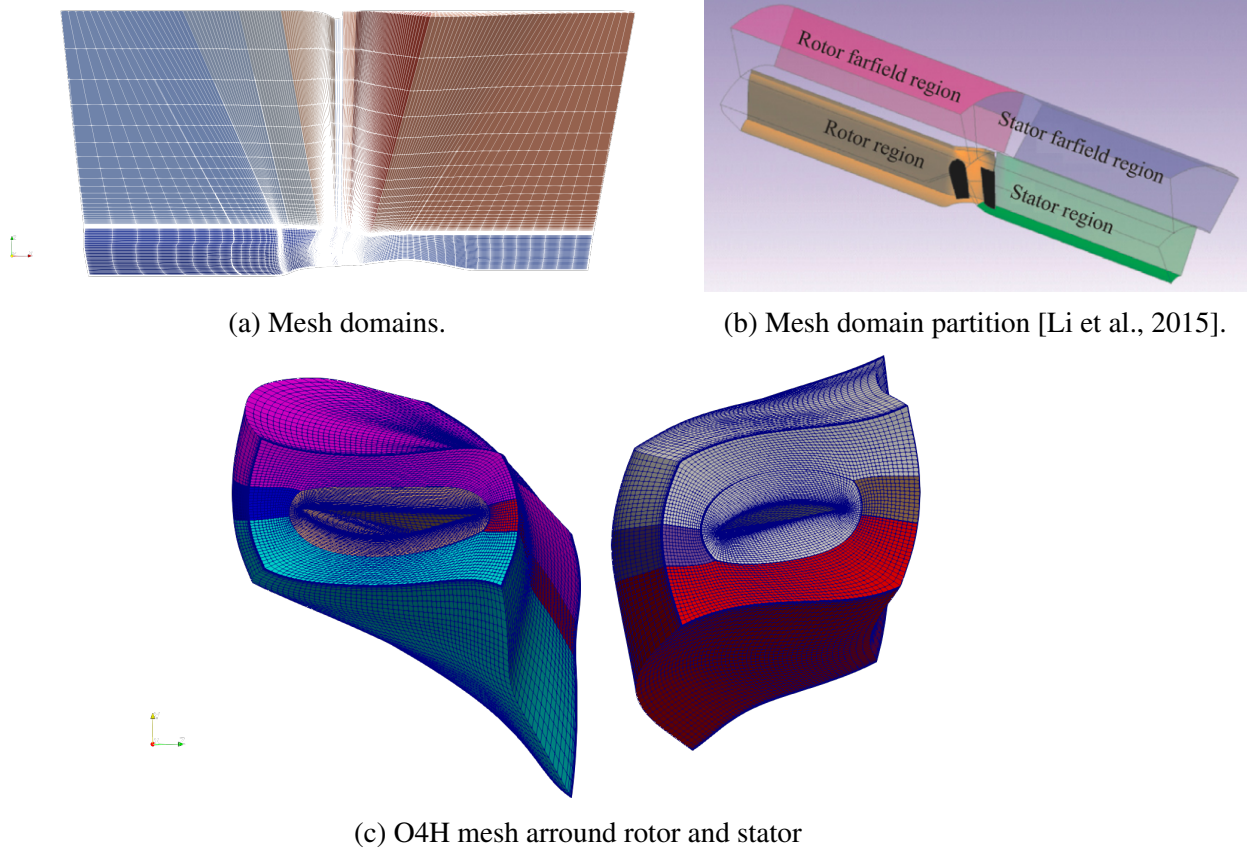


Figure 5.10: Definition of the Open-Fan aerodynamic mesh.

The discretization of this HF model is more complex than the LF discretization described above. First of all, one is in a 3D space, the other in 2D. The LF model can be defined at each blade height by panels, while the HF model refined along the span direction. In the following sections, a methodology is proposed to address the compatibility between the outputs of these two solvers, with the aim of using it on the Multi-Fidelity (MF) framework.

### 5.3 Methodology

The optimization method developed requires the use of two simulation chains (high- and low-fidelity) modeling the same physical quantities but with different levels of fidelity. In this section, the methodology used to construct the multi-fidelity model from the different available outputs of the lifting surface model (low-fidelity) and the steady RANS model (high-fidelity) is presented. The proposed meta-model MFNIRB is built from the full-field bi-fidelity simulation outputs, which allows to take into account the full-field representation instead of the scalar performance outputs.

### 5.3.1 Multi-fidelity surrogate-based optimization implementation

The objective is to perform the presented geometrical optimization using the two fidelity levels of the vector outputs  $f_{HF}(\mathbf{x}_{HF}, \chi)$  and  $f_{LF}(\mathbf{x}_{LF}, \chi)$ . It is necessary on the one hand to adapt the two outputs HF and LF, because they do not have the same shape (the discretization of the HF model  $\mathbf{x}_{LF}$  is different from that of the LF model  $\mathbf{x}_{HF}$ ).

The optimization follows a similar SBO method used in Chapters 3 and 4, except that the definition of the parameters corresponds to the shape of propeller blades (e.g., chord, torsion angles, thickness, etc.). Moreover, an additional step is needed to adapt the different fidelity levels of the vector outputs. Concerning the analytical bi-fidelity benchmark (Numerical application of Chapters 3 and 4), the functions of both levels depend on the same discretization variable. A sampling method (LHS, LCVT, etc.) is used to select the geometries within intervals defined by the designer. Once the parameter set is drawn, the two levels of simulations are run in parallel to recover the physical quantities. The adaptation of the HF to the LF discretization allows to have a common mesh variable. In the present case, this similarity is found between each blade height  $r$  (detailed in Section 5.3.2). The different steps of the MFNIRB model-assisted optimization are summarized in Figure 5.11.

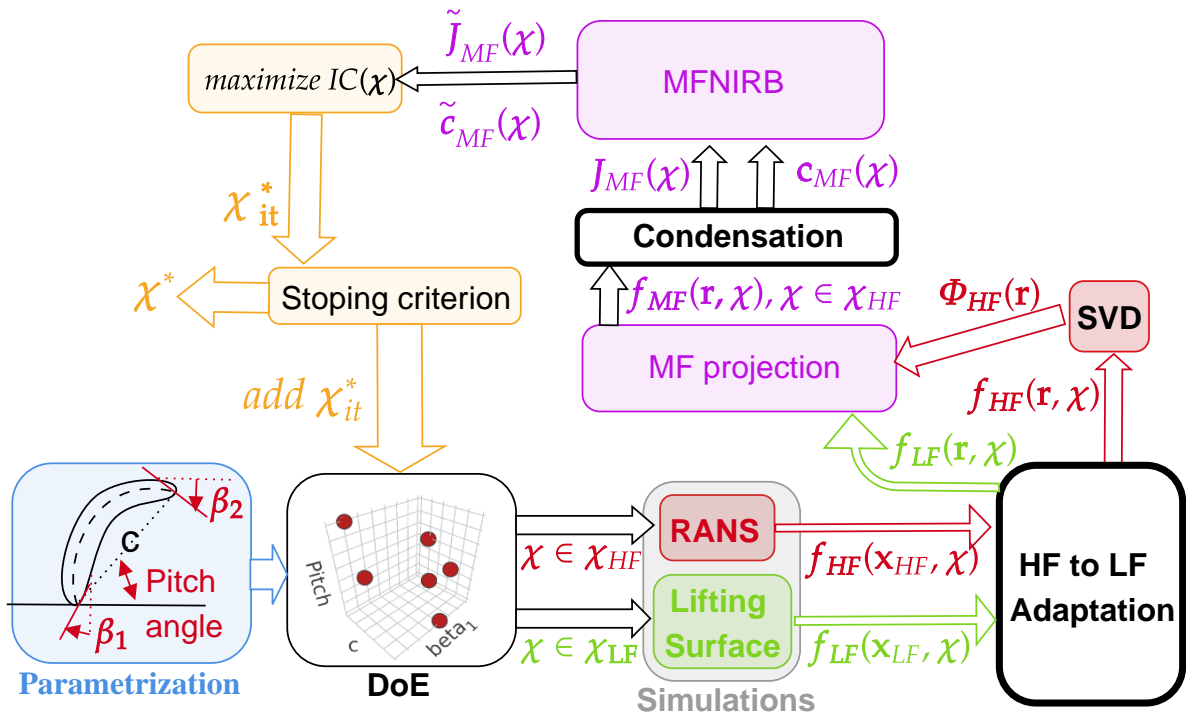


Figure 5.11: Main steps of the multi-fidelity implementation from the model construction to infill

In the present case, we are looking to optimize the efficiency subjected to thrust constraint, both are scalar quantities. Therefore, we need to perform the transition from vector to scalar quantities. The two elements mentioned above correspond to the adaptation of HF to LF and to condensation. They are represented in the diagram by two white boxes framed by a black solid line. These steps are not generalizable, there are as many possible approaches as existing simulation methods. A method is proposed in the following sections for HF to LF adaptation Section 5.3.2, and for condensation Section 5.3.3.

The whole scheme of the method MFNIRB is reproduced (see method MFNIRB). Thus, the constructed snapshot matrix allows recovering the orthogonal basis  $\Phi_{HF}$ , which will be used as the projection basis for the set of LF vectors (The LF Non-Intrusive Proper Orthogonal Decomposition (NIPOD) method is used to estimate the LF snapshots). Therefore the function MF,  $f_{MF}$  is assessed, then subjected to post-processing condensation (may be integration for example) that evaluates the trend of the model MFNIRB. The non-deterministic part (that follows a Gaussian Process) of this model will then be used to evaluate the new infill point  $\chi_{it}^*$  at each iteration until convergence of the optimization. All these steps will then be applied to solve the physical optimization problem on the Open-Fan.

### 5.3.2 High-Fidelity adaptation to Low-Fidelity full-field outputs

The main difficulty lies in the fact that the design optimization is mainly determined by the integrated quantities. In the proposed approach, these quantities are directly estimated by the meta-model. Contrary to previous experiments on the MFNIRB Chapter 4 notations and approach, it consists in predefining the components of the optimization  $\mathcal{J}$ ,  $c_h$ ,  $h$  = number of constraints, according to the output fields depending on the mesh  $\mathbf{x}$  or the height,  $\mathbf{f}(\mathbf{x}, \chi)$ . In the present case, the low- and high-fidelity representations have similar outputs for the 2D quantities in the radial and azimuthal sections. Therefore, the quantities needed to evaluate the efficiency and thrust will be evaluated within the optimization loop as a function of the radial height  $\mathbf{r}$  and the design variables  $\chi$  to estimate the global flow behavior among the entire blade. The outputs of each simulation are defined as the HF outputs

$$\mathbf{S}_{HF} = [\mathbf{f}_{HF}(\mathbf{r}, \chi^{(1)}) \dots \mathbf{f}_{HF}(\mathbf{r}, \chi^{(M_h)})] \quad (5.7)$$

and LF outputs

$$\mathbf{S}_{LF} = [\mathbf{f}_{LF}(\mathbf{r}, \chi^{(1)}) \dots \mathbf{f}_{LF}(\mathbf{r}, \chi^{(M_l)})] \quad (5.8)$$

where  $M_h$  and  $M_l$  are the total number of snapshots for the HF and LF DoEs respectively.  $\chi$  is the vector of the design variables (for example the propeller blade angles  $\beta_1$ ,  $\beta_2$ , and chord  $c$ ), the function  $\mathbf{f}$  represents HF or LF simulation depending on design variables  $\chi$  and each radial height  $\mathbf{r} = [r^{(1)} \dots r^{(n_r)}]$  illustrated in Figure 5.12.

### 5.3.3 Condensation : from full-field simulations to quantities of interest

This section presents the post-processing to be performed under the MFNIRBSBO (illustrated in Figure 5.11). To integrate the full-field physical outputs  $\mathbf{f}(\mathbf{r}, \chi)$  (obtained after the mesh adaptation detailed in the previous section) into the scalars  $\eta_p$  and  $C_T$ . As defined in the problem formulation section 5.2.3, the conditions of the flight phases Cruise (cr), Takeoff (to) and Climb (cl) are applied to the LF and HF simulations yielding with the respective outputs  $\mathbf{f}^{(cr)}(\mathbf{r}, \chi)$ ,  $\mathbf{f}^{(to)}(\mathbf{r}, \chi)$  and  $\mathbf{f}^{(cl)}(\mathbf{r}, \chi)$ . Therefore, there are as many scalar quantities as there are operation point outputs  $\eta_p^{(cr)}$ ,  $\eta_p^{(to)}$  and  $\eta_p^{(cl)}$ , for each level of simulation fidelity. The condensation operation used to integrate the full-field outputs are the functionals  $\mathcal{J}(\cdot)$  for the objective, and  $c(\cdot)$  for the constraint, as illustrated Figure 5.13.

The final scalar efficiency is evaluated for the three flight phases, climb, cruise and take-off as

$$\eta_p(\chi) = w^{(cl)} \mathcal{J}(\mathbf{f}^{(cl)}(\mathbf{r}, \chi)) + w^{(cr)} \mathcal{J}(\mathbf{f}^{(cr)}(\mathbf{r}, \chi)) + w^{(to)} \mathcal{J}(\mathbf{f}^{(to)}(\mathbf{r}, \chi)), \quad (5.9)$$

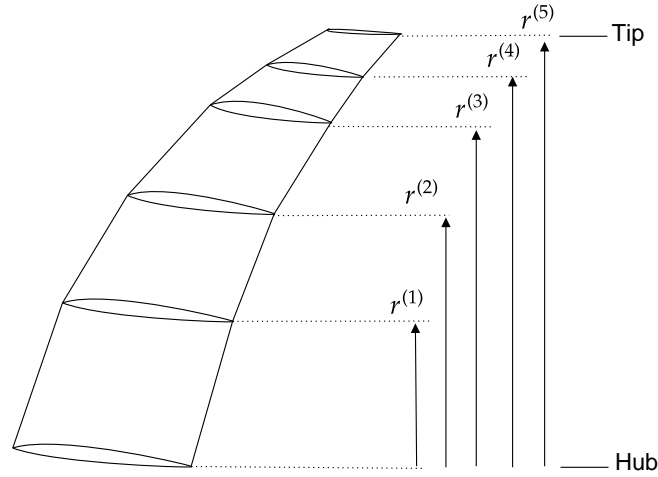


Figure 5.12: Illustration of the blade sections reconstruction from  $n_r$  sections ( $n_r = 5$  in this example)

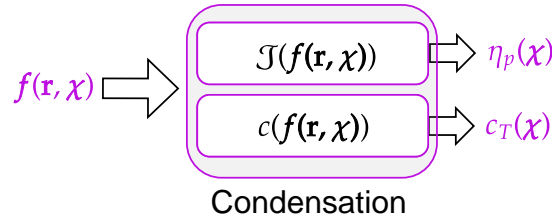


Figure 5.13: The condensation step : from input  $\mathbf{f}(\mathbf{r}, \boldsymbol{\chi})$  to the scalars quantities of interest  $\eta_p(\boldsymbol{\chi})$  and  $c_T(\boldsymbol{\chi})$ .

where the corresponding condensation of a given vector output  $\mathbf{f}(\mathbf{r}, \boldsymbol{\chi})$  is defined by

$$\mathcal{J}(\mathbf{f}(\mathbf{r}, \boldsymbol{\chi})) = \mathcal{J}(\boldsymbol{\eta}(\mathbf{r}, \boldsymbol{\chi})) = \sum_{j=1}^{n_r} \eta(r_j, \boldsymbol{\chi}), \quad (5.10)$$

and constraint

$$C_T(\boldsymbol{\chi}) = w^{(cl)} c(\mathbf{f}^{(cl)}(\mathbf{r}, \boldsymbol{\chi})) + w^{(cr)} c(\mathbf{f}^{(cr)}(\mathbf{r}, \boldsymbol{\chi})) + w^{(to)} c(\mathbf{f}^{(to)}(\mathbf{r}, \boldsymbol{\chi})), \quad (5.11)$$

where the condensation functional is

$$c(\mathbf{f}(\mathbf{r}, \boldsymbol{\chi})) = c(\mathbf{T}(\mathbf{r}, \boldsymbol{\chi})) = \sum_{j=1}^{n_r} T(r_j, \boldsymbol{\chi}), \quad (5.12)$$

where  $\mathcal{J}$  and  $c$  are the condensation operations to compute a given  $\mathbf{f}(\mathbf{r}, \boldsymbol{\chi})$  representing the climb, cruise and take-off outputs,  $\mathbf{f}^{(cr)}(\mathbf{r}, \boldsymbol{\chi})$ ,  $\mathbf{f}^{(cl)}(\mathbf{r}, \boldsymbol{\chi})$  and  $\mathbf{f}^{(to)}(\mathbf{r}, \boldsymbol{\chi})$ , respectively,  $\mathbf{r}$  is the set of points defining the discretization along the radial direction of the blade,  $\boldsymbol{\chi}$  the design variable,  $\boldsymbol{\chi} \in \mathcal{D} \subset \mathbb{R}^d$ , the design variables, with  $d = 16$  and  $\boldsymbol{\chi}^*$  is the optimum configuration of the objective function  $\eta_p(\boldsymbol{\chi}) \in \mathbb{R}$  with respect to the constraint  $C_T(\boldsymbol{\chi})$ .

The MFNIRB SBO can then be implemented and the main objective is to provide additional elements to understand the physical meaning of a MF projection. For example, that can

be difficult features there are not captured only by the LF representation. The analytical results of Chapter 3 and 4 may be linked to the different physical QoI and features that the MF representation bring to the LF compared to the HF RANS QoI.

## 5.4 Conclusion

This chapter presented a way to adapt the available LF and HF simulations to achieve a MF representation dedicated to solve an industrial-scale shape optimization problem. The MFNIRB described in chapter 3 and 4 was applied on the specific configuration of the Open Fan shape optimization. To this end, the method was adapted by yielding HF and LF configurations with similar spatial position output to perform the MF projection. Other ways of using the different mesh outputs can be explored and compared in future work. In addition, a condensation method to evaluate the performances quantities to optimize was required to apply the MFNIRB. Future applications of this approach can be generalized to similar turbomachinery applications. However, in general, CFD applications, the condensation needs the available post-processing implementation to obtain the scalars quantities from the simulation outputs. Such operation will at least require access to the post-processing part of the simulation codes.

# Chapter 6

## Conclusion

This thesis develops and applies Multi-Fidelity (MF) optimization techniques that are potentially applicable to the design of engineering systems as long as their physical behavior can be evaluated at different fidelity levels. The methods focus on Surrogate Based-Optimization (SBO) in multi-fidelity setting with online enrichment. The work presented in this thesis addresses problems where knowledge of the full field can bring additional accuracy to the solution, illustrated by a representative bi-fidelity analytical problem and industrialized SBO implementation from models of interest to aerodynamic engineers.

### 6.1 Outcomes

A literature review was conducted to address simulation cost issues in optimizing physical systems modeled with computer codes. It allows identifying the existing construction methods of surrogate models based on sequentially updated Design of Experiment (DoE). Scalar, vector, and multi-fidelity surrogates, along with their associated infill strategies, are included. Surrogate vectorial multi-fidelity models based on reduced-order approaches appeared promising for the control of the overall simulation budget. The survey also highlighted the impact of the correlation between the Low-Fidelity (LF) (supposed cheap) and High-Fidelity (HF) (supposed expensive) simulators, and their Central Processing Unit (CPU) cost ratio on the accuracy of the resulting multi-fidelity model. The development of dedicated infill techniques requires criteria for both the new site's choice and the corresponding simulation's fidelity level.

These ideas guided the present work to develop the multi-fidelity model and a corresponding enrichment strategy. The proposed methodology extends the non-intrusive Proper Orthogonal Decomposition (POD) on two levels. On the level of the field approximation, the regression of POD coefficients is replaced by a projection of LF solutions on the HF basis. On the level of quantities of interest, the interpolation property is enforced by Gaussian Process (Kriging). The statistical enrichment criteria were adapted to account for the violation of constraints such as the Probability of Improvement (PI) and the Expected Improvement (EI) criteria. The scheme was tested on a bi-fidelity benchmark case derived representative of aeronautical problems. The convergence study showed comparable performances for both multi- and single-fidelity models and was followed up with additional tests on an adapted test function with a parameterized correlation between low and high-fidelity outputs. As expected, the correlation showed a non-negligible impact on optimization performance.

Different experiments were presented for a better understanding of optimization of the proposed MFNIRB multi-fidelity model. First, a comparison between the infill criteria showed in section 4.3.3.1, a different convergence according to exploration, exploitation, and a better balance between exploration and exploitation with  $EI_w$ . This criterion was chosen to conduct the experiment in section 4.3.3.2, which compares the convergence of single and multi-fidelity models, and showed better convergence for MFNIRB on poorly explored DoE and comparable performance for an initially highly explored DoE. Finally, the chosen criterion is studied to understand the relative impact of Probability of Feasibility (PF) of the constraints, and EI. This allows investigation if the approximation is a driver of an optimal infill procedure, and what are the origins for the limitations of multi-fidelity Kriging-based optimization. An analysis was conducted in section 4.3.3.4 to compare different LF-HF ratios introducing the multi-level extension of MFNIRB employing Non-Intrusive Proper Orthogonal Decomposition (NIPOD) approximation of the LF data. It was concluded that the ratio and the HF basis truncation have an impact on the optimization performances. The results between different ratios also depend on the truncation level of the HF basis. Therefore, in the next section, truncation was evaluated at each iteration by minimizing the residual error. It was observed that there are limitations to the use of the LF when representing the HF vectors. A limited number of HF modes is sufficient to construct a MF vector close to the HF. Improving the reduced basis is not always possible if only HF outputs are used. Future work could incorporate LF to improve the orthogonal reduced basis. Finally, analyses of the impact of the LF-HF ratio are presented, as well as preliminary results of multi-level fidelity enrichment versus single-level fidelity enrichment. The final study showed the potential convergence of multi-level enrichment. However, the application on such an benchmark test case, does not show a significant difference between the multi-level and single level enriched model.

The chapter 5 deployed the proposed methodology on an industrial scale problem. The two available fidelity models have different field output sizes. The MFNIRB application imposed an adaptation of the different discretizations. Moreover, a condensation was proposed to evaluate the scalar quantities to be optimized from the full-field outputs. In such industrial context, this step is not usually provided to the user, however, is required to build the MFNIRB metamodel.

## 6.2 Perspectives

The perspectives for developing multi-fidelity approaches are threefold: improvement of algorithms, validation procedures, and industrial implementation.

The present work is based on the POD modes issued from HF simulations only. However, additional information from the LF simulations might be aggregated to the POD basis, in the spirit of different formulations proposed in [Benamara et al., 2016]’s work. An important research topic concerns the enrichment criteria that should be further developed to better account for the probability of feasibility of optimization constraints. Also, the non-intrusive character of the present work, dictated by the industrial context, is a limitation. Further research can be extended to the intrusive cases when the simulator source code is available.

The enhancement of the validation phase requires a set of multi-fidelity benchmarks. Unfortunately, to our best knowledge, the full-field benchmarks are rare in the literature. These benchmarks should ideally involve such features as variable numbers of design parameters, an

adjustable correlation between HF and LF, and, potentially, multiple (more than two) levels of fidelity. The availability of such a widely accepted benchmark database is a necessity for the multi-fidelity optimization community. Developing a standardized set of test cases, representative of problems encountered in full-scale models, is also pre-eminent to compare different methods.

The deployment of a multi-fidelity approach in the industrial setting is not straightforward due to organizational concerns. Softwares implementing different fidelity levels might be available in independent company departments. LF and HF models are also potentially performed at non-overlapping design stages. Each optimization case implies the intervention of different numerical tools using different solvers, meshes, and post-processing, even for different levels of fidelity of the same model. These issues are, to a certain degree, similar to those encountered when implementing multidisciplinary optimization frameworks. Efficient deployment of a multi-fidelity strategy requires thus further research to rethink the flow of the design process.

# Bibliography

- [Alexandrov et al., 2000] Alexandrov, N., Lewis, R., Gumbert, C., Alex, N., Green, L., & Newman, P. (2000). Optimization with variable-fidelity models applied to wing design. 2000. <https://doi.org/10.2514/6.2000-841>
- [Alexandrov et al., 1998] Alexandrov, N. M., Dennis, J. E., Lewis, R. M., & Torczon, V. (1998). A trust-region framework for managing the use of approximation models in optimization. *Structural Optimization*, 15(1), 16–23. <https://doi.org/10.1007/BF01197433>
- [Alexandrov & Lewis, 2001] Alexandrov, N. M. & Lewis, R. M. (2001). An overview of first-order model management for engineering optimization.
- [Alexandrov et al., 2001] Alexandrov, N. M., Lewis, R. M., Gumbert, C. R., Green, L. L., & Newman, P. A. (2001). Approximation and Model Management in Aerodynamic Optimization with Variable-Fidelity Models. *Journal of Aircraft*, 38(6), 1093–1101.
- [Amabili & Touzé, 2007] Amabili, M. & Touzé, C. (2007). Reduced-order models for nonlinear vibrations of fluid-filled circular cylindrical shells: Comparison of POD and asymptotic nonlinear normal modes methods. *Journal of Fluids and Structures*, 23(6), 885–903. <https://doi.org/10.1016/j.jfluidstructs.2006.12.004>
- [Amsallem et al., 2013] Amsallem, D., Deolalikar, S., Gurrola, F., & Farhat, C. (2013). Model Predictive Control under Coupled Fluid-Structure Constraints Using a Database of Reduced-Order Models on a Tablet. *21st AIAA Computational Fluid Dynamics Conference*. <https://doi.org/10.2514/6.2013-2588>
- [Amsallem et al., 2012] Amsallem, D., Zahr, M. J., & Farhat, C. (2012). Nonlinear model order reduction based on local reduced-order bases. *International Journal for Numerical Methods in Engineering*, 92(10), 891–916.
- [Arabnia, 2012] Arabnia, M. (2012). *Aerodynamic Shape Optimization of Axial Turbines in Three Dimensional Flow*. Concordia University. <https://spectrum.library.concordia.ca/973693/>
- [Aubry et al., 1988] Aubry, N., Holmes, P., Lumley, J., & Stone, E. (1988). The dynamics of coherent structures in the wall region of a turbulent boundary layer. *Journal of Fluid Mechanics*, 192, 115–173.
- [Audouze et al., 2013] Audouze, C., De Vuyst, F., & Nair, P. B. (2013). Nonintrusive reduced-order modeling of parametrized time-dependent partial differential equations. *Numerical Methods for Partial Differential Equations*, 29(5), 1587–1628. <https://doi.org/10.1002/num.21768>

- [Auer, 2002] Auer, P. (2002). Using confidence bounds for exploitation-exploration trade-offs. *Journal of Machine Learning Research*, 3, 397–422. <https://doi.org/10.1162/153244303321897663>
- [Bagheri et al., 2017] Bagheri, S., Konen, W., Allmendinger, R., Branke, J., Deb, K., Fieldsend, J., Quagliarella, D., & Sindhya, K. (2017). Constraint handling in efficient global optimization. *Proceedings of the Genetic and Evolutionary Computation Conference on - GECCO '17*, 673–680.
- [Bai, 2002] Bai, Z. (2002). Krylov subspace techniques for reduced-order modeling of large-scale dynamical systems. *Applied Numerical Mathematics*, 43(1), 9–44. [https://doi.org/https://doi.org/10.1016/S0168-9274\(02\)00116-2](https://doi.org/https://doi.org/10.1016/S0168-9274(02)00116-2). 19th Dundee Biennial Conference on Numerical Analysis
- [Bakr et al., 2000] Bakr, M. H., Bandler, J. W., Madsen, K., & Søndergaard, J. (2000). Review of the Space Mapping Approach to Engineering Optimization and Modeling. 36.
- [Balabanov et al., 1998] Balabanov, V., Haftka, R., Grossman, B., Mason, W., & Watson, L. (1998). Multifidelity response surface model for hsct wing bending material weight. <https://doi.org/10.2514/6.1998-4804>
- [Bandler et al., 2004] Bandler, J., Cheng, Q., Dakroury, S., Mohamed, A., Bakr, M., Madsen, K., & Søndergaard, J. (2004). Space Mapping: The State of the Art. *IEEE Transactions on Microwave Theory and Techniques*, 52(1), 337–361. <https://doi.org/10.1109/TMTT.2003.820904>
- [Baur et al., 2011] Baur, U., Beattie, C., Benner, P., & Gugercin, S. (2011). Interpolatory Projection Methods for Parameterized Model Reduction. *SIAM Journal on Scientific Computing*, 33(5), 2489–2518. <https://doi.org/10.1137/090776925>
- [Ben Salem, 2018] Ben Salem, M. (2018). *Model selection and adaptive sampling in surrogate modeling: Kriging and beyond*. UNIVERSITE DE LYON. <https://tel.archives-ouvertes.fr/tel-03097719>
- [Benamara, 2017] Benamara, T. (2017). *Full-field Multi-Fidelity Surrogate Models for Optimal Design of Turbomachines*.
- [Benamara et al., 2016] Benamara, T., Breitkopf, P., Lepot, I., & Sainvitu, C. (2016). Adaptive infill sampling criterion for multi-fidelity optimization based on Gappy-POD: Application to the flight domain study of a transonic airfoil. *Structural and Multidisciplinary Optimization*, 54(4), 843–855. <http://link.springer.com/10.1007/s00158-016-1440-3>
- [Benamara et al., 2017] Benamara, T., Breitkopf, P., Lepot, I., Sainvitu, C., & Villon, P. (2017). Multi-fidelity POD surrogate-assisted optimization: Concept and aero-design study. *Structural and Multidisciplinary Optimization*, 56(6), 1387–1412.
- [Benner et al., 2015] Benner, P., Gugercin, S., & Willcox, K. (2015). A survey of projection-based model reduction methods for parametric dynamical systems. *SIAM Review*, 57, 483–531. <https://doi.org/10.1137/130932715>

- [Bergmann & Cordier, 2007] Bergmann, M. & Cordier, L. (2007). Contrôle optimal par réduction de modèle POD et méthode à région de confiance du sillage laminaire d'un cylindre circulaire. *Mécanique & Industries*, 8(2), 111–118. <https://doi.org/10.1051/meca:2007028>
- [Berkooz et al., 2003] Berkooz, G., Holmes, P., & Lumley, J. (2003). The proper orthogonal decomposition in the analysis of turbulent flows. *Annual Review of Fluid Mechanics*, 25, 539–575. <https://doi.org/10.1146/annurev.fl.25.010193.002543>
- [Bjorkman, 2001] Bjorkman, M. (2001). Global Optimization of Costly Nonconvex Functions Using Radial Basis Functions. *Optimization and engineering*, 25.
- [Boopathy & Rumpfkeil, 2013] Boopathy, K. & Rumpfkeil, M. (2013). A multivariate interpolation and regression enhanced kriging surrogate model. *21st AIAA Computational Fluid Dynamics Conference*.
- [Box & Behnken, 1960] Box, G. E. P. & Behnken, D. W. (1960). Some new three level designs for the study of quantitative variables. *Technometrics*, 2(4), 455–475. <http://www.jstor.org/stable/1266454>
- [Braconnier et al., 2011] Braconnier, T., Ferrier, M., Jouhaud, J.-C., Montagnac, M., & Sagaut, P. (2011). Towards an adaptive POD/SVD surrogate model for aeronautic design. *Computers & Fluids*, 40(1), 195–209. <https://doi.org/10.1016/j.compfluid.2010.09.002>
- [Brochu et al., 2010] Brochu, E., Cora, V. M., & de Freitas, N. (2010). A Tutorial on Bayesian Optimization of Expensive Cost Functions, with Application to Active User Modeling and Hierarchical Reinforcement Learning. *arXiv:1012.2599 [cs]*. <http://arxiv.org/abs/1012.2599>. arXiv: 1012.2599
- [Brouckaert, 2015] Brouckaert, J.-F. (2015). *Engine demonstration programmes in clean sky & clean sky 2*. [https://www.cleansky.eu/sites/default/files/inline-files/Jean-Francois%20Brouckaert%20ENGINES-Aerodays-2015\\_final.pdf](https://www.cleansky.eu/sites/default/files/inline-files/Jean-Francois%20Brouckaert%20ENGINES-Aerodays-2015_final.pdf).
- [Bui-Thanh et al., 2004] Bui-Thanh, T., Damodaran, M., & Willcox, K. (2004). Aerodynamic Data Reconstruction and Inverse Design Using Proper Orthogonal Decomposition. *AIAA Journal*, 42(8), 1505–1516. <https://doi.org/10.2514/1.2159>
- [Bui-Thanh et al., 2008] Bui-Thanh, T., Willcox, K., & Ghattas, O. (2008). Model Reduction for Large-Scale Systems with High-Dimensional Parametric Input Space. *SIAM Journal on Scientific Computing*, 30(6), 3270–3288. <http://epubs.siam.org/doi/10.1137/070694855>
- [Bunnell et al., 2021] Bunnell, S., Gorrell, S., & Salmon, J. (2021). Multi-fidelity surrogates from shared principal components: Application to structural design exploration and optimization. *Structural and Multidisciplinary Optimization*. <https://doi.org/10.1007/s00158-020-02793-z>
- [Béchet et al., 2011] Béchet, S., Negulescu, C., Chapin, V., & Simon, F. (2011). Integration of cfd tools in aerodynamic design of contra-rotating propellers blades.

- [Cai et al., 2017] Cai, X., Qiu, H., Gao, L., Wei, L., & Shao, X. (2017). Adaptive radial-basis-function-based multifidelity metamodeling for expensive black-box problems. *AIAA Journal*, 55, 1–13. <https://doi.org/10.2514/1.J055649>
- [Cambier & Gazaix, 2012] Cambier, L. & Gazaix, M. (2012). *elsA - An efficient object-oriented solution to CFD complexity*. <https://doi.org/10.2514/6.2002-108>
- [Carlberg & Farhat, 2008] Carlberg, K. & Farhat, C. (2008). A Compact Proper Orthogonal Decomposition Basis for Optimization-Oriented Reduced-Order Models. *12th AIAA/ISSMO Multidisciplinary Analysis and Optimization Conference*. <http://arc.aiaa.org/doi/10.2514/6.2008-5964>
- [Chakir & Maday, 2009] Chakir, R. & Maday, Y. (2009). Une méthode combinée d'éléments finis à deux grilles/bases réduites pour l'approximation des solutions d'une E.D.P. paramétrique. *Comptes Rendus Mathématique*, 347(7-8), 435–440. <https://linkinghub.elsevier.com/retrieve/pii/S1631073X09000740>
- [Chang et al., 1993] Chang, K. J., Haftka, R. T., Giles, G. L., & Kao, P.-J. (1993). Sensitivity-based scaling for approximating structural response. *Journal of Aircraft*, 30(2), 283–288. <https://doi.org/10.2514/3.48278>
- [Cheng & Titterton, 1994] Cheng, B. & Titterton, D. M. (1994). Neural networks: A review from a statistical perspective. *Statistical Science*, 9(1), 2–30. <http://www.jstor.org/stable/2246275>
- [Cheng et al., 2016] Cheng, C., Peng, Z., Zhang, W., & Meng, G. (2016). Volterra-series-based nonlinear system modeling and its engineering applications: A state-of-the-art review. *Mechanical Systems and Signal Processing*, 87. <https://doi.org/10.1016/j.ymsp.2016.10.029>
- [Cheng et al., 2019] Cheng, K., Lu, Z., & Zhen, Y. (2019). Multi-level multi-fidelity sparse polynomial chaos expansion based on gaussian process regression. *Computer Methods in Applied Mechanics and Engineering*, 349, 360 – 377. <https://doi.org/https://doi.org/10.1016/j.cma.2019.02.021>
- [Chinesta et al., 2011] Chinesta, F., Ladeveze, P., & Cueto, E. (2011). A Short Review on Model Order Reduction Based on Proper Generalized Decomposition. *Archives of Computational Methods in Engineering*, 18(4), 395–404. <http://link.springer.com/10.1007/s11831-011-9064-7>
- [Chocat et al., 2015] Chocat, R., Brevault, L., Balesdent, M., & Defoort, S. (2015). Modified Covariance Matrix Adaptation – Evolution Strategy algorithm for constrained optimization under uncertainty, application to rocket design. *International Journal for Simulation and Multidisciplinary Design Optimization*, 6, A1. <https://doi.org/10.1051/smdo/2015001>
- [Choi et al., 2009a] Choi, S., Alonso, J. J., & Kroo, I. M. (2009a). Two-level multifidelity design optimization studies for supersonic jets. *Journal of Aircraft*, 46(3), 776–790. <https://doi.org/10.2514/1.34362>
- [Choi et al., 2009b] Choi, S., Alonso, J. J., & Kroo, I. M. (2009b). Two-level multifidelity design optimization studies for supersonic jets. *Journal of Aircraft*, (46.3), 776–790.

- [Choi et al., 2020] Choi, Y., Boncoraglio, G., Anderson, S., Amsallem, D., & Farhat, C. (2020). Gradient-based constrained optimization using a database of linear reduced-order models. *Journal of Computational Physics*, 423, 109787. <https://doi.org/https://doi.org/10.1016/j.jcp.2020.109787>
- [Chopade et al., 2021] Chopade, J., Ganvir, K., & Tiwari, H. (2021). Detection of an explosive material in landmine, aqueous and air medium through sensor operated unmanned guided vehicle. *IOP Conference Series: Materials Science and Engineering*, 1012, 012026. <https://doi.org/10.1088/1757-899X/1012/1/012026>
- [Chowdhury et al., 2013] Chowdhury, S., Mehmani, A., & Messac, A. (2013). Quantifying regional error in surrogates by modeling its relationship with sample density. <https://doi.org/10.2514/6.2013-1751>
- [Cinquegrana & Iuliano, 2015] Cinquegrana, D. & Iuliano, E. (2015). Efficient global optimization method for a multipoint airfoil design.
- [Coelho et al., 2008] Coelho, R., Breitkopf, P., & Knopf-Lenoir, C. (2008). Reduced models for coupled aerodynamic and structural optimization of a flexible wing.
- [Coelho et al., 2010a] Coelho, R., Breitkopf, P., Knopf-Lenoir, C., & Villon, P. (2010a). Bi-level model reduction for coupled problems :application to a 3d wing. *Structural and Multidisciplinary Optimization*, 39. <https://doi.org/10.1007/s00158-008-0335-3>
- [Coelho et al., 2010b] Coelho, R., Breitkopf, P., Knopf-Lenoir, C., & Villon, P. (2010b). Bi-level model reduction for coupled problems :application to a 3d wing. *Structural and Multidisciplinary Optimization*, 39. <https://doi.org/10.1007/s00158-008-0335-3>
- [Coelho & Pierret, 2017] Coelho, R. F. & Pierret, S. (2017). Optimisation aéromécanique d'aubes de turbomachines dans le cadre du projet européen VIVACE. 7.
- [Cohen et al., 2006] Cohen, K., Siegel, S., & McLaughlin, T. (2006). A heuristic approach to effective sensor placement for modeling of a cylinder wake. Volume 35, Issue 1, Pages 103–120.
- [Colomer et al., 2021] Colomer, J., Bartoli, N., Lefebvre, T., Martins, J., & Morlier, J. (2021). An mdo-based methodology for static aeroelastic scaling of wings under non-similar flow. *Structural and Multidisciplinary Optimization*. <https://doi.org/10.1007/s00158-020-02804-z>
- [Conn et al., 2009] Conn, A. R., Scheinberg, K., & Vicente, L. N. (2009). Global Convergence of General Derivative-Free Trust-Region Algorithms to First- and Second-Order Critical Points. *SIAM Journal on Optimization*, 20(1), 387–415. <https://doi.org/10.1137/060673424>
- [Courrier et al., 2016] Courrier, N., Boucard, P.-A., & Soulier, B. (2016). Variable-fidelity modeling of structural analysis of assemblies. *Journal of Global Optimization*, 64(3), 577–613.

- [Cozad et al., 2015] Cozad, A., Sahinidis, N. V., & Miller, D. C. (2015). A combined first-principles and data-driven approach to model building. *Computers & Chemical Engineering*, 73, 116–127. <https://doi.org/10.1016/j.compchemeng.2014.11.010>
- [Cressie, 1990] Cressie, N. (1990). The origins of kriging. *Mathematical Geology*, 22(3), 239–252. <https://doi.org/10.1007/BF00889887>
- [Currin et al., 1988] Currin, C., Mitchell, T., Morris, M., & Ylvisaker, D. (1988). A bayesian approach to the design and analysis of computer experiments. <https://www.osti.gov/biblio/6734087>
- [Currin et al., 1991] Currin, C., Mitchell, T., Morris, M., & Ylvisaker, D. (1991). Bayesian prediction of deterministic functions, with applications to the design and analysis of computer experiments. *Journal of the American Statistical Association*, 86(416), 953–963. <http://www.jstor.org/stable/2290511>
- [Dalle & Fidkowski, 2014] Dalle, D. J. & Fidkowski, K. (2014). Multifidelity airfoil shape optimization using adaptive meshing. *Journal of Aircraft*, (46.3), 776–790.
- [De Boor, 1978] De Boor, C. (1978). *A Practical Guide to Spline*, volume Volume 27. <https://doi.org/10.2307/2006241>
- [De Lozzo, 2013] De Lozzo, M. (2013). *Modèles de substitution spatio-temporels et multifidélité Application à l'ingénierie thermique*.
- [Deb, 2000] Deb, K. (2000). An efficient constraint handling method for genetic algorithms. *Comput. Methods Appl. Mech. Engrg.*, 28.
- [Deck et al., 2014] Deck, S., Gand, F., Brunet, V., & Khelil, S. (2014). High-fidelity simulations of unsteady civil aircraft aerodynamics: Stakes and perspectives. application of zonal detached eddy simulation. *Philosophical transactions. Series A, Mathematical, physical, and engineering sciences*, 372. <https://doi.org/10.1098/rsta.2013.0325>
- [Demange et al., 2016] Demange, J., Savill, A. M., & Kipouros, T. (2016). *A Multifidelity Multiobjective Optimization Framework for High-Lift Airfoils*. <https://doi.org/10.2514/6.2016-3367>
- [Du et al., 2019] Du, X., Ren, J., & Leifsson, L. (2019). Aerodynamic inverse design using multifidelity models and manifold mapping. *Aerospace Science and Technology*, 85, 371–385. <https://doi.org/10.1016/j.ast.2018.12.008>
- [Dupuis et al., 2018] Dupuis, R., Jouhaud, J.-C., & Sagaut, P. (2018). Surrogate Modeling of Aerodynamic Simulations for Multiple Operating Conditions Using Machine Learning. *AIAA Journal*, 56(9), 3622–3635. <https://doi.org/10.2514/1.J056405>
- [Durantin et al., 2016] Durantin, C., Rouxel, J., Desideri, J.-A., & Gliere, A. (2016). Optimization of photoacoustics gas sensor using multifidelity RBF metamodeling. *Proceedings of the VII European Congress on Computational Methods in Applied Sciences and Engineering (ECCOMAS Congress 2016)*, 6250–6259.

- [Durantin et al., 2017] Durantin, C., Rouxel, J., Désidéri, J.-A., & Glière, A. (2017). Multifidelity surrogate modeling based on radial basis functions. *Structural and Multidisciplinary Optimization*, 56(5), 1061–1075. <https://doi.org/10.1007/s00158-017-1703-7>
- [Duta et al., 2007] Duta, M., Shahpar, S., & Giles, M. (2007). Turbomachinery design optimization using automatic differentiated adjoint code.
- [Dutta et al., 2021] Dutta, S., Farthing, M., Perracchione, E., Savant, G., & Putti, M. (2021). A greedy non-intrusive reduced order model for shallow water equations. *Journal of Computational Physics*, 439. <https://doi.org/10.1016/j.jcp.2021.110378>
- [Dyn et al., 1986] Dyn, N., Levin, D., & Rippa, S. (1986). Numerical procedures for surface fitting of scattered data by radial functions. *SIAM Journal on Scientific and Statistical Computing*, 7. <https://doi.org/10.1137/0907043>
- [Efron, 1979] Efron, B. (1979). Bootstrap methods: Another look at the jackknife. *The Annals of Statistics*, 7(1), 1–26. <http://www.jstor.org/stable/2958830>
- [Everson & Sirovich, 1995] Everson, R. & Sirovich, L. (1995). Karhunen–loève procedure for gappy data. *JOSA A*, 12. <https://doi.org/10.1364/JOSAA.12.001657>
- [Farin, 2002] Farin, G. (2002). 6 - bézier curve topics. *Curves and Surfaces for CAGD (Fifth Edition)*, The Morgan Kaufmann Series in Computer Graphics, 81–93. Morgan Kaufmann, (fifth edition ed.). <https://doi.org/https://doi.org/10.1016/B978-155860737-8/50006-5>
- [Feliot et al., 2017] Feliot, P., Bect, J., & Vazquez, E. (2017). A bayesian approach to constrained single-and multi-objective optimization. *Journal of Global Optimization*, 67(1-2), 97–133.
- [Fernández-Godino et al., 2016] Fernández-Godino, M. G., Park, C., Kim, N.-H., & Haftka, R. T. (2016). Review of multi-fidelity models. 41.
- [Forrester & Keane, 2009] Forrester, A. I. & Keane, A. J. (2009). Recent advances in surrogate-based optimization. *Progress in Aerospace Sciences*, 45(1-3), 50–79. <https://doi.org/10.1016/j.paerosci.2008.11.001>
- [Forrester et al., 2007] Forrester, A. I., Sóbester, A., & Keane, A. J. (2007). Multi-fidelity optimization via surrogate modelling. *Proceedings of the Royal Society A: Mathematical, Physical and Engineering Sciences*, 463(2088), 3251–3269. <http://www.royalsocietypublishing.org/doi/10.1098/rspa.2007.1900>
- [Froude, 1878] Froude, W. (1878). On the elementary relation between pitch, slip and propulsive efficiency. *Inst. Naval Arch.*, 19, 47–57.
- [Gallard, 2014] Gallard, F. (2014). *Aircraft shape optimization for mission performance*.
- [Galvan et al., 2003] Galvan, B., D., G., J., P., Sefrioui, M., & Winter, G. (2003). Parallel evolutionary computation for solving complex cfd optimization problems : A review and some nozzle applications. *Parallel Computational Fluid Dynamics 2002*, 573–604. North-Holland. <https://doi.org/https://doi.org/10.1016/B978-044450680-1/50072-3>

- [Giselle Fernández-Godino et al., 2019] Giselle Fernández-Godino, M., Park, C., Kim, N. H., & Haftka, R. T. (2019). Issues in Deciding Whether to Use Multifidelity Surrogates. *AIAA Journal*, 57(5), 2039–2054. <https://doi.org/10.2514/1.J057750>
- [Giunta et al., 2007] Giunta, A., Golivodov, O., Knill, D., Grossman, B., Mason, W., Watson, L., & Haftka, R. (2007). *Multidisciplinary design optimization of advanced aircraft configurations*, volume 490, 14–34. <https://doi.org/10.1007/BFb0107076>
- [Giunta et al., 2003] Giunta, A., Wojtkiewicz, S., & Eldred, M. (2003). Overview of Modern Design of Experiments Methods for Computational Simulations (Invited). *41st Aerospace Sciences Meeting and Exhibit*. <https://doi.org/10.2514/6.2003-649>
- [Glauert, 1983] Glauert, H. (1983). *The Elements of Aerofoil and Airscrew Theory*. Cambridge Science Classics. Cambridge University Press. <https://doi.org/10.1017/CBO9780511574481>
- [Glover, 1989] Glover, F. (1989). Tabu search-part i. *ORSA Journal on Computing*, 1(3), 190–206. <https://doi.org/10.1287/ijoc.1.3.190>
- [Goel et al., 2007] Goel, T., Haftka, R., Shyy, W., & Queipo, N. (2007). Ensemble of surrogates. *Structural and Multidisciplinary Optimization*, 33, 199–216. <https://doi.org/10.1007/s00158-006-0051-9>
- [Gruber et al., 2015] Gruber, M., Lonfils, T., Dumont, C., Vion, L., Dubois, A., & Williams, T. (2015). On the fast prediction of open rotor tonal interaction noise. V02BT41A006. <https://doi.org/10.1115/GT2015-42579>
- [Guermond, 1990] Guermond, J.-L. (1990). A generalized lifting-line theory for curved and swept wings. *Journal of Fluid Mechanics*, 211, 497–513.
- [Gunes et al., 1997] Gunes, H., Liakopoulos, A., & Sahan, R. (1997). Low-dimensional description of oscillatory thermal convection: The small prandtl number limit. *Theoretical and Computational Fluid Dynamics*, 9, 1–16. <https://doi.org/10.1007/s001620050028>
- [Guo et al., 2021] Guo, Q., Hang, J., Wang, S., Hui, W., & Xie, Z. (2021). Design optimization of variable stiffness composites by using multi-fidelity surrogate models. *Structural and Multidisciplinary Optimization*, 63(1), 439–461. <https://doi.org/10.1007/s00158-020-02684-3>
- [Gur & Rosen, 2008] Gur, O. & Rosen, A. (2008). Comparison between blade-element models of propellers. *The Aeronautical Journal*, 112, 689–704. <https://doi.org/10.1017/S0001924000002669>
- [Gutmann, 2001] Gutmann, H.-M. (2001). A Radial Basis Function Method for Global Optimization. *Journal of Global Optimization*, 27.
- [Guy Norris, 2021] Guy Norris (2021). *Cfm unveils 'open fan' demonstrator plan for next-gen engine*. URL: <https://aviationweek.com/aerospace/cfm-unveils-open-fan-demonstrator-plan-next-gen-engine?elq2=4131999b257444b98241708cfa00955a>.

- [Guénot et al., 2013] Guénot, M., Lepot, I., Sainvitu, C., Goblet, J., & Filomeno Coelho, R. (2013). Adaptive sampling strategies for non-intrusive POD-based surrogates. *Engineering Computations*, 30(4), 521–547. <https://doi.org/10.1108/02644401311329352>
- [Görtz et al., 2013] Görtz, S., Zimmermann, R., & Han, Z.-H. (2013). *Variable-Fidelity and Reduced-Order Models for Aero Data for Loads Predictions*, volume 123, 99–112. <https://doi.org/10.1007/978-3-642-38877-4-8>
- [Haftka, 1991] Haftka, R. (1991). Combining global and local approximations. *AIAA Journal*, 29, 1523–1525. <https://doi.org/10.2514/3.10768>
- [Hall et al., 2002] Hall, K. C., Thomas, J. P., & Clark, W. S. (2002). Computation of unsteady nonlinear flows in cascades using a harmonic balance technique. *AIAA Journal*, 40(5), 879–886. <https://doi.org/10.2514/2.1754>
- [Halton, 1960] Halton, J. (1960). On the efficiency of certain quasi-random sequences of points in evaluating multi-dimensional integrals. *Numerische Mathematik*, 2, 84–90.
- [Hampton & Doostan, 2018] Hampton, J. & Doostan, A. (2018). Basis adaptive sample efficient polynomial chaos (BASE-PC). *Journal of Computational Physics*, 371, 20–49. <https://doi.org/10.1016/j.jcp.2018.03.035>
- [Han & Görtz, 2012] Han, Z.-H. & Görtz, S. (2012). Hierarchical kriging model for variable-fidelity surrogate modeling. *AIAA Journal*, 50(9), 1885–1896. <https://doi.org/10.2514/1.J051354>
- [Han et al., 2020] Han, Z.-H., Xu, C.-Z., Liang, Z., Zhang, Y., Ke-Shi, Z., & Song, W.-P. (2020). Efficient aerodynamic shape optimization using variable-fidelity surrogate models and multilevel computational grids.
- [Han & Zhang, 2012] Han, Z.-H. & Zhang, K.-S. (2012). Surrogate-Based Optimization. 21.
- [Hao et al., 2020] Hao, P., Feng, S., Li, Y., Wang, B., & Chen, H. (2020). Adaptive infill sampling criterion for multi-fidelity gradient-enhanced kriging model. *Structural and Multidisciplinary Optimization*, 62(1), 353–373. <https://doi.org/10.1007/s00158-020-02493-8>
- [He et al., 2021] He, Y., Sun, J., Song, P., & Wang, X. (2021). Variable-fidelity expected improvement based efficient global optimization of expensive problems in presence of simulation failures and its parallelization. *Aerospace Science and Technology*, 111, 106572. <https://doi.org/https://doi.org/10.1016/j.ast.2021.106572>
- [Hennig & Schuler, 2011] Hennig, P. & Schuler, C. (2011). Entropy search for information-efficient global optimization. *Journal of Machine Learning Research*, 13.
- [Hirsch, 2007] Hirsch, C. (2007). Numerical computation of internal and external flows: The fundamentals of computational fluid dynamics. *Numerical Computation of Internal and External Flows: The Fundamentals of Computational Fluid Dynamics*. <https://doi.org/10.1016/B978-0-7506-6594-0.X5037-1>

- [Hu et al., 2018] Hu, J., Yang, Y., Zhou, Q., Jiang, P., Shao, X., Shu, L., & Zhang, Y. (2018). Comparative studies of error metrics in variable fidelity model uncertainty quantification. *Journal of Engineering Design*, 29(8-9), 512–538. <https://doi.org/10.1080/09544828.2018.1513126>
- [Huang et al., 2006a] Huang, D., Allen, T. T., Notz, W. I., & Miller, R. A. (2006a). Sequential kriging optimization using multiple-fidelity evaluations. *Structural and Multidisciplinary Optimization*, 32(5), 369–382. <https://doi.org/10.1007/s00158-005-0587-0>
- [Huang et al., 2006b] Huang, D., Allen, T. T., Notz, W. I., & Zeng, N. (2006b). Global Optimization of Stochastic Black-Box Systems via Sequential Kriging Meta-Models. *Journal of Global Optimization*, 34(3), 441–466. <https://doi.org/10.1007/s10898-005-2454-3>
- [Huang et al., 2015] Huang, E., Xu, J., Zhang, S., & Chen, C.-H. (2015). Multi-fidelity Model Integration for Engineering Design. *Procedia Computer Science*, 44, 336–344. <https://doi.org/10.1016/j.procs.2015.03.002>
- [Hutchison et al., 1994] Hutchison, M. G., Unger, E. R., Mason, W. H., Grossman, B., & Haftka, R. T. (1994). Variable-complexity aerodynamic optimization of a high-speed civil transport wing. *Journal of Aircraft*, 31(1), 110–116. <https://doi.org/10.2514/3.46462>
- [ICSA, 2019] ICSA (2019). *Icsa's vision for a "Zero Climate Impact" international aviation pathway towards 2050*. [https://www.icao.int/Meetings/a40/Documents/WP/wp\\_561\\_en.pdf](https://www.icao.int/Meetings/a40/Documents/WP/wp_561_en.pdf).
- [Jameson, 2000] Jameson, A. (2000). An introduction to the adjoint approach to design. *Flow, Turbulence and Combustion*. <https://doi.org/https://doi.org/10.1023/A:1011430410075>
- [Jameson & Fatica, 2003] Jameson, A. & Fatica, M. (2003). Using computational fluid dynamics for aerodynamics.
- [Jameson et al., 2002] Jameson, A., Martinelli, L., & Vassberg, J. (2002). Using computational fluid dynamics for aerodynamics- a critical assessment.
- [Jiang et al., 2019] Jiang, P., Cheng, J., Zhou, Q., Shu, L., & Jiexiang, H. (2019). Variable-fidelity lower confidence bounding approach for engineering optimization problems with expensive simulations. *AIAA Journal*, 57, 1–15. <https://doi.org/10.2514/1.J058283>
- [Jolliffe & Cadima, 2016] Jolliffe, I. T. & Cadima, J. (2016). Principal component analysis: a review and recent developments. *Philosophical Transactions of the Royal Society A: Mathematical, Physical and Engineering Sciences*, 374(2065), 20150202. <https://doi.org/10.1098/rsta.2015.0202>
- [Jones & Schonlau, 1998] Jones, D. R. & Schonlau, M. (1998). Efficient Global Optimization of Expensive Black-Box Functions. *Journal of Global Optimization*, 38.

- [Kandasamy et al., 2016] Kandasamy, K., Dasarathy, G., Oliva, J., Schneider, J., & Póczos, B. (2016). Multi-fidelity gaussian process bandit optimisation. *Journal of Artificial Intelligence Research*, 66. <https://doi.org/10.1613/jair.1.11288>
- [Kandasamy et al., 2017] Kandasamy, K., Krishnamurthy, A., Schneider, J., & Póczos, B. (2017). Asynchronous Parallel Bayesian Optimisation via Thompson Sampling. *arXiv:1705.09236 [cs, stat]*. <http://arxiv.org/abs/1705.09236>. arXiv: 1705.09236
- [Kast et al., 2019] Kast, M., Guo, M., & Hesthaven, J. S. (2019). A non-intrusive multifidelity method for the reduced order modeling of nonlinear problems.
- [Kennedy & Eberhart, 1995] Kennedy, J. & Eberhart, R. (1995). Particle swarm optimization. *Proceedings of ICNN'95 - International Conference on Neural Networks*, volume 4, 1942–1948 vol.4. <https://doi.org/10.1109/ICNN.1995.488968>
- [Kennedy, 2000] Kennedy, M. (2000). Predicting the output from a complex computer code when fast approximations are available. *Biometrika*, 87(1), 1–13. <https://doi.org/10.1093/biomet/87.1.1>
- [Khatouri et al., 2020] Khatouri, H., Benamara, T., Breikopf, P., Demange, J., & Feliot, P. (2020). Constrained multi-fidelity surrogate framework using Bayesian optimization with non-intrusive reduced-order basis. 23.
- [Kirkpatrick et al., 1983] Kirkpatrick, S., Gelatt, C. D., & Vecchi, M. P. (1983). Optimization by simulated annealing. *Science*, 220(4598), 671–680. <https://doi.org/10.1126/science.220.4598.671>
- [Kleijnen, 2009] Kleijnen, J. P. (2009). Kriging metamodeling in simulation: A review. *European Journal of Operational Research*, 192(3), 707–716. <https://doi.org/10.1016/j.ejor.2007.10.013>
- [Knill et al., 1999] Knill, D. L., Giunta, A. A., Baker, C. A., Grossman, B., Mason, W. H., Haftka, R. T., & Watson, L. T. (1999). Response surface models combining linear and euler aerodynamics for supersonic transport design. *Journal of Aircraft*, 36(1), 75–86. <https://doi.org/10.2514/2.2415>
- [Kohavi, 2001] Kohavi, R. (2001). A study of cross-validation and bootstrap for accuracy estimation and model selection. 14.
- [Kokoska & Zwillinger, 1999] Kokoska, S. & Zwillinger, D. (1999). Crc standard probability and statistics tables and formulae, student edition.
- [Kontogiannis et al., 2020] Kontogiannis, S. G., Demange, J., Savill, A. M., & Kipouros, T. (2020). A comparison study of two multifidelity methods for aerodynamic optimization. *Aerospace Science and Technology*, 97, 105592. <https://doi.org/10.1016/j.ast.2019.105592>
- [Krige, 1951] Krige, D. (1951). A statistical approach to some basic mine valuation problems on the witwatersand. *Journal of chemical, metallurgical and mining society of South Africa*.
- [Kuik, 2018] Kuik, G. (2018). *The fluid dynamic basis for actuator disc and rotor theories*. <https://doi.org/10.3233/978-1-61499-866-2-i>

- [LAAME-CROW, 2016] LAAME-CROW (2016). *Low-speed aeroacoustic advanced measurement for Contra-Rotating Open-Rotor (CROR) structure test, clean sky*. [https://www.icao.int/Meetings/a40/Documents/WP/wp\\_561\\_en.pdf](https://www.icao.int/Meetings/a40/Documents/WP/wp_561_en.pdf).
- [Lam et al., 2015] Lam, R., Allaire, D. L., & Willcox, K. E. (2015). Multifidelity Optimization using Statistical Surrogate Modeling for Non-Hierarchical Information Sources. *56th AIAA/ASCE/AHS/ASC Structures, Structural Dynamics, and Materials Conference*. <https://doi.org/10.2514/6.2015-0143>
- [Lancaster & Salkauskas, 1981] Lancaster, P. & Salkauskas, K. (1981). Surfaces generated by moving least squares methods. *Mathematics of Computation*, 37, 141–158.
- [Lataniotis et al., 2018] Lataniotis, C., Marelli, S., & Sudret, B. (2018). Extending classical surrogate modeling to ultrahigh dimensional problems through supervised dimensionality reduction: a data-driven approach. Technical report.
- [Le Gratiet, 2013] Le Gratiet, L. (2013). *Multi-fidelity Gaussian process regression for computer experiments*.
- [Le Gratiet & Garnier, 2014] Le Gratiet, L. & Garnier, J. (2014). Recursive co-kriging model for design of computer experiments with multiple levels of fidelity. *International Journal for Uncertainty Quantification*, 4(5), 365–386. <http://www.dl.begellhouse.com/journals/52034eb04b657aea,2f7b99cc281f2702,4c83626c5e64207a.html>
- [Le Quilliec et al., 2014] Le Quilliec, G., Raghavan, B., & Breitkopf, P. (2014). A manifold learning-based reduced order model for springback shape characterization and optimization in sheet metal forming. *Computer Methods in Applied Mechanics and Engineering*, 285, 621–638. <https://doi.org/10.1016/j.cma.2014.11.029>
- [Le Riche et al., 2020] Le Riche, R., Garland, N., Richet, Y., & Durrande, N. (2020). Multifidelity for MDO using Gaussian Processes. *Aerospace System Analysis and Optimization in Uncertainty*, volume 156 of *Springer Optimization and its Applications*, 295–320. Springer. [https://doi.org/10.1007/978-3-030-39126-3\\_8](https://doi.org/10.1007/978-3-030-39126-3_8)
- [Leborgne et al., 2015] Leborgne, M., Lonfils, T., & Lepot, I. (2015). Development and Application of a Multi-Disciplinary Multi-Regime Design Methodology of a Low-Noise Contra-Rotating Open-Rotor. *Volume 2C: Turbomachinery*, V02CT45A019. <https://doi.org/10.1115/GT2015-43432>
- [Leifsson & Koziel, 2015] Leifsson, L. & Koziel, S. (2015). Aerodynamic shape optimization by variable-fidelity computational fluid dynamics models: A review of recent progress. *Journal of Computational Science*, 10, 45–54. <https://doi.org/10.1016/j.jocs.2015.01.003>
- [Li et al., 2010] Li, G., Aute, V., & Azarm, S. (2010). An accumulative error based adaptive design of experiments for offline metamodeling. *Structural and Multidisciplinary Optimization*, 40, 137–155. <https://doi.org/10.1007/s00158-009-0395-z>
- [Li et al., 2018] Li, J., Cai, J., & Qu, K. (2018). Adjoint-based two-step optimization method using proper orthogonal decomposition and domain decomposition. *AIAA Journal*, 56(3), 1133–1145. <https://doi.org/10.2514/1.J055773>

- [Li, 2019] Li, Q. (2019). *Towards optimum swirl recovery for propeller propulsion systems*.
- [Li et al., 2015] Li, Q., Yangang, W., & Eitelberg, G. (2015). An investigation of tip vortices unsteady interaction for fokker 29 propeller with swirl recovery vane. *Chinese Journal of Aeronautics*, 29. <https://doi.org/10.1016/j.cja.2015.12.004>
- [Li & Zheng, 2017a] Li, Z. & Zheng, X. (2017a). Review of design optimization methods for turbomachinery aerodynamics. *Progress in Aerospace Sciences*, 93, 1–23. <https://doi.org/https://doi.org/10.1016/j.paerosci.2017.05.003>
- [Li & Zheng, 2017b] Li, Z. & Zheng, X. (2017b). Review of design optimization methods for turbomachinery aerodynamics. *Progress in Aerospace Sciences*, 93, 1–23. <https://doi.org/https://doi.org/10.1016/j.paerosci.2017.05.003>
- [Lickenbrock et al., 2020] Lickenbrock, M., Rumpfkeil, M., Beran, P., & Kolonay, R. (2020). Multi-fidelity, multidisciplinary analysis of an efficient supersonic air vehicle. <https://doi.org/10.2514/6.2020-2223>
- [Liu et al., 2018] Liu, H., Ong, Y.-S., & Cai, J. (2018). A survey of adaptive sampling for global metamodeling in support of simulation-based complex engineering design. *Structural and Multidisciplinary Optimization*, 57(1), 393–416. <http://link.springer.com/10.1007/s00158-017-1739-8>
- [Liu, 2012] Liu, J. (2012). Comparison of Infill Sampling Criteria in Kriging-based Aerodynamic Optimization. 10.
- [Lu et al., 2019] Lu, K., Jin, Y., Chen, Y., Yang, Y., Hou, L., Zhang, Z., Li, Z., & Fu, C. (2019). Review for order reduction based on proper orthogonal decomposition and outlooks of applications in mechanical systems. *Mechanical Systems and Signal Processing*, 123, 264–297. <https://linkinghub.elsevier.com/retrieve/pii/S0888327019300184>
- [Lumley et al., 1967] Lumley, J., Yaglom, A., & Tartarsky, V.I., E. (1967). The Structure of Inhomogeneous Turbulent flows. 166–177.
- [Mackman & Allen, 2010] Mackman, T. J. & Allen, C. B. (2010). Investigation of an adaptive sampling method for data interpolation using radial basis functions. *International Journal for Numerical Methods in Engineering*, n/a–n/a. <https://doi.org/10.1002/nme.2885>
- [Manlig & Koblasa, 2014] Manlig, F. & Koblasa, F. (2014). Design of simulation experiments using doe. *Applied Mechanics and Materials*, 693, 219–224. <https://doi.org/10.4028/www.scientific.net/AMM.693.219>
- [March & Willcox, 2012a] March, A. & Willcox, K. (2012a). Multifidelity airfoil shape optimization using adaptive meshing. *Structural and Multidisciplinary Optimization*, (46.1), 93–109.
- [March & Willcox, 2012b] March, A. & Willcox, K. (2012b). Multifidelity Approaches for Parallel Multidisciplinary Optimization. *12th AIAA Aviation Technology, Integration, and Operations (ATIO) Conference and 14th AIAA/ISSMO Multidisciplinary Analysis and Optimization Conference*.

- [Marinius, 2011] Marinius, B. G. (2011). *Multidisciplinary Optimization of Aircraft Propeller Blades*.
- [Martins & Lambe, 2013] Martins, J. & Lambe, A. (2013). Multidisciplinary design optimization: A survey of architectures. *AIAA Journal*, 51, 2049–2075. <https://doi.org/10.2514/1.J051895>
- [Martins et al., 2003] Martins, J., Sturdza, P., & Alonso, J. (2003). The complex-step derivative approximation. *ACM Trans. Math. Softw.*, 29, 245–262.
- [Mason et al., 2003] Mason, R. L., Gunst, R. F., & Hess, J. L. (2003). *Fractional Factorial Experiments*, (Chapter 7, 228–270). John Wiley & Sons, Ltd. <https://doi.org/https://doi.org/10.1002/0471458503.ch7>
- [Matheron, 1963] Matheron, G. (1963). Principles of geostatistics. *Economic Geology*, 58(8), 1246–1266. <https://doi.org/10.2113/gsecongeo.58.8.1246>
- [McKay et al., 1979] McKay, M. D., Beckman, R. J., & Conover, W. J. (1979). Comparison of three methods for selecting values of input variables in the analysis of output from a computer code. *Technometrics*, 21(2), 239–245. <https://doi.org/10.1080/00401706.1979.10489755>
- [Mehmani et al., 2015] Mehmani, A., Chowdhury, S., & Messac, A. (2015). Predictive quantification of surrogate model fidelity based on modal variations with sample density. *Structural and Multidisciplinary Optimization*, 52(2), 353–373. <https://doi.org/10.1007/s00158-015-1234-z>
- [Meng et al., 2018] Meng, L., Breitkopf, P., Le Quilliec, G., Raghavan, B., & Villon, P. (2018). Nonlinear shape-manifold learning approach: Concepts, tools and applications. *Archives of Computational Methods in Engineering*, 25. <https://doi.org/10.1007/s11831-016-9189-9>
- [Meng et al., 2015] Meng, L., Breitkopf, P., Raghavan, B., Mauvoisin, G., Bartier, O., & Heriot, X. (2015). Identification of material properties using indentation test and shape manifold learning approach. *Computer Methods in Applied Mechanics and Engineering*, 297, 239–257. <https://doi.org/10.1016/j.cma.2015.09.004>
- [Mifsud et al., 2016] Mifsud, M. J., MacManus, D. G., & Shaw, S. (2016). A variable-fidelity aerodynamic model using proper orthogonal decomposition: A Variable-Fidelity Aerodynamic Model Using POD. *International Journal for Numerical Methods in Fluids*, 82(10), 646–663. <https://doi.org/10.1002/flid.4234>
- [Mohammadi & Raisee, 2019] Mohammadi, A. & Raisee, M. (2019). Stochastic field representation using bi-fidelity combination of proper orthogonal decomposition and Kriging. *Computer Methods in Applied Mechanics and Engineering*, 357, 112589. <https://doi.org/10.1016/j.cma.2019.112589>
- [Morris & Mitchell, 1995] Morris, M. D. & Mitchell, T. J. (1995). Exploratory designs for computational experiments. 22.
- [Mukherjee et al., 2021] Mukherjee, S., Lu, D., Raghavan, B., Breitkopf, P., Dutta, S., Xiao, M., & Zhang, W. (2021). Accelerating large-scale topology optimization : state-of-the-art and challenges. *Archives of Computational Methods in Engineering*.

- [Myers, 1984] Myers, D. E. (1984). *Co-Kriging — New Developments*, 295–305. Springer Netherlands. [https://doi.org/10.1007/978-94-009-3699-7\\_18](https://doi.org/10.1007/978-94-009-3699-7_18)
- [Myers et al., 1989] Myers, R. H., Khuri, A. I., & Carter, W. H. (1989). Response surface methodology: 1966-1988. *Technometrics*, 31(2), 137–157. <http://www.jstor.org/stable/1268813>
- [Nachar et al., 2020] Nachar, S., Boucard, P.-A., Néron, D., & Rey, C. (2020). Multi-fidelity bayesian optimization using model-order reduction for viscoplastic structures. *Finite Elements in Analysis and Design*, 176, 103400. <https://doi.org/10.1016/j.finel.2020.103400>
- [Ng & Eldred, 2012] Ng, L. & Eldred, M. (2012). Multifidelity uncertainty quantification using non-intrusive polynomial chaos and stochastic collocation. <https://doi.org/10.2514/6.2012-1852>
- [Nguyen et al., 2010] Nguyen, C., Rozza, G., Phuong, D., Patera, A., Tenorio, L., Waanders, B., Mallick, B., Willcox, K., Biegler, L., Biros, G., Ghattas, O., Heinkenschloss, M., & Keyes, D. (2010). Reduced basis approximation and a posteriori error estimation for parametrized parabolic pdes; application to real-time bayesian parameter estimation.
- [Palar & Shimoyama, 2017] Palar, P. & Shimoyama, K. (2017). Multi-fidelity uncertainty analysis in cfd using hierarchical kriging. <https://doi.org/10.2514/6.2017-3261>
- [Parr et al., 2012] Parr, J., Keane, A. J., Forrester, A. I., & Holden, C. M. (2012). Infill sampling criteria for surrogate-based optimization with constraint handling. *Engineering Optimization*, 44(10), 1147–1166. <https://doi.org/10.1080/0305215X.2011.637556>
- [Parr et al., 2010] Parr, J. M., Holden, C. M. E., Forrester, A. I. J., & Keane, A. J. (2010). Review of Efficient Surrogate Infill Sampling Criteria with Constraint Handling. 10.
- [Paulson & Ragkousis, 2015] Paulson, C. & Ragkousis, G. (2015). *pykriging: A python kriging toolkit*. <https://doi.org/10.5281/zenodo.21389>
- [Peherstorfer et al., 2018] Peherstorfer, B., Willcox, K., & Gunzburger, M. (2018). Survey of Multifidelity Methods in Uncertainty Propagation, Inference, and Optimization. *SIAM Review*, 60(3), 550–591.
- [Pellegrini et al., 2018] Pellegrini, R., Serani, A., Diez, M., Wackers, J., & Queutey, P. (2018). Adaptive sampling criteria for multi-fidelity metamodels in CFD-based shape optimization. 11.
- [Perdikaris et al., 2015] Perdikaris, P., Venturi, D., Royset, J. O., & Karniadakis, G. E. (2015). Multi-fidelity modelling via recursive co-kriging and Gaussian–Markov random fields. *Proceedings of the Royal Society A: Mathematical, Physical and Engineering Sciences*, 471(2179), 20150018.
- [Perron et al., 2020] Perron, C., Rajaram, D., & Mavris, D. (2020). Development of a multi-fidelity reduced-order model based on manifold alignment. <https://doi.org/10.2514/6.2020-3124>

- [Phalippou et al., 2020] Phalippou, P., Bouabdallah, S., Breilkopf, P., Villon, P., & Zarroug, M. (2020). ‘On-the-fly’ snapshots selection for Proper Orthogonal Decomposition with application to nonlinear dynamics. *Computer Methods in Applied Mechanics and Engineering*, 367, 113120. <https://doi.org/10.1016/j.cma.2020.113120>
- [Philippe, 1999] Philippe, J.-L. (1999). Hélices aériennes. *Techniques de l'ingénieur*.
- [Picheny et al., 2013] Picheny, V., Wagner, T., & Ginsbourger, D. (2013). A benchmark of kriging-based infill criteria for noisy optimization. *Structural and Multidisciplinary Optimization*, 48(3), 607–626. <https://doi.org/10.1007/s00158-013-0919-4>
- [Piegl, 1991] Piegl, L. (1991). On nurbs: a survey. *IEEE Computer Graphics and Applications*, 11(1), 55–71. <https://doi.org/10.1109/38.67702>
- [Pierret, 2005] Pierret, S. (2005). Multi-objective and multi-disciplinary optimization of three-dimensional turbomachinery blades.
- [Pinto et al., 2017] Pinto, R. N., Afzal, A., D’Souza, L. V., Ansari, Z., & Mohammed Samee, A. D. (2017). Computational Fluid Dynamics in Turbomachinery: A Review of State of the Art. *Archives of Computational Methods in Engineering*, 24(3), 467–479.
- [Poethke et al., 2019] Poethke, B., Völker, S., & Vogeler, K. (2019). *Aerodynamic Optimization of Turbine Airfoils Using Multi-fidelity Surrogate Models*, 556–568. [https://doi.org/10.1007/978-3-319-97773-7\\_50](https://doi.org/10.1007/978-3-319-97773-7_50)
- [Pope, 2000] Pope, S. B. (2000). *Turbulent Flows*. Cambridge University Press. <https://doi.org/10.1017/CBO9780511840531>
- [Powell, 2001] Powell, M. (2001). Radial basis function methods for interpolation to function of many variables.
- [Queipo et al., 2005] Queipo, N. V., Haftka, R. T., Shyy, W., Goel, T., Vaidyanathan, R., & Kevin Tucker, P. (2005). Surrogate-based analysis and optimization. *Progress in Aerospace Sciences*, 41(1), 1–28. <https://doi.org/10.1016/j.paerosci.2005.02.001>
- [Raghavan et al., 2013] Raghavan, B., Breilkopf, P., & Tourbier, Y. (2013). Towards a space reduction approach for efficient structural shape optimization. *Structural Multidisciplinary Optimization*, 48, 987–1000. <https://doi.org/https://doi.org/10.1007/s00158-013-0942-5>
- [Raghavan et al., 2012a] Raghavan, B., Hamdaoui, M., Xiao, M., Breilkopf, P., & Villon, P. (2012a). A bi-level meta-modeling approach for structural optimization using modified pod bases and diffuse approximation. *Comput. Struct.*, 127(C), 19–28.
- [Raghavan et al., 2012b] Raghavan, B., Xiao, M., Breilkopf, P., & Villon, P. (2012b). Implicit constraint handling for shape optimisation with pod-morphing. *European Journal of Computational Mechanics*, 21(3-6), 325–336. <https://doi.org/10.1080/17797179.2012.719316>
- [Rajaei et al., 1994] Rajaei, M., Karlsson, S. K. F., & Sirovich, L. (1994). Low-dimensional description of free-shear-flow coherent structures and their dynamical behaviour. *Journal of Fluid Mechanics*, 258, 1–29. <https://doi.org/10.1017/S0022112094003228>

- [Rankine, 1865] Rankine, W. (1865). On the mechanical principles of the action of propellers. *Transaction of the Institute of Naval Architects*, 13–39.
- [Rasmussen & Williams, 2006] Rasmussen, C. E. & Williams, C. K. I. (2006). *Gaussian processes for machine learning* (3. print ed.). Adaptive computation and machine learning. MIT Press. OCLC: 552376743.
- [Regis, 2015] Regis, R. (2015). Trust regions in kriging-based optimization with expected improvement. *Engineering Optimization*, 1–23. <https://doi.org/10.1080/0305215X.2015.1082350>
- [Regis & Shoemaker, 2006] Regis, R. G. & Shoemaker, C. A. (2006). Improved Strategies for Radial basis Function Methods for Global Optimization. *Journal of Global Optimization*, 37(1), 113–135. <https://doi.org/10.1007/s10898-006-9040-1>
- [Regis & Shoemaker, 2013] Regis, R. G. & Shoemaker, C. A. (2013). Combining radial basis function surrogates and dynamic coordinate search in high-dimensional expensive black-box optimization. *Engineering Optimization*, 45(5), 529–555. <https://doi.org/10.1080/0305215X.2012.687731>
- [Regis & Wild, 2017] Regis, R. G. & Wild, S. M. (2017). CONORBIT: constrained optimization by radial basis function interpolation in trust regions. *Optimization Methods and Software*, 32(3), 552–580. <https://doi.org/10.1080/10556788.2016.1226305>
- [Reisenthel et al., 2006] Reisenthel, P., Love, J., Lesieutre, D., & Dillenius, M. (2006). Innovative fusion of experiment and analysis for missile design and flight simulation. <https://doi.org/10.14339/RTO-MP-AVT-135-23-pdf>
- [Reisenthel & Allen, 2014] Reisenthel, P. H. & Allen, T. T. (2014). Application of Multifidelity Expected Improvement Algorithms to Aeroelastic Design Optimization. *10th AIAA Multidisciplinary Design Optimization Conference*.
- [Rendall & Allen, 2007] Rendall, T. & Allen, C. (2007). *Multidimensional Aircraft Data Interpolation Using Radial Basis Functions*. <https://doi.org/10.2514/6.2007-4058>
- [Robinson et al., 2008] Robinson, T., Eldred, M., Willcox, K., & Haimes, R. (2008). Surrogate-based optimization using multifidelity models with variable parameterization and corrected space mapping. *Aiaa Journal - AIAA J*, 46, 2814–2822. <https://doi.org/10.2514/1.36043>
- [Robinson et al., 2006] Robinson, T., Willcox, K., Eldred, M., & Haimes, R. (2006). Multifidelity Optimization for Variable-Complexity Design. *11th AIAA/ISSMO Multidisciplinary Analysis and Optimization Conference*.
- [Rodriguez et al., 2000] Rodriguez, J., Renaud, J., Wujek, B., & Tappeta, R. (2000). Trust region model management in multidisciplinary design optimization. *Journal of Computational and Applied Mathematics*, 124, 139. [https://doi.org/10.1016/S0377-0427\(00\)00424-6](https://doi.org/10.1016/S0377-0427(00)00424-6)

- [Rozza et al., 2008] Rozza, G., Huynh, D. B. P., & Patera, A. T. (2008). Reduced Basis Approximation and a Posteriori Error Estimation for Affinely Parametrized Elliptic Coercive Partial Differential Equations: Application to Transport and Continuum Mechanics. *Archives of Computational Methods in Engineering*, 15(3), 229–275.
- [Ruan et al., 2020] Ruan, X., Jiang, P., Zhou, Q., Hu, J., & Shu, L. (2020). Variable-fidelity probability of improvement method for efficient global optimization of expensive black-box problems. *Structural and Multidisciplinary Optimization*, 62(6), 3021–3052. <https://doi.org/10.1007/s00158-020-02646-9>
- [Ruan et al., 2019] Ruan, X., Jiang, P., Zhou, Q., & Yang, Y. (2019). An improved co-kriging multi-fidelity surrogate modeling method for non-nested sampling data. <https://doi.org/10.18178/ijmerr.8.4.559-564>
- [Rumpfkeil et al., 2021] Rumpfkeil, M. P., Lickenbrock, M., Beran, P. S., & Kolonay, R. M. (2021). *Multi-fidelity, Aeroelastic Analysis and Optimization with Control Surface Deflections of an Efficient Supersonic Air Vehicle*. <https://doi.org/10.2514/6.2021-0732>
- [Sacks et al., 1989] Sacks, J., Welch, W. J., Mitchell, T. J., & Wynn, H. P. (1989). Design and analysis of computer experiments. *Statist. Sci.*, 4(4), 409–423. <https://doi.org/10.1214/ss/1177012413>
- [Safran, 2017] Safran (2017). *Open-rotor, Istres 2017*. [https://www.safran-group.com/fr/file/download/20171003\\_safran\\_evenement\\_open\\_rotor\\_istres\\_presse\\_vf.pdf](https://www.safran-group.com/fr/file/download/20171003_safran_evenement_open_rotor_istres_presse_vf.pdf).
- [Sahab et al., 2013] Sahab, M. G., Toropov, V. V., & Gandomi, A. H. (2013). 2 - a review on traditional and modern structural optimization: Problems and techniques. *Metaheuristic Applications in Structures and Infrastructures*, 25–47. Elsevier. <https://doi.org/10.1016/B978-0-12-398364-0.00002-4>
- [Saka et al., 2007] Saka, Y., Gunzburger, M., & Burkardt, J. (2007). Latinized, improved lhs, and cvt point sets in hypercubes.
- [Scott et al., 2011] Scott, W., Frazier, P., & Powell, W. (2011). The Correlated Knowledge Gradient for Simulation Optimization of Continuous Parameters using Gaussian Process Regression. *SIAM Journal on Optimization*, 21(3), 996–1026. <https://doi.org/10.1137/100801275>
- [Sefrioui et al., 2000] Sefrioui, M., Srinivas, K., & Periaux, J. (2000). Aerodynamic shape optimization using a hierarchical genetic algorithm. *Journal of Aircraft*.
- [Sen et al., 2018] Sen, R., Kandasamy, K., & Shakkottai, S. (2018). Multi-fidelity black-box optimization with hierarchical partitions. *Proceedings of the 35th International Conference on Machine Learning*, volume 80 of *Proceedings of Machine Learning Research*, 4538–4547. <http://proceedings.mlr.press/v80/sen18a.html>
- [Settles, 2010] Settles, B. (2010). Active Learning Literature Survey. 67.

- [Shan & Wang, 2010] Shan, S. & Wang, G. G. (2010). Survey of modeling and optimization strategies to solve high-dimensional design problems with computationally-expensive black-box functions. *Structural and Multidisciplinary Optimization*, 41(2), 219–241. <https://doi.org/10.1007/s00158-009-0420-2>
- [Shewry & Wynn, 1987] Shewry, M. C. & Wynn, H. P. (1987). Maximum entropy sampling. *Journal of Applied Statistics*, 14(2), 165–170. <https://doi.org/10.1080/02664768700000020>
- [Shinde et al., 2019] Shinde, V., Lacazedieu, E., Baj, F., Hoarau, Y., & Braza, M. (2019). Galerkin-free model reduction for fluid-structure interaction using proper orthogonal decomposition. *Journal of Computational Physics*, 396. <https://doi.org/10.1016/j.jcp.2019.06.073>
- [Shoesmith et al., 1987] Shoesmith, E., Box, G., & Draper, N. (1987). Empirical model-building and response surfaces. *The Statistician*, 37, 82–82.
- [Simpson et al., 1998] Simpson, T., Mauery, T., Korte, J., & Mistree, F. (1998). Comparison of response surface and kriging models for multidisciplinary design optimization. <https://doi.org/10.2514/6.1998-4755>
- [Simpson et al., 2001] Simpson, T., Poplinski, J., Koch, P. N., & Allen, J. (2001). Metamodels for Computer-based Engineering Design: Survey and recommendations. *Engineering with Computers*, 17(2), 129–150. <https://doi.org/10.1007/PL00007198>
- [Simpson et al., 2008] Simpson, T., Toropov, V., Balabanov, V., & Viana, F. (2008). Design and Analysis of Computer Experiments in Multidisciplinary Design Optimization: A Review of How Far We Have Come - Or Not. *12th AIAA/ISSMO Multidisciplinary Analysis and Optimization Conference*. <https://doi.org/10.2514/6.2008-5802>
- [Sirovich, 1987] Sirovich, L. (1987). Turbulence and the dynamics of coherent structures. i - coherent structures. ii - symmetries and transformations. iii - dynamics and scaling. *Quarterly of Applied Mathematics - QUART APPL MATH*, 45. <https://doi.org/10.1090/qam/910463>
- [Skinner & Zare-Behtash, 2017] Skinner, S. & Zare-Behtash, H. (2017). State-of-the-art in aerodynamic shape optimisation methods. *Applied Soft Computing*, 62. <https://doi.org/10.1016/j.asoc.2017.09.030>
- [Smarandache, 2008] Smarandache, F. (2008). Alternatives to pearson's and spearman's correlation coefficients. *SSRN Electronic Journal*. <https://doi.org/10.2139/ssrn.2725499>
- [Smola & Schölkopf, 2004] Smola, A. & Schölkopf, B. (2004). A tutorial on support vector regression. *Statistics and Computing*, 14, 199–222. <https://doi.org/10.1023/B%3ASTCO.0000035301.49549.88>
- [Sobieszczanski-Sobieski & Haftka, 1996] Sobieszczanski-Sobieski, J. & Haftka, R. (1996). *Multidisciplinary aerospace design optimization - Survey of recent developments*. <https://doi.org/10.2514/6.1996-711>

- [Sobol, 1967] Sobol, I. (1967). On the distribution of points in a cube and the approximate evaluation of integrals. *Ussr Computational Mathematics and Mathematical Physics*, 7, 86–112.
- [Song et al., 2018] Song, C., Yang, X., & Song, W. (2018). Multi-infill strategy for kriging models used in variable fidelity optimization. *Chinese Journal of Aeronautics*, 31(3), 448–456. <https://doi.org/10.1016/j.cja.2018.01.011>
- [Song et al., 2019a] Song, J., Chen, Y., & Yue, Y. (2019a). A General Framework for Multi-fidelity Bayesian Optimization with Gaussian Processes. 11.
- [Song et al., 2019b] Song, X., Lv, L., Sun, W., & Zhang, J. (2019b). A radial basis function-based multi-fidelity surrogate model: exploring correlation between high-fidelity and low-fidelity models. *Structural and Multidisciplinary Optimization*, 1–17.
- [Srinivas et al., 2010] Srinivas, N., Krause, A., Kakade, S., & Seeger, M. (2010). Gaussian process optimization in the bandit setting: No regret and experimental design. 1015–1022.
- [Stroh, 2018] Stroh, R. (2018). Planification d’expériences numériques en multi-fidélité: Application à un simulateur d’incendies. 255.
- [Sóbester et al., 2005] Sóbester, A., Leary, S. J., & Keane, A. J. (2005). On the Design of Optimization Strategies Based on Global Response Surface Approximation Models. *Journal of Global Optimization*, 33(1), 31–59. <http://link.springer.com/10.1007/s10898-004-6733-1>
- [Tang et al., 2005] Tang, C., Gee, K., & Lawrence, S. (2005). *Generation of Aerodynamic Data using a Design Of Experiment and Data Fusion Approach*. <https://doi.org/10.2514/6.2005-1137>
- [Taylor & Einbeck, 2013] Taylor, J. & Einbeck, J. (2013). Challenging the curse of dimensionality in multivariate local linear regression. *Computational Statistics*, 28(3), 955–976. <https://doi.org/10.1007/s00180-012-0342-0>
- [Thenon, 2017] Thenon, A. (2017). *Utilisation de méta-modèles multi-fidélité pour l’optimisation de la production des réservoirs*.
- [Toal, 2015] Toal, D. J. (2015). Some considerations regarding the use of multi-fidelity kriging in the construction of surrogate models. *Structural and Multidisciplinary Optimization*, 51, 1223–1245.
- [Toal, 2014] Toal, D. J. J. (2014). On the Potential of a Multi-Fidelity G-POD Based Approach for Optimization and Uncertainty Quantification. *Volume 2B: Turbomachinery*, V02BT45A002. <https://doi.org/10.1115/GT2014-25184>
- [Toal et al., 2008] Toal, D. J. J., Bressloff, N. W., & Keane, A. J. (2008). Kriging hyperparameter tuning strategies. *AIAA Journal*, 46(5), 1240–1252. <https://doi.org/10.2514/1.34822>
- [Ukeiley et al., 2001] Ukeiley, L., Cordier, L., Manceau, R., Delville, J., Glauser, M., & BONNET, J. (2001). Examination of large-scale structures in a turbulent plane mixing layer. part 2. dynamical systems model. *Journal of Fluid Mechanics*, 441, 67 – 108. <https://doi.org/10.1017/S0022112001004803>

- [van Rijn et al., 2018] van Rijn, S., Schmitt, S., Olhofer, M., van Leeuwen, M., & Bäck, T. (2018). Multi-fidelity surrogate model approach to optimization. *Proceedings of the Genetic and Evolutionary Computation Conference Companion on - GECCO '18*, 225–226. <https://doi.org/10.1145/3205651.3205757>
- [Veroy et al., 2003] Veroy, K., Prud'homme, C., & Rovas, D. (2003). A posteriori error bounds for reduced-basis approximation of parametrized noncoercive and nonlinear elliptic partial differential equations. *16th AIAA Computational Fluid Dynamics Conference*. <https://doi.org/10.2514/6.2003-3847>
- [Villemontheix, 2009] Villemontheix, J. (2009). Optimisation de fonctions coûteuses Modèles gaussiens pour une utilisation efficace du budget d'évaluations: théorie et pratique industrielle. 172.
- [Volpi et al., 2015] Volpi, S., Diez, M., Gaul, N. J., Song, H., Iemma, U., Choi, K. K., Campana, E. F., & Stern, F. (2015). Development and validation of a dynamic metamodel based on stochastic radial basis functions and uncertainty quantification. *Structural and Multidisciplinary Optimization*, 51(2), 347–368. <https://doi.org/10.1007/s00158-014-1128-5>
- [Wackers et al., 2020] Wackers, J., Visonneau, M., Ficini, S., Pellegrini, R., Serani, A., & Diez, M. (2020). Adaptive N-Fidelity Metamodels for Noisy CFD Data. *AIAA AVIATION 2020 FORUM*. <https://doi.org/10.2514/6.2020-3161>
- [Wang et al., 2019] Wang, H., Jin, Y., Sun, C., & Doherty, J. (2019). Offline Data-Driven Evolutionary Optimization Using Selective Surrogate Ensembles. *IEEE Transactions on Evolutionary Computation*, 23(2), 203–216. <https://doi.org/10.1109/TEVC.2018.2834881>
- [Wang et al., 2020] Wang, X., Kou, J., & Zhang, W. (2020). Multi-fidelity surrogate reduced-order modeling of steady flow estimation. *International Journal for Numerical Methods in Fluids*, 92(12), 1826–1844. <https://doi.org/https://doi.org/10.1002/flid.4850>
- [Xia et al., 2013] Xia, L., Raghavan, B., Brei tkopf, P., & Zhang, W. (2013). Numerical material representation using proper orthogonal decomposition and diffuse approximation. *Appl. Math. Comput.*, 224, 450–462. <https://doi.org/10.1016/j.amc.2013.08.052>
- [Xiao, 2016] Xiao, D. (2016). *Non-intrusive reduced order models and their applications*.
- [Xiao et al., 2017] Xiao, D., Fang, F., Pain, C., & Navon, I. (2017). A parameterized non-intrusive reduced order model and error analysis for general time-dependent nonlinear partial differential equations and its applications. *Computer Methods in Applied Mechanics and Engineering*, 317, 868–889. <https://doi.org/10.1016/j.cma.2016.12.033>
- [Xiao et al., 2010] Xiao, M., Brei tkopf, P., Coelho, R., Knopf-Lenoir, C., Sidorkiewicz, M., & Villon, P. (2010). Model reduction by cpod and kriging: Application to the shape optimization of an intake port. *Structural and Multidisciplinary Optimization*, 41. <https://doi.org/10.1007/s00158-009-0434-9>

- [Xiao et al., 2020] Xiao, M., Lu, D., Breitkopf, P., Raghavan, B., Dutta, S., & Zhang, W. (2020). On-the-fly model reduction for large-scale structural topology optimization using principal components analysis. *Structural and Multidisciplinary Optimization*, 1–22. <https://doi.org/10.1007/s00158-019-02485-3>
- [Xiao et al., 2018] Xiao, M., Zhang, G., Breitkopf, P., Villon, P., & Zhang, W. (2018). Extended co-kriging interpolation method based on multi-fidelity data. *Applied Mathematics and Computation*, 323, 120–131. <https://doi.org/10.1016/j.amc.2017.10.055>
- [Xu et al., 2014] Xu, S., Liu, H., Wang, X., & Jiang, X. (2014). A robust error-pursuing sequential sampling approach for global metamodeling based on voronoi diagram and cross validation. *Journal of Mechanical Design*, 136, 071009. <https://doi.org/10.1115/1.4027161>
- [Yao & Jaiman, 2016] Yao, W. & Jaiman, R. K. (2016). A harmonic balance technique for the reduced-order computation of vortex-induced vibration. *Journal of Fluids and Structures*, 65, 313–332. <https://doi.org/https://doi.org/10.1016/j.jfluidstructs.2016.06.002>
- [Ye & Pan, 2019] Ye, P. & Pan, G. (2019). Surrogate-based global optimization methods for expensive black-box problems: Recent advances and future challenges. 96–100. <https://doi.org/10.1109/IRCE.2019.00026>
- [Yondo et al., 2018] Yondo, R., Andrés, E., & Valero, E. (2018). A review on design of experiments and surrogate models in aircraft real-time and many-query aerodynamic analyses. *Progress in Aerospace Sciences*, 96, 23–61. <https://doi.org/10.1016/j.paerosci.2017.11.003>
- [Yondo et al., 2019] Yondo, R., Bobrowski, K., Andres, E., & Valero, E. (2019). *A Review of Surrogate Modeling Techniques for Aerodynamic Analysis and Optimization: Current Limitations and Future Challenges in Industry*, 19–33. [https://doi.org/10.1007/978-3-319-89988-6\\_2](https://doi.org/10.1007/978-3-319-89988-6_2)
- [Zhang et al., 2018] Zhang, Y., Han, Z.-H., & Zhang, K.-S. (2018). Variable-fidelity expected improvement method for efficient global optimization of expensive functions. *Structural and Multidisciplinary Optimization*, 58(4), 1431–1451.
- [Zheng et al., 2013] Zheng, J., Shao, X., Gao, L., Jiang, P., & Li, Z. (2013). A hybrid variable-fidelity global approximation modelling method combining tuned radial basis function base and kriging correction. *Journal of Engineering Design*, 24(8), 604–622. <https://doi.org/10.1080/09544828.2013.788135>
- [Zhou et al., 2017] Zhou, Q., Jiang, P., Shao, X., Hu, J., Cao, L., & Wan, L. (2017). A variable fidelity information fusion method based on radial basis function. *Advanced Engineering Informatics*, 32, 26–39.
- [Zimmermann & Görtz, 2010] Zimmermann, R. & Görtz, S. (2010). Non-linear reduced order models for steady aerodynamics. *Procedia Computer Science*, 1(1), 165–174. <https://doi.org/10.1016/j.procs.2010.04.019>

- [Ștefănescu et al., 2015] Ștefănescu, R., Sandu, A., & Navon, I. (2015). POD/DEIM reduced-order strategies for efficient four dimensional variational data assimilation. *Journal of Computational Physics*, 295, 569–595. <https://doi.org/10.1016/j.jcp.2015.04.030>
- [Žilinskas, 1992] Žilinskas, A. (1992). A review of statistical models for global optimization. *Journal of Global Optimization*, 2(2), 145–153. <http://link.springer.com/10.1007/BF00122051>